OPEN ACCESS

University of BRISTOL

This electronic thesis or dissertation has been downloaded from Explore Bristol Research, http://research-information.bristol.ac.uk

Author:
Showkat Ali, Syamir Alihan

Title:
Flow Over and Past Porous Surfaces

General rights
Access to the thesis is subject to the Creative Commons Attribution - NonCommercial-No Derivatives 4.0 International Public License. A copy of this may be found at https://creativecommons.org/licenses/by-nc-nd/4.0/legalcode This license sets out your rights and the restrictions that apply to your access to the thesis so it is important you read this before proceeding.

Take down policy
Some pages of this thesis may have been removed for copyright restrictions prior to having it been deposited in Explore Bristol Research. However, if you have discovered material within the thesis that you consider to be unlawful e.g. breaches of copyright (either yours or that of a third party) or any other law, including but not limited to those relating to patent, trademark, confidentiality, data protection, obscenity, defamation, libel, then please contact collections-metadata@bristol.ac.uk and include the following information in your message:

• Your contact details
• Bibliographic details for the item, including a URL
• An outline nature of the complaint

Your claim will be investigated and, where appropriate, the item in question will be removed from public view as soon as possible.

Flow Over and Past Porous Surfaces

By

SYAMIR ALIHAN SHOWKAT ALI

Department of Mechanical Engineering
University of Bristol

A dissertation submitted to the University of Bristol in accordance with the requirements of the degree of DOCTOR OF PHILOSOPHY in the Faculty of Engineering.

AUGUST 2018

Word count: 75,724

The capacity to learn is a gift;

The ability to learn is a skill;

The willingness to learn is a choice.

My Lord, increase me, and increase me in knowledge.

(Quran,20:114)

Abstract

With air travel continually rising, the effects of aircraft noise exposure have turned into a major global issue, which has direct consequences for the nation's economy. Many approaches have been taken to improve the quality and capacity of airports by adapting a new tighter noise regulations, and as a result, there have been a great deal of research directed by major aviation industries, namely the Embraer S.A., Airbus and Rolls-Royce to better understand the noise generation mechanism and the flow and noise control methods for a quieter aircraft.

In the present study, various airfoil self-noise mechanisms have been investigated, such as the blunt trailing-edge noise and the vortex-structure interaction noise, which is of relevance to the aircraft and wind turbine aerodynamic noise. With regard to the noise abatement applications, porous materials have been chosen as the passive flow and noise control method in the present work. The mechanisms of flow interaction and sound generation with the porous surface have been studied experimentally, for different configurations, namely the flat plate and blunt trailing-edge bodies with different porosities, permeability constants and surface roughness features. The noise generation mechanisms related to the flow-porous interaction have been investigated from both the aerodynamic and aeroacoustic points of view. The two main topics of interest are addressed here: (i) to investigate the zero pressure gradient boundary layer interaction with a permeable wall, and (ii) to investigate the effects of porous treatments on the blunt trailing-edge for flow and noise control. To carry out this task, various wind-tunnel investigations were conducted.

In the first experimental campaign, the interaction of a standard boundary layer with a rough porous surface has been investigated experimentally. The flow characteristics of a zero pressure gradient turbulent boundary layer flow have been tested using a long flat plate equipped

with several surface pressure transducers and pressure taps. In order to reveal the effects of the interaction of a boundary layer with a porous surface, three types of porous materials with different porosity and permeability constants are examined. To reveal the behaviour of turbulent flows over porous surfaces, measurements were performed for the boundary layer growth, energy content of the turbulent structure within the boundary layer and surface pressure fluctuations, before, over and after the porous test-section. The interaction of the flow with the porous substrate was found to significantly alter the energy cascade within the boundary layer. Results have also shown that the boundary layer interaction with the rough porous surfaces leads to an increase in the pressure fluctuations exerted on the wall, particularly at low frequencies. The near-field investigations have shown that the penetration of the boundary layer flow into the porous medium can generate an internal hydrodynamic field within the porous medium. This, in turn, reduces the frequency-energy content of the large boundary layer coherent structures and their spanwise correlation length.

In the second experimental campaign, the application of porous treatments at the blunt trailing-edge as a means of flow and aerodynamic noise reduction has been examined. An extensive experimental investigation is undertaken to study the effects of flow interaction with porous media, in particular in the context of the manipulation of flow over blunt trailing-edges and attenuation of vortex shedding. Comprehensive boundary layer and wake measurements have been carried out for a flat-plate with solid and porous blunt trailing-edges. Unsteady velocity and surface pressure measurements have also been performed to gain an in-depth understanding of the changes to the energy-frequency content and coherence of the boundary layer and wake structures as a result of the flow interaction with a porous treatment. Results have shown that permeable treatments can effectively delay the vortex shedding and stabilize the flow over the blunt edge via mechanisms involving flow penetration into the porous medium and discharge into the near-wake region. It has also been shown that the porous treatment can effectively destroy the spanwise coherence of the boundary layer structures and suppress the velocity and pressure coherence, particularly at the vortex shedding frequency. The flow-porous scrubbing and its effects on the near-the-wall and large coherent structures have also been studied. The emergence of a quasi-periodic recirculating flow-field inside highly permeable surface treatments

has also been investigated.

The results in the present work have identified several important mechanisms concerning the application of porous treatments for aerodynamic and aeroacoustic purposes, which are of great importance for the better understanding of the flow-porous interaction mechanisms and essential in controlling the generation of flow-induced noise in many engineering applications. The findings here can help the design and fabrication of more effective and tailored passive flow-control designs for specific applications.

Dedication and acknowledgements

Alhamdulillah, all praises to *Allah, the Most Gracious and the Most Merciful* of all, for the strengths, determinations, sustenance, guidance and blessing during the tenure of my research and completing the thesis.

My special appreciation and sincere gratitude go to my supervisor *Dr. Mahdi Azarpeyvand*, Reader in Aeroacoustic, for his supervision, utmost continuous support, guidance and motivation during the research period. Honestly, I didn't know much when I chose the aeroacoustic field as my Ph.D. research, which is also not related to the field I worked during my bachelor degree. It has been a tremendous change in my life journey. I simply enjoyed learning about the new subject although I found many difficulties through it. Certainly, it wasn't what I expected when I started my research. I always dreamed of applying my research concept in many aspects as I found it irresistible. In fact, I have always wanted to study things that involved improvement, controlling and are visible with my bare eyes. I managed to obtain all these experiences when I was assigned for an experimental-based research study, which gave me the opportunity to specialize in the area of my research. I would like to honestly thank again my supervisor for his immense knowledge of research and all his constructive comments, contributions of time and ideas, which were really helpful and inspiring throughout my Ph.D. journey. I would like to also appreciate the support of the *technicians* of the wind tunnel laboratory, Faculty of Engineering, University of Bristol for all the physical helps given that have facilitated a very smooth work of my research.

I would like to express my priceless love and sincere thanks to my beloved *parents, grandmother, brothers, and sister* for their fortitude, greatest support, prayers, and encouragement, mentally and spiritually at every stage of my personal and academic life over the years. My family will always be my number one priority in life, and every breath of my life and drop of blood in my body is devoted to each and every single person in my family. Moreover, I am very thankful to all my *colleagues and friends* for the valuable discussions, criticism, suggestions and particularly, the moral support and encouragement, which have kept me going through the past years. Thanks to everyone who have participated and contributed in many ways to the success of this study; I say thank you for giving me such a blessed and joyful time.

I wouldn't want miss using this opportunity to sincerely acknowledge the *University Malaysia Perlis (UniMAP)* and the *Government of Malaysia*, for providing financial assistance which buttressed me to perform my work comfortably. I would like to also gratefully acknowledge the financial support from *Embraer S.A.* which has significantly boost the growth of this research.

Thank you for an unforgettable experience!

Syamir Alihan Showkat Ali
Malaysia-UK
2014-2018

List of Publications

Some of the research work and results presented in this thesis have been published in journals or presented at international conferences. These publications serve as a foundation of the thesis and are listed as below,

Journal articles:

1. ***S. A. Showkat Ali***, M. Azarpeyvand, and C. R. Ilario da Silva, "Trailing-edge flow and noise control using porous treatments", *Journal of Fluid Mechanics*, vol. 850, pp. 83-119, 2018.

2. ***S. A. Showkat Ali***, M. Azarpeyvand, M. Szoke and C. R. Ilario da Silva, "Boundary layer flow interaction with a permeable wall", *Physics of Fluids* 30, 085111, 2018.

3. ***S. A. Showkat Ali***, M. Azarpeyvand, and C. R. Ilario da Silva, "Effect of porous trailing-edge on the blunt flat plate self-noise", *Journal of Sound and Vibration*, 2018. (*Manuscript Submitted*)

Conference papers:

4. ***S. A. Showkat Ali***, M. Szoke, M. Azarpeyvand and C. R. Ilario da Silva, "Turbulent flow interaction with porous surfaces", in *Proceedings of the 24th AIAA/CEAS Aeroacoustic Conference. Atlanta, Georgia. AIAA 2018-2801.*

5. ***S. A. Showkat Ali***, M. Azarpeyvand and C. R. Ilario da Silva, "Experimental study of porous treatment for aerodynamic and aeroacoustic purposes", in *Proceedings of the 23rd AIAA/CEAS Aeroacoustic Conference. Denver, Colorado. AIAA 2017-3358.*

6. ***S. A. Showkat Ali***, M. Azarpeyvand and C. R. Ilario da Silva, "Boundary layer flow interaction with porous surfaces", in *Proceedings of the 24th International Congress on Sound and Vibration*. *London, United Kingdom. ICSV 2017*.

7. ***S. A. Showkat Ali***, M. Szoke, M. Azarpeyvand and C. R. Ilario da Silva, "Trailing-edge bluntness flow and noise control using porous treatments", in *Proceedings of the 22nd AIAA/CEAS Aeroacoustic Conference*. *Lyon, France. AIAA 2016-3358*.

8. ***S. A. Showkat Ali***, X. Liu, and M. Azarpeyvand, "Bluff Body Flow and Noise Control Using Porous Media", in *Proceedings of the 22nd AIAA/CEAS Aeroacoustic Conference*. *Lyon, France. AIAA 2016-2754*.

9. ***S. A. Showkat Ali***, M. Azarpeyvand and C. R. Ilario da Silva, "Boundary layer interaction with porous surface and implications for aerodynamic noise reduction", in *Proceedings of the 23rd International Congress on Sound and Vibration*. *Athens, Greece. ICSV 2016*.

10. W. Elsahhar, ***S. A. Showkat Ali***, R. Theunissen, and M. Azarpeyvand, "An experimental investigation of the effect of bluff body bluntness factor on wake-vortex noise generation", in *Proceedings of the 24th AIAA/CEAS Aeroacoustic Conference*. *Atlanta, Georgia. AIAA 2018-3288*.

11. A. Cambray, E. Pang, ***S. A. Showkat Ali***, D. Rezgui, and M. Azarpeyvand, "Investigation towards a better understanding of noise generation from UAV propellers", in *Proceedings of the 24th AIAA/CEAS Aeroacoustic Conference*. *Atlanta, Georgia. AIAA 2018-3450*.

12. X. Liu, ***S. A. Showkat Ali***, and M. Azarpeyvand, "On the application of trailing-edge serrations for noise control from tandem airfoil configuration", in *Proceedings of the 23rd AIAA/CEAS Aeroacoustic Conference*. *Denver, Colorado. AIAA 2017-3716*.

13. X. Liu, ***S. A. Showkat Ali***, and M. Azarpeyvand, "Noise control for a tandem airfoil configuration using trailing-edge serration", in *Proceedings of the 24th International Congress on Sound and Vibration*. *London, United Kingdom. ICSV 2017*.

AUTHOR'S DECLARATION

I declare that the work in this dissertation was carried out in accordance with the requirements of the University's Regulations and Code of Practice for Research Degree Programmes and that it has not been submitted for any other academic award. Except where indicated by specific reference in the text, the work is the candidate's own work. Work done in collaboration with, or with the assistance of, others, is indicated as such. Any views expressed in the dissertation are those of the author.

SIGNED: ..... DATE: .....

NOMENCLATURE

Roman Symbols

A	Cross sectional area of porous sample [mm^2]
b_{ij}	Reynolds stress anisotropy tensor
C	Inertial loss term [m^{-1}]
C_d	Drag coefficient
C_{D_W}	Drag coefficient based on the wake velocity results
C_p	Pressure coefficient [$C_p = (p_i - p_\infty)/(0.5\rho U_\infty^2)$]
C_f	Skin friction coefficient
d	Wire diameter [μm] and pinhole diameter [mm]
d_p	Particle displacement [μm]
d_t	Steel pipe diameter (Calibration cone) [mm]
E	Output voltage [v]
f	Frequency [Hz]
f_s	Sampling frequency [Hz]
h	Plate thickness [mm]
h_s	Sand height [mm]
H	Boundary layer shape factor
k_1, k_2	Yaw coefficients
k	Average turbulent kinetic energy
l	Wire length [mm]
L_c	Sound pressure level [dB]
L_f	Length of the recirculation region [mm]

L_n	Nominal sound pressure level [dB]
L_v	Volume correction [dB]
L_x,L_z	Blunt plate streamwise and spanwise lengths [mm]
L_p,W_p	Porous section streamwise and spanwise lengths [mm]
L_{px}	Porous section streamwise length, length of the new porous sections [mm]
L_s	Porous sample sampling length [mm]
l_t	Steel pipe length (Calibration cone) [mm]
N_T	Number of total records
$p^{'}$	Fluctuating surface pressure [Pa]
p_i	Static pressure at the i^{th} location [Pa]
p_∞	Free-stream static pressure at the i^{th} location [Pa]
P_a	Ambient pressure [Pa]
P_{corr}	Pressure correction [dB]
P_r	Reference pressure [Pa]
Ra	Arithmetical mean height (average roughness) [μm]
Rp	Maximum profile peak height [μm]
Rv	Maximum profile valley depth [μm]
Re	Reynolds number
$R_{p'_i p'_j}$	Wall pressure cross-correlation coefficient between transducers p'_i and p'_j
Q	Volumetric flow rate [m^3/s]
$R_{p'_i p'_i}$	Wall pressure autocorrelation coefficient of transducers p'_i
$R_{u'_i u'_i}$	Velocity autocorrelation coefficient
St	Strouhal number
SPL	Sound pressure level [dB]
t_{ii}	Integral time scale[s]
t_s	Sampling time [s]
t_x	Porous thickness in the direction of the x-ray beam [mm]
U_∞	Free stream velocity [m/s]
U	Mean velocity [m/s]

U_{rms}	Root mean square velocity $[m/s]$
U_c	Convection velocity $[m/s]$
U_{cal1}, U_{cal2}	Calibration velocities $[m/s]$
U_p	Instantaneous velocity field based on particle displacement $[m/s]$
$u^{'}, v^{'}$	Streamwise and vertical velocity fluctuations $[m/s]$
$\overline{u^{'}u^{'}}, \overline{v^{'}v^{'}}$	Reynolds normal stress components $[m^2/s^2]$
$-\overline{u^{'}v^{'}}$	Reynolds shear stress components $[m^2/s^2]$
u_τ	Wall friction velocity $[m/s]$
V_V	Volume of void space $[mm^3]$
V_T	Total volume of the porous sample $[mm^3]$
W_p	Test-section spanwise length $[mm]$
x, y, z	Cartesian coordinates $[mm]$
$\overline{X}^{\cdot}$	Bootstrap mean
x_{vc}	Vortex core region $[mm]$
y_i	Profile height function
$y^{'}$	Vertical coordinate defined from the top surface of the plate $[mm]$

Greek Symbols

α	Angle
ε	Porous sample void fraction
$\widehat{\sigma}_{boot}$	Bootstrap standard deviation
ρ	Fluid density $[kg/m^3]$
φ	Porosity [%]
κ	Permeability $[m^2]$
$\lambda_1, \lambda_2, \lambda_3$	Eigenvalues of the Reynolds stress tensors
$\bigtriangleup p$	Pressure drop across the porous sample [Pa]
Δf	Frequency resolution [Hz]
Δt	Time step $[s]$
δ_{ij}	Kronecker delta function

ν	Kinematic viscosity of air [m^2/s]
ν_D	Darcian velocity [m/s]
ν_p	Pore velocity [m/s]
τ	Time delay [s]
$\tau_{ij}^{'}$	Traceless tensor
τ_{ij}°	Isotropic tensor
δ	Boundary layer thickness [mm]
δ^*	Boundary layer displacement thickness [mm]
δ_p	Pressure difference [Pa]
θ	Boundary layer momentum thickness [mm], angle [deg]
μ_c	Uncertainty of the form drag
μ_k	Uncertainty of the permeability
μ_x	Linear attenuation coefficient of the porous sample
I_1, I_2, I_3	First, second and third invariant of b_{ij}
II, III	Second and third anisotropy invariants
$\underline{n_1}, \underline{n_2}, \underline{n_3}$	Orthonomal basis
ϕ_{uu}	Power spectral density of velocity fluctuations [dB/Hz]
ϕ_{pp}	Power spectral density of pressure fluctuations [dB/Hz]
$\gamma^2_{p_i' p_j'}$	Wall pressure coherence between transducers p_i' and p_j'
Λ_p	Spanwise coherence length [mm]
$\Phi(p_i', p_j')$	Cross-power spectral density between transducers p_i' and p_j' [Pa^2/Hz]
$\Phi(p_i', p_i')$	Cross-power spectral density from transducer p_i' [Pa^2/Hz]
$\Phi(p_j', p_j')$	Cross-power spectral density from transducer p_j' [Pa^2/Hz]
$\Phi(u', p')$	Cross-power spectral density between velocity and pressure signals [(m/s) Pa/Hz]
$\Phi(u', u')$	Streamwise velocity spectra [(m/s)^2 Pa/Hz]
$\Phi(p', p')$	Pressure spectra [Pa^2/Hz]
ξ_x, ξ_y, ξ_z	streamwise, vertical and spanwise separation distance [mm]

Superscripts

+	Normalization based on viscous time scale (u_τ^2/ν) or viscous length scale (ν/u_τ)

Acronyms

AIM	Anisotropy Invariant Map
APE	Acoustic Perturbation Equation
AR	Aspect Ratio
BL	Boundary Layer
CCD	Charge-Coupled Device
CFD	Computational Fluid Dynamics
FFT	Fast Fourier Transform
FoV	Field of View
IUPAC	International Union of Pure and Applied Chemistry
IW	Interrogation Window
LES	Large Eddy Simulation
LPCE	Linearized Perturbed Compressible Equations
MPP	Micro Perforated Panel
MDF	Medium Density Fibre
PIV	Particle Image Velocimetry
PPI	Pores Per Inch
PSD	Power Spectral Density
QALY	Quality-Adjusted Life Years
WS	Window Size
LBM	Lattice Boltzmann Method
LES	Large Eddie Simulation

TABLE OF CONTENTS

List of Tables

List of Figures

CHAPTER 1

INTRODUCTION

1.1 Research motivation

Over the last two decades, a great deal of national and regional programmes have been proposed to reinforce research aimed at further reduction of environmental noise exposure, in particular, the aviation noise from aircraft operations. With air travel continually rising, the effects of aircraft noise exposure have turned into a major public and global issue, which has direct economic impacts on the nation's gross domestic product. There are millions of people who are victims of noise pollution daily, especially those who live under flight pathways. Studies show that the aircraft induced noise not only creates a nuisance by affecting amenity, quality of life, productivity and learning, but also significantly impairs well-being [1]. Research today shows that about 10-20% of hospital admissions and deaths from heart disease and stroke are associated with this aircraft noise. It also causes anxiety, speech complications, hearing difficulties, sleep disturbance, tinnitus, annoyance, cognitive impairment, physiological stress, depression, etc. A detailed summary of the various health impacts based on the different levels of aviation noise exposure are given in Table 1.1. For instance, the table shows that chances of developing heart disease (cardiovascular) occur at aircraft noise level of 65 dB Leq, 16hr and more, with 0.1 and 0.2 QALYs per person, respectively, *i.e.* QALYs or quality-adjusted life years

indicates the average person loses due to the noise effects.

Table 1.1: Noise exposure levels of different adverse health effects. *(Leq=equivalent continuous sound level; Lnight=average sound pressure level over 1 night; Lden=avaerage sound pressure level over all days in a year; figures in each dB column refers to the number of QALYs lost per person as a result of the health effect)* [1, 2]

Health Effect	**Noise metric**	**Noise Band**				
		50 dB	**55 dB**	**60 dB**	**65 dB**	**70 dB**
Cardiovascular – AMI	Leq,16hr				(0.1)	(0.2)
Sleep disturbance	Lnight	(0.005)	(0.007)	(0.010)	(0.013)	(0.017)
Cognitive impairment	Leq,16hr		(0.1)	(0.1)	(0.2)	(0.3)
Hypertensive stroke	Leq,16hr	(0.1)	(0.3)	(0.4)	(0.6)	(0.8)
Hypertensive dementia	Leq,16hr	(0.3)	(0.5)	(0.8)	(1)	(1.3)
Annoyance	Lden	(0.1)	(0.2)	(0.3)	(0.5)	(0.7)

Moreover, according to the World Health Organization, the traffic noise-related effects cause a loss of up to 1.6 million disability-adjusted life years (DALYs) in the western European region, which cost up to £100 billion per annum. This includes an estimation of cumulative loss of about 903,000, 654,000, 61,000 and 45,000 DALYs due to sleep disturbance, annoyance, heart disease and child's cognitive impairment, respectively. In response to this, aircraft manufacturers and researchers are pushed to develop high-pay-off technologies and new designs in an effort to make a quieter aircraft. The Advisory Council for Aeronautics Research in Europe (ACARE) highlighted the goals to reduce aviation noise by 50%, equivalent to a 10 dB reduction and correspondingly, to secure a sustainable future for the European aviation industry by the year 2020. More recently, the Federal Aviation Administration (FAA) has initiated the 'Stage 5 Airplane Noise Standards' policy to ensure the latest robust noise reduction technology is integrated into new aircraft designs, ensuring they run at least 7 decibels (dBs) quieter compared to the aircraft in the current fleet. Hence, in order to mitigate the current aircraft noise issues and meet the global goals, one needs to understand the underlying physics associated with the aircraft noise generation, in particular the different aircraft noise sources. The noise source breakdown at take-off and flight path for a twin-engine long-range transport aircraft is shown in Fig. 1.1. It can be observed that the engine noise, mainly from the jet and fan, is the major contributor to the overall aircraft signature during the take-off operation. In contrast, the airframe noise, especially the high-lift devices and landing gears noise sources are shown to contribute the most to the overall aircraft

noise signature during the approach operation. Generally, most of the research has focussed on tackling the most dominant component, *i.e.* engine noise of the aircraft, leading to a significant reduction in engine noise over the past decades. Hence, with the advancement of low-noise aircraft engine, airframe noise now has become the major noise source during the aircraft's take-off and approach phase, which is of particular interest in the present study and should be explored more within future studies.

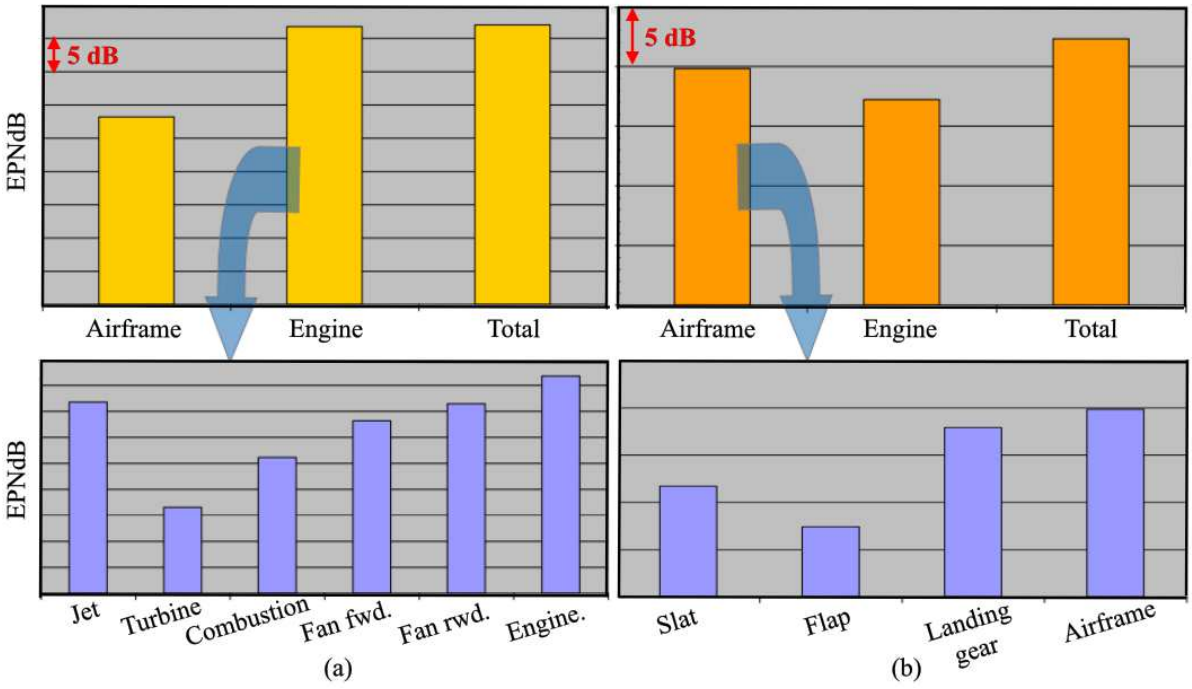

Figure 1.1: Noise source breakdown at the flight (a) take-off phase and (b) approach phase, for the twin-engine long range transport aircraft [3].

Besides concentrating on the impact of aviation noise solely, another strongly interrelated field has also been considered in the present study, namely the noise generated from wind turbines. Wind power is becoming one of the fastest growing renewable energy sources, which has enforced governments worldwide to mandate the predicted increase in wind power from 150 TWh in 2008 to 1068 TWh per annum by 2030 [4]. Figure 1.2 shows an example of typical modern wind turbines and an idealised picture of the outer blade moving through the air, with major aerodynamic and aeroacoustic influence on the wind turbine blades. The increase in the wind power demands over the years mean that many more wind turbines need to be installed, inevitably nearer to

more people and their homes. The results from the survey conducted on the perception and annoyance due to wind turbine noise [5] have shown that the noise from the wind turbines has been perceived to be annoying to people and is anticipated to be more annoying than other industrial noises at an equal level. This highlights the need for more stringent environmental regulation and certifications to address wind turbine noise.

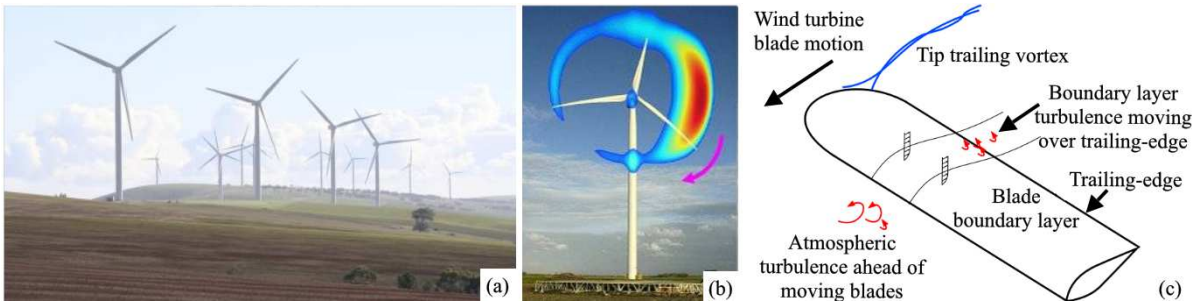

Figure 1.2: (a) Clement Gap wind farm, (b) Sound levels from turbine blade locations (Red contour zone: greater sound intensities) [6], (c) The flow over a wind turbine blade tip [7].

Thus, in order to overcome the potential increase in the environmental nuisance due to the aircraft and wind turbine noise, a great deal of research has been directed towards better understanding the noise generation mechanism and the development of an effective and robust flow and noise control technologies.

The unique adaptations of the owl's flexible wings and intricate feathers for a silent flight have served as a motivation for numerous engineers and scientists to reduce the flow-induced noise through serrations, porosity and elasticity, particularly to address the noise from the airframe, wind turbines, propellers, and fans. Owls fly in a very similar way to an aircraft at the high angle of attack when approaching/landing. The flow-induced noise sources of the owl are often associated with the pseudo-turbulent pressure fluctuations in the wing boundary layers and the owl's legs [8], which also resemble the airframe noise sources, with much lower-noise generation. The use of owl wings and feathers for assessing various airframe noise reduction techniques, such as serrations and porous trailing-edges have been comprehensively studied by many researchers, principally by investigating the features of the leading-edge comb [9–12], the trailing-edge fringe [9–11, 13, 14] and the downy wing surface [10–13, 15] of the owl wing/ feathers. Amongst all the other features of the owl, downy wing surface, in particular, have

received considerable interest due to its simple yet efficient surface/ structure characteristics for noise reduction capabilities. Kroeger *et al.* [11] revealed that the downy surface (a) allows the penetration of a thin film of air between the feathers through evenly distributed porosity structure, and (b) acts as a lubricant which enables quiet motion of the feathers as they slide. Inspired by these intrinsic-delicate-structures of the owl, specifically the porosity of the feathers, the present study will emphasise the use of 'porous structured materials' as a passive flow control method. Besides the owl's wings, the other nature-inspired ideas related to the porous structure are bones, rocks and zeolite, as shown in Fig. 1.3.

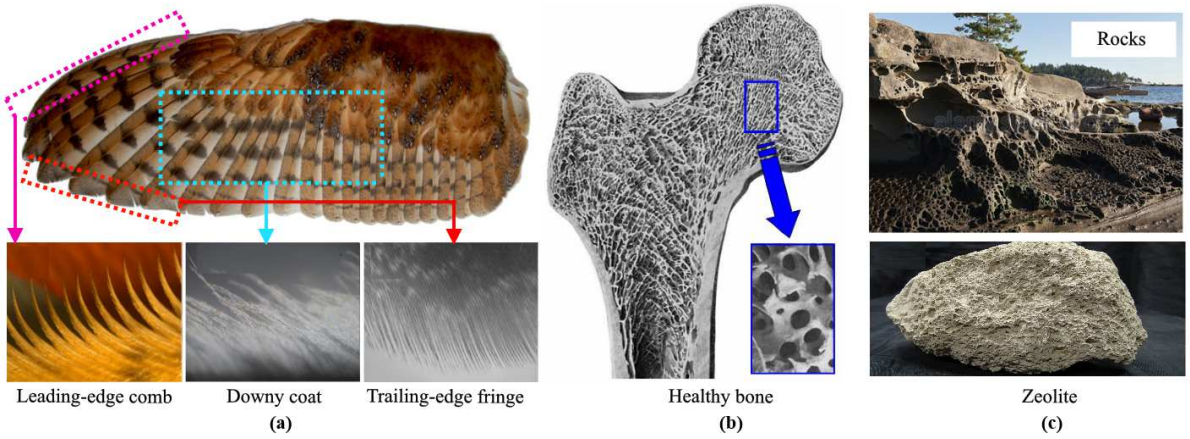

Figure 1.3: Bio-inspired fluid-flow porous structure, (a) The owl hush kit [16], (b) Human's bone structure [17], (c) Rocks/ Zeolite [18].

The use of porous materials for flow control and heat transfer is a multi-billion dollar business worldwide. The application of porous materials for flow and thermal purposes has received considerable academic and industrial attention over the past five decades, particularly in the areas of fluid mechanics, aerospace, underwater vehicles, etc. Of particular interest, the mechanisms of flow interaction and sound generation with the porous surface are investigated for different configurations, such as the flat plates with surface roughness and permeability and blunt edge bodies, which encompasses of various flow and noise problems. As part of this work-package, various airfoil self-noise mechanisms defined by Brooks *et al.* [19] have been investigated, such as the blunt trailing-edge noise and the vortex-structure interaction noise. The detail explanations of these noise mechanisms are given in Section 2.1. The importance of

the subject at hand provides motivation to the intensive experimental research, primarily in the area of flow-induced noise; *i.e.* controlling the flow and noise simultaneously using the porous material, as a passive flow control method and to improve the flow-physics understanding related to the porous medium as a whole. The results obtained from this study can lead to an unforeseen impact on the broad spectrum of industrial applications.

1.2 Research objectives

The goal of this study is to improve our understanding of the effect of porous surfaces on the fluid-flow for aerodynamic and aeroacoustic purposes. In order to optimize the flow and noise control, it is imperative to better understand the physics of the flow transport through porous media for different aero-structures' applications by carrying out a systematic set of extensive experimental investigations. To that end, the following objectives are addressed in this study:

i. To understand the interaction of flow with porous material experimentally over a wide range of Reynolds numbers, involving the metal-type porous foams with different mechanical properties and flow resistivity.
ii. To utilize porous materials for flow/noise control purposes for a range of aero-structures' applications. The following applications are envisaged to be of direct use and interest: flow and noise control using porous materials for airfoil self-noise and blunt edges noise.
iii. To investigate the flow field manipulation and boundary layer modifications on the noise producing flow structures as a result of the porous treatment and their potential implications on noise generation.
iv. To demonstrate the aerodynamic and the associated noise control of porous treatments.

1.3 Research scope and present challenges

The present study addresses a principal and industrially high-impact research whose understanding requires fundamental and extensive experimental research. The study provides original results for aerodynamics and aeroacoustics of porous materials, useful for a wide range of engineering applications, such as aerospace, chemical, energy, etc. Although the research will be

carried out at a fundamental level, all cases chosen are those encountered in real-world applications and are of great importance to the industry. The understanding of the flow interaction with porous materials has, however, remained limited due to the complexity of the problem, measurement difficulties and strong dependence of modelling techniques on empirical values. Although the main part of the research involves experimentation, the empirical data will be of great help for improving the existing computational fluid dynamics (CFD) models for treating flow/porous interaction problems. To the researcher's knowledge, this study is the only comprehensive research work in the field of porous materials for flow-induced noise/vibration control in the aerospace industry and encompasses all aspects of flow instability, noise generation and controlling mechanisms.

1.4 Outline of the dissertation

Extensive experimental studies on flow over and past the porous surfaces have been performed in order to better understand the effect of porous material for flow-induced noise control. The thesis is organized as follows. A comprehensive review of the literature concerning the applications of porous materials for aerodynamic and aeroacoustic purposes has been presented in Chapter 2. The experimental setup including the experimental facilities, measurement systems and the instrumentation techniques is described in Chapter 3. A brief description of the test-rig model configurations used in this study is further reviewed in Chapters 5 and 6, respectively. Chapter 4 provides a detailed overview of the characterization of porous materials including methods used to measure and evaluate the porosity, permeability and surface roughness of the porous material. The mechanisms of flow interaction and sound generation with the porous surface have been presented in Chapter 5. In this chapter, the effect of the porous surface on the boundary layer and their energy content, the pressure exerted on the surface with and without the porous treatment, flow velocity and pressure correlation, coherence and the formation of the internal hydrodynamic field and its dependency on the flow penetration critical length have been discussed. Chapter 6 outlines an inclusive and systematic experimental investigation study on various aspects of flow-porous interaction, such as the aerodynamic forces, break-up of boundary layer coherent

structures, flow penetration, emergence of an internal hydrodynamic field, flow discharge and vortex shedding attenuation. Finally, Chapter 7 concludes the thesis and summarizes the findings concerning the application of porous materials for aerodynamic and aeroacoustic applications.

1.5 Research contribution

This dissertation exposes the performance of the passive flow and noise control techniques related to the applications of porous materials for aerodynamic and aeroacoustic purposes. The principal contributions of this research are summarised below:

i. A detailed characterization of porous material in regards to its volume porosity, permeability and surface roughness has been performed using the non-intrusive computed tomographic scanning, in-house built permeability test-rig and non-contact profilometer Scantron Proscan 2100 analysis tools, respectively. The information gathered here will be used as an indicator and foundation to parametrize the type of materials. Data gathered eloquently delineates the performance capabilities of the porous material used in the relevant applications Chapters 5 and 6.

ii. A set of benchmark methodologies are provided to install miniature transducers inside porous materials without damaging the intricate structures within the porous domain, which can be used as a tool for the measurement of wall pressure fluctuations and its performance evaluation and analysis.

iii. A detailed classification of the integral parameters and boundary layer profiles under turbulent boundary layers with and without the porous treatment has been presented. Despite the fact that the research regarding the fluid-flow interaction with porous material has been extensively studied in the literature, there is hardly any published information on the mean velocity, turbulence intensity of the boundary layer profile over a porous surface.

iv. The results obtained experimentally in the present study give more insights into understanding the effect of the porous material on the flow above it, where the effect of micro-scale measurement is taken into consideration compared to that of the numerical analysis in the literature. The discrepancy between the experiment and simulation mostly lies on

the difficulties to generally set the boundary conditions for the fluid-permeable interfaces without ignoring the effect of friction over the porous surface, flow penetration and the emergence of the hydrodynamic field inside the porous medium. These effects, however, are able to be quantified, to a large extent, in the present experimental studies.

v. Simultaneous measurements of the surface pressure fluctuations and velocity fluctuations (velocity-pressure correlation/ coherence) in the boundary layer and wake have been studied to demonstrate the changes on the boundary layer flow structures, including the spatio-temporal characteristics of the boundary layer structures in streamwise and lateral directions, which is responsible for the wall pressure generation.

vi. In order to evaluate the possibility of the emergence of any hydrodynamic field inside the porous medium, a benchmark investigation has been conducted by filling the porous medium with fine grain sand at different heights. The process is quite complex and meticulous due to the intricate structure of the porous material.

vii. The critical length of the porous sections to enable a proper flow penetration and to achieve effective flow control has been investigated. The emergence of the quasi-periodic internal hydrodynamic field and its relationship with the porous treatment length has also been quantified using the pressure autocorrelation and velocity-pressure coherence studies.

viii. The experimental results obtained in this research can be used and exploited in the longer-term for future projects, and one of the near future works planned is to investigate the use of isotropic and functionally graded anisotropic porous treatments to control the generation of aerodynamic noise from different configurations.

CHAPTER 2

LITERATURE REVIEW

This chapter provides a comprehensive survey of the literature related to the possible applications of porous materials for aerodynamic and aeroacoustic purposes. Of particular interest is the investigation of the effects of the application of porous materials for bluff bodies, airfoil leading and trailing-edges and blunt trailing-edges. The literature is discussed under a number of headings. Section 2.1 discusses the aerodynamic noise sources and some of the basic flow and noise control theories. Section 2.2 gives a review of the aerodynamic flow control technologies, including the active and passive control methods used for various applications. Section 2.3 provides a list of references concerning the application of porous materials as a passive flow/ noise control method, in particular for bluff bodies, airfoil and blunt trailing-edges. The studies concerning the effect of roughness for the rough porous-type surfaces are detailed in § 2.4. Section 2.5 contains the references concerned with the existing theoretical analysis for flow and noise control using porous media and their limitations prior to the current work. The literature review provided here is focuses on some of the most relevant papers in each of the above-mentioned areas and the significant research outcomes, which are in line with the scope of the present experimental study.

2.1 Airfoil self-noise mechanisms

Turbulent flows and aerodynamically generated noise and vibration are ubiquitous in various engineering applications, in particular for those involving bluff bodies and airfoils. Aerodynamic noise is associated with the noise generated by unsteady turbulent flow, which is also referred to as the flow-induced noise or aeroacoustics. The airfoil self-noise generation, known as one of the main contributor for flow-induced noise and vibration is associated with the interaction of the airfoil boundary layer with the airfoil components, such as the trailing-edge and wing-tip (Brooks *et al.* [19]). The airfoil bluntness, laminar boundary layer instability interaction with the trailing-edge and the flow separation from the airfoil surface are amongst other sources of noise from airfoils. A brief description of the airfoil noise sources and the associated noise generation mechanisms is given as follows,

(a) **Turbulent boundary layer trailing-edge noise**

The trailing-edge noise is caused by the interaction of the turbulent boundary layer with the blade trailing-edge, which is the case for the airfoils used in jet engines, rotor blades and high lift devices as well as the wind turbines. The boundary layer becomes turbulent at higher Reynolds number owing to the early transition, where a large extent of randomly arranged vortical structures being present in the vicinity of the trailing-edge, see Fig. 2.1. The noise generation mechanism of this case is associated with the abrupt change in the boundary layer and the pressure difference acting on the airfoil pressure and suction side, leading to the acoustic waves emission. The disorganized small-scale structures in the boundary layer result in a broadband type acoustic radiation, which is the main source of the high-frequency noise (750 $Hz < f < 2000\ Hz$).

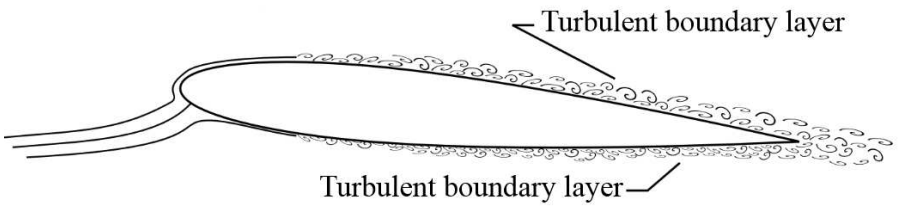

Figure 2.1: Turbulent boundary layer trailing-edge interaction noise [19, 20].

(b) **Laminar boundary layer noise**

The laminar boundary layer noise is generated due to the presence of viscous shear forces acting on the fluid and the airfoil surface. The underlying mechanism related to this case is almost similar to that of the trailing-edge turbulent boundary layer noise, which is believed to be due to the interaction of the non-linear boundary layer instabilities with the blade/ airfoil surface. The laminar boundary (no fluctuations) is usually amplified coherently at relatively low to moderate Reynolds number ($50000 \leqslant Re \leqslant 500000$), due to flow perturbations over a separated shear layer or the laminar separation bubble in the trailing-edge vicinity, which can be related to the instability mechanisms. As shown in Fig 2.2, the instability waves produced tend to roll-up into vortical structures, and the interaction between these vortical structures with the trailing-edge will eventually scatter the acoustic waves, which propagates upstream of the blade/ airfoil and triggered the formation of the new instability waves [21, 22]. The instability waves are also attributed to the large spanwise coherent structures, leading to the emission of high-intensity tonal frequency [22]. The boundary layer instability noise occurs at low Reynolds number for aerofoil at low angles of attack is caused by the non-linear coupling between the trailing-edge sound waves and the laminar boundary layer Tollmien-Schlichting (T-S) instability waves, resulting in strong vortex shedding tones. The laminar boundary layer instability noise generated through the vortex shedding is a tonal type noise, which can be avoided using various flow control tools. For instance, the well-defined tonal peaks are often anticipated in the low-velocity flow, mainly for small-scale airfoils, such as the glider, cooling fan, compressors, submarines, unmanned air vehicles, etc.

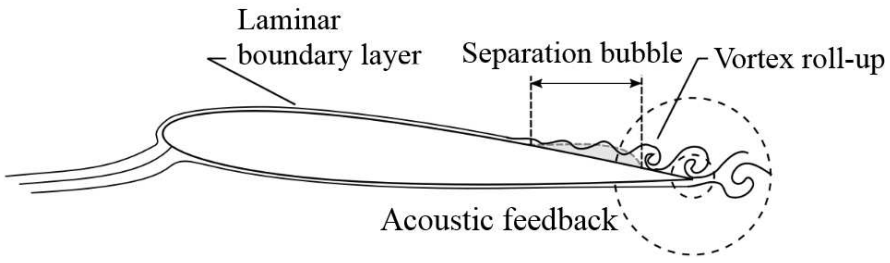

Figure 2.2: Laminar boundary layer instability noise [19, 20].

(c) **Tip noise**

The tip noise is a common mechanism encountered on finite airfoils/ wings, which is attributed to the formation of the vortex on a wing tip, as shown in Fig. 2.3. The tip noise is believed to be one of the aerodynamic noise sources, especially for the modern wind turbine [7]. The underlying mechanism related to this case is believed to be due to the interaction of the airfoil tip turbulence with the blade tip/ surface, where the wing tip vortices are usually in the highly unsteady turbulent form and hence generate noise. A steady wing tip vortex, on the other hand, is able to convect the fluctuating energy content within the boundary layer region passing the tip edge and correspondingly generates noise, which is similar to that of the noise emission mechanism seen in Fig. 2.1. The tip noise is a broadband noise source which is not fully understood and difficult to quantify.

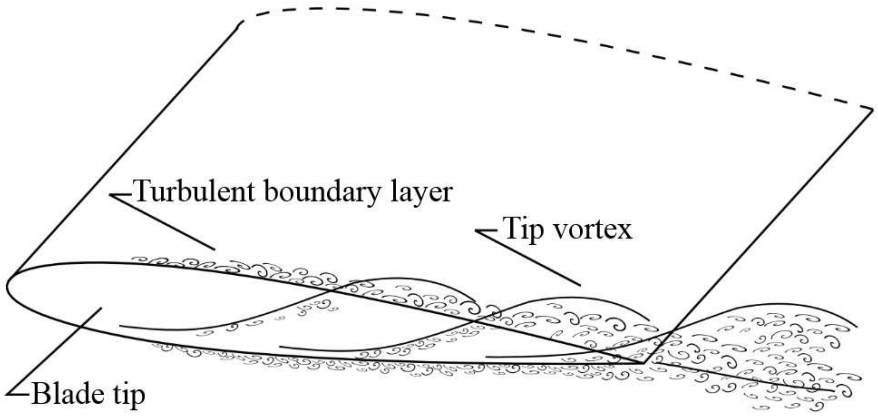

Figure 2.3: Tip noise [19, 20].

(d) **Separation and stall noise**

At high angles of attack, the flow velocity on the airfoil can lead to a condition referred to as the 'deep stall' which is merely due to the separated shear layer which occurs further upstream on the airfoil suction side, see Fig. 2.4. The occurrence of the large-scale flow separation is associated with the formation of large-scale vortex shedding structures, which is the primary mechanism responsible for the generation of the low-frequency noise [19]. The stall generated noise is a broadband type noise which is quite difficult to quantify and locate.

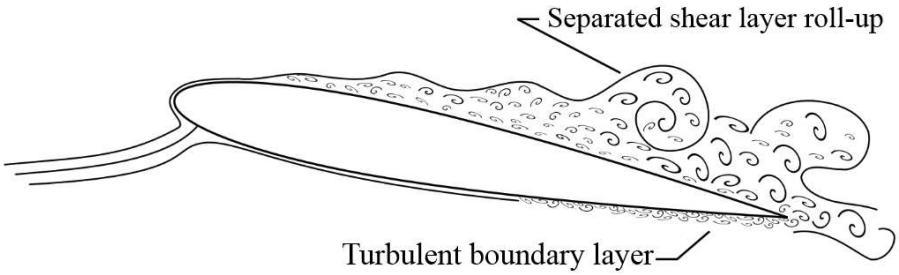

Figure 2.4: Stall, separation noise [19, 20].

(e) **Trailing-edge bluntness vortex shedding noise**

The blunt trailing-edge is fundamentally associated with the existence of large vortex shedding structures, which occurs behind the trailing-edge over a recirculating region, as shown in Fig.2.5(a). The vortex structure, unlike in the turbulent boundary layer, occurs in the small separated region in the blunt trailing-edge proximity, near the wake location. The vortex shedding developed is limited to narrow band frequencies (*i.e.* tonal nature), based on the trailing-edge bluntness thickness and the corresponding free-stream velocity (the relationship can be demonstrated as a function of Strouhal number St, where the vortex shedding frequency is about St=0.2 for bluff bodies over a large range of Reynolds number [23]). The vortex shedding phenomena can also be attributed to the large spanwise coherent structures [22] over the associated frequency band. The blunt trailing-edge with periodic vortex shedding structures can lead to the emission of high-intensity bluntness vortex shedding tonal peak, which this can be avoided by removing the bluntness effect or using the appropriate passive or/ and active control method on the surface of the blade/ airfoil.

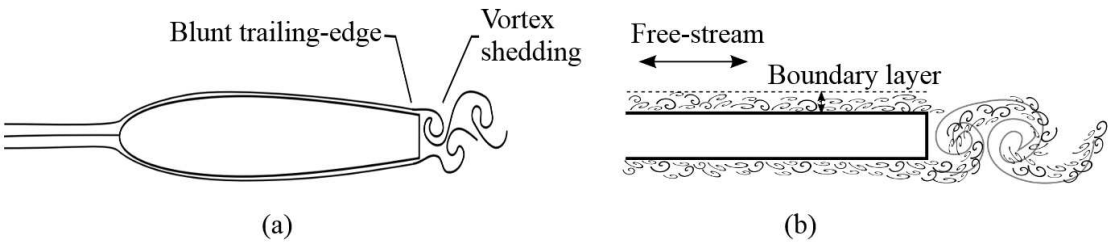

Figure 2.5: Blunt trailing-edge noise (a) airfoil and (b) flat plate [19, 20].

This case is of particular interest to the present study and the noise reduction techniques prior to

blunt trailing-edges for a flat plate configuration (see Fig. 2.5(b)) will be demonstrated hereinafter.

2.2 Flow and noise control methods

The ability to control, alter and manipulate the flow-field is of great importance in order to obtain a desired change in the fluid flow and its corresponding aerodynamic performance. Accordingly, various aerodynamic flow control technologies have been developed and being attempted in many multi-disciplinary science and technology applications over the past few decades. The conventional applications include, drag reduction, lift enhancement, noise suppression and mixing augmentation, which is imperative to achieve several engineering goals such as, the transition delay or advancement, avoiding separation and turbulence enhancement or suppression [24]. To successfully achieve all of these goals simultaneously is rather challenging, not to mention that one goal needs to be compromised with the other for the preferred design goals. In other words, pursuing one goal, in some cases can have an adverse effect on another goal, which such adverse effect could be inevitable. The interrelation between the aerodynamic flow control goals is shown in Fig. 2.6.

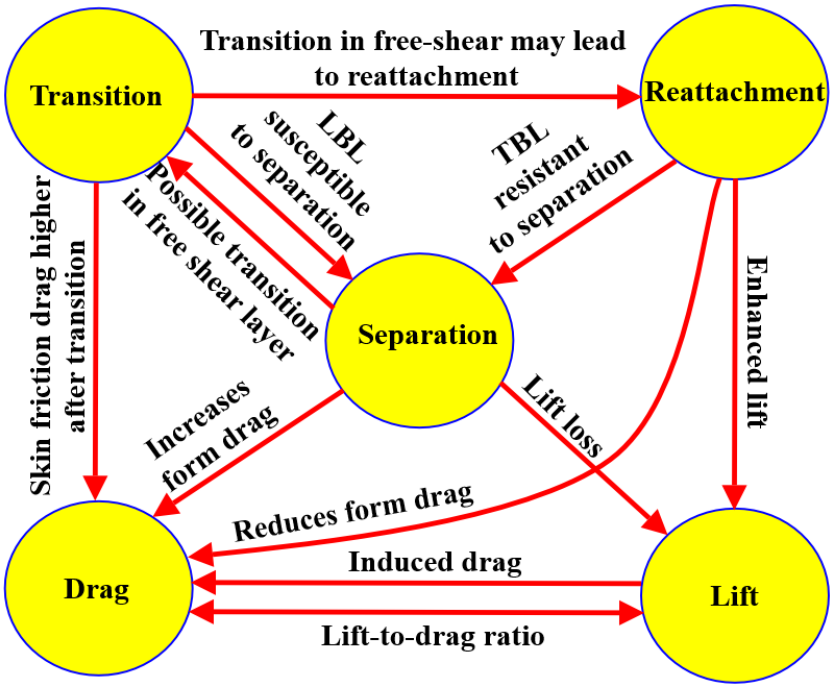

Figure 2.6: Partial representation of interrelation between flow control goals [24] (LBL: Laminar boundary layer, TBL: Turbulent boundary layer).

As can be seen, a potential conflict can take place if one requires enhancing the lift with no drag penalty simultaneously. Likewise, it is quite difficult to improve the quality of the aerodynamic performance and noise reduction mutually. Therefore, in order to compromise and realize the desired designated goals, an ideal flow control method is required. The flow control methods include the active flow control method, the passive control method or the combination of both the active and passive control methods.

2.2.1 Active flow control method

Active control techniques are described by the implementation of devices that introduce energy or auxiliary power into the flow. This system is generally more desirable than the passive control system due to its adaptability (*i.e.* the system can be turned on or off as required) and the large potential in modifying and controlling the flow. Howewer, such systems require additional energy and costs due to maintenance. Active control method can be divided into two different approaches, namely the predetermined and interactive methods. In the case of predetermined methods, the energy input is introduced without considering the condition of the flow-field. Examples include the lift enhancement and drag reduction using oscillatory blowing [25] and jet vectoring using piezoelectric actuators [26]. The interactive method, on the other hand, involves adjusting the power input controller continuously based on the measurement sensor, which comprises either an open or a closed loop system to control the flow-field parameter. Table 2.1 summarizes selections of different control method and the flow control goals using the active control techniques. Images of some of the active flow control methods are shown in Fig. 2.7.

2.2.2 Passive flow control method

The passive flow control techniques are generally related to the shape optimization and/ or customizing the physical properties of the body. The implementation of these type of methods do not require any external energy sources and the system is more sophisticated in terms of its reliability, cost and maintenance capabilities. As the main drawback, passive methods are typically less efficient than the active methods, specifically in situations that need control flexibility based on the structural response. Due to the high interest in the use of passive

systems, different passive flow control methods, such as control rods [27, 28], splitters [29, 30], O-rings [31], helical wires [32], dimple [33, 34], hairy flaps [35], longitudinal groove [36], surface treatments [37], serrations [38–42], morphing [43] and porous treatments [44–46] have been examined over the years for improving the aerodynamic performance of such devices or suppress vortex shedding and reduce flow induced noise and vibration. Table 2.2 summarizes selections of different control method and the flow control goals using the passive control techniques. Images of some of the passive flow control methods are shown in Fig. 2.8.

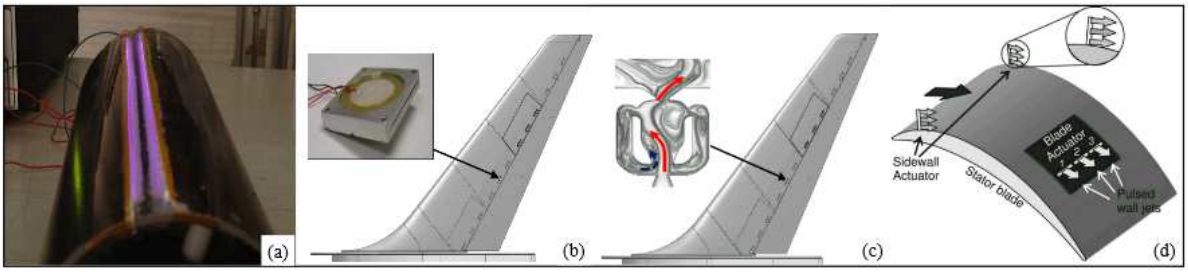

Figure 2.7: Examples of active flow control methods. (a) Plasma actuator attached on a PVC cylinder [Source: Smart Blade], (b) Synthetic jet actuators for adaptive control [Source: Barron Associate], (c) Sweeping jets [47], (d) Pulsed wall jets [48].

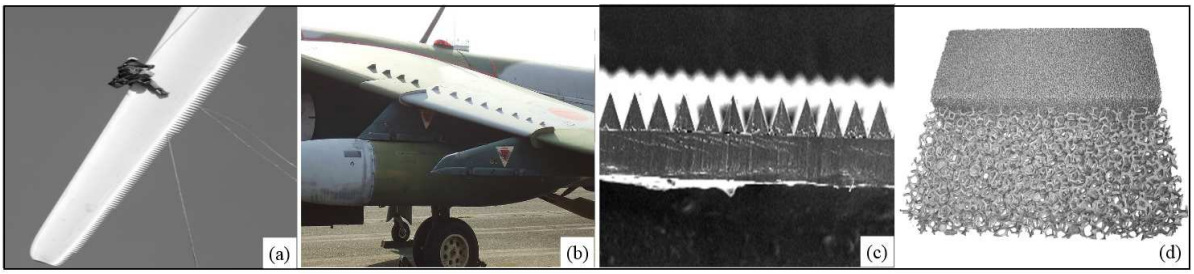

Figure 2.8: Examples of passive flow control methods. (a) Trailing-edge serration [49], (b) Miniature vortex generators (MVGs) [50], (c) Riblets [51], (d) Porous materials [52].

Table 2.1: Summary of the different flow control objectives using the active control techniques.

Reference	Control objective	Control method	Remarks
Mostafa et al. (1996) [53]	Control of jets	Pulsating vortex generating jets	Jet spreading over the continuous vortex generator jets
Suzuki et al. (2004) [54]		Electromagnetic flat actuators	Modified the large scale vortex structure significantly
Tamburello & Amitay (2008) [55]		Single synthetic jets	Enhanced mixing, deflects majority of the jet flow
Liepmann & Nosenchuk (1982) [56]	Delay transition (Laminar-to-turbulence transition)	Periodic heating/ fluid mounted heating elements	Elimination of the T-S wave, increasing the transition of the Reynolds number
Gobert et al. (2000) [57]		Disturbance generator	Substantial delay of transition
Wright & Nelson (2007) [58]		Suction	Delayed the desired transition, maintain aerodynamic performance
Lanchman (1961) [56], Gad-el-Hak et al. (1998) [59]	Separation control	Shaping, transpiration, wall-jets, suction, moving walls	Enhanced skin friction, delay separation
Cai et al. (2014) [60]		Pulsed air jets	Significant delay of separation, increase the lift by up to 10%-15%.
Artana et al. (2003) [61]	Wake vortex control	Electro-hydrodynamic actuators	Modifying the shear stresses of the fluid layers and the size of the mean recirculation region
Greenblatt D. et al. (2008) [62]		Retrofitted devices decoupled from the conventional method	Manipulation of the vortex street, breaking up vortices
Gupta M. (2011) [63]		Sinusoidal perturbations by low aspect ratio induced flap (LAROF)	Tilting the vortex plane at high Reynolds number, quicker decay of vortices
Williams and Amato (1989) [64]	Drag control	Continuous or pulsating base bleed	Reduce the pressure drag, modified the flow in the separated region
Schoppa and Hussain (1998) [65]		Large-scale flow forcing using rugged actuators	Streak stabilization, suppress/ prevent vortex formation, reduce/ avoid drag
Seifert et al. (2015) [66]		Steady suction and pulsed blowing	Drag reduction can be achieved with different test configurations, not optimal for the circular arc shape designed test

Table 2.2: Summary of the different flow control objectives using the passive control techniques.

Reference	Control objective	Control method	Remarks
Parker et al. (2011) [67]	Control of jets	Thin wing ring	Substantial reduction in the turbulence intensities in the jet mixing layer, suppression of vortex formation
Chen et al. (2015) [68]		Passive windward suction combined with leeward jet	Suppression of the instantaneous lift forces, reduction in TKE levels in the wake
Ost et al. (2000) [69]	Delay transition (Laminar-to-turbulence transition)	Oblique roughness elements	Significantly delays the flow with K-type transition, deformation of T-S waves with lower growth rate
Fransson (2015) [50]		Miniature vortex generators (MVGs)	Substantial delay of transition, reduce skin-friction drag and successfully attenuates the oblique waves
Favier et al. (2009) [70]	Separation control	Self-adaptive hairy coating	Drag reduction by up to 15%, decrease in lift fluctuations by about 40% and stabilization of the wake
Shan et al. (2014) [71]		Static vortex generators	Reduction in the size of the separation zone by up to 80%
Chen et al. (2008) [72]	Wake vortex control	Suction/ jet flow (holes)	Suppression of the unsteady vortex shedding and manipulation of the alternating vortex shedding
Huang (2011) [73]		Triple-start helical grooves	Suppression of the vortex induced vibration (VIV), reduction in the maximum cross-flow VIV amplitude by up to 64%
Gao et al. (2015) [74]		Surface roughness (sand with different particle diameters)	Vortex shedding frequency increases with increase in surface roughness and decreases displacement response
Bearmen and Owen (1998) [75]	Drag control	Spanwise sinusoidal wavy plate	Reduction of drag by up to 30%, complete suppression of vortex shedding
Mimeau et al. (2014) [76]		Porous layer	Significant drag reduction using thin layer of porous layer with intermediate permeability
Zhou et al. (2015) [77]		Surface roughness (sand paper)	Mean drag coefficient and rms of the lift coefficient decrease with increase in surface roughness

2.3 Porous material as the passive flow control method

The use of porous material has prompted a large number of studies with an aim to better understand the underlying mechanisms of flow control, with researchers approaching the problem mainly from theoretical and numerical perspectives. The porous materials have been used for the control of aerodynamic noise and vibration for various engineering applications, such as bluff bodies, blunt edges and airfoils. It has been generally shown that the use of porous treatments can lead to the stabilization of turbulence, vortex shedding suppression, control of flow instabilities and also reduction of noise from airfoils. In what follows, a comprehensive review of the application of porous materials for bluff body vortex shedding and noise control, airfoil noise control and the blunt trailing-edge flow and noise control is provided.

2.3.1 Vortex shedding and noise control

The fundamental problem of flow over bluff bodies and the issue of suppression of vortex shedding, lift and drag fluctuations and noise generation have been the subject of extensive research. The use of porous treatments, as a passive flow control method, has also attracted much attention and has extensively been studied in the past two decades. Bhattacharyya *et al.* [44] and Bhattacharyya & Singh [78] showed that the use of porous wraps for round cylinders lead to significant reduction of drag, control of vortex shedding and dampening of the structure oscillations compared to a bare cylinder. Experimental studies conducted by Sueki *et al.* [79] showed that the use of open-cell metal foam wraps for an isolated single circular cylinder can lead to significant noise reduction by stabilizing the vortices and the turbulence structure within the wake region, see Fig. 2.9.

Naito & Fukagata [45] have shown that porous treatments for flow control of a single cylinder are more effective at high Reynolds numbers where the growth of instability in the boundary and shear layers would be delayed by the porous surface and therefore the critical Reynolds number for laminar-to-turbulent transition would be shifted. It was also shown that in the fully turbulent regime, a wide low energy region would be created in the near-wake and the unsteady nature of the flow-field would be largely stabilized. Figure 2.10 clearly shows that the use of porous treatments can lead to the stabilization of the shear layer in the vicinity of the cylinder

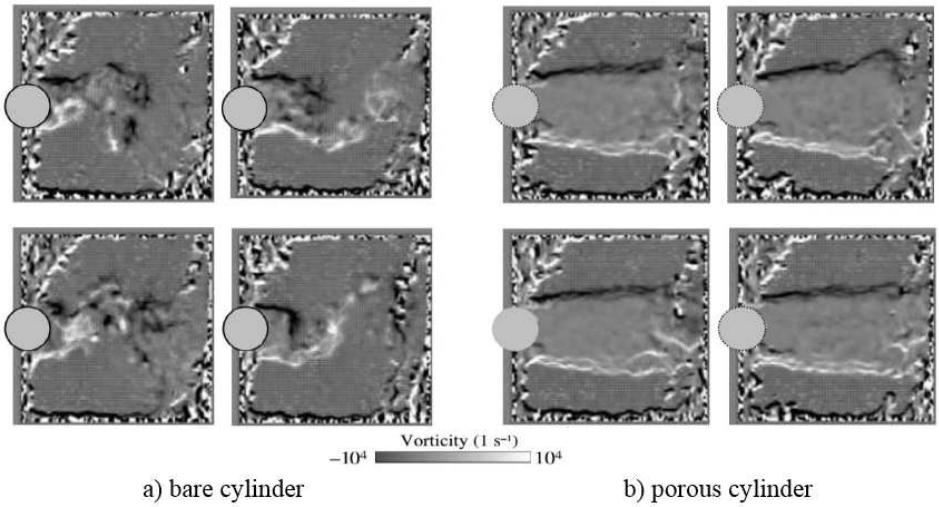

Figure 2.9: Instantaneous wake vorticity for bare cylinder and porous metal [79].

weakening the spanwise vortices in the near wake and suppressing the small-scale structures due to the streamwise vortices, resulting in more two-dimensional flow behaviour compared to that of the untreated cylinder case.

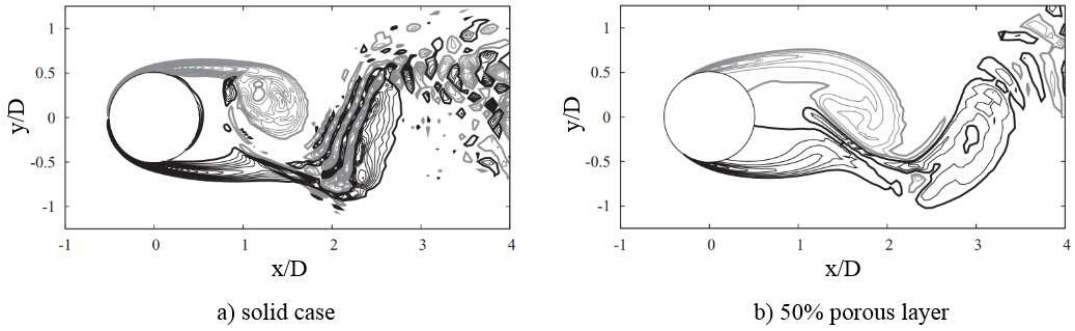

Figure 2.10: Instantaneous vorticity field, (Re=1000, 3D DNS): (a) solid case and (b) 50 % porous layer; Contour lines: $-15 \leq \omega_z \leq 15$ with increment of 0.6; black, $\omega_z > 0$; gray, $\omega_z < 0$; thick lines, $\omega_z \pm 0.6$ [45].

Furthermore, an unsteady CFD simulation carried out by Liu *et al.* [46] showed that the implementation of porous coatings can lead to the stabilization of the wake flow, reduction of the cylinder fluctuations and ultimately significant reduction of radiated noise by up to 20 dB, as shown in Fig. 2.11, particularly at the vortex shedding frequencies. The results also showed the changes to the velocity slip condition in the case of porous surface and the flow penetration

into the porous medium. Liu *et al.* [80] also investigated the influence of porous coatings on the near-wake structures of a round cylinder and showed that the porous cover can significantly change the flow characteristic of the cylinder near-wake by detaching the recirculation zone, which consequently results in the reduction of aerodynamic forces acting on the cylinder.

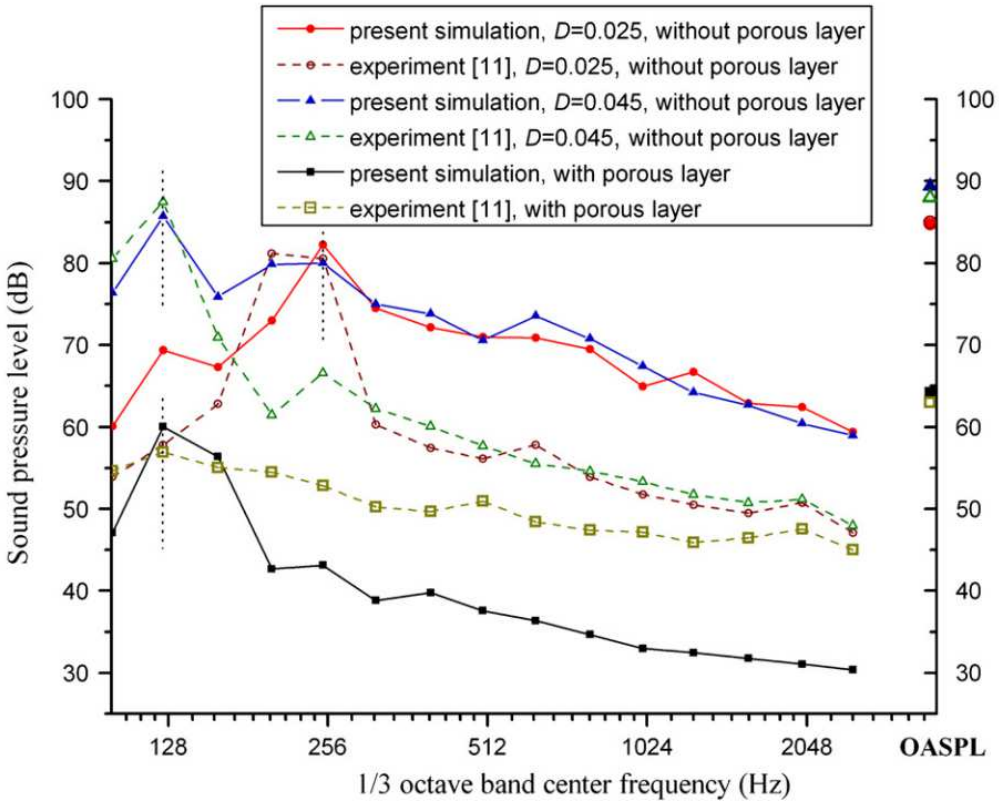

Figure 2.11: Comparison of the predicted aerodynamic noise of Liu *et al.* [46] with the measured results (experiment[11]) of Sueki *et al.* [79].

More recently, Liu *et al.* [81] studied the flow characteristics within the gap region of two round cylinders using unsteady CFD and demonstrated that the overall noise level can be reduced by up to 15 dB by using the porous covers, which is believed to be due to the stabilization of the gap flow and reduction of turbulence impingement on the rear cylinder. The results in Fig. 2.13 show that a significant reduction of the noise amplitude can be seen at the first dominant tonal frequency and the overall broadband frequency range, particularly at high porosity constant.

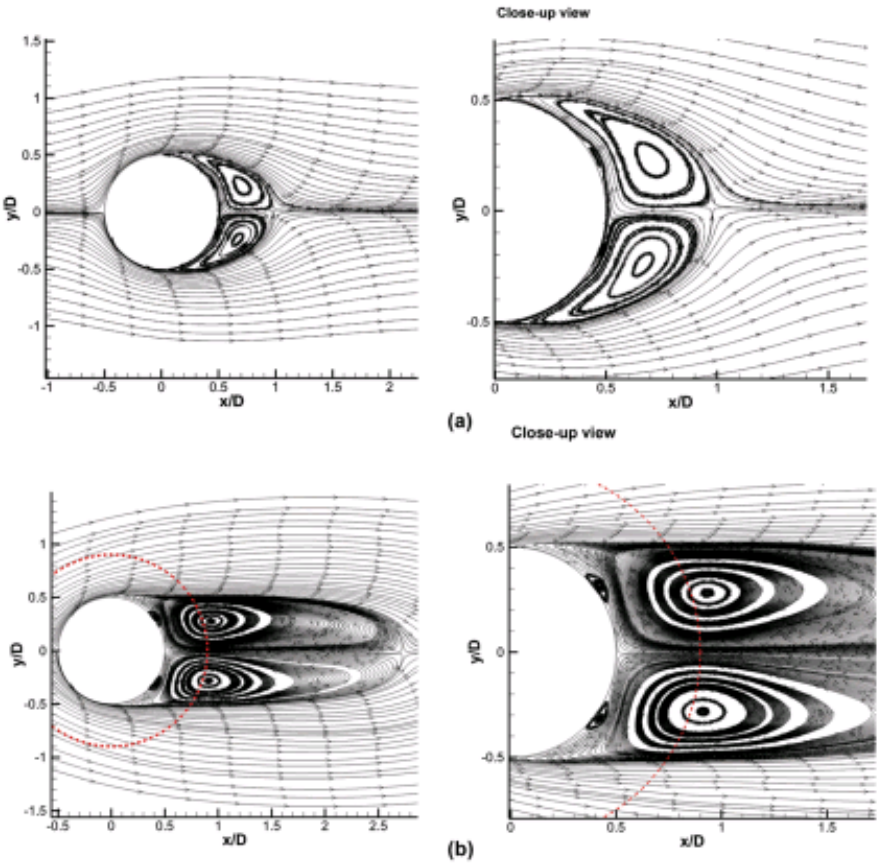

Figure 2.12: Time-mean streamlines: (a) smooth cylinder; (b) PMC cylinder (dashed line denotes porous surface [80].

2.3.2 Airfoil noise control

The reduction of airframe noise and airfoil self-noise using porous treatments have also been the subject of some recent research activities. Substantial research has been directed towards the application of porous materials for the reduction of airfoil trailing-edge noise. As one of the very first works, Fink and Bailey [82] performed some experimental studies on the possibility of noise reduction from high-lift devices by applying porous treatments to the flap trailing-edge and slat leading-edge of a high lift device. They found that the flap noise can generally be reduced by about 2-3 dB over a moderate frequency range and that using a perforated slat leading-edge can also lead to 2 dB reduction over a large frequency range. Revell *et al.* [83] studied the application of porous treatments for airframe systems and showed that an appropriate porous treatment in the vicinity of a flap side-edge can significantly reduce the flap side-edge contribution to

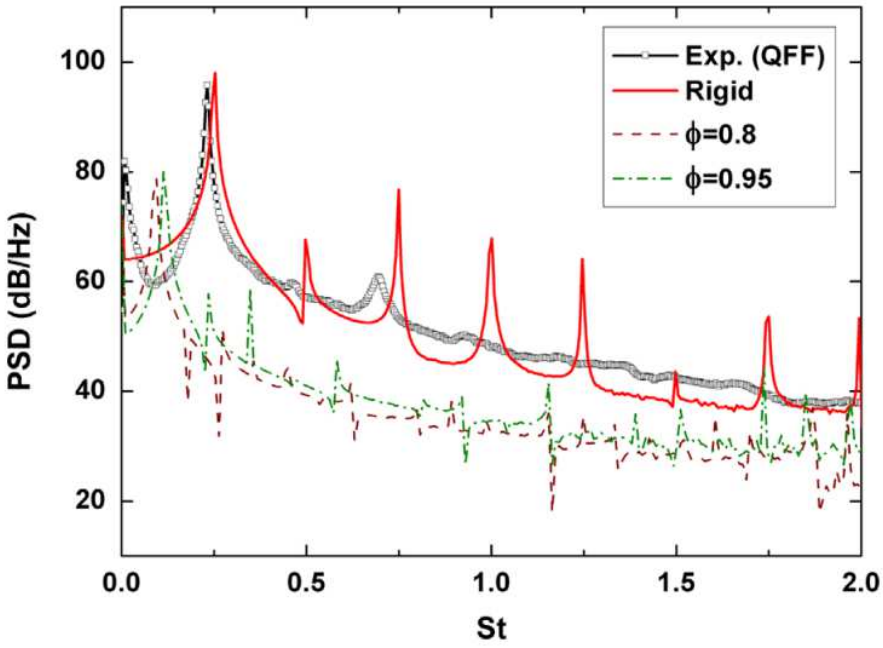

Figure 2.13: The effect of porosity of the coating on the noise from tandem cylinders [81].

airframe noise at landing with a minimal aerodynamic penalty. Several flow-porous interaction mechanism potentially responsible for the noise reduction have been identified and discussed in the paper, such as the flow dissipation, flow penetration into the porous flap medium, porous surface impedance reduction, and a mechanism referred to as the "flow-through-leakage", which mitigates the strength of the side-edge vortex and believed to be the main reason for the noise reduction. Choudhari and Khorrami [84] have also studied the application of porous materials for modifying the flap side-edge flow field computationally. The results based on the Reynolds-averaged Navier-Stokes CFD simulations had shown that the application of the porous treatment over a miniscule fraction of the wetted flap area can lead to significantly weaker side-edge vortex structures through modification of the vortex initiation and roll-up processes. It was also shown that at high flap deflections, the region of axial flow reversal associated with the breakdown of the side-edge vortex is eliminated, as shown in Fig. 2.14, suggesting an absence of vortex bursting in the presence of the porous treatment. The study had concluded that airframe noise reduction benefit via the porous treatment is achievable without compromising the aerodynamic performance of the high lift device.

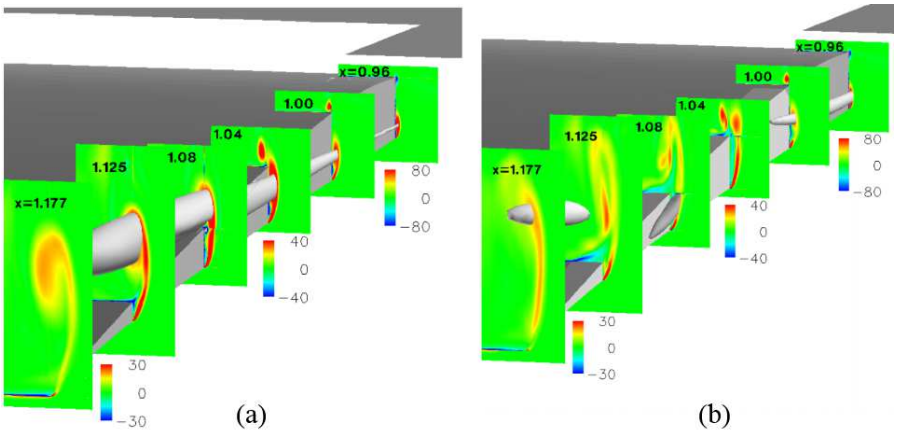

Figure 2.14: Global view of streamwise vorticity (a) baseline and (b) treated case [84].

A computational study on the possibility of slat noise reduction using porous trailing-edge treatment was performed by Khorrami and Choudhari [85]. The use of porous treatment over a small fraction of the slat surface was shown to reduce the pressure fluctuations in the vicinity of the treated edge in excess of 20 dB, through reduction of the strength of the Strouhal-shedding from the finite thickness trailing-edge and an upward shift in the Strouhal-shedding frequency to a frequency band of reduced auditory sensitivity. More recently, wind-tunnel experiments were performed by Angland *et al*. [86] to examine the impacts of porous-treated flap side-edge on airframe noise and vortex shedding. The side-edge vortex was found to be displaced further downstream from the porous flap and the turbulent stresses in the shear layer were reduced significantly. The near-field pressure fluctuations, hence, were found to be significantly reduced, suggesting the weakening of the aerodynamic noise source in the vicinity of the flap side-edge. Herr [87] carried out several experiments on the effects of a flow-permeable section or comb-type edges applied to a flat plate and a symmetric NACA0012 airfoil. The results obtained confirmed that such edge treatments can potentially reduce the broadband trailing-edge noise by up to 10 dB. The trailing-edge noise reduction was linked to “hydrodynamic absorption” and dampening of the turbulent flow pressure fluctuations. The experimental investigations by Sarradj and Geyer [88] on the utilization of porous materials for airfoil self-noise reduction also demonstrated that noise reduction of up to 10 dB at low frequencies can be obtained with minimum aerodynamic penalty. Aerodynamic and noise measurements had been carried out

for semi-symmetrical SD7003 airfoils and it was shown that the noise reduction is strongly dependent on the flow resistivity of the porous materials. Furthermore, the impact of porous flow resistivity on the level of noise reduction, effects of surface roughness and the possibility of noise increase at high frequencies have been the subject of some more studies by Geyer *et al.* [89, 90]. It was observed that the boundary layer displacement thickness of the porous airfoils for both the suction and pressure side increases with decreasing flow resistivity. The use of a poro-elastic carper on the suction side of a symmetric NACA0012 airfoil at a low Reynolds number regime at high angles of attacks has shown to result in significant drag reduction, delay in the formation of vortex shedding and reduction of lift and drag fluctuations of the airfoil (Venkataraman and Bottaro [91]). More recently, Geyer and Sarradj [92] investigated the trailing-edge noise by applying porous treatments to the trailing-edge of airfoils. It was found that using larger porous sections leads to higher noise reduction and that airfoils which are only partially porous can still deliver noise reduction with better aerodynamic performance. The noise reduction obtained using the porous treatment was explained to be due to the changes to the energy spectrum of the turbulence structures and the "hydrodynamic damping" effect of the porous treatment. However, no near-field boundary layer or surface pressure measurements were provided to demonstrate such phenomena.

2.3.3 Blunt trailing-edge flow and noise control

Airfoils with blunt trailing-edges, also called flatback airfoils, feature in various applications, such as the inboard region of large wind turbine blades and provide several structural and aerodynamic advantageous. The flatback airfoils are known to be aerodynamically superior due to their higher sectional maximum lift coefficient and lift curve slope (Standish and Van Dam [93], Winnemoller and Dam [94]) and also reduced sensitivity of the lift properties of the blade to surface soiling (Jonathon and Dam [95]). However, the presence of a blunt trailing-edge can also result in vortex shedding and hence an increase in the drag of the airfoil (Jonathon and Dam [95]), structural vibration and emergence of Strouhal peaks in the noise signature of the wind turbine. Several studies have been carried out on the application of porous treatments for improving the aerodynamic and aeroacoustic performance of flatback type structures. Bruneau *et al.* [96] had

numerically studied the use of porous interfaces on blunt bodies in order to regularise the flow and reduce drag. Results had shown the capability of the porous layer in reducing the pressure gradient in the near-wake region by up to 67% and considerable drag reduction of up to 45%. The effect of porous treatments on the noise generation from a flat plate with blunt trailing-edge was also investigated by Bae *et al.* [97]. The three-dimensional turbulent flow over the blunt trailing-edge flat plate was computed using incompressible large eddy simulation (LES), while the acoustic field was calculated using the linearized perturbed compressible equations (LPCE) coupled with the LES. It was found that the porous surface can reduce the far-field noise by up to 13 dB at the fundamental Strouhal peak and this was shown to be due to the weakening of the surface pressure fluctuations near the trailing-edge and also breaking of the wall pressure fluctuations spatial correlation. In a later study, Schulze & Sesterhenn [98] investigated the use of porous materials for trailing-edge noise control and developed a methodology to maximise the noise reduction by optimizing the porous material. Koh *et al.* [99] performed numerical simulations based on LES and acoustic perturbation equations (APE) on the possibility of bluntness noise reduction and found that the use of porous trailing-edges can reduce the sound pressure level at the fundamental vortex shedding frequency by 10 dB and the overall sound pressure level in the range of 3-8 dB. In addition, Zhou *et al.* [100] developed an LES-based discrete adjoint-based optimization framework to obtain the optimal distribution of porous materials on trailing-edge of a flat plate. The results obtained showed that the optimized design using porous treatment can significantly minimize the instantaneous turbulence intensity near the trailing-edge and effectively destroy the trailing-edge roll-up structures and the spanwise correlation, as shown in Fig. 2.15.

More recently, Koha *et al.* [101] performed an LES-based computational study on the impact of porous surfaces on trailing-edge noise and showed that the implementation of porous trailing-edge can lead to reduction of the overall sound pressure by up to 11 dB in the case of a flat plate at zero angle-of-attack. The results also indicated that the porous trailing-edge is effective in reducing the vortex shedding tone noise and that the viscous effects induced by the porous structures directly influence the acoustic attenuation by reducing the flow acceleration near the trailing-edge.

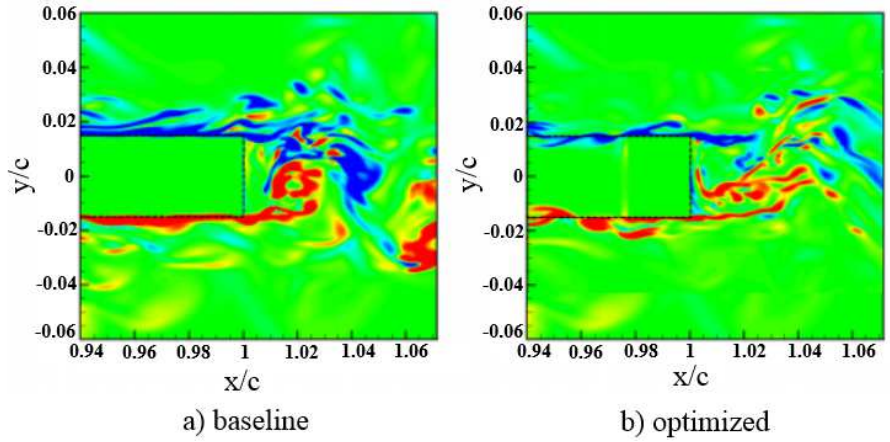

Figure 2.15: Vorticity field of the (a) baseline and (b) optimized design using porous material [100].

2.4 The flow mechanisms over a rough and permeable surfaces

While much of the literature on this topic focuses on the universal aspects of the mean flow field and turbulent statistics over the porous wall, several studies have also been directed towards the understanding of the influence of permeability on fluid flows. Suga [102] carried out several experiments on the effects of a flow-permeable wall with a varying permeability value, but with similar porosity ($\varepsilon \approx 0.8$) using the Particle Image Velocimetry (PIV). The experiments were conducted at low Reynolds numbers ($Re \leqslant 10,200$) and it was shown that the transition to turbulence occurs at lower Reynolds number over the porous surface, with the increase in the permeability. The near-field wall velocity fluctuations were found to be higher with increasing permeability in the flow-vertical direction, which leads to higher shear stress at the porous surface. Recently, Manes *et al.* [103] showed that the flow resistance and the shear penetration on permeable walls increase with increasing the permeability (κ)-based Reynold's number Re_κ, where the penetration depth is defined as the inner length scales of the turbulent flows. It was observed that the rms of the streamwise velocity decreases at the near-wall region with increasing permeability and increases the energy content of the vertical velocity fluctuations and correspondingly, the Reynolds shear stress. The results also showed that the boundary layer flow structures on the surfaces with higher permeability are influenced by an unstable mode of turbulent mixing layers which allows the production of the Kelvin-Helmholtz shear instabilities,

while such instability eddies were not seen for the surfaces with low permeability. The shear instability was observed to dominate the near-wall flow structures, in the cases where the shear penetration depth is relatively larger than the boundary layer thickness. Breugem *et al.* [104] have studied the effect of the flow inside a permeable wall with different porosities (ε=0.6, 0.8 and 0.95). It was shown that the mean velocity profile decreases significantly for the porous surface with higher porosity, and this was accompanied by a strong increase in the Reynolds shear stress near the porous wall. This results in an increase in the skin friction coefficient of about 30 %, which is also evident in the experimental study by Kong and Schetz [105]. It was also found that the quasi-streamwise vortices and high-speed streaks observed near a solid wall have significantly weakened over the porous surface due to the reduction in the mean shear and in the wall-blocking effect while enhancing the turbulent transport across the porous medium. Breugem *et al.* also showed that the weakening of the vortices over the porous surface leads to a reduction in the streamwise rms velocity peak and an increase in the spanwise and vertical rms velocity peak, caused by the flow penetration in the porous medium. It has also been shown that the rms velocity profile inside the porous medium exhibit an exponential-like tail, and that the turbulence motions established inside the porous are not responsible for the increase in the Reynolds shear stress near the porous wall.

In addition to the effects of permeability, the roughness of the porous surfaces has also been found to be a determining factor in the behaviour of the flow over and past such surfaces. The mechanisms involved in the interaction of flows with rough and permeable surfaces, *i.e.* foams, perforated sheets, beds of packed spheres, *etc.*, have been experimentally and numerically investigated in numerous studies [102–110]. Kong and Schetz [105] studied the effect of small-scale roughness and porosity through the development of the turbulent boundary layers over smooth, rough and porous surfaces. They found that the porosity of the porous surface can generally shift the wall logarithmic region downward by $\Delta U^+ \approx 3 \sim 4$ compared to the smooth wall, leading to an increase of the skin friction values by about 30 % ~ 40 %. It was also shown that the streamwise and vertical flow turbulence intensities and the Reynolds stress are increased in the boundary layer region, with a significant increase closer to the wall region. Jiminez *et al.* [108] studied the effect of passive porous wall and its contribution in delaying the boundary

layer separation. It was shown that a significant increase in the skin friction of about 40 % at the porous walls, along with the presence of the local flow separation. This is due to the emergence of the large spanwise rollers, originating from the Kelvin-Helmholtz instability and the neutral inviscid shear waves of the mean velocity profile. Finnigan [106] studied the turbulent shear flows generated by a plant canopy, which resembles, to some extent, the flow over porous media and a rough-wall boundary layer. The results showed that the inflected velocity profile at the canopy top, unlike in a standard boundary layer profile, is exhibited by an inviscid instability mechanism and consequently generates more energetic coherent structures than in the inertial sub-layer or log-layer at transporting momentum. The influence of the vegetation density on the canopy sub-layer is later investigated by Poggi *et al.* [107] and the results demonstrated that (a) the flow in the lowest layer within the canopy is dominated by small-scale von Karman vortices, (b) the flow is superimposed of a mixing layer and the wall roughness effect in the boundary layer in the middle layer of the canopy region, and (c) the upper layer of the canopy region can be expressed using the surface layer similarity theory.

As reviewed above, despite a large body of literature on the interaction of flow on rough permeable surfaces, there are only a few studies on the pressure fluctuations for boundary layers over rough [111–114] and porous [52] surfaces, which are of great importance for understanding the noise and vibration generation from such structures. Blake [111] studied the pressure fluctuations for turbulent boundary layers over a smooth and different rough walls. It is claimed that the different roughness parameters, such as the roughness separation and height affect the very large-scale structure and small-scale turbulence structure, respectively. It was also found that the coherence loss in the pressure eddies for rough walls is higher than the smooth walls due to the high turbulence production rate near the surface. Varano [112], on the other hand, investigated the rough surface with fetches of hemispherical roughness and found that the turbulent kinetic energy and shear stress production increases downstream of the element due to the delay in the flow separation over the top of the element. A recent effort by Meyers *et al.* [113] presented a comprehensive study on wall pressure spectrum of a flat plate with smooth and rough walls with sparse arrays of different size and distribution of hemispherical bumps at high Reynolds numbers. The results showed that the boundary layers of both the rough and smooth

surfaces have similar outer boundary layer scales at the low frequencies of the wall-pressure spectrum, and have a universal viscous form at the higher frequency range. It was also confirmed that the friction velocity obtained in the case of rough-wall boundary layers is always less than the conventional friction velocity found for a smooth-wall boundary layer and confirmed that the boundary layer parameters and the wall pressure spectrum are nearly independent of the surface roughness for the conditions considered in the study. Building on the work of Meyers, Liselle *et al.* [114] have investigated rough walls with two fetches of hemispherical roughness elements with two different spacing ratio. It has been demonstrated that the pressure spectral shape changes at mid frequencies with the roughness density, and it was speculated that the spectral changes are not due to the changes in the turbulence structure but rather due to the displacement of the pressure fluctuations over the roughness elements. In a more recent work, Showkat Ali *et al.* [52] have shown that the use of porous treatments can lead to a significant reduction in the energy content of the large low-frequency boundary layer structures. It was also found that surfaces with high permeability are able to greatly alter the boundary layer and attenuate vortex shedding frequency. Moreover, results also showed that the spanwise coherence of the large coherent structures can be significantly reduced using high permeable materials.

2.5 Theoretical analysis available for flow and noise control using porous media

2.5.1 Theoretical analysis for *flow control* using porous media

The proper numerical or mathematical modelling of the problems concerning aerodynamic noise control using porous treatments has remained as a challenging task as none of the existing models can capture the whole physics involved, namely the flow-porous interaction (*i.e.* flow penetration and discharge, roughness effects, hydrodynamic and sound absorption effects, and finally scattering effects). A complete description of the entire flow field in the porous media at the microscopic level was fundamentally determined using the Stokesian dynamic equations. However, due to the complex solid surface geometry in the porous medium, the Stokes equation is generally challenging. Darcy, on the other hand, established an empirical model on the

macroscopic level (known best as Darcy's law) by performing volume averaging of the Stokes equation [115, 116]. However, it is rather difficult to ascertain the exact range of the validity of Darcy's law, which is limited only to a relatively small velocity region. Darcy's law has been quite useful for many different applications, owing to its reduced order of statistical equivalent of the Navier-Stokes equations. In order to improve the available continuum flow models, a better understanding of the governing flow physics of pore-scale flow models and transport processes is required. A general equation that interpolates between the Stokes equation and Darcy's law was then developed by Brinkman [117], which allows the solution of flow around a particle with the effect of no-slip boundary conditions on the surface. The relevance and applicability of the Brinkman equation have still remained as an open question, particularly in describing the flow behaviour in the porous medium at higher porosity value, although the theoretical predictions of the porous permeability factor agree well with the experimental data [118]. Forchheimer [119] derived an extended version of Darcy's law to investigate the fluid flow through porous media in the high velocity regime, which mainly dominated by the inertial effects of the flow and suggested the inclusion of an inertial term of the kinetic energy of the fluid to the Darcy equation. The Forchheimer flow resistance and the dispersion were found reasonably due to the turbulent mixing from the diffusion effect in the porous medium. Lee and Howell [120] developed a $k-\varepsilon$ model for the flow through the high porosity porous medium and acknowledged the same eddy viscosity for the porous medium, similar to the one used commonly for the pure fluid condition. Travkin *et al.* [121], on the other hand, proposed the turbulence model for porous media with high porosity and permeability, together with a statistical and numerical solution method. The modelling of the flow interaction with porous walls, with the porous medium being fully resolved, has been considered by numerous researchers (Larson and Higdon [122], Durlofsky and Brady [123], Vafai and Kim [124], Hsu and Cheng [125], Kladias and Prasad [126], Chen and Chen [127]). The flow simulation, particularly, on the effect of porosity and permeability of the porous material has also been investigated extensively using the numerical techniques, including the boundary integral method [122], finite element method [128, 129], finite difference method [130], Lattice Boltzman method [131, 132] and Lattice gas automata method [133, 134]. A number of models have been developed to manage the solid grain shaped of the porous medium that varies from

the general simple cylindrical and spherical models [122, 129, 135]. Several models have been devoted to replicate an actual porous media for flow models and the reconstruction of such models are obtained using the digital image processing [136, 137] and computer microtomography [138, 139].

2.5.2 Theoretical analysis for *noise control* using porous media

The possibility to accurately measure and predict the sound absorption, transmission and propagation in porous media is vital for many engineering fields and have been widely investigated. Most of the models used to predict the sound propagation in the porous media are based on an equivalent fluid medium model, with frequency dependent acoustic impedance and complex wavenumber. The acoustic transmission and propagation through porous media using such models has been the subject of numerous studies. The concept of temporal impedance consisting the resistance and reactant factors were introduced by Zorumski and Parrott [140] in their theoretical and experimental studies on the acoustic non-linearity in rigid porous media. They found that the instantaneous resistance of the porous material is independent of the frequency and equal to the material flow resistance, while the instantaneous reactant is established as a function of the acoustic fluid velocity. Wilson *et al.* [141] developed a simplified nonlinear theory based on the classical rigid frame theory by considering the Forchheimer-type through a complex density operator for many types of air-saturated fibrous porous materials. They have also demonstrated a numerical solution for the nonlinear wave propagation and attenuation inside rigid porous materials restricted to pure tone excitation. In order to predict the nonlinear acoustic performance of a porous metal plate with a finite thickness, particularly at high sound pressure level, Peng *et al.* [142] have developed a one-dimensional model using a linearization and finite difference method to solve the particle velocity inside the porous plate. Lambert and McIntosh [143] put forward an approximate analytical solution for surface acoustic admittance using a wave perturbation method for infinite rigid porous materials at high sound pressure levels. However, the analytical solution is not valid at frequencies below 500 Hz in the case with high surface particle velocity situations. An analytical model for the propagation of high amplitude continuous sound through a hard-backed rigid porous layer was developed by Umnova *et al.* [144],

based on the modified fluid model, however, the solution predicted by the model is mainly suitable for an acoustic wave with slowly varying amplitude. The models used to estimate the acoustic impedance and the wavenumber have also been shown by Johnson *et al.* [145] and Champoux and Allard [146] via the concept of the viscous characteristic length which is taken as the ratio of the seepage velocity in the material pores which is excited by the incident sound wave [147, 148]. The acoustic transmission through porous media have also been studied using the finite element numerical method by numerous researchers (Kang and Bolton [149], Panneton [150], Panneton and Atalla [151], Atalla *et al.* [152], Dauchez [153], Hamdi *et al.* [154], Sgard *et al.* [155]). These methods are quite effective for in the low frequency range and cannot be used in the high frequency range. However, for simple porous media structures, several analytical methods can be adapted to examine the middle and high frequencies efficiently (Allard [156], Allard *et al.* [157, 158], Bolton and Shiau [159], Bolton [159], Lauriks*et al.* [160], Song and Bolton [161]). Jaworski and Peake [14] have recently developed an analytical model based on Wiener-Hopf method for the understanding and prediction of the aerodynamic noise radiation from trailing-edges with porous treatments. As mentioned above, although various numerical and mathematical models have been developed to better understand the flow and porous medium interaction, in the case of aerodynamic noise generation, the problem involves several different physical processes and no modelling technique can yet fully capture all aspects of the problem. Considering the complexity of the problem, it is important to carry out more high quality experiments to help better understand the physical processes involved. The results from such experiments can be used as benchmark for high-fidelity numerical studies or validation for new analytical models.

2.6 Summary

The literature review summarized and discussed several aerodynamic noise sources and provides a concise list of the flow and noise control techniques which have been avidly pursued by scientists and engineers in the past. The passive flow control methods, particularly, the porous media, is one of the most promising techniques of fluid dynamics, which has caught the attention of many researchers in the recent years, resulting in the rapid research in this field. Even though the

ability to control the flow-field and noise using the porous media has shown to have a lot of weight in the practical applications, the mechanisms through which the noise is reduced have not been completely studied and understood. The limitations of the literature reviews regarding the application of porous materials are listed below.

i. The use of porous media for aerodynamic and aeroacoustic purposes has been the subject of several computational and a limited number of experimental studies. A number of flow and porous interaction mechanisms have been identified as the potential candidates for the noise reduction, break-up of large coherent structures, vortex shedding control, *etc.* in the literature. The experimental investigation carried out to date, however, lack an in-depth study of the effects of such porous treatments on the boundary layer and wake turbulence structures, the growth and evolution of turbulence structure as they travel over porous surfaces and the coherence of the boundary layer structures and the surface pressure fluctuations.

ii. Even though the research regarding the fluid-flow interaction with porous material has been extensively studied in the literature, there is barely any published information on the mean velocity and the turbulence intensity of the boundary layer profile over a porous surface. Moreover, there is no research related to the near-field studies, particularly for surface pressure measurements in the vicinity of the porous surface.

iii. The flow field inside the porous media as a result of flow penetration inside the porous medium have not been discussed. Moreover, the effect of porous surface roughness and the emergence of the hydrodynamic field inside the porous medium has not been isolated/ separated from each other, *i.e.* porosity-permeability and porosity-roughness effects.

iv. A high quality analytical model for flow-porous interaction using the CFD modelling to provide a realistic and holistic micro-to-macro-modelling has not been carried out at this moment, *i.e.* taking into accounts the effect of friction over the porous surface, flow penetration and the emergence of the hydrodynamic field inside the porous medium.

v. There are numerous different analytical models for flow and noise control through porous media, however the validity of these models and its governing concepts, is a subject of ongoing scientific debate, due to ambiguous connections between the models physical quantities

and the porous media parameters characteristics (porosity, permeability, tortuosity, and etc.).

vi. Although there are various models available for simulating turbulent flows in porous media, questions have been raised about its applicability in all circumstances due to the material complexity. For instance, the majority of the existing models does not take all the flow-porous interaction aspects into accounts, such as the flow penetration and discharge, roughness effects, porous-flow viscous interaction and hydrodynamic absorption effects in the porous media.

The flow-porous interaction including the flow penetration and discharge, roughness effects, porous-flow viscous interaction and hydrodynamic absorption effects in the porous media will be broadly investigated in the present study. Considering the complexity of the problem, it is important to carry out more high-quality experiments to help better understand the physical processes involved. The study proposed in this work will include a comprehensive and systematic experimental investigation and study various aspects of flow-porous interaction, such as scrubbing effects, break-up of boundary layer coherent structures, flow penetration, internal hydrodynamic field, flow discharge and vortex shedding attenuation. The study also includes interesting complex physics about the application of porous materials for possible aerodynamic and aeroacoustic purposes.

CHAPTER 3

DESCRIPTION OF EXPERIMENTS

This chapter outlines the details of the experimental facility, measurement techniques and instrumentation methods employed in the present study. A series of experimental studies have been specifically designed and conducted to investigate the effect of porous materials on the aerodynamic and aeroacoustic performance for different model configurations. The experimental campaign is divided into two separate set of experiments using a flat plate model and a blunt trailing-edge model. The information about the experimental facilities, test-rigs and the instrumentation are reviewed in § 3.1. The detailed descriptions of the measurement designs and the model configurations are described individually in Chapters 5 and 6, respectively. Section 3.2 outlines the various measurement techniques applied in this study. The aerodynamic and aeroacoustic behaviour of the test models with and without the porous treatments have been evaluated using the force balance, hotwire Anemometry, Particle Image Velocimetry (PIV), steady and unsteady surface pressure and far-field pressure measurement. These experimental techniques were selected to achieve the research objectives specified in Chapter 1 and to answer the research questions identified in Chapter 2. The uncertainty calculation method of the measurement devices and the test results are presented in § 3.4.

3.1 Experimental setup

The experimental setup comprising the wind tunnels, different model configurations and the probe instrumentation used in the present study is discussed in the next subsections.

3.1.1 Wind tunnel

The flow and noise measurements were performed in different wind tunnel facilities of the University of Bristol for various aerodynamic and aeroacoustics testing, *i.e.* the low turbulence wind tunnel, open jet wind tunnel and the open jet anechoic wind tunnel. A brief description of the wind tunnels used in this study is provided below.

i. **Low turbulence wind tunnel:** The low turbulence wind tunnel is a closed-return type tunnel with an octagonal test section of 0.8 m × 0.6 m × 1 m and has a contraction ratio of 12:1. The wind tunnel is capable of a maximum flow speed of 100 m/s, with a turbulence intensity of 0.05 % at 20 m/s. This wind tunnel has been specifically utilized the Particle Image Velocimetry (PIV) measurements for the blunt trailing-edge studies in Chapter 6.

ii. **Open jet wind tunnel:** The open jet wind tunnel is a closed-return type tunnel with a test section of 1.1 m × 2 m. The wind tunnel is capable of a maximum reliable speed of 30 m/s and with a turbulence intensity of 0.5 % at 20 m/s. The wind tunnel has been used extensively for the majority of the tests presented in this study using the force balance, hotwires anemometry and the steady and unsteady surface pressure measurements.

iii. **Aeroacoustic wind tunnel:** The open jet anechoic wind tunnel is a closed-loop feedback type tunnel with an external dimension of 7.9 m length, 5.0 m width and 4.6 m height, including the surrounding acoustic walls. The nozzle used in the present studies has a dimension of 0.6 m width and 0.2 m height. The nozzle is capable of a maximum reliable speed of 100 m/s at the contraction nozzle exit and with a turbulence intensity of 0.2 % at 30 m/s. The anechoic chamber was designed to be fully anechoic down to 160 Hz. In order to completely absorb any sound reflections, the ceilings and all the walls are covered by

wedges with a base dimension of 0.3 m × 0.3 m, with a length of 0.34 m. The aeroacoustic characteristics of the blunt edge bodies were carried out using this wind tunnel.

3.1.1.1 Wind tunnel background noise

The experimental results related to the flow characteristics using the near-field surface pressure measurements system were studied mainly in the open jet wind tunnel, which is neither a 'quiet' wind tunnel nor within an anechoic environment. Hence, the surface pressure signals acquired from the measurements can be easily contaminated by the wind tunnel background noise (*i.e.* wind tunnel fan, blower, etc.), sensor vibration-induced noise, etc., especially at low frequencies. The low frequency noise contamination can be generally ignored at high velocities, which the turbulent surface pressure fluctuations are relatively higher than the low frequency background noise. Increasing the flow velocities to minimize the effect of background noise, however, is not a reliable approach as it leads to greater measurement error due to transducers sensing area integration and averaging effects [162], and also will be a hindrance to different engineering interest. Some researchers have utilized the high-pass filtering to remove the contaminated noise from the surface pressure signal. This method, however, is not agreeable because not only does it eliminate the noise but also results in losing the information pertaining to the turbulent energy, especially concerning the large-scale turbulent structures.

In order to evaluate the quality of the measured data, the background noise of the open jet wind tunnel has been measured experimentally using the flush surface-mounted transducers and also with transducers placed in the flow, parallel to the flow direction. It was observed, that the sound pressure level at the wind tunnel test section at 20 m/s is less than 20 dB in the frequency band from 100 Hz to 1000 Hz, and even more reduced in frequency above 1000 Hz (up to 15000 Hz), which is still applicable in the frequency range of interest. The surface pressure fluctuations results in this thesis are presented only when the pressure signal is at least 10 dB higher than the background noise.

3.1.2 Model configurations and instrumentations

Two different experimental test rigs have been designed and manufactured as part of this project, namely the flat plate model and blunt trailing-edge model. The flat plate test rig is used for studying the effects of permeable surfaces on boundary layer flow passing over the porous section. Figure 3.1 shows the schematic of the model, the location of the porous section, and the instrumentation of the plate. Figure 3.1 shows the test rig placed in the working section of the open jet wind tunnel. The detail description of the test rig is provided in Chapter 5.

(a) Flat plate model experimental setup

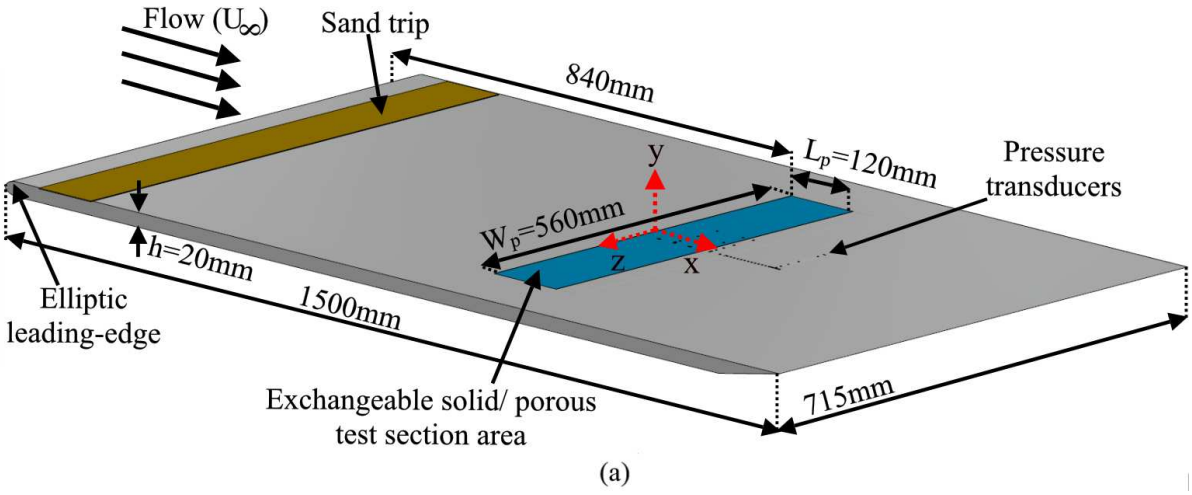

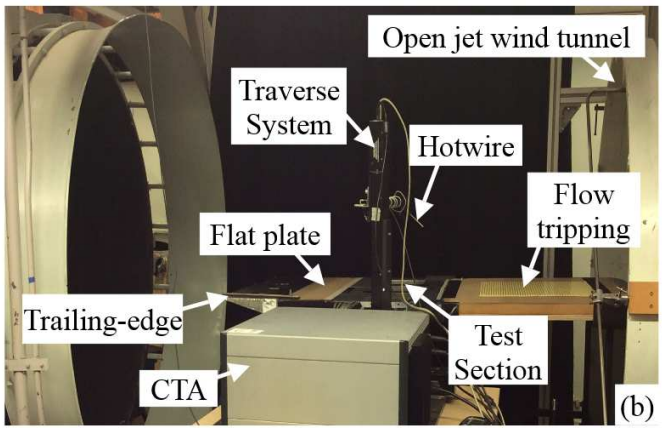

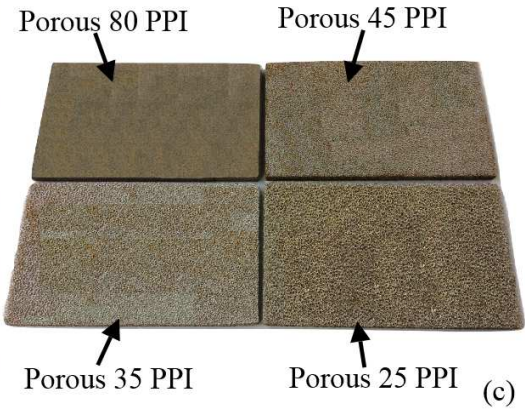

Figure 3.1: (a) Flat plate model, (b) Flat plate model experimental setup in the open jet wind tunnel and (c) Porous treatments used in the study.

The blunt trailing-edge test rig was used for studying the effect of porous trailing-edges on the trailing-edge flow, vortex shedding and the possibility of flow and noise control using porous treatments. Figure 3.2 provides a schematic of the rig and shows the model placed in the open jet wind tunnel. The test rig and the results are further discussed in Chapter 6.

(b) Blunt trailing-edge plate model experimental setup

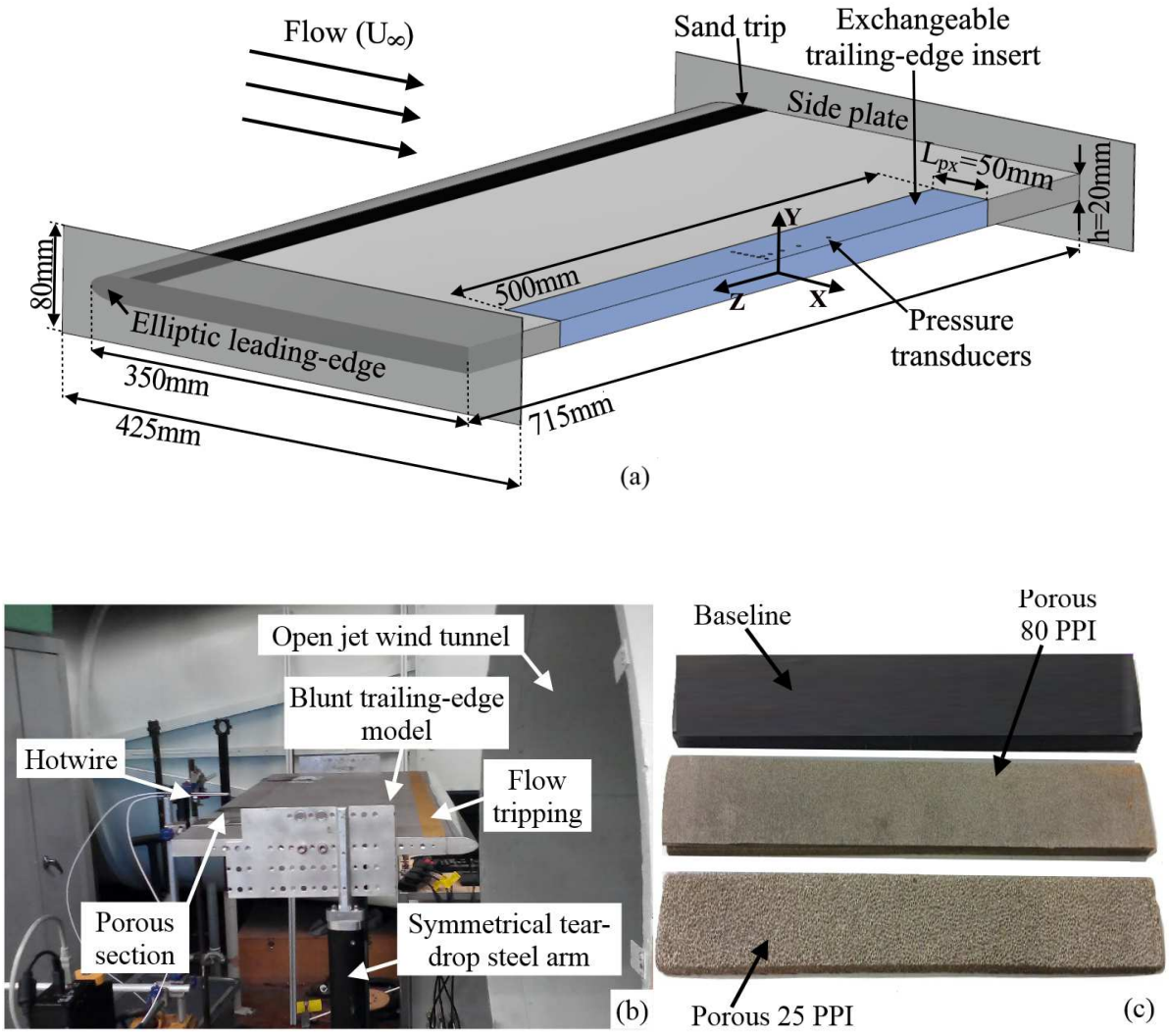

Figure 3.2: (a) Blunt trailing-edge model, (b) Blunt trailing-edge experimental setup in the open jet wind tunnel and (c) Porous treatments used in the study.

The blunt trailing-edge test rig was also used for studying the effect of porous trailing-edges on the trailing-edge noise. Figure 3.3 provides the schematic of the test rig placed in the open jet

anechoic wind tunnel, the location of the far-field pressure transducers and the isometric view of the contraction nozzle used for the aeroacoustic measurements. The detail description of the test rig and the acoustic results are further detailed and discussed in Chapter 6.

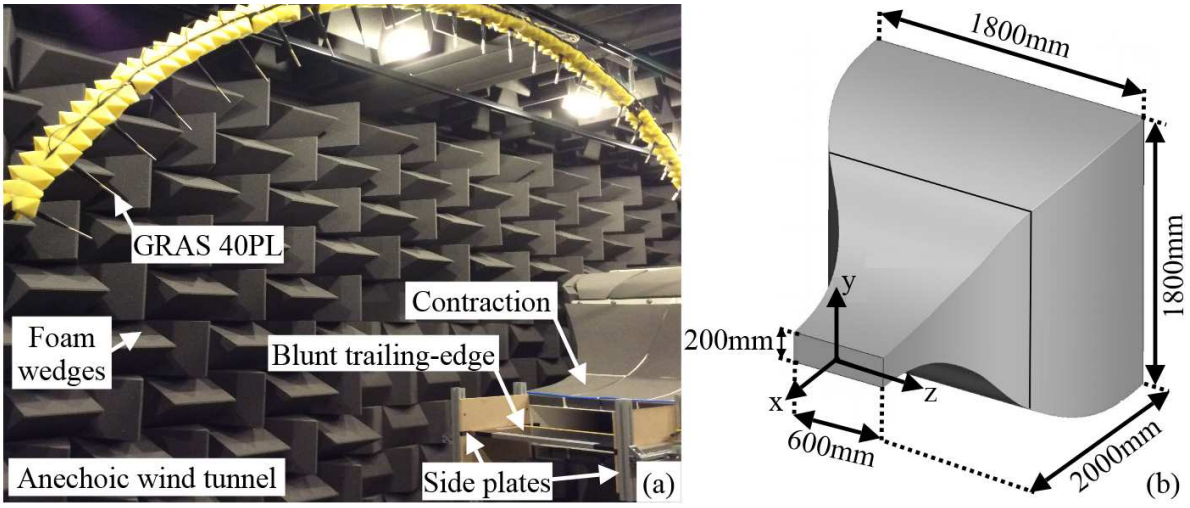

Figure 3.3: (a) Blunt trailing-edge experimental setup in the anechoic wind tunnel and (b) Isometric view of the contraction nozzle.

Figure 3.4 shows the instrumentation of the flat plate and blunt trailing edge model, with and without the porous treatment. The flat plate (Fig. 3.4 (a)) is equipped with a total number of 14 pressure taps to study the static pressure changes over the plate after the porous treatment. The pressure taps were installed into the 2 mm × 2 mm grooves filled with a resin along the span and a hole of 0.4 mm was applied on the pressure taps at the middle of the span. The pressure taps type and dimensions and the calculation of the static pressure coefficient distribution are given in § 3.2.4. The unsteady surface pressure measurements were carried out using miniature Knowles FG-23329-P07 pressure transducers. The FG-23329-P07 miniature transducers (see Fig. 3.11) used are 2.5 mm in diameter and have a circular sensing area of 0.8 mm. The transducers are flush mounted under a pinhole mask of 0.4 mm diameter. A brief explanation of the technique used is provided in § 3.2.5. The installation of the transducers in the porous material is a challenging task, influenced by the porous intricate complex structure. Care should be taken to avoid the unnecessary structural damage within the porous domain during the transducer installation procedure. The transducer cable is aligned in a way that it gives the least

intrusive effect on the flow measurements over the porous surface. Two different techniques have been used to embed the cables in the porous medium, *i.e.* vertically and horizontally. The results of the surface pressure fluctuations using both the techniques were found to be very similar. Thus, to avoid hindrance or obstruction of the flow within the porous section, the transducer cables were placed horizontally into a $2\ mm \times 2\ mm$ groove, with minimum damage to the inner structure of porous samples. The transducers arrangement for the flat plate case (Fig. 3.4 (a)) were concentrated in the middle section of the plate to fully study the effect of turbulent boundary layer flow interaction with porous surfaces. In the case of blunt trailing-edge plate (Fig. 3.4 (b)), the transducers were placed close to the trailing-edge (2 % of the fore-body length, L_x), in order to study the effect of blunt trailing-edge, with and without the porous treatments on the aerodynamic and aeroacoustic performance.

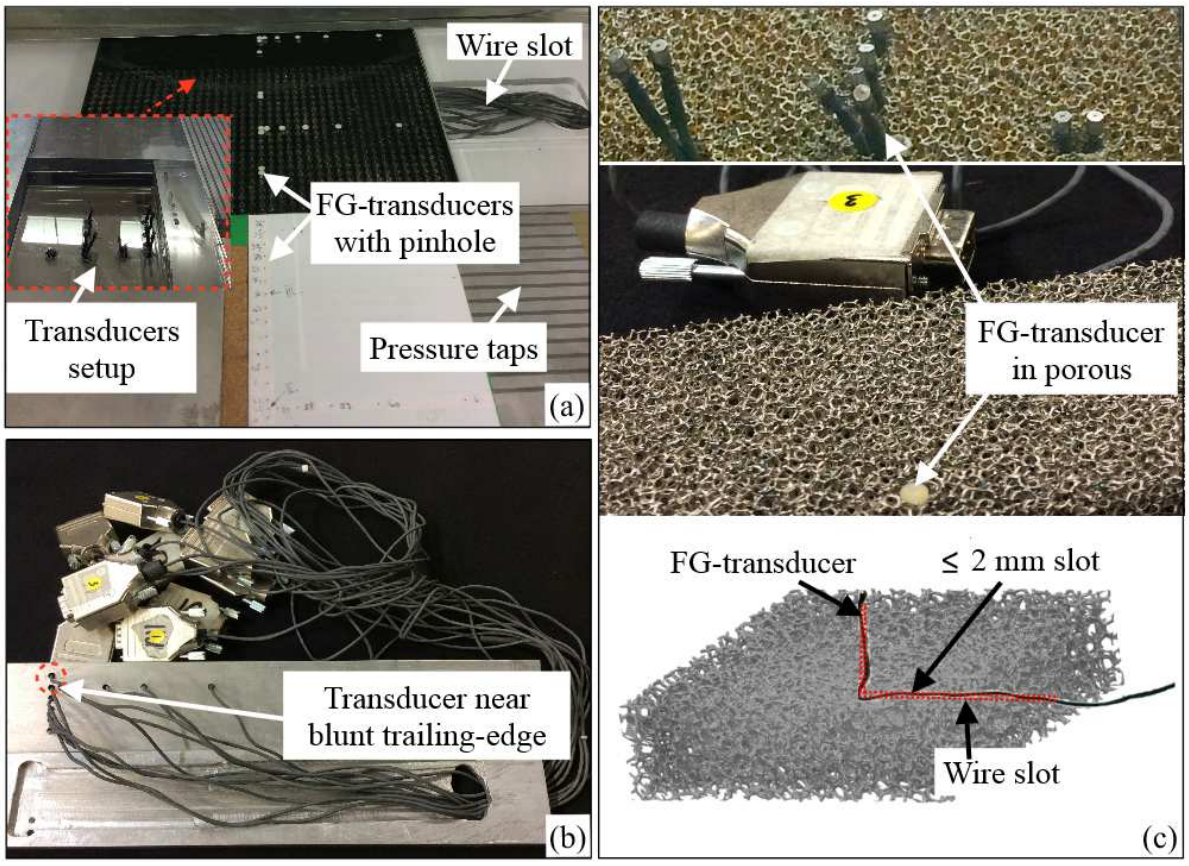

Figure 3.4: Experimental instrumentation. (a) Flat plate and (b) Blunt trailing-edge and (c) FG-transducer in porous.

3.2 Flow and noise measurement techniques

This section summarizes the flow, surface pressure and far-field noise measurement techniques used in this study. We shall review the operation, calibration and the error analysis of each measurement technique. A summary of the experiments performed with the measurement techniques is tabulated in Table 3.1.

Table 3.1: Summary on the measuring techniques used for the investigated cases

Measurement techniques	**Project/ Test specimens**	
	Flat plate scrubbing	**Blunt trailing-edge**
Force balance	-	✓
Particle Image Velocimetry (PIV)	-	✓
Hotwire anemometry	✓	✓
Pressure distribution measurement	✓	-
	Used to evaluate the permeability value of the porous material (Chapter 4)	
Unsteady surface pressure measurement	✓	✓
Far-field noise measurement	-	✓

3.2.1 Aerodynamic force balance measurements

The aerodynamic lift and drag force measurements were performed in the open jet wind tunnel for the blunt trailing-edge case. The drag and lift forces were recorded using an AMTI OR6-7-2000 3-axis force-plate unit. The flat plate setup was mounted on a set of steel extension arms with a symmetrical tear-drop shape to minimise any additional drag forces acting on the rig. The force-plate was load tested prior to the experiment. The generated voltage signal from the force-plate passed through an AMTI MSA-6 strain gauge amplifier and the final data from this unit was captured using a LabView system. A detailed uncertainty and data independency test has been conducted and the sampling frequency of 45 Hz with the least uncertainty value [163] was chosen for all the steady aerodynamic force measurements. Measurements were carried out for velocities between 6 m/s to 26 m/s wind speed and data have been collected for 30 seconds at each velocity. The unsteady lift fluctuations measurement, on the other hand, are taken for 3 seconds at each velocity with a sampling frequency of 20 kHz, giving a suitably high Nyquist

frequency of 10 kHz. The speeds were set such that all data were recorded once the deviation of the velocity was 0.2 m/s or less. To ascertain the repeatability of the measurements, repeated tests were conducted and the uncertainty was found to be less than 1%. The drag coefficient (C_D) is calculated as,

$$C_D = \frac{D}{0.5\rho U_\infty^2 A}, \tag{3.1}$$

where D is the force acting on the plate in the streamwise direction and A is the plate plan view area.

3.2.2 Particle Image Velocimetry (PIV)

The particle image velocimetry (PIV) technique was used to obtain time-averaged flow quantities over the $x-y$ plane. All measurements were performed in the low turbulence wind tunnel at the University of Bristol. The FlowSense 4 MP CCD camera was mounted on a traverse system next to the wind tunnel which is in line with a 210 mm glass window width perpendicular to the laser sheet, and the experiments were carried out at the midplane of the test specimen bodies. A schematic overview of an experimental setup is shown in Fig. 3.5.

The time interval and the laser sheet thickness were chosen to attain the maximum amount of particles in the interrogation window. A dual-cavity laser of 200 mJ Nd:YAG with a wavelength of 532 nm was used to produce 1 mm laser sheet thickness with the time interval between each snapshot of 25 μs and repetition rate of 15 Hz to obtain a maximum amount of particles in the interrogation window, for the blunt trailing-edge cases. A mixed Polyethylene glycol 80 based seeding with a particle size of 1 to 5 μm was used to seed the flow. The seeding particles are illuminated twice by the laser sheet, produced by two laser pulses at a time-step of Δt apart, when travelling over the plane of interest. The snapshots of the particles during illumination were captured by the CCD camera at the same time as the laser pulses, where the snapshots are consist of two images containing the specific particle positioning. In order to acquire the average particle displacement, the images are divided into various smaller separate segments, which is also called as the interrogation windows. The average particle displacement is detected through

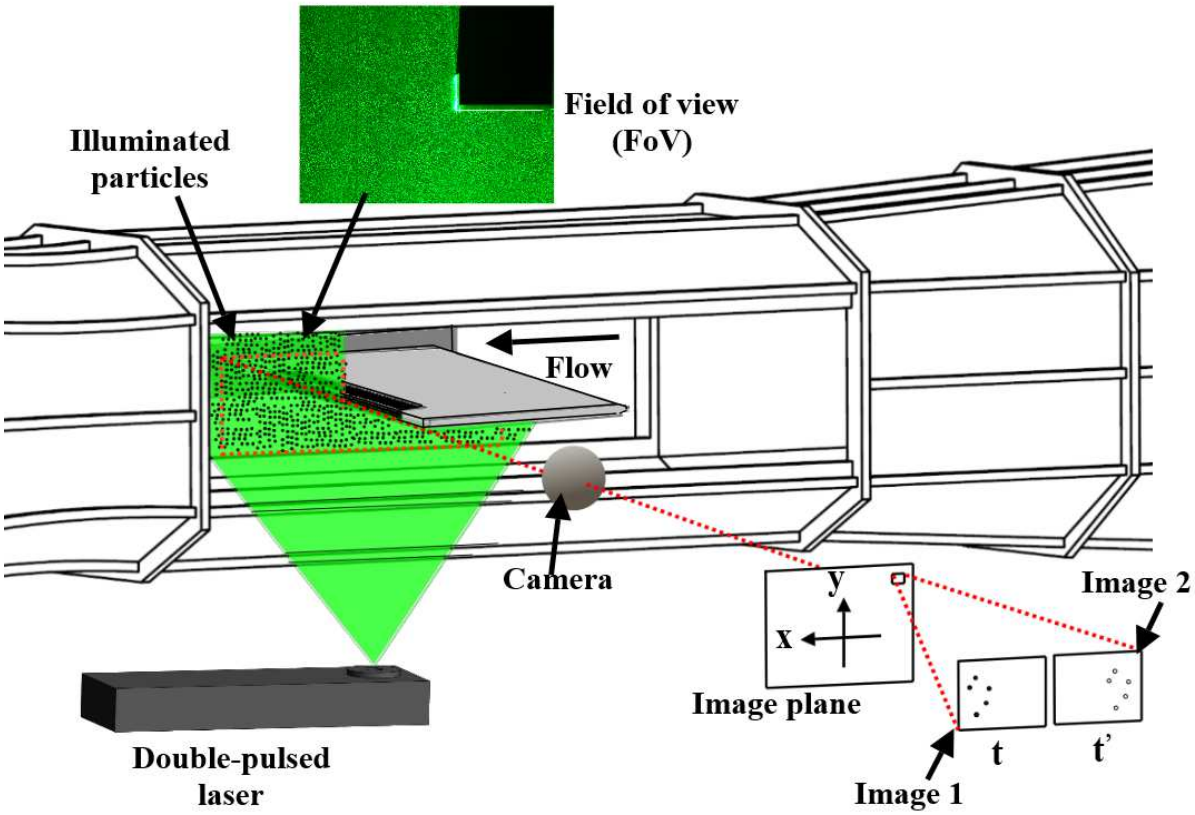

Figure 3.5: Schematic overview of the experimental setup for PIV in the low turbulence wind tunnel using the blunt trailing-edge plate.

a cross-correlation between the two images interrogation windows over the time-step Δt between the images. The image windowing and the cross-correlation map principle is shown in Fig. 3.6.

The particle displacement d_p is calculated by reorganizing the results achieved in pixels using the magnification factor. The instantaneous velocity field U_p is obtained based on the fraction of the particle displacement over the time-step between the subsequent images given as,

$$U_p = \frac{d_p}{\Delta t}. \tag{3.2}$$

The uncertainty is measured by considering the uncertainty in the subpixel displacements [164] and was found to be below 1 %. A total number of 1600 image pairs were taken with a resolution of 2048 x 2048 pixels for each case and used to compute the statistical turbulent flow quantities. The measurements were made for a field-view (FoV) of 158 mm × 158 mm, which

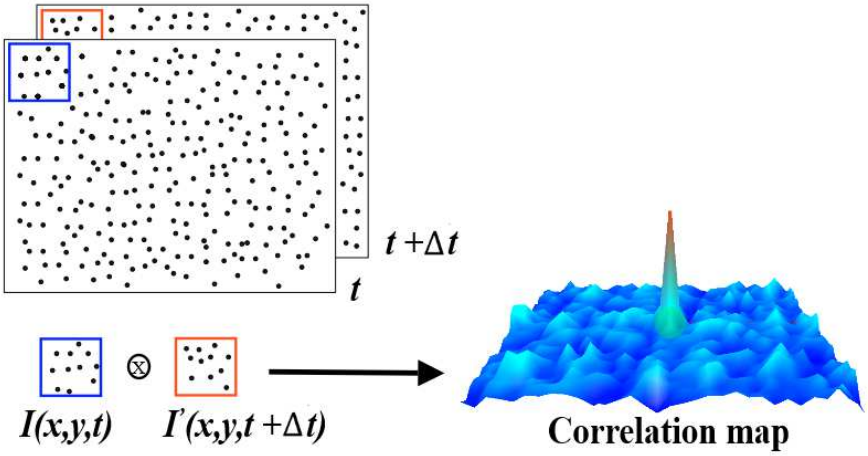

Figure 3.6: Image windowing principle.

corresponds to a domain of $7.9h \times 7.9h$ for the blunt trailing-edge case in the streamwise and vertical directions. The measurements iterative process yields grid correlation window of 16 × 16 pixels with an overlap of 50%, resulting in a final vector spacing of 1.23 mm, corresponds to the plate thickness of $0.062h$ for the blunt trailing-edge case. The summary of the parameters used for the investigated case is summarized in Table 3.2.

Table 3.2: PIV setup parameters

Setup parameters	**Blunt trailing-edge**
Snapshot time interval (Δt) , [μm]	25
Repitition rate, [Hz]	15
Field of view (FoV), [mm^2]	158 ×158
Interrogation window (IW), [pixel]	16×16
IW overlap, [%]	50
Spatial resolution, [pixel/mm]	13.11
Vector spacing, [mm]	1.23

3.2.3 Hotwire anemometry

The boundary layer and wake flow measurements were carried out using the single-wire Dantec 55P16 probes, with a platinum-plated tungsten wire of 5 μm diameter and 1.25 mm length, and cross hotwire Dantec 55P51 probes with 5 μm diameter and 3 mm length platinum-plated tungsten wires. This gives a length-to-diameter (l/d) ratio of 250 (single-wire probe) and 600

(cross-wire probe) with good spatial resolution and high-frequency response. In order to minimize attenuation caused by end conduction effects in hotwires, *i.e.* convective heat transfer between the heated wire and the flow, Ligrani and Bradshaw's [165] proposed that the l/d ratio of hotwire sensor should exceed 200 ($l/d > 200$). Ligrani and Bradshaw shows that an insufficient l/d may cause substantial errors in the measured broadband turbulence intensities. Moreover, insufficient l/d can also results in the spatial attenuation at all distances from the wall [166], *i.e.* length scales of up to $\lambda_x \approx 2\delta$. The Ligrani and Bradshaw's [165] criterion for $l/d > 200$ has been complied to in the present study, which provides sufficient sensitivity in measuring the velocity (mean and fluctuations) with minimal thermal effects. The probes were operated by a Dantec StramlinePro frame with CTA91C10 modules. The hotwires used in the study and the schematic of the probe wires are shown in Fig. 3.7. The signals were low-pass filtered by the StreamlinePro frame with a corner frequency of 30 kHz before they were A/D converted, with an applied overheat ratio of 0.8 [167]. The calibration of the probes was performed using the Dantec 54H10 type calibrator. The hotwire probes were installed on a two-axis ($x - y$) ThorLabs LTS300M traverse system, covering a $300mm$ by $300mm$ domain with a typical minimum positioning accuracy of $\pm 5\ \mu m$. The spectral analysis requires the sampling rate to be at least twice the highest frequency to avoid aliasing, giving a suitable high Nyquist frequency. The data have been acquired by a National Instrument 9215 type 4-channel module, with a sampling frequency of 40 kHz. The hotwire measurements were taken for 16 seconds at each location. The boundary layer measurement was repeated three times at a sampling frequency of 2^{16} for 16 seconds at each location to ensure repeatability. The sampling parameters chosen were sufficient for convergence of the velocity statistics, power spectral density, coherence and correlation measurements. The uncertainty of the measured velocity signals, obtained using the manufacturer's method [167], were found to be within ± 1%.

3.2.3.1 Hotwire calibration

The calibration process was performed before and after each measurement and the polynomial constants were averaged prior to the post-processing of the data. Below, we will explain the calibration process for both the single- and cross-wire probes.

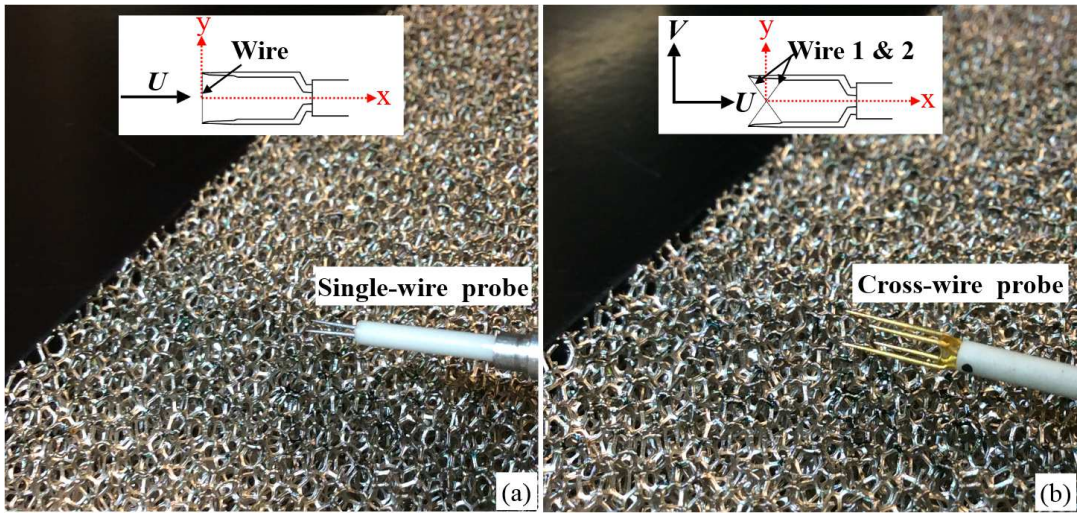

Figure 3.7: (a) Single wire probe and (b) Cross-wire probe used in the study and the schematic of the probe wires.

Single-wire calibration and data conversion: The two-point velocity calibration is used to calibrate the single-wire probe, see Fig. 3.8. Two fixed velocity points, approximately 1.5 m/s and 50 m/s were used as the setting for the low and high velocity calibration of the free jet. The calibration forms the relationship between the flow velocity (U) and the voltage output (E) obtained from the Constant Temperature Anemometry (CTA). The actual conversion of the voltage to velocity data is achieved via curve fitting over the points (E,U) using Eq. 3.3. The curve fitting of the calibrated data for a single-wire probe is shown in Figure 3.8.

The curve fitting of the calibrated voltage data is carried out using the Power Law method, where E^2 is plotted as the function of U^n in double logarithmic scale, where n can vary to provide the best curve fit. A set of best-fit parameters must be calculated using the King's law equation,

$$E^2 = A + B \times U^n, \tag{3.3}$$

where A, B and n are the calibration constants, E is the CTA output voltage and U is the velocity. The standard least square fit is used to calculate the calibration constant.

Cross-wire calibration and data conversion: The two-point velocity calibration and directional calibration were used to calibrate the cross-wire. The cross-wire probe (*i.e.* dual-sensor

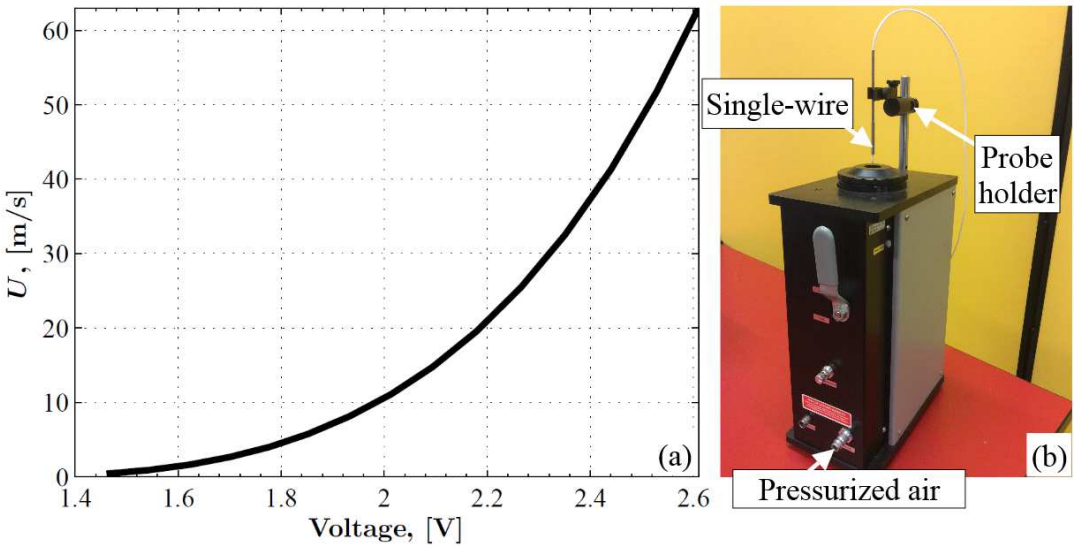

Figure 3.8: (a) Curve fitting of the single-wire calibration data, (b) hot-wire calibrator (single hot-wire probe)

probe) provides the individual directional sensitivity coefficients which are the yaw factor k for the sensors. The yaw coefficients, k_1 and k_2 are then used to break down the calibration velocities, U_{cal1} and U_{cal2} into the actual flow velocity components, U and V. In order to calculate the average yaw factors for the two sensors of the cross-wire, the probe was rotated using the rotation unit in which the calibration is performed through the crossing point of the wires perpendicular to the wire plane. Figure 3.9 refers to the yaw calibration voltage results obtained from the directional calibration.

A maximum angle of α_{max}=45° was taken in the experiment between the probe axis and the velocity vector. The probe was rotated from −45° to +45° to obtain the voltages from the two sensors. The sensitivity factors for the two sensors are then calculated via averaging the k_1 and k_2 values. This yaw factor acquired will be applied in the data conversion to obtain the velocity components, U and V. The decomposition of the cross-wire probe voltages into the velocity components, U and V was computed together with the yaw factors. Firstly, the calibrated velocities of U_{cal1} and U_{cal2} are calculated using the linearisation functions for both sensor 1 and 2. Next, the velocities U_1 and U_2 in the wire coordinate system is calculated using,

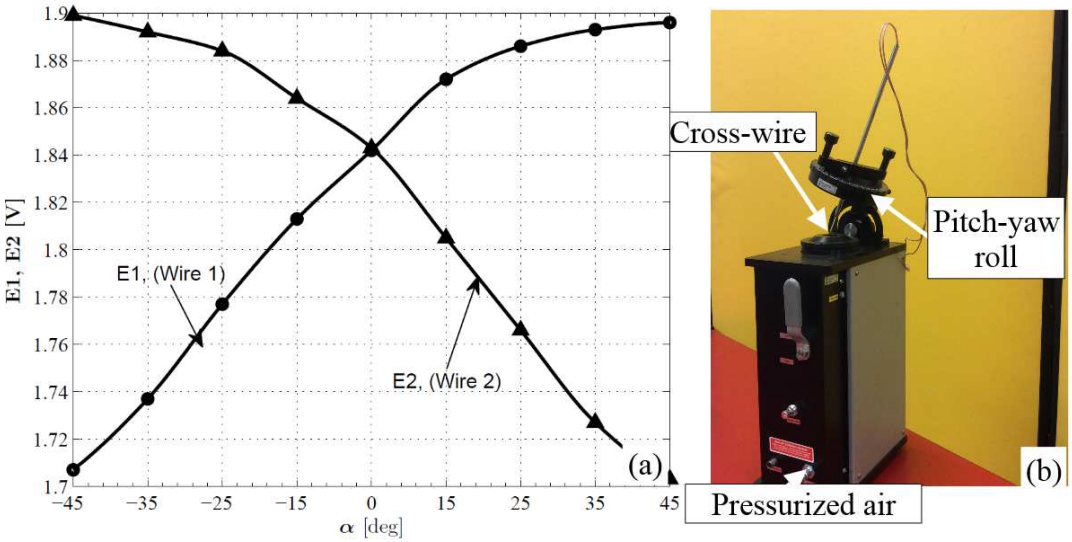

Figure 3.9: (a) The yaw calibration voltage results obtained from the cross-wire probe, (b) hot-wire calibrator (cross-wire probe).

$$
\begin{aligned}
k_1^2 \times U_1^2 + U_2^2 &= \frac{1}{2} \times (1 + k_1^2) \times U_{cal1}^2, \\
U_1^2 + k_2^2 \times U_2^2 &= \frac{1}{2} \times (1 + k_2^2) \times U_{cal2}^2.
\end{aligned}
\tag{3.4}
$$

The velocities, U and V in the probe coordinate system was then calculated using,

$$
\begin{aligned}
U &= \frac{\sqrt{2}}{2} \times U_1 + \frac{\sqrt{2}}{2} \times U_2, \\
V &= \frac{\sqrt{2}}{2} \times U_1 - \frac{\sqrt{2}}{2} \times U_2.
\end{aligned}
\tag{3.5}
$$

The hotwire signal digitization results is N statistically independent sample distribution. The mean value of the U and V is evaluated by averaging of the velocity signals $u(t)$ and $v(t)$ as,

$$
\begin{aligned}
U &= \frac{1}{N} \sum_{i=1}^{N} u, \\
V &= \frac{1}{N} \sum_{i=1}^{N} v.
\end{aligned}
\tag{3.6}
$$

The velocity fluctuations, $u^{'}(t)$ and $v^{'}(t)$ are computed by subtracting the mean component of the velocity signals $U(t)$ and $V(t)$ as,

$$\begin{aligned} u^{'}(t) &= u(t) - U, \\ v^{'}(t) &= v(t) - V. \end{aligned} \tag{3.7}$$

The root mean square (RMS) of the velocities components and the Reynolds shear stress have been calculated as,

$$\begin{aligned} U_{rms} &= \sqrt{\frac{1}{N}\sum_{i=1}^{N}(u')^2}, \\ V_{rms} &= \sqrt{\frac{1}{N}\sum_{i=1}^{N}(v')^2}, \\ \overline{u'v'} &= \frac{1}{N}\sum_{i=1}^{N} u^{'}v^{'}. \end{aligned} \tag{3.8}$$

Note that the measurements from the two wires of the cross-wire are taken to be simultaneous, which is assumed to neglect the small time lag during the A/D data transfer.

3.2.4 Pressure distribution measurements

The static pressure measurements were performed using a 32 channel Chell MicroDaq Smart Pressure Scanner, shown in Fig. 3.10. The static pressure tappings were made from 1.6 mm diameter brass tube with 0.4 mm surface diameter holes, which were drilled normal to the plate surface in order to avoid any aerodynamic interference between the pressure taps. The pressure tappings were connected to the MicroDaq pressure scanner using 0.8 mm internal diameter of PVC tubing. The scanner is able to measure the pressure difference of up to 1 Psi, with the system accuracy of ± 0.05% full-scale. The static pressure data for the flat plate test rig was acquired for 60 seconds, with a sampling frequency of 500 Hz. The accuracy of the pressure measurements carried out for the flat plate scrubbing case was below 5 Pa. The static pressure coefficient is calculated using,

$$C_p = \frac{p_i - p_\infty}{\frac{1}{2}\rho_\infty U_\infty^2} = \frac{p_i - p_\infty}{p_o - p_\infty}, \tag{3.9}$$

where p_i is the measured static pressure at the i^{th} location along the plate, p_∞ is the free-stream static pressure and p_o is the stagnation pressure.

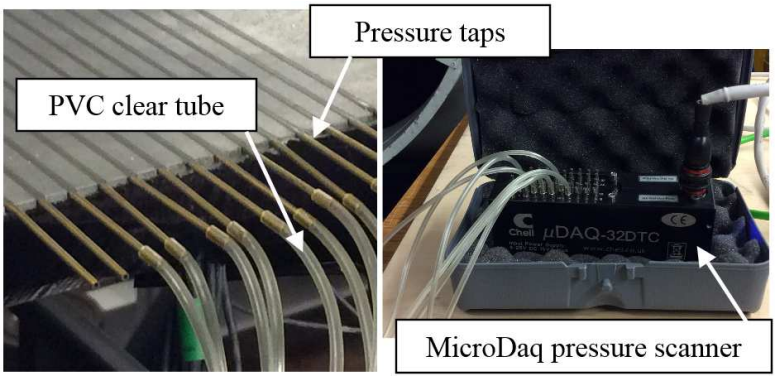

Figure 3.10: MicroDaq pressure scanner used for flat plate scrubbing configuration

3.2.5 Unsteady surface pressure measurements

To achieve a better understanding of the boundary layer flow characteristics, surface pressure fluctuation measurements have been performed using an array of miniature Knowles FG-23329-P07 transducers. These miniature transducers, shown in Fig. 3.11 have regularly been used in aeroacoustic applications, particularly for boundary layer surface pressure measurements [168, 169], due to their small size and good frequency response.

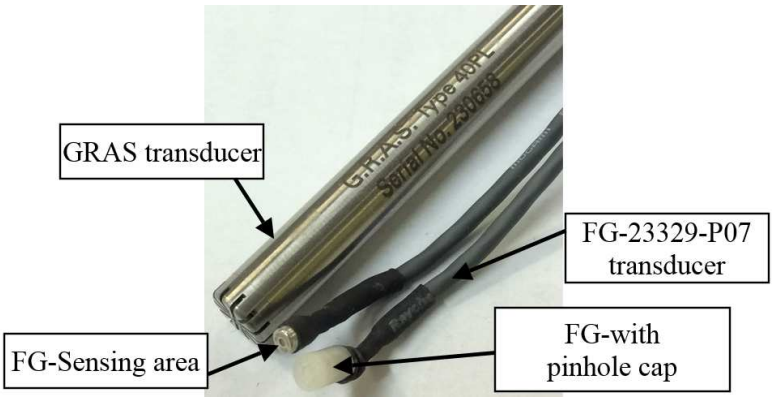

Figure 3.11: GRAS 40PL transducer, FG-23329-P07 transducer and FG-23329-P07 transducer with pinhole cap

It is known that at high frequencies, where the acoustic wavelength is smaller than the transducer sensing area, the measurement errors may arise due to the spatial integration of the pressure fluctuations [170]. In order to eliminate the errors present in the wall pressure spectrum measurement, a small-sized pinhole transducer sensing area is employed. The both test-rigs, *i.e.* flat plate and blunt trailing-edge plate, used in the study are instrumented with flush mounted miniature Knowles-transducers under a pinhole mask of 0.4 mm diameter. The geometrical dimensions of the pinhole configuration are chosen from a series of test based on its diameter and length of the pinhole to ensure the resonance frequency associated with the pinhole design does not affect the measurements within frequency range of interest. The desired resonance frequency is set out to be greater than 20 kHz, which is outside the frequency of interest. An illustration of the transducer arrangement with the pinhole mask is shown in Fig. 3.12 and the frequency response (amplitude and phase) from the transducers with and without the pinhole is shown in Fig. 3.13.

According to the studies carried out by Gravante [171], to avoid attenuation due to the pinhole size, the pinhole nondimensional diameter (d^+=$d\ u_\tau/\nu$), *i.e.* u_τ is the friction velocity and ν refers to the kinematic viscosity, should be in the range of $12 < d^+ < 18$ for frequencies up to $f^+ = f\nu/u_\tau^2 = 1$. The pinhole diameter (d) to the wall unit ν/u_τ ratio, *i.e.* d^+=$d\ u_\tau/\nu$, determines the significance of the pressure fluctuations attenuation. The pinhole mask used for the current study for the free-stream velocity of 20 m/s, gives a non-dimensionalized diameter, $d^+ \approx 12$ for flat plate scrubbing case and a diameter range of $12 < d^+ < 19$ for blunt trailing-edge case, which is close to the pinhole diameter suggested by Gravante. The uncertainty obtained from the surface pressure measurements were found to be within ±0.5 dB with 99% of confidence level. The data have been acquired using a National Instrument PXIe-4499, with a sampling rate of 204.8 kHz. The surface pressure data have been collected using a sampling frequency of $2^{16}\ Hz$ and measurement time of 32 seconds. The uncertainty of the surface pressure data due to the statistical convergence error [168] is calculated by dividing the pressure time series data to a sequence of records. A total of 2048 records were applied and the uncertainty value calculated is about 2.2 % ($1/\sqrt{N_T}$, N_T is the number of records used). The transducers are arranged in the form of an L-shaped array in the streamwise and spanwise directions (see Fig. 3.4). The

transducers located in the spanwise direction will be used for the calculation of the spanwise coherence and length-scale of boundary layer structures, while the transducers employed in the streamwise direction provide information on the evolution of the turbulence structures as they move downstream towards the trailing-edge and their convection velocity. The detailed locations of the pressure transducers on the test specimens will be further deliberated in Chapters 5 and 6.

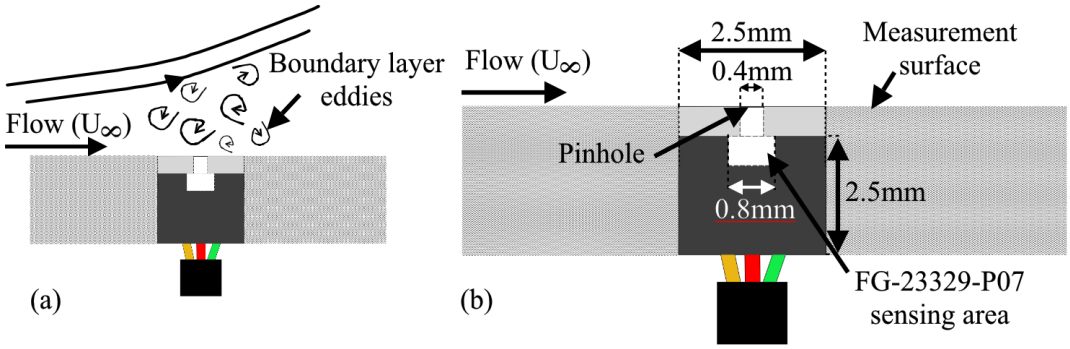

Figure 3.12: (a) Schematic drawing of the in situ sensing configuration (b) Dimension of the pinhole and transducer configuration

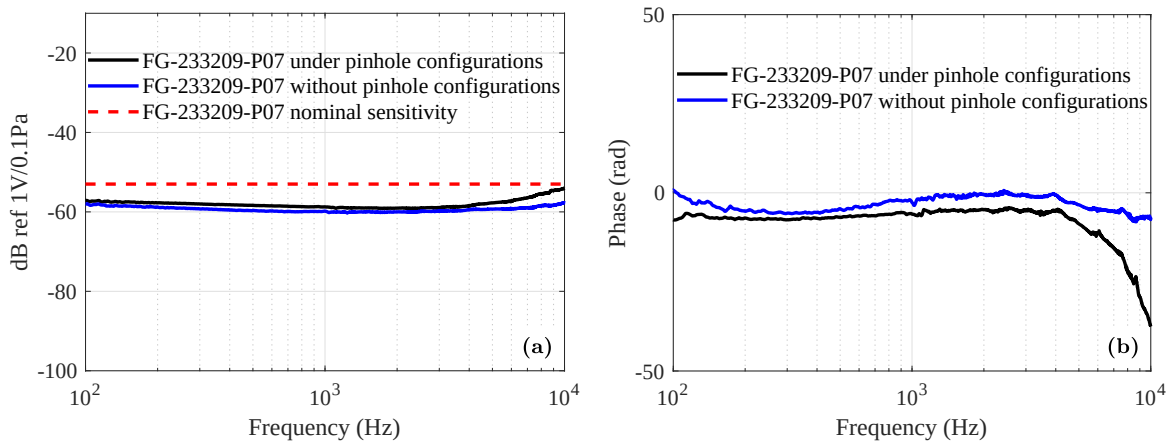

Figure 3.13: The frequency response ((a)amplitude and (b) phase) from the transducers with and without the pinhole

3.2.6 Far-field microphone measurements

To achieve a better understanding of the effect of the porous treatment on the radiated noise from the blunt flat plate, far-field noise measurements have been performed using an array of 23 GRAS 40PL free-field microphones, with a frequency range of 10 Hz to 20 kHz and a dynamic range of 142 dB. The GRAS 40PL microphones exhibit a flat frequency response, with variation of ±1 dB for frequencies from 10 Hz to 10 kHz, which covers the frequency range of interest in the present study. The microphone array in the anechoic chamber was placed 1.75 m from the plate trailing-edge, which covers the polar angle range of 25° to 135°, with a regular interval of 5°. The microphones were assembled using mounting clips on an aluminium arc array. The microphone array arc was attached directly to the ceilings of the acoustic chamber. In order to accommodate acoustics measurements of bodies with different dimensions, the aluminium microphone arc was designed such that it can move along the axial distance of the nozzle. The arc was covered with 50 mm thick pyramid profiles acoustic foam insulation to prevent reflections from the aluminium surface underneath from reaching the microphones. Great care was taken to ensure that the expanding jet does not impinge upon the microphones. The GRAS 40PL microphone was connected to a 15 m coaxial SMB (SubMiniature version B)-BNC (Bayonet Neill–Concelman) cable with an excellent electrical performance from DC to 4 GHz, and the voltage signals were transmitted to the National Instrument PXIe-4499 data acquisition system. A schematic of microphone assembly and the hardware support is shown in Fig. 3.14.

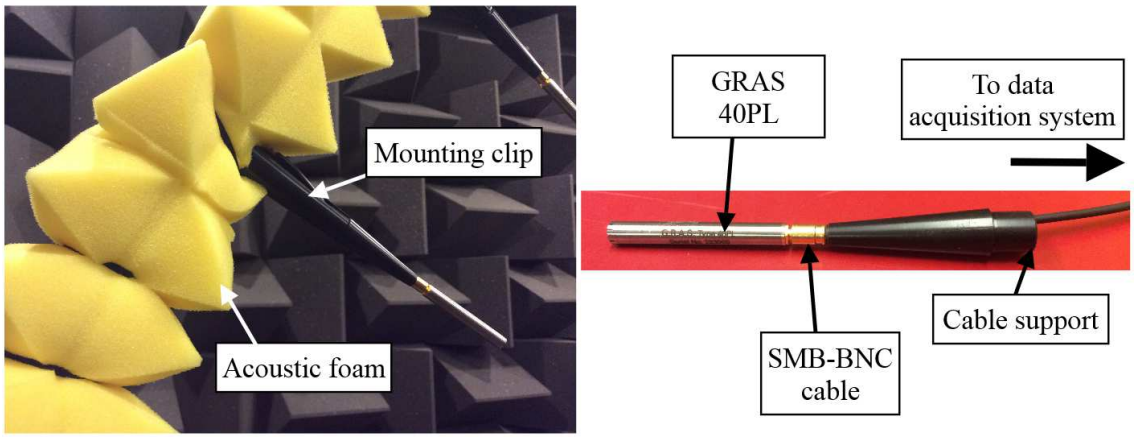

Figure 3.14: Far-field microphone setup

The acoustic data have been acquired using a National Instrument PXle-4499 with a sampling rate of 204.8 kHz. The far-field measurements have been carried out with a sampling frequency of 2^{16} Hz and measurement time of 32 seconds. The uncertainty of the pressure data due to the statistical convergence error [168] is calculated by dividing the pressure time series data to a sequence of records. A total of 4096 records were applied and the uncertainty value calculated is about 1.6 % ($1/\sqrt{N_T}$, N_T is the number of records used). A schematic diagram of the acoustic experimental setup for the far-field measurements using a blunt flat plate is shown in Chapter 6.

3.2.7 Surface pressure transducer calibration

The FG-23329-P07 transducers were calibrated in situ against a GRAS 40PL reference transducer, whose sensitivity was known to within a very small tolerance, with an almost flat frequency response up to 10 kHz, and uncertainty level of ±1 dB. The calibration process involves the simultaneous measurement of the white noise with the flush-mounted FG-transducer and the reference GRAS-transducer (*i.e.* both the transducers are exposed to the same white noise signal). Figure 3.15 shows the calibrator design used to acquire the sensitivity and the transfer function values of the FG-transducers.

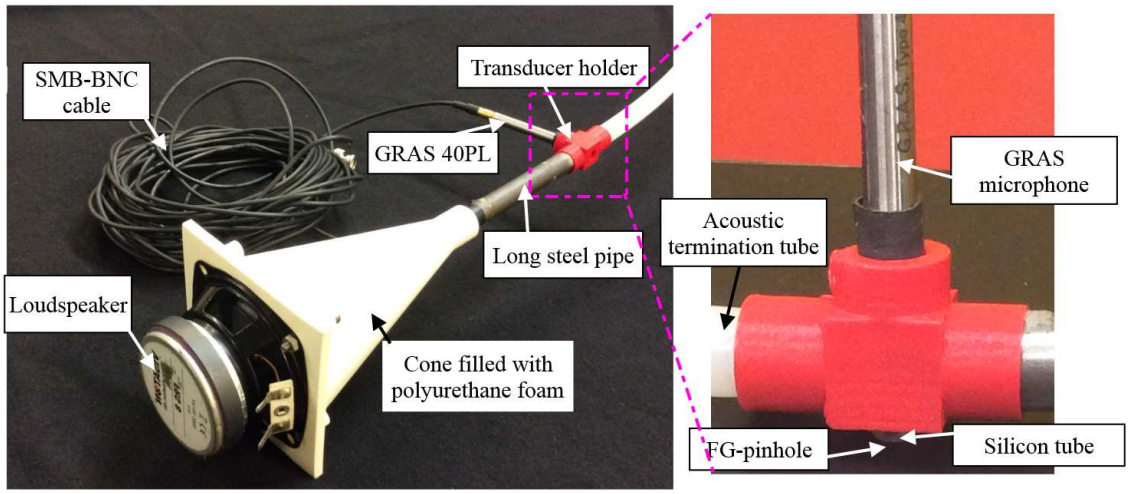

Figure 3.15: In situ FG-23329-P07 calibration device

The calibrator is made out of a cone with a long steel pipe connected to a loudspeaker. Plane

waves form in the long steel pipe when a white noise is fed into the pipe using the speaker, through the cone. The pipe is composed of a length (l_t) of 120 mm and a diameter (d_t) of 10 mm. In order to assure a plane wave propagation through the whole channel, the cone was manufactured with the smallest angle possible. The plane waves develop in the pipe in the acoustic range of $kd_t/2 < 1.84$, where $k = 2\pi f/c$ is the wavenumber term [172]. In the present work, the plane waves can develop of up to 20 kHz, which is beyond the frequency range of interest. The polyurethane foam was used to fill the cone cavity to ensure the attenuation of any possible higher order modes and to eliminate the effects of any external noise. The end of the steel pipe was connected by a small transducer holder to allow both of the transducers to be held at equal distances from the central axis of the cone, with an extension tube for acoustic termination. A silicon tube with a length of $\approx 3mm$ is used to enable a smooth transmission of pressure waves to the flush mounted microphone. Note that, standing waves will form in the pipe as a result of the acoustic excitation. The nodal frequency of the standing waves is given as $f_n = nc/4l_t$, where n is the number of the acoustic mode and c is the speed of sound. Based on the configuration used in the present work, the first acoustic mode is found at about $f_n \approx 715$ Hz, its harmonics can be seen at $f_n = n.715$ Hz. The sound field inside the pipe is well defined by the geometry constraints (d_t,l_t), and also the properties of the speaker. In order to ensure the repeatability of the calibration, the calibration procedure has been carried out in-situ, before and after each measurement. The calibration method employed follows the procedure documented by Mish [173], and an illustration of this method is shown in Fig. 3.16.

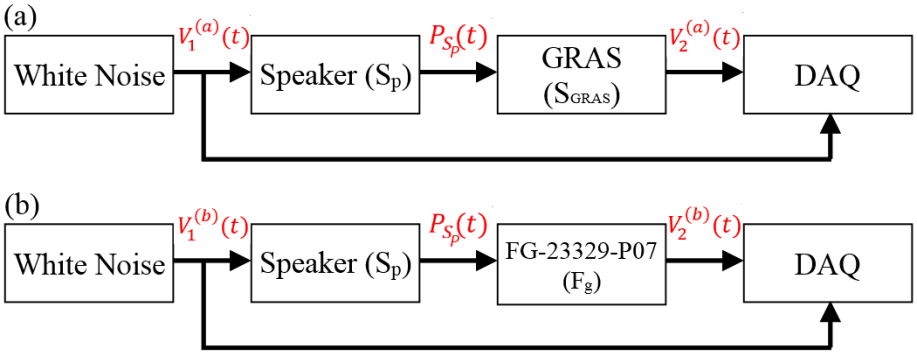

Figure 3.16: Transducer calibration procedure, (a) Speaker response measurement using GRAS transducer, (b) FG-23329-P07 transducer frequency response calibration

The surface pressure FG-23329-P07 transducer calibration method are performed to obtain (a) the speaker response using the GRAS transducer and (b) the frequency response of the FG-23329-P07 transducer. The detail description of the procedure is provided below.

(a) Speaker response measurement using GRAS transducer: In order to measure the speaker response ($S_p(f)$), a simultaneous measurement of the white noise source,$V_1^a(t)$ and the GRAS transducer output signals, $V_2^a(t)$ was performed. Since the broadband sensitivity, S_{GRAS} of the GRAS transducer is known, the output signal from the speaker, $P_{S_p}(t)$ can be calculated from,

$$P_{S_p}(t) = \frac{V_2^a(t)}{S_{GRAS}} \quad [Pa]. \tag{3.10}$$

The speaker response, $S_p(f)$ can then be calculated in the frequency domain from,

$$S_p(f) = \frac{E[P_{S_p}(f) \cdot V_1^a(f)]}{E[V_1^a(f) \cdot V_1^a(f)]} = \frac{G_{V_2^a V_1^a}}{G_{V_1^a V_1^a}} \cdot \frac{1}{S_{GRAS}} \quad \left[\frac{Pa}{V}\right], \tag{3.11}$$

where E is the expected operator value, G is the cross- spectrum between the two signals (V_1^a and V_2^a).

(b) FG-23329-P07 transducer frequency response calibration: In order to measure the frequency response of the surface pressure FG-23329-P07 transducer, a simultaneous measurement of the white noise source,$V_1^b(t)$ and the FG-23329-P07 transducer output signals, $V_2^b(t)$ was conducted. The speaker and FG-transducer frequency response can be measured from,

$$S_p(f) \cdot S_{FG}(f) = \frac{E[V_2^b(f) \cdot V_1^b(f)]}{E[V_1^b(f) \cdot V_1^b(f)]} = \frac{G_{V_2^b V_1^b}}{G_{V_1^b V_1^b}}. \tag{3.12}$$

Since the output of the speaker response is known from Eq. 3.11, the FG-transducer frequency response can be evaluated from,

$$S_{FG}(f) = \frac{G_{V_2^b V_1^b}}{G_{V_1^b V_1^b}} \cdot \frac{G_{V_1^a V_1^a}}{G_{V_2^a V_1^a}} \cdot S_{GRAS} \quad \left[\frac{V}{Pa}\right]. \tag{3.13}$$

The calibration procedure detailed above provides the amplitude and phase calibration information for each embedded FG-23329-P07 transducer used in our experiments, which will then be employed in the surface pressure fluctuations data processing. Figure 3.17 shows the comparison of the calibrated transducer sensitivity value and the one described by the manufacturer. The reliability of the calibration results has been quantified using the coherence and phase spectrum and also presented in Fig. 3.17. Figure 3.17(c) illustrates that the coherence between the noise signals and FG signals (black line) is almost negligible. Results have also shown that the coherence is always found to be greater than 0.99 over the whole frequency range (100 Hz-10 kHz), indicating that the calibration is highly accurate and precise.

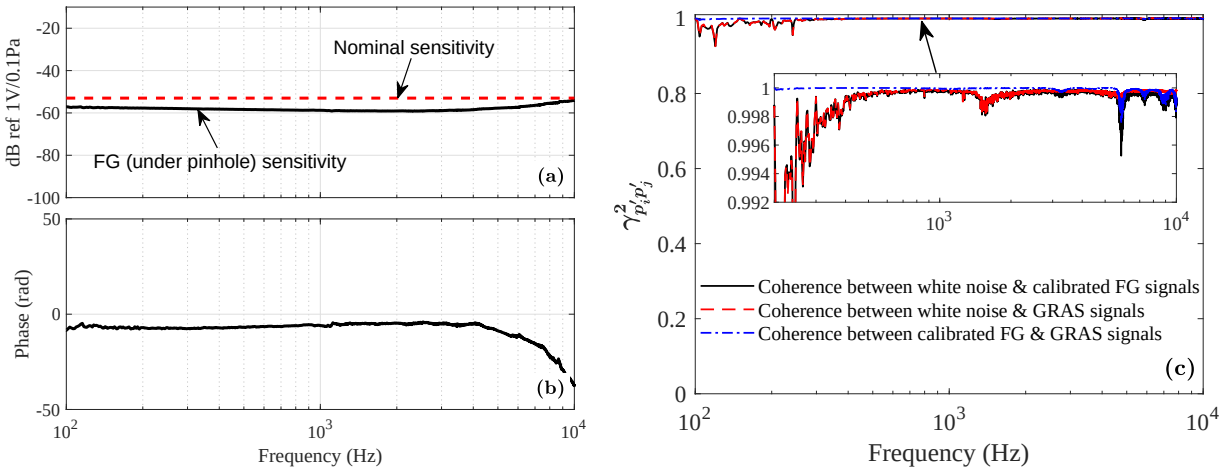

Figure 3.17: Typical (a) broadband sensitivity, (b) the phase spectrum of the FG-flush mounted transducer, and (c) the coherence function between the white noise, FG and GRAS signals.

3.2.8 Far-field microphone calibration

The GRAS Pistonphone Type 42AA was used to provide an end-to-end mechanical calibration of the GRAS microphones, see Fig. 3.18. The pistonphone is operated by a battery and produces a constant sound pressure level of 114 dB with the uncertainty of about ±0.5 dB (under reference conditions), which induced a pressure of 10 Pa at 250 Hz (or equivalent to 105.4 dB(A)). The microphone sensitivities for each microphone were acquired by placing the portable pistonphone directly over the microphone. The pistonphone generates sinusoidal pressure signals using two

reciprocating pistons actuated by a rotating cam and have an accuracy of ±0.5 dB at the reference pressure of 20 μPa [174]. The calibrator produces a time-varying volume displacement in a small cavity of known volume, relative to the wavelength of sound to ensure a precise sound pressure level is obtained. The frequency at which the calibrator operates has been limited to 250 Hz, which enables pistonphone to be used at low frequency. The output voltage at 250 Hz (pistonphone frequency) was computed using the fast Fourier Transform (FFT) and the amplitude obtained was then used to calculate the microphone sensitivity. The GRAS microphone sensitivity (S_{GRAS}) is calculated from,

$$S_{GRAS} = \frac{E}{20 \cdot 10^{-6} \cdot 10^{L_C/20}}, \tag{3.14}$$

where E is the output voltage and L_C denotes the sound pressure level generated by the pistonphone. The sound pressure level (L_C) consists of a nominal sound pressure level (L_n=114 dB), the static pressure correction (L_b=114 dB) and the volume correction (L_v). No correction factors are applied at a static ambient pressure of 101.3 kPa. The pressure correction P_{corr} in decibels can be found from,

$$P_{corr} = 20 \cdot \log_{10}\left(\frac{P_a}{P_r}\right), \tag{3.15}$$

where P_a is the current ambient pressure and P_r is the reference pressure at 101.3 kPa. The corrections for ambient pressure can be made using Barometer ZC0002K when necessary (see Fig. 3.18).

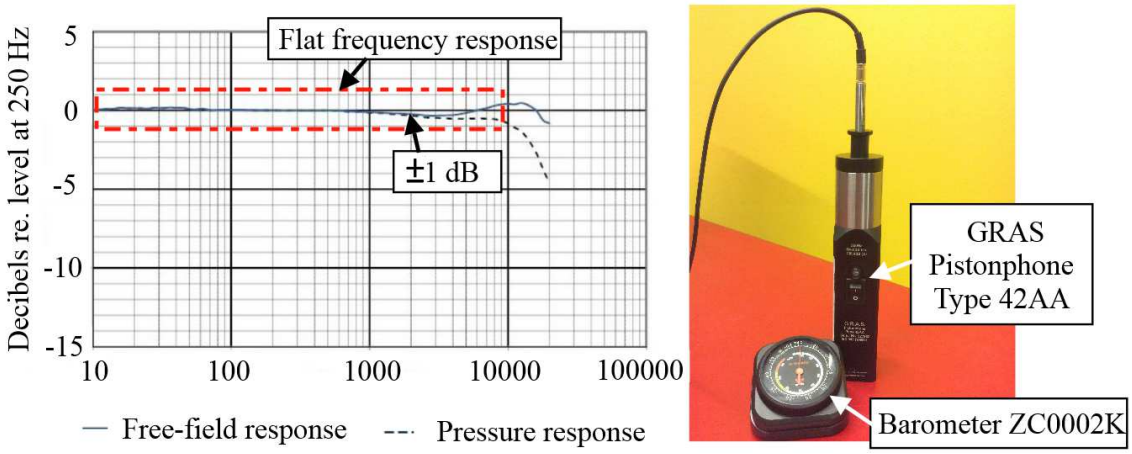

Figure 3.18: GRAS 40PL calibration device

3.3 Estimation of the power spectrum

One of the classical ways to estimate the power spectrum is by using the Fourier transform method. This method is only effective with the measurements involving one frequency and the method is prone to bias and variance with the measurements with more frequencies. In order to minimize the bias and variance, the measurement data can be divided into overlapping sequences and the estimated ensemble averages of the data can be obtained using the Fourier transform, which is also referred to as the Welch's method [175]. The power spectral density using the Welch's method is generally more accurate for statistical estimates than the Fourier transform method and can be found from,

$$\hat{P}_W(e^{j\omega}) = \frac{1}{KLU} \sum_{i=0}^{K-1} \left| \sum_{i=0}^{L-1} w(n)x(n+iD)e^{-jn\omega} \right|^2 \tag{3.16}$$

where $\hat{P}_W(e^{j\omega})$ is power spectrum estimate, $U = \frac{1}{N} \sum_{n=0}^{N-1} |w(n)|^2$ and $w(n)$ is the data for windowing process used to modify each data sequence. The length L is the overlapping D points with the successive sequence. K refers to the number of sequences needed to cover all the data points for N total data points, j denotes the imaginary unit and $e^{j\omega}$ indicates the frequency in units of π.

The quality of the signals obtained can be improved using windowing. The windowing, in principle, reduces the amplitude of the discontinues of each finite sequence. Windowing is computed by multiplying between the time sample record (finite window length) with an amplitude which diverges gradually towards zero at the edges (end-points). This enables the generation of a continuous waveform without any sharp transitions. There are different types of window functions, namely the Rectangular, Hamming, Hanning and Blackman windows, etc. Each window has its own advantageous and disadvantageous based on the signals collected. For instance, the rectangular window may lead to a spectral leakage and although the spectral estimates for the Hamming and Hanning windows are almost identical, the Hamming window exhibits greater weight to the edge points [176], etc. In the present study, the Hamming window function has been chosen to be integrated into the estimation of the power spectrum using the Welch's method. The Hamming window function provides a better accuracy closer to the frequency limits region of the power spectrum compared to that of the rectangular window and

therefore, more precise power spectrum estimates can be obtained [177]. In order to obtain the energy frequency spectra at different boundary layer and wake locations, the Welch's power spectral density [175] with a Hamming window function was performed on the time-domain data for segments of equal length with 50% overlap. The number of segments is chosen such that it provides us with the desired frequency resolution. The frequency resolution for both the experiments are given in Chapters 5 and 6.

3.4 Estimation of experimental uncertainty

The uncertainty analysis of the experimental measurements provides a rationale and reasonable statistics in ascertaining quality data. Experimental errors can arise from the fixed or bias error (e.g., calibration error, etc.) and the variable or random error (e.g., electronic noise, etc.). As for the data acquisition for the actual data, the data uncertainty analysis must also be repeated several times to ensure its repeatability. A more accurate approach using the Kline and McClintock [178] and Bootstrap analysis [179] methods have been applied in this work to estimate the uncertainties involved in the present experimental results.

3.4.1 Kline and McClintock method

According to Kline and McClintock [178], the uncertainty is a 'possible value the error might have'. The uncertainty can be calculated by analyzing the partial derivative of the function that relates an unknown dependent variable (Z) to the independent variables (X,Y), expressed as,

$$Z = f(X,Y). \tag{3.17}$$

The maximum uncertainty is then calculated by adding all the uncertainty terms given by,

$$\partial Z = \sqrt{\left(\frac{\partial f}{\partial X}\bigg|_Y \partial X\right)^2 + \left(\frac{\partial f}{\partial Y}\bigg|_X \partial Y\right)^2}, \tag{3.18}$$

where ∂X, ∂Y and ∂Z are the uncertainties with respect to the variables X, Y and Z, respectively. The values of ∂X, ∂Y and ∂Z are determined from any single or repeated observations, calibrated data, instruments specifications or judgement based on experience. An example of the derivation

using this method is provided in § 4.3.3.1 for the calculation of the uncertainty of the permeability coefficient.

3.4.2 Bootstrap algorithm method

The bootstrap algorithm technique proposed by Efron [179], has also been used in the present uncertainty measurements, especially to determine the sampling frequency and sampling time in § 3.2.1. The bootstrap method estimates the probability density function (PDF) of the statistical data using random sampling method and measures its accuracy in terms of the error prediction, confidence intervals, bias and variance. The bootstrap estimation works in following way.

i. A bootstrap sample $X = (X_1, X_2, ..., X_N)$ is obtained randomly resampling the original data $x_1, x_2, ..., x_N$, with replacement of N times. This approximation is done according to Monte Carlo [180] method by repetitively resampling from the original data in order to obtain the desired accuracy.

ii. The distribution of the bootstrap sample F_N is assumed to be very close to the real distribution F. This is true since each element of the new sample X_i has probability N^{-1} equal to any of the elements of the original sample x_i.

iii. We resample data from the empirical distribution F_N, F_N is known to approach F as $N \longrightarrow \infty$.

iv. The bootstrap algorithm resampling process is repeated by a large number of times B and therefore, the B bootstrap samples of $X^1, X^2, ..., X^B$ are generated, each of size N.

v. The bootstrap sample mean, $\overline{X}_N$ is then calculated for each X^B from,

$$\overline{X}_N = \frac{1}{N} \sum_{i=1}^{N} X_i. \tag{3.19}$$

vi. A schematic representation of the bootstrap process is presented in Fig. 3.19.

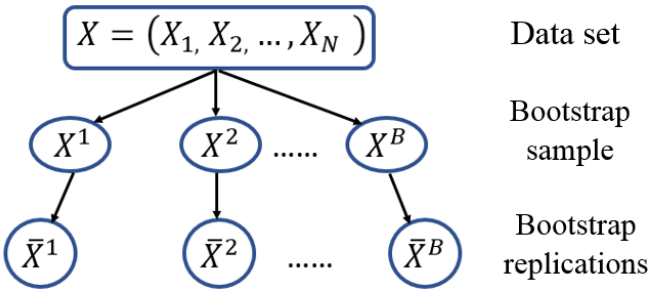

Figure 3.19: Estimation of the standard error of the sample mean using Bootstrap process. The bootstrap samples ($X^1, X^2, \ldots, X^B$) are obtained from the original data $x = x_1, x_2, \ldots, x_N$. The bootstrap replications ($\overline{X}^1, \overline{X}^2, \ldots, \overline{X}^B$) are calculated from the bootstrap samples.

vii. The distribution of the mean from the calculated B bootstrap approximation of the mean is found from,

$$\overline{X}^{\cdot} = \frac{1}{B} \sum_{i=1}^{B} \overline{X}_N, \tag{3.20}$$

where $\overline{X}^{\cdot}$ is the bootstrap mean. The estimation of the standard deviation $\widehat{\sigma}_{boot}$ of the bootstrap distribution can be obtained from,

$$\widehat{\sigma}_{boot} = \frac{1}{\sqrt{B-1}} \left(\sum_{i=1}^{B} (\overline{X}^i - \overline{X}^{\cdot})^2 \right)^{1/2}. \tag{3.21}$$

The probability density function (PDF) is then evaluated by estimating multiple samples of data using the mean value of the measurement data, and the uncertainty interval can then be defined such that the area under the probability density function is 0.95 (95% uncertainty interval). An example of the bootstrap uncertainty analysis in determining the force balance sampling frequency in § 3.2.1 is provided in Fig. 3.20.

The force balance test have been carried out using different sampling frequencies from 15 Hz to 100 Hz with the incremental of 5 Hz. The PDF of the actual signals x, bootstrap mean $\overline{X}^{\cdot}$ and the bootstrap standard deviation $\widehat{\sigma}_{boot}$ are shown in Fig. 3.20 (a), (b) and (c), respectively. The results in Fig. 3.20 show that the maximum fractional error in mean and standard deviation at 95% confidence is about 2σ=±1.1827% and ±2.2578%, respectively. It can be said that the PDF of the variable x of the sampling frequency at 45 Hz, does follow a normal distribution with 95% confidence uncertainty interval.

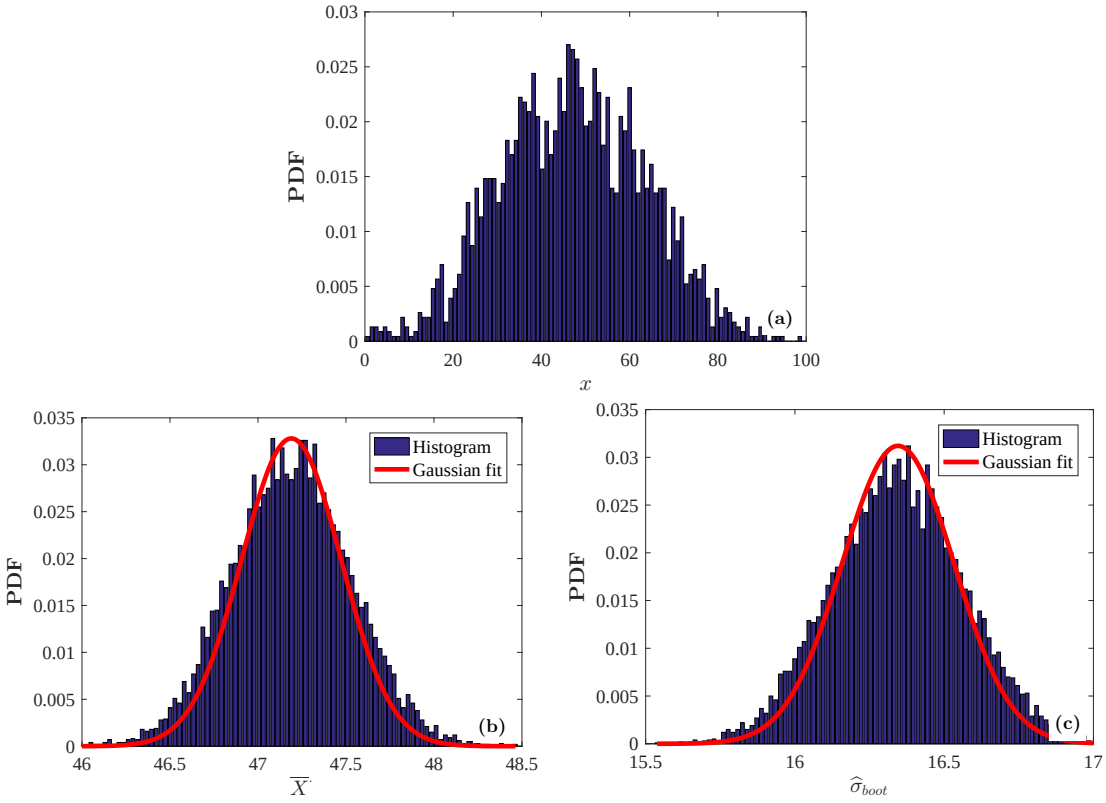

Figure 3.20: Probability density function of bootstrap uncertainty analysis obtained for force balance sampling frequency (§ 3.2.1). (a) PDF of signal, (b) PDF of bootstrap mean and (c) PDF of bootstrap standard deviation.

3.5 Summary

This chapter summarized the description of experiments including the experimental setup, measurement techniques and instrumentation implemented in the present study. There are several different experiments conducted in the present study, hence the implementation of each of the measurement techniques for each of the experiments is reported in detail in Chapters 5 and 6, respectively. The experimental design to characterize the porous materials is briefly explained and reviewed in Chapter 4. This chapter also introduces all the measurement techniques being used namely, the force balance, Particle Image Velocimetry (PIV), Hotwire anemometry, steady and unsteady surface pressure measurements and the far-field noise measurement. The uncertainty analysis for each method used have also been included in this chapter. The experimental campaign conducted in different wind tunnel facilities using different measurement techniques and how the experimental design relates to the research objectives is summarized in Table 3.3.

Table 3.3: Summary of the experimental measurements taken in this study.

Experiment	Facility	Measurements	Research objectives
Experiment 1: Boundary layer flow interaction with a permeable wall. Test-rig: *Flat plate*	Open jet wind tunnel	Hotwire boundary layer and wake velocity	To investigate the flow field manipulation and boundary layer modifications on the noise producing flow structures as a result of the porous treatment and their potential implications on noise generation.
		Steady and unsteady surface pressure	
		Velocity-pressure coherence and correlation	
	Low turbulence wind tunnel	Particle Image Velocimetry (PIV)	
Experiment 2: Bluntness Flow and Noise Control Using Porous Treatments. Test-rig: *Blunt trailing-edge*	Open jet wind tunnel	Force balance	To demonstrate the aerodynamic and the associated noise control of porous treatments.
		Hotwire boundary layer and wake velocity	
		Surface pressure	
		Velocity-pressure coherence and correlation	
	Open jet anechoic wind tunnel	Far-field noise	

CHAPTER 4

POROUS MEDIA CHARACTERIZATION

As discussed in Chapter 2, the use of porous foams for passive or semi-active control of flow-induced noise and vibrations, i.e. controlling the flow and noise simultaneously, has been shown to be quite effective. However, to optimize the flow/noise control, it is crucial to better understand the physics of flow transport through porous materials for different aero-structures by carrying out a systematic set of experimental and theoretical studies. The intricate structures of the porous materials, owing to its large surface area to volume ratio and the effect of permeability, make them useful for a wide range of engineering applications, such as aerospace, chemical, energy, etc. This chapter reviews and discusses the various factors influencing the flow control using porous media, including the porosity, permeability and the surface roughness. Section 4.1 outlines the general framework of the fundamentals of porous materials. Section 4.2 discusses the computed tomographic scanning methods for the measurement of the porosity of the samples. Section 4.3 discusses the methods used to measure the permeability and characterizes the interrelationship between the porosity and the permeability of the material. Section 4.4 reviews the method used to evaluate the surface roughness profile of the porous materials. These parameters will provide additional information towards a better understanding of the material properties and their influence on the fluid flow and porous interaction and flow induced noise generation and control.

4.1 Porous Structure: Theory and Fundamentals

Porous materials can generally be categorized into two main types, namely the open- and closed-pore porous materials, with various shapes and sizes. The open-pore porous materials is distributed within the solid form of pores or cavities which exhibits an interconnected open channels structure, *i.e.* allowing access of external fluid into the porous media. The closed-pore materials, on the other hand, contain pores that are completely isolated from the external surface, *i.e.* not allowing access of external fluid into the porous media. The porous media used in the present study are all of open-pores type, which can potentially controls all relevant physical and chemical properties as well being a medium for fluid flow transport processes in the porous substrate. Figure 4.1 shows the structure of a porous material with different shapes, *i.e.* cylindrical open, cylindrical blind, ink bottle shaped, funnel shaped and roughness and fluid-flow accessibility including the open and closed pores, blind pores and through pores.

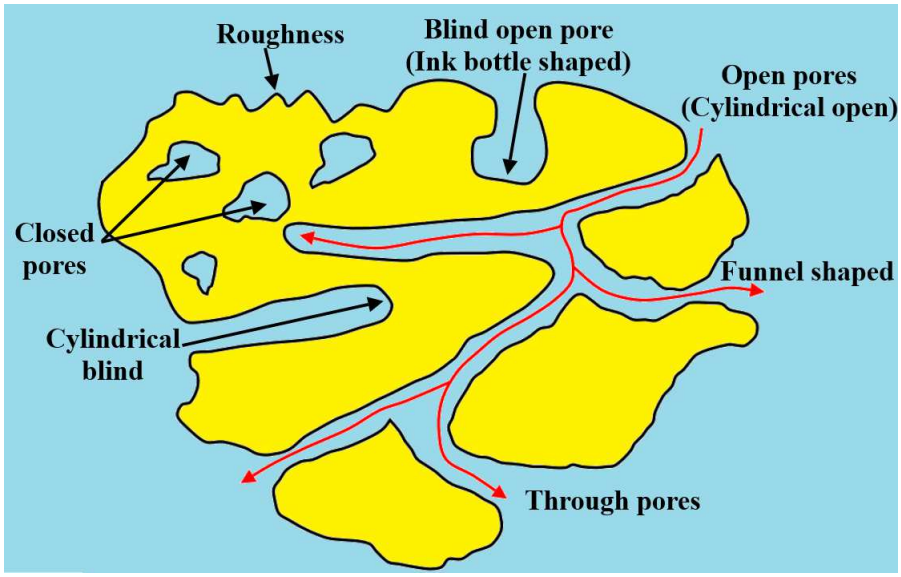

Figure 4.1: Connected pores allowing fluid to flow [181].

There are different types of open-cell foam material manufactured commercially, which include rigid polyurethane foams, uncompressed aluminium metal foams, felt materials, etc., suitable for a variety of engineering applications. In the present study, five uncompressed metal foams with the PPI (pores per inch) of 25, 35, 45, 50 and 80 have been chosen and are used

selectively depending on the different investigated applications. The pictures of the porous materials used are shown in Fig. 4.2.

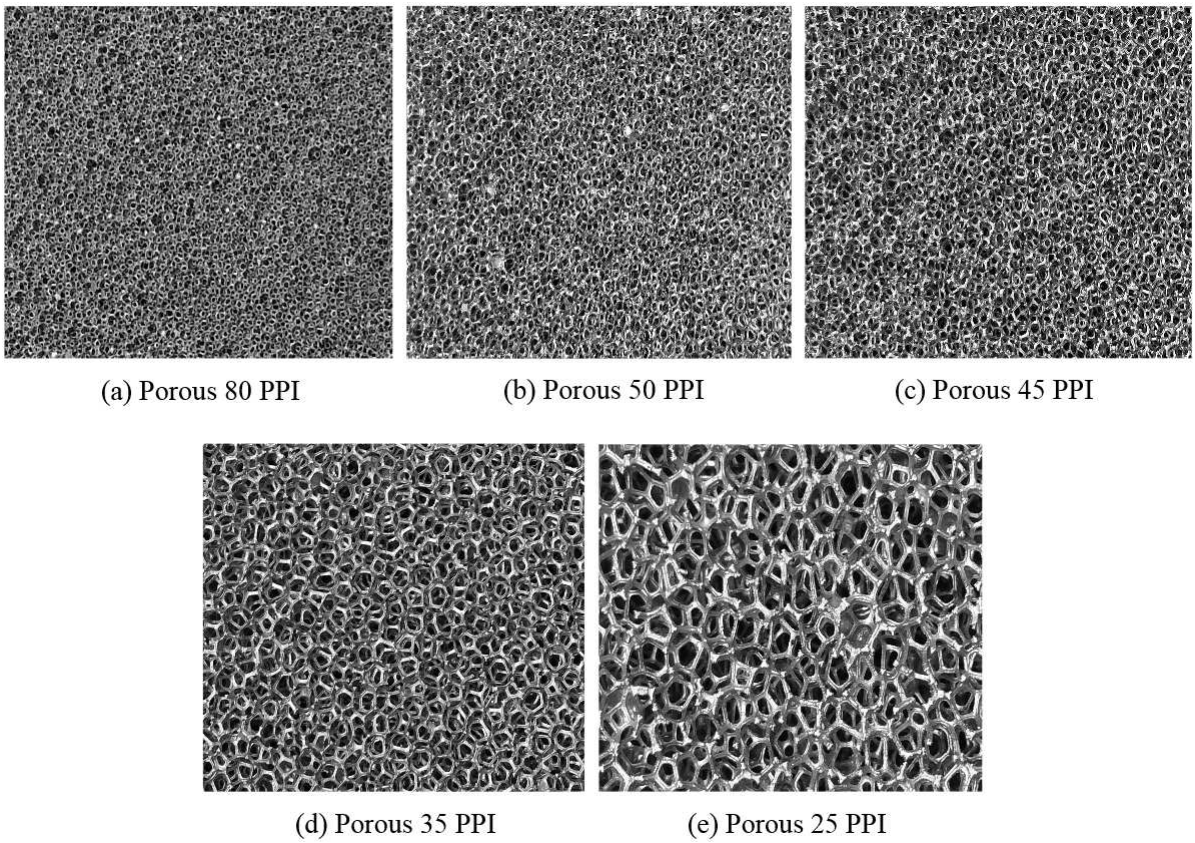

(a) Porous 80 PPI (b) Porous 50 PPI (c) Porous 45 PPI

(d) Porous 35 PPI (e) Porous 25 PPI

Figure 4.2: Photographs of different type of porous materials.

The pore size is a property of major attention in the practical application of porous materials. However, it is quite difficult to precisely define this complicated structure as it usually comprises of highly irregular, complex geometrical shape (*i.e.* cylindrical pores, conical pores, slit-shaped pores and etc.). As a simple method, the pores dimension can be defined using the diameter of the pores, and the pore size regimes can be described following the definitions adopted in the IUPAC (International Union of Pure and Applied Chemistry) [182]. The three types of pore regimes with their generic diameters are defined as follows:

- Micro-pores: diameters smaller than 2 nm and can be used for an activated transport or micro-pore diffusion mechanism [182],

- Meso-pores: diameters in the range between 2 and 50 nm and dominated by Knudsen diffusion, surface diffusion and capillary condensation [182],
- Macro-pores: diameters larger than 50 nm and often influenced by bulk diffusion and viscous flow transport mechanisms [182].

As for the present study, the porous materials are of rigid structure with regular round pores. The porous material properties can be classified using the macroscopic parameters (macro-pores), which is governed by the geometrical and mechanical properties of the material, namely, porosity, air flow permeability, tortuosity, thermal permeability, viscous characteristics, thermal viscous characteristics, surface roughness, etc. [183]. The definitions and descriptions of the porous material properties are as follows:

- The volume porosity (φ): The ratio between the pores volume to the overall total volume,
- The air flow permeability (κ): The capacity of the porous medium in allowing fluids to penetrate/permeate through it,
- The tortuosity (τ): The ratio of the effective flow length though pores to the minimum length of the flow inlet and outlet,
- The thermal permeability ($\kappa^{'}$): The thermal analogue to the dynamic viscous permeability,
- The viscous characteristic dimension (λ): The irregularity of the pore cross-section,
- The thermal viscous characteristic dimension ($\lambda^{'}$): The high-frequency behaviour of the pores compressibility,
- The surface roughness (Ra): The divergence of the normal vector direction of a surface from its ideal form.

It is known from prior experimental [184, 185] and computational [80, 186] works that the effectiveness of porous materials as a flow control technique depends heavily on their porosity and permeability coefficients. Since it is proven that the porosity, φ and the air flow permeability, κ are the properties of major importance that will significantly affect the flow structures, these

parameters will be used to describe the porous materials in the present thesis. Additionally, the surface roughness (Ra) of the open-pore porous substrates are also being investigated as another parameter which can potentially affect the flow structures. The other parameters highlighted above, such as the tortuosity (τ), thermal permeability ($\kappa^{'}$), viscous characteristic dimension (λ) and thermal viscous characteristic dimension ($\lambda^{'}$), have not been used as they are of minor importance for the aerodynamic and aeroacoustics studies presented in this thesis. The porosity (φ), the air flow permeability (κ) and the surface roughness (Ra) of all the porous materials have been investigated and are further discussed in the next sections.

4.2 Volume Porosity

Porosity is a basic geometric property of a porous material and is a measure of the proportion of the total volume of the material occupied by pores [187]. Despite its simple definition, the accurate measurement of the porosity is not easy. There are numerous $2D$ and $3D$ imaging techniques that can be used to evaluate the porosity of porous materials. For instance, the $2D$ methods include the scanning electron microscopy (SEM), transmission electron microscopy (TEM), optical light microscopy (OM), energy dispersive X-ray spectroscopy (EDX), focused ion beam (FIB) and field emission scanning electron microscopy (FESEM). The $3D$ methods include the atomic force microscopy (AFM), nuclear magnetic resonance (NMR) and the X-ray computed tomography scanning. With the use of $3D$ measurement techniques, it is possible to investigate the three-dimensional volume of the porous material with very high resolution and thus, the inner structure of the porous samples. In the present study, a Computed Tomography (CT) scanner with high precision has been used to evaluate the porosity of the samples.

4.2.1 Theory and principle of Computed Tomographic Scanning

The porosity study was carried out using a Nikon XT H 320 LC computed tomography scanner. The principle of the Computed Tomography scan method used for porous sample scanning is shown in Fig. 4.3. A number of X-ray radiographs projection images were taken at different projection angles through the porous sample, as seen on a detector. The X-ray beam energy

attenuation relies upon the density and the thickness of the porous sample in the direction of the beam and the attenuation behaves exponentially in nature in relative to the thickness of the porous sample. This can be simply represented mathematically as [188];

$$I = I_0 \exp(-\mu_x t_x), \tag{4.1}$$

where I is the X-ray beam intensity passing through the porous sample, I_0 is the X-ray beam energy at the source, μ_x is the linear attenuation coefficient of the porous sample and t_x is the porous thickness in the direction of the X-ray beam.

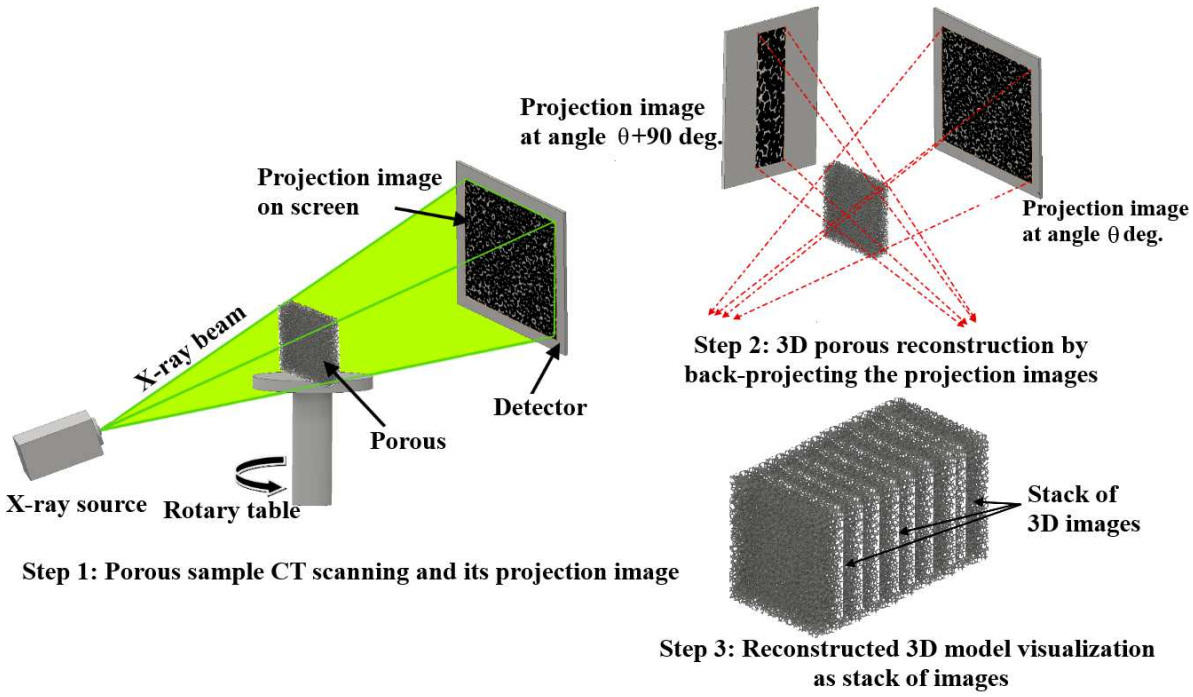

Figure 4.3: Computed tomography scanning principle used for porous sample scanning.

The net intensity I of the X-ray beam appeared from the porous sample along the beam direction is represented by the gray level value of each pixel in every single projection image. The $2D$ projection images which consist of the X-ray attenuation information through different voxels at the various direction of the porous sample are integrated together in order to reconstruct the $3D$ volume of the porous sample, using the filtered back-projection technique [188]. The rebuilt $3D$ volume is then considered as a stack of porous images, in which each of the images

is associated with a finite thickness equal to the voxel size. The $3D$ data obtained are then partitioned into multiple segments with different sets of pixels. The image segmentation provides simplified representation of an image, where each of the pixels in the image shares certain similar features, such as the intensity, texture or colour, and the threshold value attained is used for further data analysis.

4.2.2 Porous sample and CT scanning details

In the present work, the porous samples with a volume of 50 mm × 50 mm × 15 mm were used in order to acquire higher magnification results with greater voxel scanning resolution. The porosity inspections were carried out on 225 kV module reflection X-ray source with a minimum achievable spot size of about 3 μm, using a tungsten target and a flat panel detector. The X-ray voltage was set to 90 kV, while the X-ray current was set to 125 μA, for all porous samples (25, 35, 45, 50 and 80 PPI). A total of 2000 projections were taken, averaging over four frames per projection with 500 ms image exposure. All the data obtained were then visualized and analyzed using the Volume Graphics (VGStudio MAX 2.2) software. Specifically, the 'defect detection' module was used for the porosity voids calculation. A 35 μm of voxel resolutions is used in each set of test. The data recorded by the CT-scan is presented in a voxel data set, which obtained in a stack of gray scales images. A gray level histogram illustrates the number of pixels of an image that shares the same gray level with one another and this information is used to calculate the threshold value of the porosity data. The threshold value chosen is important in determining the porosity value. For instance, poor quality data due to defective or overzealous data processing may lead to increase in the user bias during thresholding. It was observed that the change in the porosity value at smaller voxel size (3 μm to 35 μm, higher scan resolution), *i.e.* 3 μm is the minimum voxel size, is about 1-2% whereas the porosity value changes by 4-5% with the larger voxel size (≥ 35 μm, smaller scan resolution). In other words, the discrepancy in the porosity value obtained is higher at lower scan resolution. The data segmentation probability threshold value is set to 1.0 for the computation of the porosity value. The porous image stack is represented by the grey value between air and metal and is shown in Fig. 4.4.

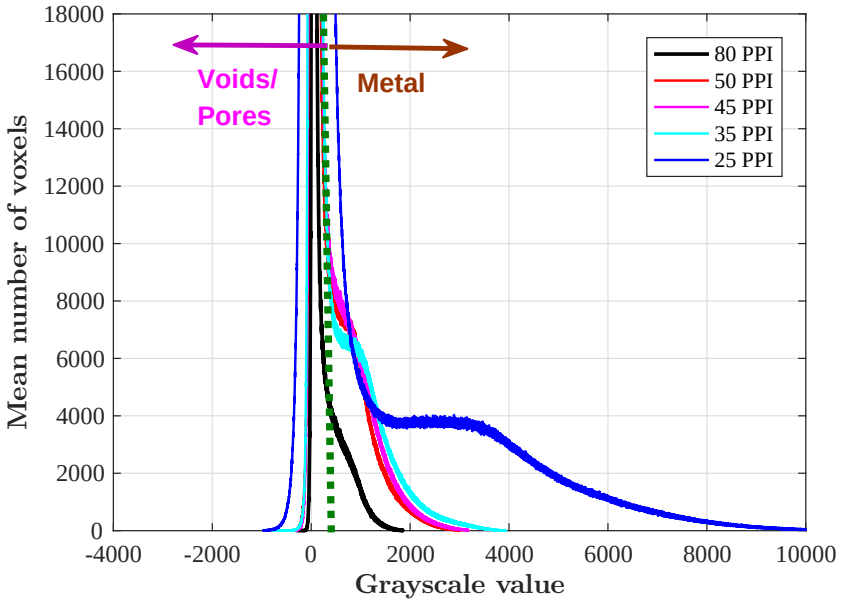

Figure 4.4: Histograms of grayscale values of porous specimens cross sections from micro-CT images.

4.2.3 Data analysis and porosity values

The selection of the volume region is important for the accurate estimation of the porosity of the porous samples. In order to avoid the effect of background volume (*i.e.* resulting in easier distinction of the porous voxels from the background) and to reduce the effects of changing the volumetric region (*i.e.* various properties of the voxels in the selected volume) in different scans on the calculated porosity value, a regular common volume within the porous sample is chosen to realize the porosity calculation. Figures 4.5 to 4.9 show the selected volume for porosity analysis in three different porous slice views (top, front and side views) and also with its $3D$ volume structure. The porosity is then calculated as,

$$\varphi = \frac{V_V}{V_T}, \tag{4.2}$$

where φ is the porosity, V_V is the volume of void space and V_T is the total volume of the sample. The porosity values for all the porous materials used in the present study is shown in Table 4.1 as part of the overall discussion in § 4.3.3.1. The results obtained indicate that the 25 PPI porous sample, with largest pore diameter, has the highest porosity value of 90.92%, while the 80 PPI porous sample, with smallest pore diameter, has the lowest porosity value of 74.76%.

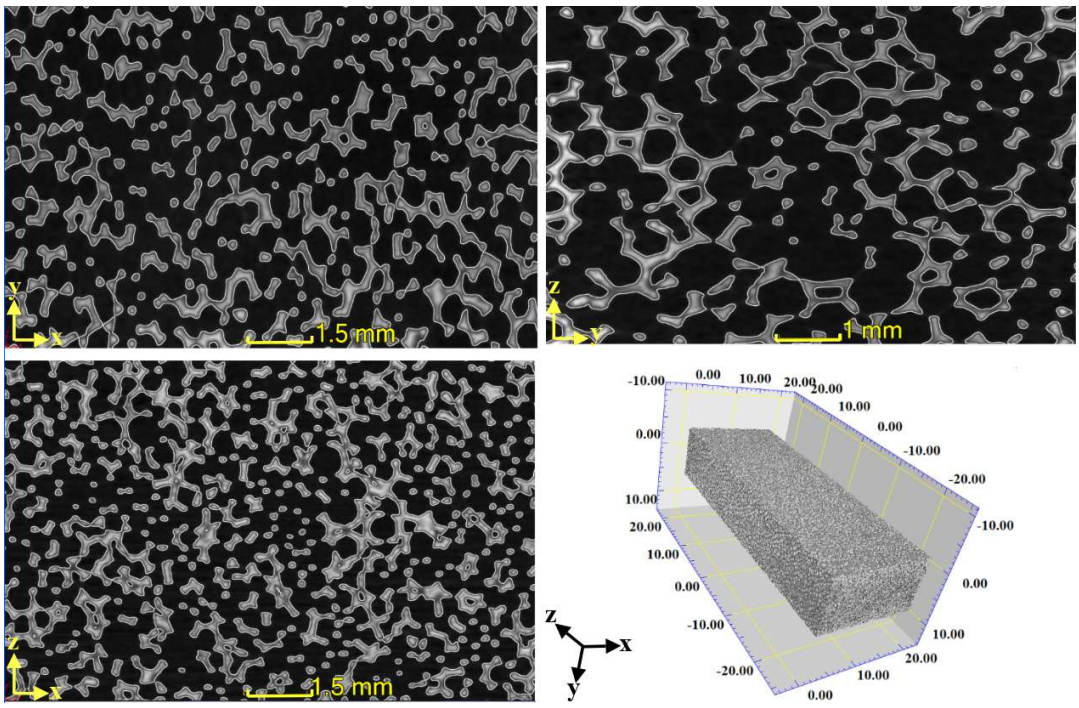

Figure 4.5: Porous 80 PPI selected volume for porosity analysis.

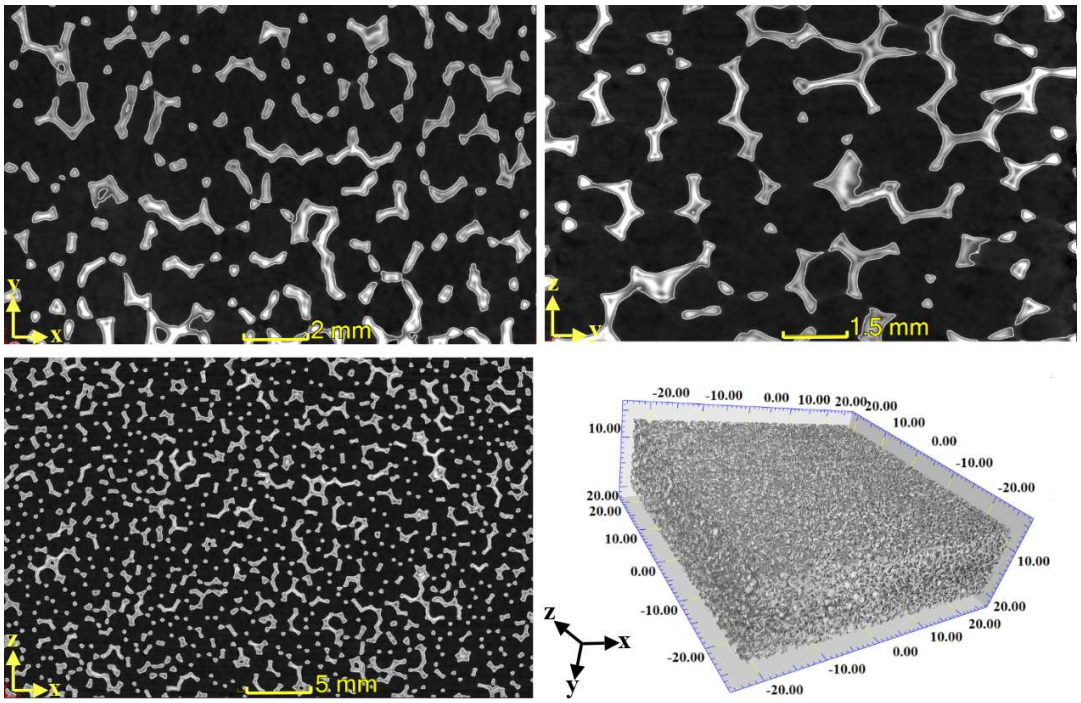

Figure 4.6: Porous 50 PPI selected volume for porosity analysis.

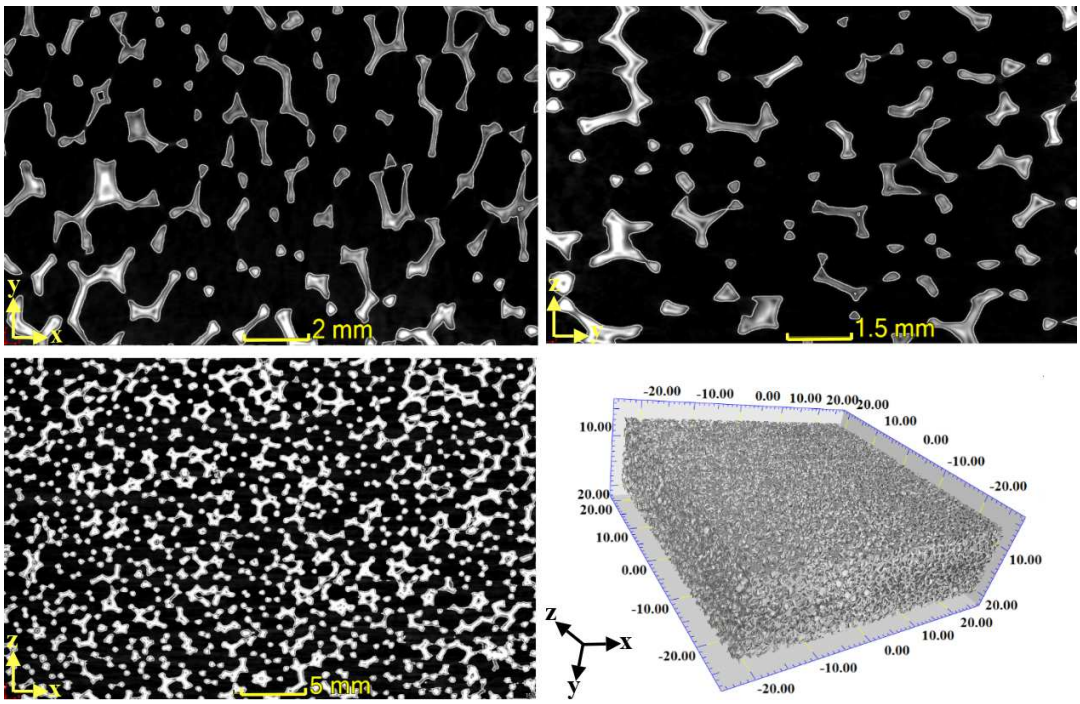

Figure 4.7: Porous 45 PPI selected volume for porosity analysis.

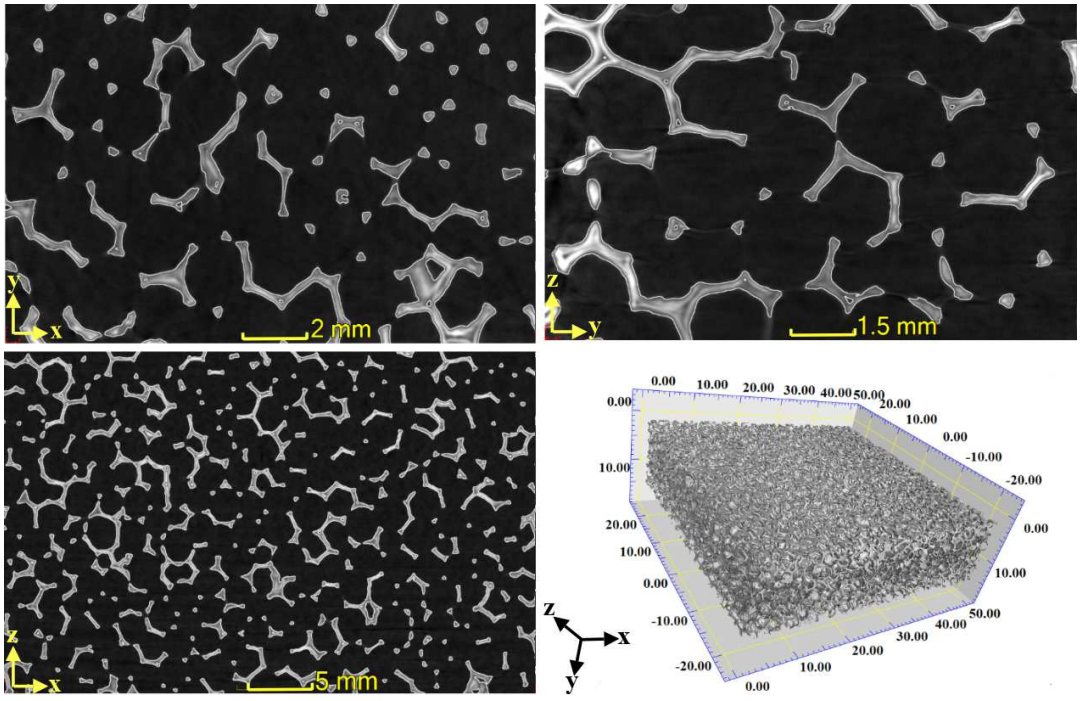

Figure 4.8: Porous 35 PPI selected volume for porosity analysis.

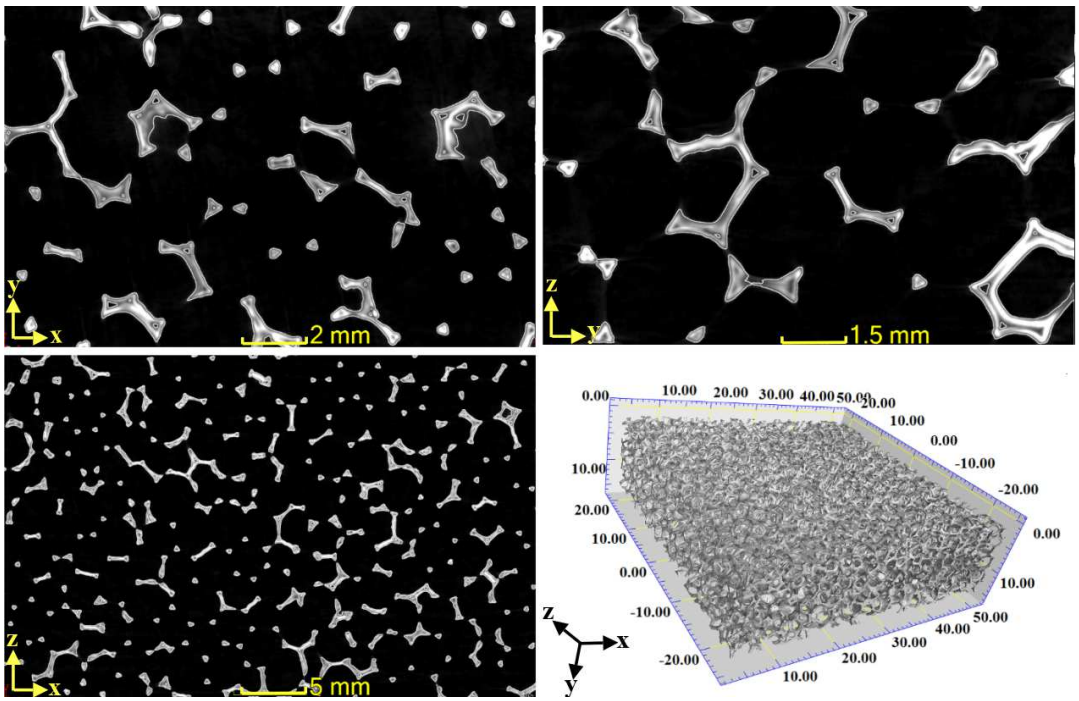

Figure 4.9: Porous 25 PPI selected volume for porosity analysis.

4.3 Air Flow Permeability

The permeability (κ) is a measure of the ease with which fluid can flow through the porous medium [187]. It simply measures how effortlessly liquid moves through a permeable porous material. It can also be inferred as the conductivity of a porous medium with respect to the fluid flow [189]. This intrinsic characteristic of porous media, however, is greatly dependent on the material porosity (size and shape of the pores). In what follows, the methods used to measure the permeability of the porous materials will be briefly discussed.

4.3.1 Permeability experimental setup

A permeability test-rig was designed and built to measure the permeability of each porous material used in this study. The permeability rig is comprised of a 2.5 m long tube, with a square section, equipped with static and dynamic pressure taps, with the porous sample being placed 1.2m from the inlet as shown in Fig. 4.10 (a). Experiments were performed on porous sample

inserts of 80 × 80 mm cross-sectional area and thickness of 10 mm and were retained firmly inside the tube. Static pressure taps were flush mounted on the inner surface of the apparatus, perpendicular to the airflow, either side of the porous sample, see Fig. 4.10 (b). In principle, the flow will accelerate as it penetrates into the porous medium due to the reduction in the effective cross-sectional area of the channel and thus, the fluid velocity will decrease as it leaves the porous medium due to the pressure drop experienced by the flow. The static pressure taps are placed at a distance of 50 mm on both sides of the porous samples to minimize errors due to the flow acceleration and deceleration near the porous section. Additional static pressure ports and pitot-tube were mounted inside the channel in order to measure the Darcy velocity (*i.e.* flow per unit cross sectional area of the porous medium) within the channel. The pressure measurements were obtained using the MicroDaq Smart Pressure Scanner-32C (see § 3.2.4) with an accuracy output of ± 0.05% full-scale.

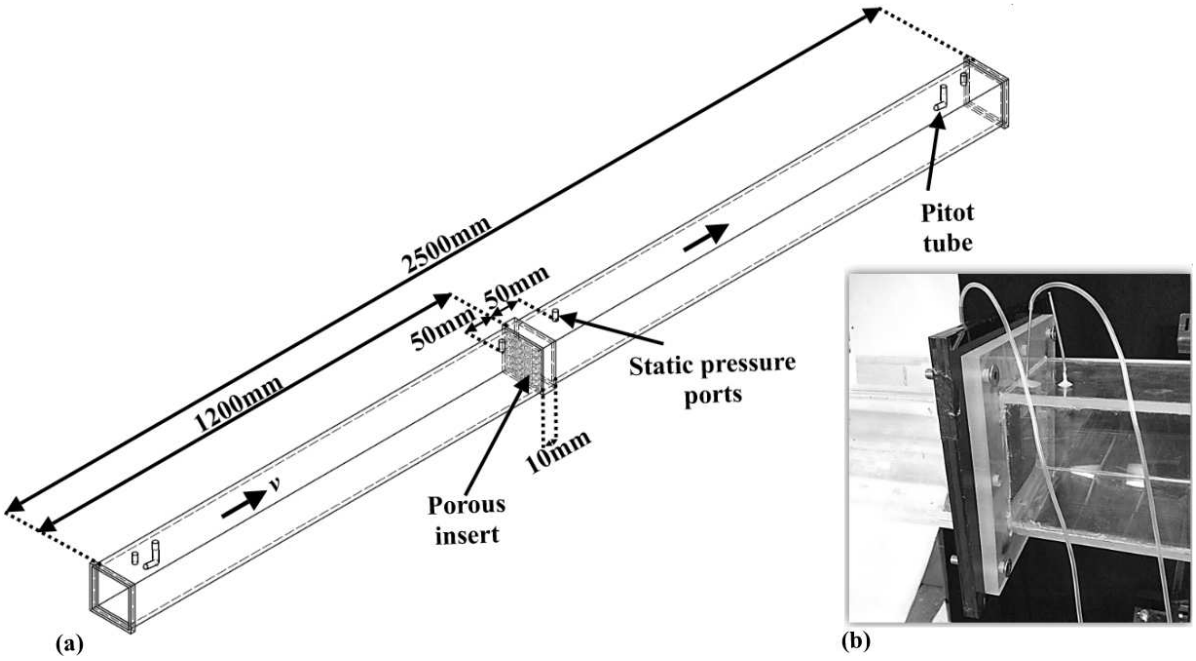

Figure 4.10: Experimental setup of the measurement of air flow permeability κ of porous material.

4.3.2 Theory of permeability

The foundation of the theory describing the flow through porous media was levied by Henry Darcy [115] through his well-established Darcy's law, based on the work on the water flow through beds of soils. Darcy's law clearly states that the pressure drop per unit length for the flow of a fluid through a porous medium is directly proportional to the fluid-flow velocity and inversely proportional to the permeability of the medium. Krüger [190] later added that the fluid flow through porous media is also proportional to the dynamic viscosity of the flow. The quantities used in the equations of permeability based on Darcy's law is shown in Fig. 4.11.

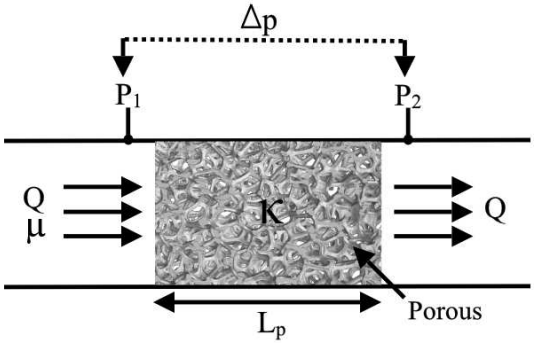

Figure 4.11: Definitions used in the equations of permeability (Eq. 4.3).

Darcy's first fundamental equation is expressed as,

$$Q = \frac{-\kappa A \Delta p}{\mu L}, \tag{4.3}$$

where Q is the volumetric flow rate, Δp is the pressure drop across the sample, L is the thickness of the sample, defined as the distance travelled by the fluid, κ is the material permeability, A is the cross-sectional area of the sample and μ is the fluid viscosity. However, Darcy's law is only valid for low volumetric flow rates or seepage flows, in which the permeability-based Reynolds number is relatively low. The permeability-based Reynolds number is defined as,

$$Re_\kappa = \rho \frac{\sqrt{\kappa}}{\mu} v, \tag{4.4}$$

It is noted that the velocity term v in Eq. 4.4 can be considered either as the Darcian velocity (v_D) of the fluid flow, which is defined as the volume flow rate divided by cross-sectional area of

sample (v_D=Q/A) or by using the pore velocity (v_p=v_D/ε), where ε is the volumetric void fraction of the porous medium in an isotropic medium.

The calculation of the permeability value in this thesis is based on the Darcian velocity method. It is acclaimed that the form drag becomes more important at high velocities and therefore it important to consider this effect for an accurate estimation of the pressure-drop across the porous medium [191]. Hence, an additional second-order velocity term is included to compensates the presence of form drag (C) due to the inertia at higher velocities, known as the Dupuit-Forchheimer equation [192],

$$\frac{\Delta p}{L} = \frac{\mu}{\kappa} v_D + \rho C v_D^2, \tag{4.5}$$

where ρ is the density of the fluid and C is the form drag (inertia) coefficient, which may differ with the porosity of the sample medium. The calculation of permeability, κ, and the form drag coefficient, C, can be calculated through experimentation using several methods. Equation 4.5 can be rewritten into a linear form and the coefficient value can be determined by using extrapolation method [193], however, it was found that this method is subject to greater uncertainty and is likely to be more inaccurate. Antohe *et al.* [194], on the other hand, proposed a more accurate model for determining the permeability and the inertia coefficient using the least mean squared quadratic function via curve fitting the pressure-drop as a function of the fluid-flow velocity. To realize this, Eq. 4.5 is modified by rearranging the equation as,

$$\frac{\Delta p}{L\, v_D} = A + B\, v_D, \tag{4.6}$$

where A= $\frac{\mu}{\kappa}$ and B=ρC. The permeability value can be calculated by plotting $\frac{\Delta p}{L\, v_D}$ versus v_D, which allows the constants A and B to be found through the least mean squared curve fitting method, as shown in Fig. 4.12.

4.3.3 Data analysis and permeability values

Figure 4.12 shows the normalized pressure drop data and the associated curve fitting, using the least square method, as a function of the Darcian velocity for all metal porous samples. The

flow-rate obtained in the channel varies with the sample porosity. The permeability and form drag coefficient values for all the porous cases are tabulated in Table 4.1. As seen, the permeability and form drag coefficient value of the porous materials varies with the pore size of the samples. The pore diameter is directly proportional to the permeability and indirectly proportional to the form drag coefficient. In other words, the porous material with smaller pore diameter, have relatively lower permeability value and higher form drag coefficient. The 25 PPI porous material, with the largest pore diameter, is found to have the highest flow permeability with a permeability of 8.19 $\times 10^{-8} m^2$ and a form drag coefficient of 71.82 m^{-1}. In contrast, the 80 PPI porous material, with smallest pore size, has a significantly lower flow permeability of 0.77 $\times 10^{-8} m^2$ and form drag coefficient of 305.96 m^{-1}. The decrease in flow permeability (higher flow resistance) can be also related to the effective surface area of the porous sample.

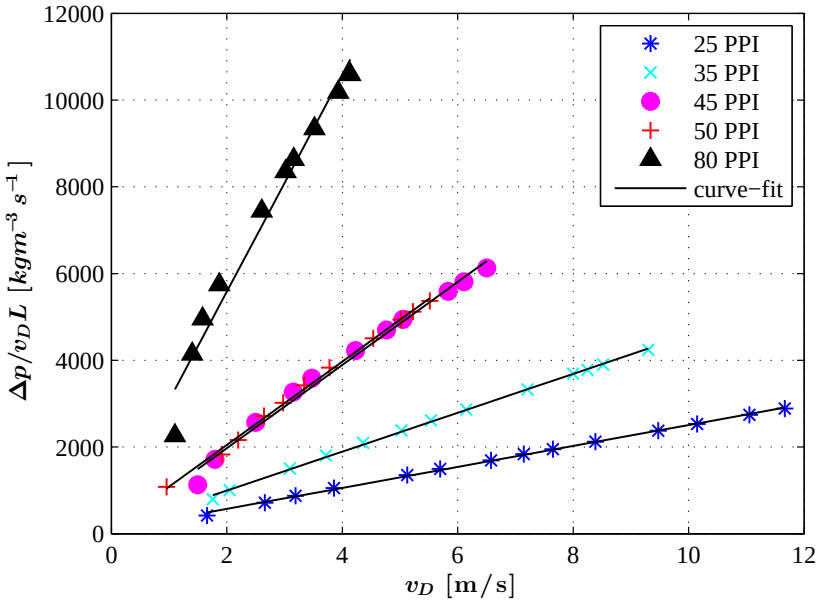

Figure 4.12: Pressure-drop versus fluid-flow velocity. The curve-fits are obtained using the least squared method.

4.3.3.1 Permeability uncertainty analysis

The Kline and McClintock error propagation method [178] (described in § 3.4.1) was implemented to the least mean squared quadratic function in order to obtain the uncertainty values associated

with the technique for finding the constant coefficients A and B in Eq. 4.6 for the calculation of the permeability. The coefficients A and B are obtained as [195],

$$A = \frac{\left(\sum_{i=1}^{N} x_i y_i\right)\left(\sum_{i=1}^{N} x_i^4\right) - \left(\sum_{i=1}^{N} x_i^2 y_i\right)\left(\sum_{i=1}^{N} x_i^3\right)}{\left(\sum_{i=1}^{N} x_i^2\right)\left(\sum_{i=1}^{N} x_i^4\right) - \left(\sum_{i=1}^{N} x_i^3\right)\left(\sum_{i=1}^{N} x_i^3\right)}, \tag{4.7}$$

$$B = \frac{\left(\sum_{i=1}^{N} x_i^2 y_i\right)\left(\sum_{i=1}^{N} x_i^2\right) - \left(\sum_{i=1}^{N} x_i y_i\right)\left(\sum_{i=1}^{N} x_i^3\right)}{\left(\sum_{i=1}^{N} x_i^2\right)\left(\sum_{i=1}^{N} x_i^4\right) - \left(\sum_{i=1}^{N} x_i^3\right)\left(\sum_{i=1}^{N} x_i^3\right)}, \tag{4.8}$$

where the x_i's indicate the fluid flow velocities and the y_i's represent the pressure-drop per unit length values. The uncertainty of the A and B coefficients of Eq. 4.6 is calculated using the equations [195],

$$\Delta A = \sqrt{\sum_{i=1}^{N} \left(\frac{\partial A}{\partial x_i}\Delta x_i\right)^2 + \sum_{i=1}^{n} \left(\frac{\partial A}{\partial y_i}\Delta y_i\right)^2}, \tag{4.9}$$

$$\Delta B = \sqrt{\sum_{i=1}^{N} \left(\frac{\partial B}{\partial x_i}\Delta x_i\right)^2 + \sum_{i=1}^{n} \left(\frac{\partial B}{\partial y_i}\Delta y_i\right)^2}. \tag{4.10}$$

By assuming that the dynamic viscosity and the density term exhibit zero uncertainty, the uncertainty of both the permeability and the form drag coefficients were calculated using the equations, $A = \frac{\mu}{\kappa}$ and $B = \rho C$, respectively. The uncertainty of the permeability and the form drag coefficient can be calculated using,

$$u_\kappa = \frac{\Delta A}{A} \times 100\%, \tag{4.11}$$

$$u_C = \frac{\Delta B}{B} \times 100\%. \tag{4.12}$$

The uncertainties values of the permeability and the form drag coefficients are tabulated in Table 4.1.

Table 4.1: Porosity and permeability values of the porous specimens

Foam	**Porosity**			**Permeability**		
	Void volume $[mm^3]$	**Porosity,** φ **[%]**	**C** $[m^{-1}]$	u_κ	**Permeability,** κ**,** $[\times 10^{-8} m^2]$	u_C
25 PPI	26780.39	90.92	71.8231	4.7820	8.1934	6.8795
35 PPI	26458.27	88.39	78.0563	3.6658	4.4166	10.0740
45 PPI	26151.07	85.37	80.9351	3.1008	2.0557	13.3481
50 PPI	25613.51	83.64	92.5938	3.3415	2.0468	13.9392
80 PPI	5991.32	74.76	305.9594	3.2163	0.7688	15.1111

4.4 Surface roughness profile

The morphology of porous surfaces, particularly the surface roughness, is also found to be a crucial factor in characterizing the porous materials and its effect in the flow field. There are a few methods that are normally used for estimating the microstructure features of rough surfaces, namely the scanning tunnelling, X-ray scattering, electron microscopy, optical methods, etc. Porous materials have a more intrinsic complex structure with the combination of depth profile with voids and the metal surface, and therefore a well-defined method is needed to construe the surface roughness parameter. For instance, the porous material used in the present study is of a rigid structure with regular round pores and hence, the Rayleigh model with round capillaries can be utilized to describe the structure of the porous surface [196]. The Rayleigh model indicates that the pore size of the porous surface is strongly affected by the roughness density, while the skeletal or the solid material between the pores can be assumed as identical or proportionate to the roughness particles. Therefore, the surface with larger pores will have a larger gap length between the solid wall and thus, a higher roughness density. It is evident from § 4.2.3 and § 4.3.3, that the porous material with higher flow permeability, κ, and porosity, φ are characterized by the larger pores. This means that the porous samples with larger permeability and porosity (larger pores) values are associated with the higher surface roughness. The surface roughness as a function of the flow permeability and porosity are further detailed in § 4.4.3. A simple approach has been taken to analyze the surface roughness of the porous samples for the present study.

4.4.1 Surface roughness experimental setup

In the present work, the morphology of the porous surface was studied using the high-resolution non-contact profilometer Scantron Proscan 2100, which can provide detailed three-dimensional surface information for numerous applications. The laser profilometer's scanning operation was conducted with the porous sample with 3 mm in the x-direction and 3 mm in the y-direction (porous scanning area), with the thickness of ≈ 1 mm in order to acquire higher magnification results. The S65/9 sensor model was selected with the measuring resolution of 9.5 μm, suitable for the porous morphology scanning. The step size was set at 50 μm and within 1 μm tolerance. The measurements were repeated for three times, and have been proven to be reproducible. All the data obtained were then visualized and analyzed using the Proform software module and the data collected is then reproduced using the Matlab software.

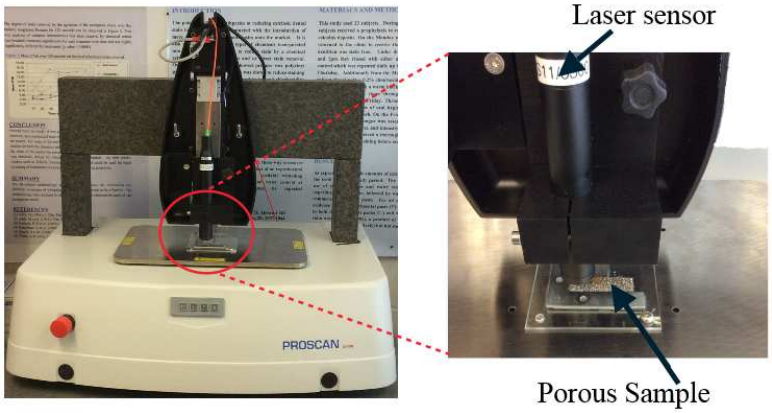

Figure 4.13: Scantron Proscan 2100 analysis tool.

4.4.2 Data analysis and surface roughness values

The roughness of each porous surface was characterized by calculating the statistical parameters known as the average roughness parameter or the arithmetical mean height (R_a), the maximum profile peak height (R_p) and the maximum profile valley depth (R_v). The average roughness parameter (R_a), is universally recognized and is one of the most used parameters for describing the surface roughness [197]. As described in ISO 4287-1996 [198], R_a is the arithmetical mean of the absolute values of the profile deviations (y_i) from the mean line of the surface profile (see

Fig. 4.14) or simply put R_a reveals the average of a set of measurements of the surface peak (height). As shown in Fig. 4.14, R_p denotes the list of profile peaks over the surface of the porous sample section. The peaks are taken at the region where the surface profile surpasses the average line. As shown in Fig. 4.14, R_v or the maximum profile valley depth indicates the lowest points of curve over the sampling length of the porous section, where the valleys are taken at the regions below the average line. The illustration of the roughness profiles for all these parameters is depicted in Fig. 4.14. The R_a, R_p and R_v values can be calculated from,

$$R_a = \frac{1}{L_s} \sum_{i=1}^{L_s} |y_i|, \tag{4.13}$$

$$R_p = \max_i y_i, \tag{4.14}$$

$$R_v = \min_i y_i, \tag{4.15}$$

where L_s is the number of data points within the profile evaluation length or the sampling length and y_i is the profile height function or the variation of the vertical distance from the mean surface line to the i^{th} data point.

Figures 4.15 to 4.19 show the illustration of the porous sample size used in the surface roughness measurement and the $2D$ and $3D$ graphical representation of the surface roughness profiles for porous 80, 50, 45, 35 and 25 PPI. Table 4.2 presents the results of the surface roughness measurements for all three parameters, R_a, R_p and R_v. The results obtained indicate that porous 25 PPI has the highest mean surface roughness, R_a, and that the surface becomes smoother as the porosity of the material decreases. The lowest R_a is observed for the case of 80 PPI material. A similar trend is also noticed for R_p and R_v. Based on the results in Figs 4.15 to 4.19 and Table 4.2, it is clear that the surface feature of porous materials is strongly related to the porosity and permeability conditions of the material.

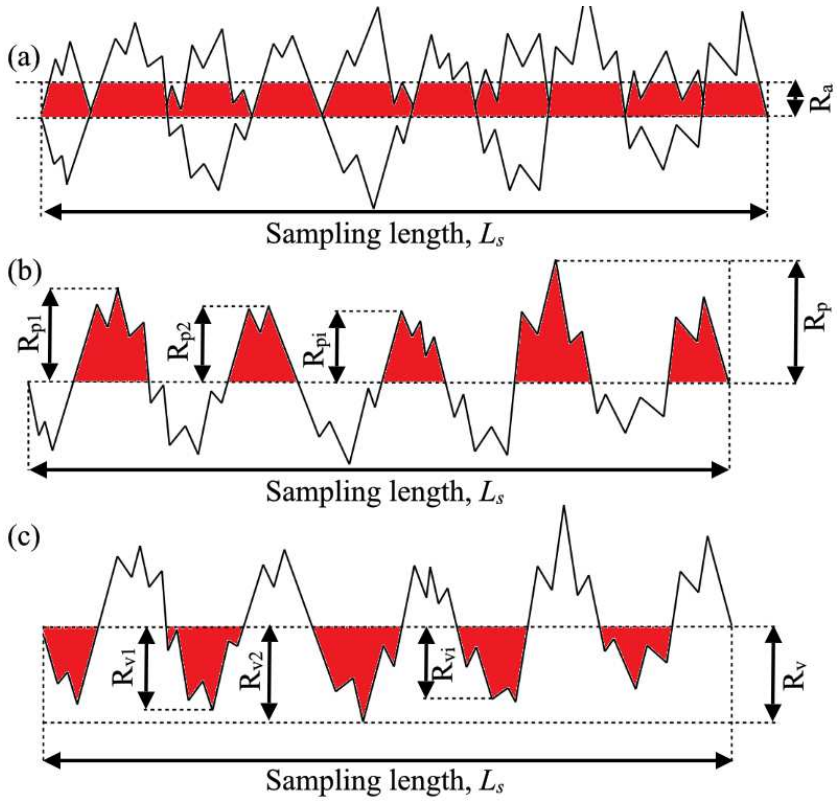

Figure 4.14: An illustration of roughness profile (a) Arithmetical mean height, (b) Maximum profile peak height and (c) Maximum profile valley depth.

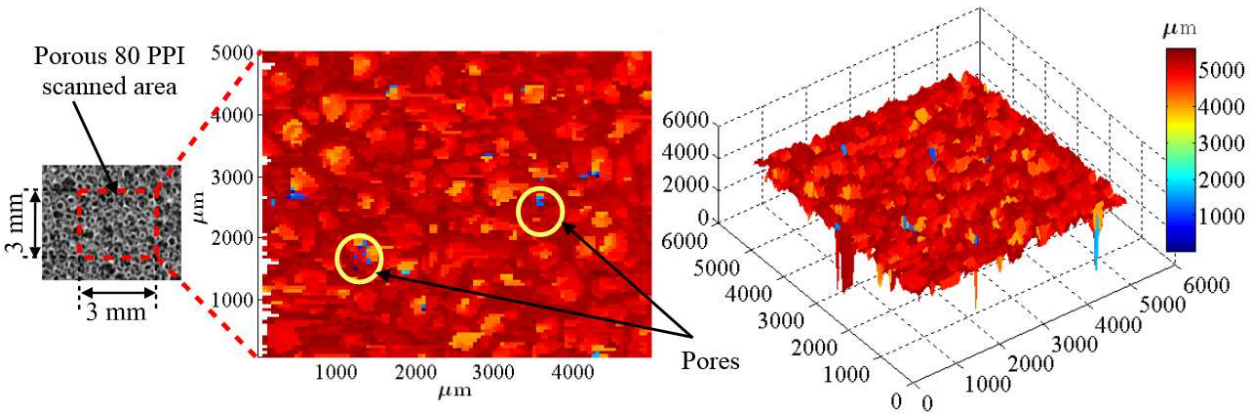

Figure 4.15: Illustration of porous sample size measurement and the 2D and 3D graphical representation of surface roughness profiles for porous 80 PPI.

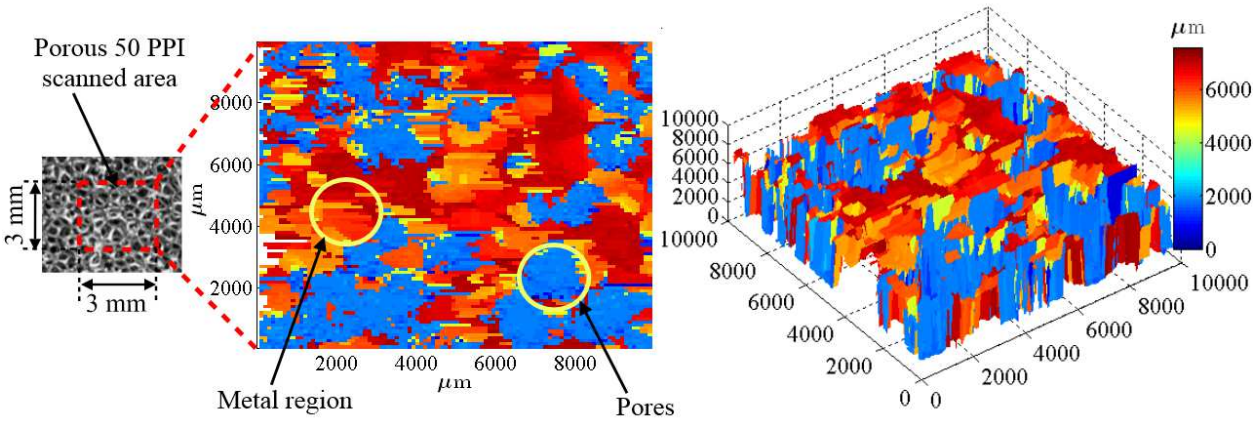

Figure 4.16: Illustration of porous sample size measurement and the 2*D* and 3*D* graphical representation of surface roughness profiles for porous 50 PPI.

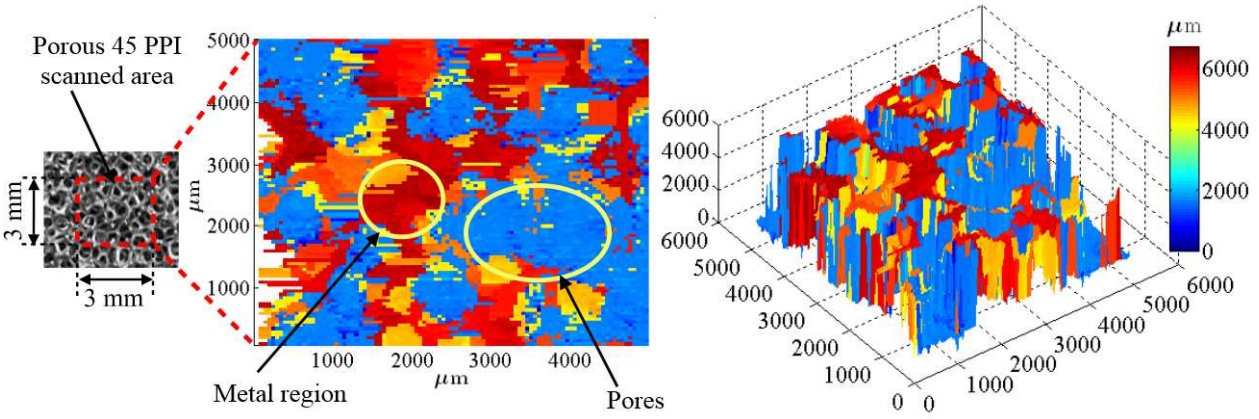

Figure 4.17: Illustration of porous sample size measurement and the 2*D* and 3*D* graphical representation of surface roughness profiles for porous 45 PPI.

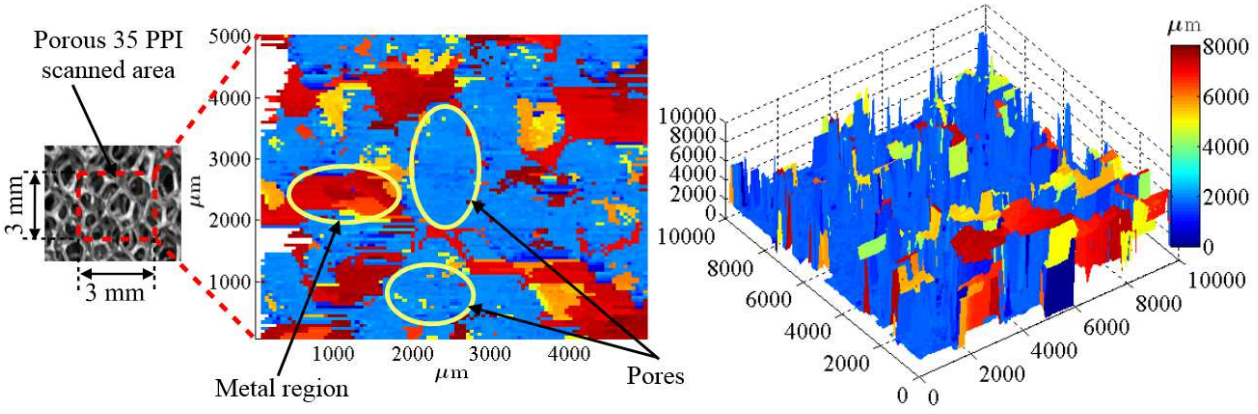

Figure 4.18: Illustration of porous sample size measurement and the 2*D* and 3*D* graphical representation of surface roughness profiles for porous 35 PPI.

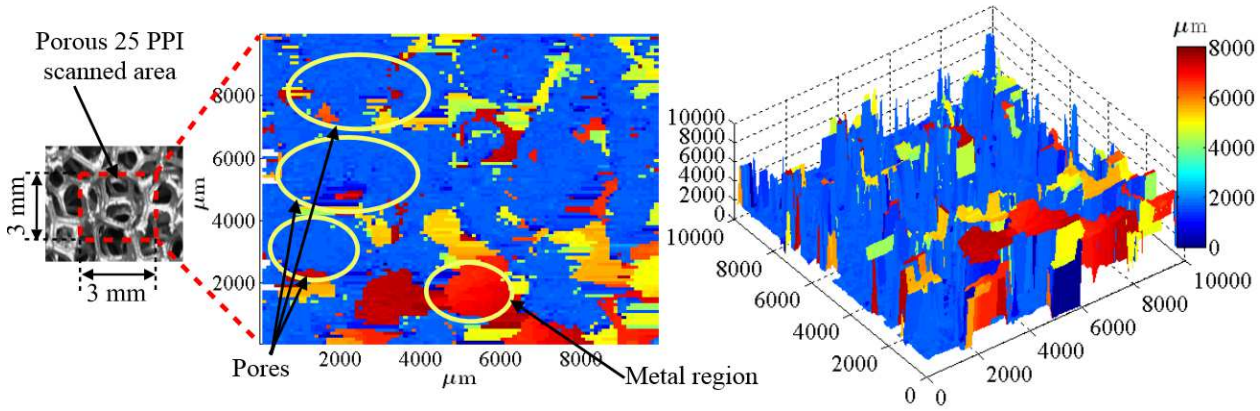

Figure 4.19: Illustration of porous sample size measurement and the 2D and 3D graphical representation of surface roughness profiles for porous 25 PPI.

Table 4.2: Surface roughness values of the porous specimens

Foam	**Surface Roughness**		
	Mean roughness ISO Ra [μm]	**Mean maximum peak height ISO Rp [μm]**	**Mean maximum valley depth ISO Rv [μm]**
25 PPI	1922.279	4720.703	3062.438
35 PPI	1791.044	3943.338	2388.606
45 PPI	1760.869	2966.502	2199.826
50 PPI	1310.443	2915.796	1849.163
80 PPI	211.752	392.826	890.777

4.4.3 Porosity dependency of the permeability and surface roughness

Figure 4.20 summarizes the porosity, permeability and roughness results obtained in this chapter for all the five different porous samples. In general, the results obtained for the permeability and the surface roughness is nearly directly proportional to the porosity of the material. Although it is quite common to consider that the permeability value of a porous sample to depend on its porosity, the factors determining the permeability and porosity are still dependent on the other parameters, such as the pore size distribution, pore shape, etc. of the porous medium. For example, two different porous materials can have the same porosities but different permeabilities and vice versa. Essentially, this is evident in the present study where two different porous materials (45 PPI and 50 PPI) have different porosity values but with almost the same permeability values. A similar observation is also made for the surface roughness of the porous samples, where the 35 PPI and 45 PPI materials exhibit almost the same roughness values. In Fig. 4.20, the curve becomes almost steeper at higher porosities (φ). Hence, increasing the porosity by a mere of 16%

as represented by the 25 PPI and 80 PPI material, caused the permeability to increase of about 91%. It is also clear that the roughness of the porous surfaces is strongly related to the porosity and permeability condition of the samples.

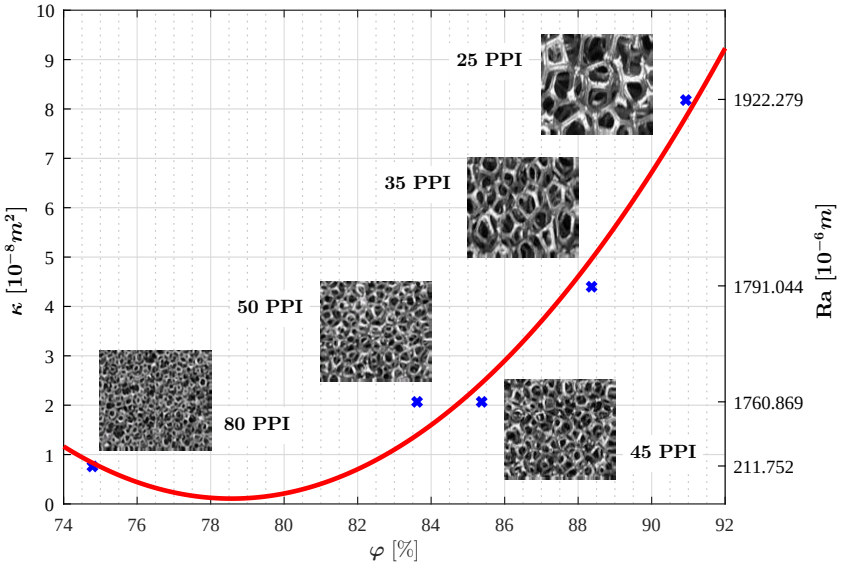

Figure 4.20: Permeability and surface roughness as a function of porosity.

4.5 Summary

The accurate estimation of permeability, porosity and surface roughness values are of pivotal importance for the characterization of porous material. This is particularly important for aerodynamic and aeroacoustic applications as these parameters are known to greatly affect the flow field. This chapter describes the techniques used to measure the porosity, permeability and the surface roughness profile of the porous samples used in the present study. The porosity, permeability and the surface roughness values for all the porous materials are found to be dependent on each other. The 25 PPI material was shown to have the largest porosity and permeability values, but also with the highest surface roughness. In contrast, the 80 PPI material exhibits the smallest porosity and permeability values has a smoother surface compared to the materials with lower PPI value. This work provides insight into the physics responsible for the flow-field and acoustic noise modification and the use of porous materials as a passive control method. The use of porous materials for controlling the flow field will be further investigated and discussed in Chapters 5 and 6.

CHAPTER 5

BOUNDARY LAYER FLOW INTERACTION WITH A PERMEABLE WALL

In this chapter, the interaction of a zero-pressure gradient turbulent boundary layer flow with a rough permeable surface has been investigated experimentally for different porous configurations. The flow interaction characteristics have been examined using a flat plate equipped with several surface pressure transducers and surface pressure taps, using different types of porous inserts, with different porosities and permeability constants. To reveal the effects of the flow interaction with porous surfaces, measurements were performed for the boundary layer growth, energy content within the boundary layer, surface pressure fluctuations, coherence and correlation of the flow structures, before, over and after the porous test section. The chapter is organized as follows. The experimental setup, including the measurement apparatuses and the model configuration, is described in § 5.1. The effect of the porous surface on the boundary layer velocity profile and their energy content is discussed in § 5.2. The analysis of the wall pressure power spectra, coherence and correlation studies are outlined in § 5.3, § 5.4 and § 5.5. In this section, the hypothesis regarding the formation of an internal recirculation hydrodynamic field inside the porous medium is formulated and demonstrated detailed flow and pressure measurements. Section § 5.6 further elaborates on the existence of the internal hydrodynamic field and provides results on the dependency of the internal hydrodynamic field on the porous-flow interaction length. Finally, the findings concerning the boundary layer flow interaction with a

porous surface are summarized in § 5.7.

5.1 Measurement setup

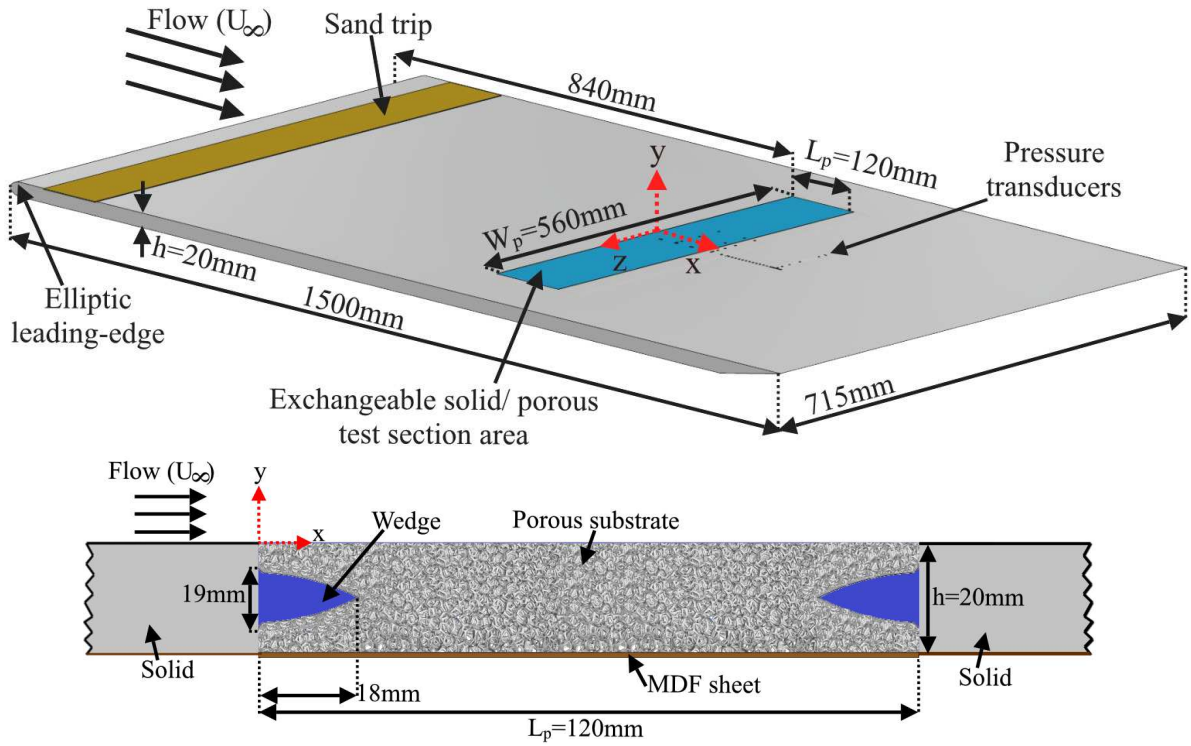

Figure 5.1: Flat plate experimental setup and illustration of the porous substrate installation.

The flow measurements have been performed using a flat plate with a streamwise length of L=1500 mm, spanwise length of W=715 mm and thickness of h=20 mm. The general layout of the flat plate test-rig is shown in Fig. 5.1(a). In order to prevent flow separation and strong adverse pressure gradient, the flat plate was designed with an elliptical leading-edge with a semi-minor and semi-major axis of 10 mm and 27 mm, respectively. To realize a zero-pressure gradient turbulent boundary layer on the top side of the plate, particularly near to the trailing-edge, a 12° beveled trailing-edge was employed [199]. The coordinate system (x, y, z) is placed at the beginning of the porous section, as illustrated in Fig. 5.1(a). In addition, to ensure the zero-pressure gradient condition on the plate, static pressure measurements along the flat plate, after the test section region were conducted using 12 static pressure ports within x= 160 mm to 240 mm at the free-stream velocity of 20 m/s. The static pressure measurements were performed

using a 32 channel Chell MicroDaq Smart Pressure Scanner. The scanner is able to measure the pressure difference of up to 1 Psi, with the system accuracy of ± 0.05% full-scale. The static pressure data for the flat plate test rig was acquired for 60 seconds at the maximum sampling frequency of 500 Hz. The accuracy of the pressure measurements carried out for the flat plate was below 5 Pa. Figure 5.2 shows that the pressure coefficient C_p distributions along the flat plate is constant within the uncertainty levels of 2σ=± 0.97 % at 95 % confidence level, indicating the absence of pressure gradient along the plate. A 100 mm wide section of 80 grit sand trip, equivalent to the average roughness of Ra=1.8 μm was applied at 120 mm after the leading-edge, on the top side of the plate, to ensure a well-developed turbulent flow transition before the porous section (x=0). The porous section is placed in a cavity space, 840 mm downstream of the plate leading-edge with a streamwise length L_p of 120 mm, width W_p of 560 mm and depth h of 20 mm. Figure 5.1(b) provides a schematic of the porous insert installation. A 18 mm wide solid wedge is placed on the either sides of the porous insert to avoid any possible flow separation at the porous-solid interface (x = 0 and x = 120mm). In order to avoid air bleeding through the porous inserts, the bottom part of the porous samples were covered and sealed using a solid MDF sheet, see Fig. 5.1.

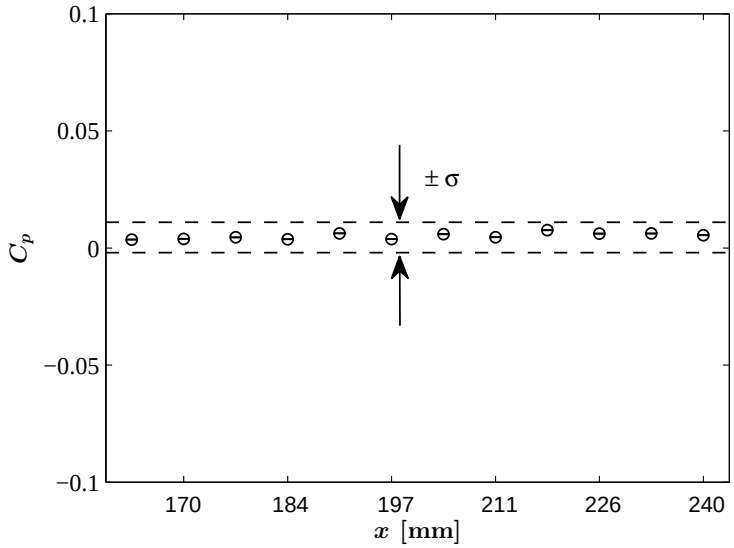

Figure 5.2: Pressure distribution (C_p) in the streamwise direction within x= 160 mm to 240 mm for the flat plate with fully solid surface at the free-stream velocity of 20 m/s.

Four metal foams with the PPI value (pores per inch) of 25, 35, 45 and 80 were used for this study. The flow measurement results will only be presented for the porous materials with 25, 45 and 80 PPI, as the 35 PPI material was found to give very similar results to that of the 25 PPI material. The porosity values for the 25 PPI, 45 PPI and 80 PPI porous samples are 90.92 %, 85.37 % and 74.76 %, respectively whereas the permeability values for porous 25 PPI, 45 PPI and 80 PPI are found to be 8.2× 10^{-8} m^2, 2.1× 10^{-8} m^2 and 7.7× 10^{-9} m^2, respectively (see Fig. 4.20. The average roughness (Ra) values for porous 25 PPI, 45 PPI and 80 PPI are found to be 1922 μm, 1761 μm and 212 μm, respectively. The plate was instrumented with 41 miniature pressure transducers (Knowles FG-23329-P07) for the measurement of the unsteady boundary layer surface pressure fluctuations. The transducers were installed inside the plate parallel to the surface and were distributed over and downstream of the porous section. The transducers are arranged in the form of L-shaped arrays in the streamwise and spanwise directions, see Fig. 3.4 (a). A total number of four spanwise locations, each with five transducers, are used to calculate the spanwise coherence and length-scale of the boundary layer coherent structures over and at the downstream locations of the porous surfaces. The transducers located in the streamwise direction will be used to study the changes of the boundary layer structures as they travel downstream over the porous section and their associated convection velocity.

The surface pressure fluctuations data have been acquired using a National Instrument PXIe-4499, with a sampling frequency of 2^{16} Hz and measurement time of 60 seconds. The pressure transducers locations in the streamwise and spanwise directions on the flat plate over and after the porous test section are detailed in Tables 5.1 and 5.2, respectively. In order to measure the statistical turbulence properties of turbulent flow, the boundary layer measurements were carried out using a single hot-wire Dantec 55P16 probe with a platinum-plated tungsten wire of 5 μm diameter and 1.25 mm length, giving a length-to-diameter (l/d) ratio of 250. These correspond to the viscous length scale (ν/u_τ) of 16.25 μm, viscous-scaled wire length l^+ of 64.1 and viscous-scaled wire diameter d^+ of 0.25. In the present study, the signals were recorded at a sampling frequency of 2^{16} for 16 seconds at each location, which equates to a viscous-scale sample interval of Δt^+=0.62. This sample interval exceeds the minimum time-scale ($t^+ \gtrsim 3$) for the turbulent energy content [166].

Table 5.1: Positions of the pinhole transducers in the streamwise direction over and after the porous test-section

Section	**Transducer number,** p	**Axial locations,** x (mm)
Porous/ Solid (x**=0**mm **to 120**mm)	1, 2, 3, 8, 9, 10, 11	30, 33, 60, 63, 90, 93, 110
Solid (x**>120**mm)	16, 21, 22, 23, 24, 25, 26, 27, 28, 29, 30, 31, 32, 33, 34, 35, 40, 41	130, 150, 165, 171, 178, 185, 191, 198, 205, 212, 217, 225, 232, 234, 249, 255, 262, 266

Table 5.2: Positions of the pinhole transducers in the spanwise direction over and after the porous test-section

Section	**Transducer number,** p	**Axial locations,** x (mm)	**Transverse locations,** z (mm)
Porous/ Solid	3, 4, 5, 6, 7	60	0, 3.2, 11.4, 24.2, 42.6
(x**=0**mm **to 120**mm)	11, 12, 13, 14, 15	110	
Solid	16, 17, 18, 19, 20	130	
(x**>120**mm)	35, 36, 37, 38, 39	255	

5.2 Boundary layer flow structures

While in many applications, such as low drag surfaces, flow laminarization, etc, it is common to present the boundary layer results in wall units format, *i.e.* normalized by quantities such as y^+, u^+, u_τ, etc, in applications relevant to aerodynamic noise generation, we are often interested in the overall size of the boundary layer. The boundary layer and hydrodynamic results in most studies in the areas of aerodynamic noise generation and control are, therefore, presented in terms of the overall boundary layer thickness quantities, such as the boundary layer, displacement or momentum thickness, particularly when the low frequency aspect of the noise generation is of concern. However, in order to ensure that the flat plate test rig developed as part of this study provides a standard zero pressure gradient boundary layer, the series of thorough measurements had been carried out prior to the actual tests using only the solid surfaces. The validation test matrix included $y^+ - u^+$ and the surface pressure fluctuation ϕ_{pp}. The $y^+ - u^+$ results had been compared and validated against the prior experimental [200, 201] and DNS [202] data and

good agreement was found. In the present study, the non-dimensional mean velocity profile at momentum-based Reynolds number Re_θ of 3971 has been compared against Ghanadi *et al.* (2003), Silvestri *et al.* (2018) and Schlatter and Orlu (2010) at Re_θ=3920, 3771 and 4064, respectively, as shown in Fig. 5.3. In comparison of the results obtained by Silvestri *et al.*, a maximum error of 6.28 % occurs at the buffer region ($5 < y^+ < 30$), which this variation can be considered negligible as our focus in this paper is the logarithmic and outer layer region of the boundary layer. In the logarithmic region of the boundary layer ($30 < y^+ < 200$), the maximum error was found to be about 9.10% between the present data and the data published by Ghanadi *et al.*, which the Reynolds number is much closer to the boundary layer measured. The surface pressure fluctuation results were also checked against the Goody model for a zero pressure gradient flat plate case [203] and good agreement was obtained (see § 5.3).

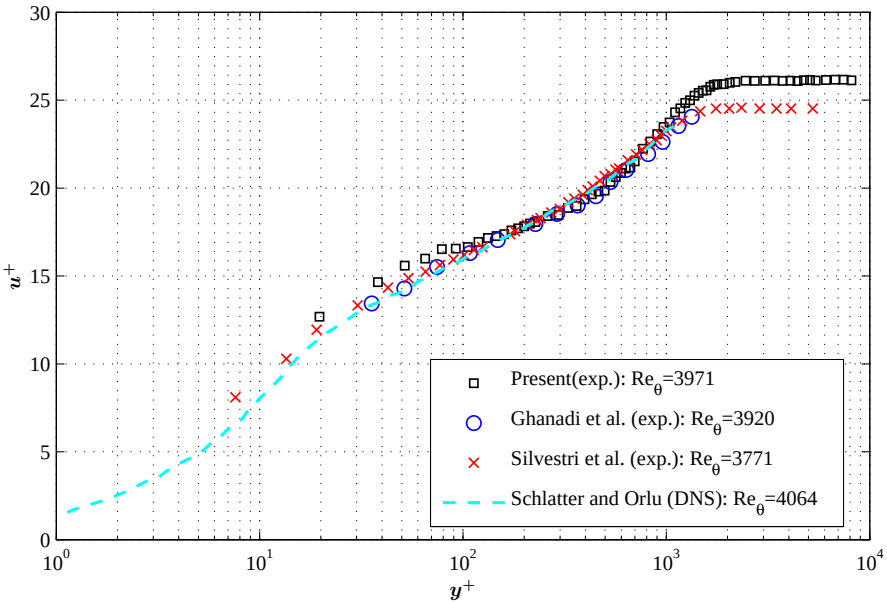

Figure 5.3: Non-dimensionalized mean velocity profile error analysis of the boundary layer for: present experimental work at Re_θ=3971 [square (black)], Ghanadi *et al.* (2015) at Re_θ=3920 [circle (blue)], Silvestri *et al.* (2018) at Re_θ=3771 [x (red)], Schlatter and Orlu (2010) at Re_θ=4064 [– (cyan)].

To better understand the boundary layer flow structures and the effect of the porous surface on the boundary layer development, the boundary layer velocity and the energy content of the boundary layer flow structures are studied in this section. The mean and root-mean-square (rms)

velocities can be obtained from the velocity time history as,

$$U = \frac{1}{N}\sum_{i=1}^{N} U_i, \tag{5.1}$$

and

$$U_{rms} = \sqrt{\frac{1}{N}\sum_{i=1}^{N}(U_i - U)^2}, \tag{5.2}$$

where N is the total number of velocity samples in time, U_i refers to the time history of the velocity collected and U is denoted as the mean velocity.

The governing boundary layer parameters, namely the boundary layer thickness δ, displacement thickness δ^* and the momentum thickness θ were measured using Eq. 5.3 and 5.4. The boundary layer thickness δ corresponds to the normal to wall location where the velocity reaches 99 % of the free-stream velocity U_∞. The displacement and momentum thickness can then be found from,

$$\delta^* = \int_{y=0}^{\delta}\left(1 - \frac{U(y)}{U_\infty}\right)\mathrm{d}y, \tag{5.3}$$

and

$$\theta = \int_{y=0}^{\delta}\frac{U(y)}{U_\infty}\left(1 - \frac{U(y)}{U_\infty}\right)\mathrm{d}y. \tag{5.4}$$

The boundary layer shape factor is defined as the ratio of the boundary layer displacement thickness to the momentum thickness ($H = \delta^*/\theta$). The shape factor for turbulent flows, varies typically from 1.3 - 1.4 [204].

The location of the boundary layer measurement (BL_2-BL_7) relative to the porous section position is shown systematically in Fig. 5.4. The boundary layer integral parameters including the boundary layer thickness (δ), displacement thickness (δ^*), momentum thickness (θ) and shape factor ($H = \delta^*/\theta$) measured for the flat plate with and without the porous inserts at U_∞ of 20 m/s are tabulated in Table 5.3.

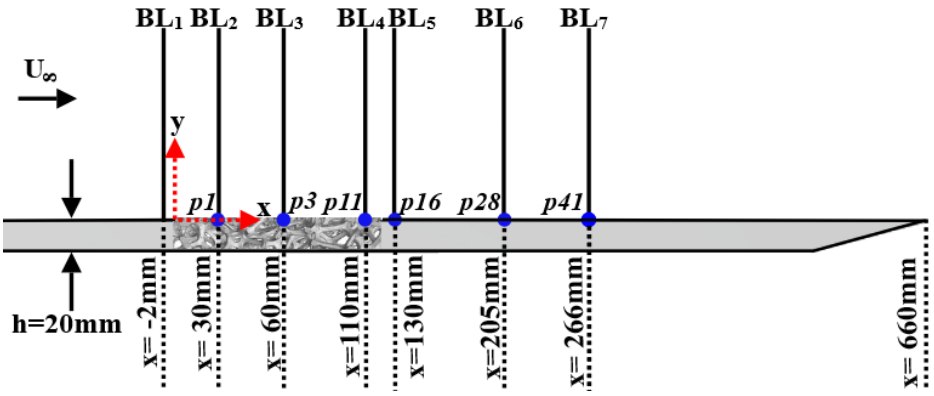

Figure 5.4: The schematic of the flat plate and the position of the hot-wire for boundary layer (BL_i) measurements.

Table 5.3: Boundary layer integral parameters for flat plate with and without porous treatment at Re_L of 1.99×10^6

Location	**Test section**	δ (mm)	δ^* (mm)	θ (mm)	H	U_τ (m/s)	C_f $\times 10^{-3}$
BL_1	Solid	25.4	3.8	2.9	1.3	0.8	1.56
	80 PPI						
	45 PPI						
	25 PPI						
BL_2	Solid	26.1	3.8	3.0	1.3	0.9	1.56
	80 PPI	31.9	5.2	3.7	1.4	0.8	1.61
	45 PPI	29.7	5.4	3.8	1.4	0.8	1.63
	25 PPI	28.0	4.7	3.6	1.3	0.9	1.59
BL_3	Solid	26.9	3.8	3.0	1.3	0.9	1.56
	80 PPI	32.5	5.3	3.9	1.4	0.8	1.61
	45 PPI	35.8	5.5	3.9	1.4	0.8	1.61
	25 PPI	30.7	5.0	3.7	1.4	0.9	1.59
BL_4	Solid	30.0	4.0	3.2	1.3	0.9	1.56
	80 PPI	30.8	5.1	3.6	1.4	0.8	1.62
	45 PPI	32.5	6.0	4.3	1.4	0.8	1.62
	25 PPI	28.3	5.0	3.5	1.4	0.9	1.59
BL_5	Solid	31.1	4.0	3.2	1.3	0.9	1.56
	80 PPI	31.7	5.7	4.0	1.4	0.8	1.62
	45 PPI	33.2	5.3	3.7	1.4	0.8	1.62
	25 PPI	29.1	5.4	3.7	1.4	0.9	1.59
BL_6	Solid	33.2	4.2	3.3	1.3	0.9	1.55
	80 PPI	35.3	5.9	4.2	1.4	0.8	1.62
	45 PPI	36.6	6.6	4.7	1.4	0.8	1.61
	25 PPI	33.1	6.1	4.1	1.5	0.9	1.58
BL_7	Solid	33.9	4.0	3.2	1.3	0.9	1.55
	80 PPI	37.3	6.1	4.4	1.4	0.8	1.61
	45 PPI	36.9	6.1	4.3	1.4	0.8	1.62
	25 PPI	36.1	6.2	4.4	1.4	0.9	1.58

The results are only presented for some selected boundary layer locations for the sake of brevity. Results show that in the case of less permeable surfaces (80 PPI and 45 PPI), the boundary layer thickness, displacement thickness and momentum thickness increase compared to the baseline case (solid surface) at each measurement locations. In the case of the highly permeable surface (25 PPI surface), results show that the boundary layer displacement thickness and momentum thickness increase compared to the solid case, however, shows a reduction compared to the 80 PPI and 45 PPI surfaces. The boundary layer thickness for the 25 PPI surface is found to be the lowest compared to the other cases, which is believed to be due to the material being very permeable and that the boundary layer more able to penetrate and sink into the porous media, which causes a reduction in the boundary layer thickness.

Figure 5.5 presents the normalized time-averaged mean and root-mean-square (rms) boundary layer velocity profiles at various streamwise locations (BL_2-BL_7). The measurements were conducted at the free-stream velocity of U_∞=20 m/s, corresponding to the Reynolds number of Re_{BL_1}=3.6×10^4. A single wire probe was used and the data had been collected with a very fine spatial resolution between $y \approx 0$ mm and 120 mm. The measurements were taken over the whole test section area (x=30mm, 60mm and 110mm), and at the region upstream (x=-2mm) and downstream (x=130mm, 205mm and 266mm) of the surface treatment section to obtain a full picture of the boundary layer behaviour. The y-axis of the boundary layer profiles were normalized by the boundary layer thickness at BL_1, x=-2 mm (before the test section), upstream of the test section area. This is because, at BL_1, the fluid velocity in the x-direction approaches zero when the fluid is in direct contact with the solid boundary, bringing about no-slip condition. This will not be the same in the case of the porous boundary, which involves the penetration of flow into the porous medium [205]. As expected, the mean velocity profiles at BL_1, upstream of the test section are found to be similar for all cases and are therefore not presented here. For the solid wall, the turbulent boundary layer growth observed is almost similar in all the measurement locations, while a distinct growth of the boundary layer profiles is observed in the case of the porous walls, downstream of BL_1 for all the porous cases, except for the highly permeable surface (25 PPI material). The different behaviour of the 25 PPI case can also be related to the flow penetration effects. The difference between the highly permeable surface

(25 PPI) with the other cases will be further discussed in the following sections.

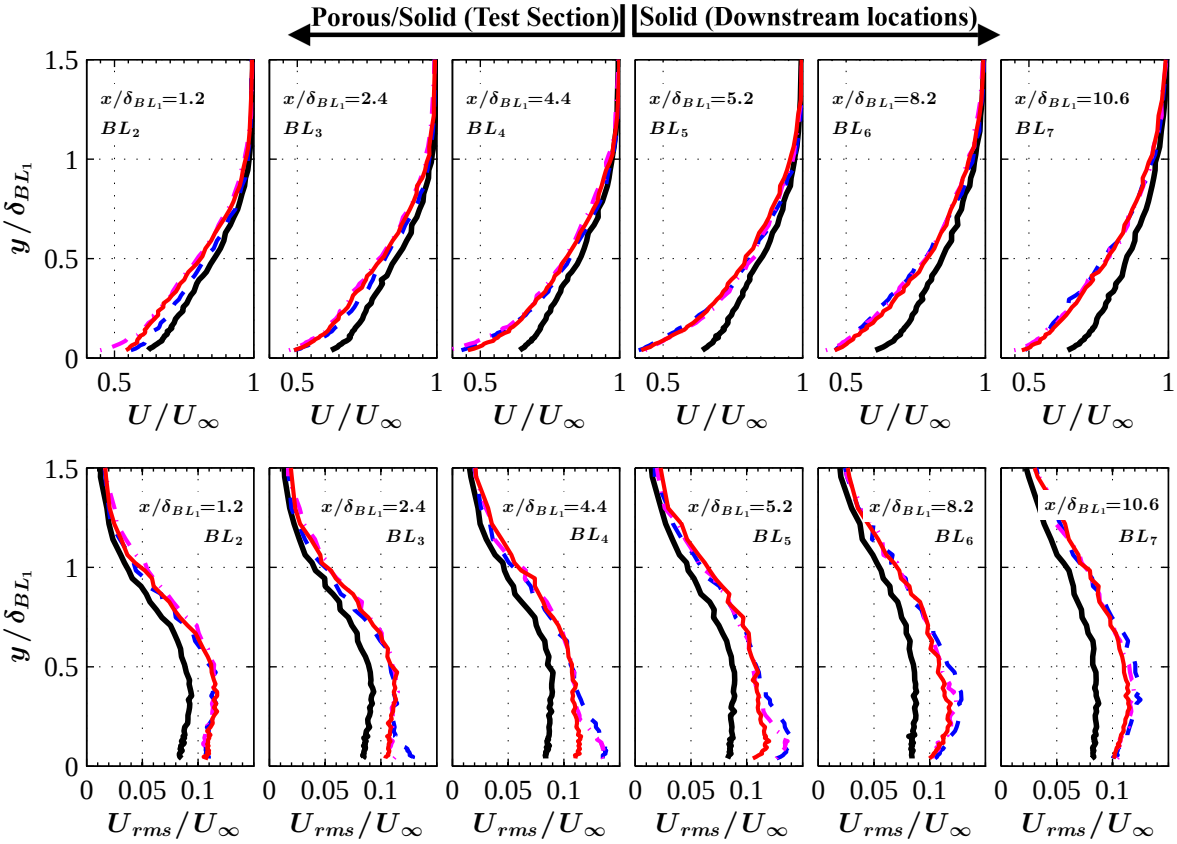

Figure 5.5: Boundary layer mean and RMS velocity profiles at different streamwise locations over the flat plate. *Solid(—), Porous 80 PPI(—), Porous 45 PPI(- - -), Porous 25 PPI(- - -).*

The normalized rms of the fluctuating flow velocity, on the other hand, clearly show that the whole energy cascade of the boundary layer changes significantly as a result of the flow interaction with the porous surfaces. The rms velocity results for the solid wall shows a lower level of velocity fluctuations compared to that of the porous cases at the near-the-wall locations and then gradually decreases to the rms velocity of the free-stream flow away from the surface. In contrast, the rms velocity results for the porous cases, especially for the highly permeable materials at BL_3 (x/δ_{BL_1}=2.4) and BL_4 (x/δ_{BL_1}=4.4) (over the porous section) and at BL_5 (x/δ_{BL_1}=5.2), BL_6 (x/δ_{BL_1}=8.2) and BL_7 (x/δ_{BL_1}=10.6) (downstream of the porous section) revealed drastically different boundary layer behaviour. A significant increase in the rms velocity magnitude and the emergence of the peak velocities ($y/\delta_{BL_1} \approx 0.05 - 0.5$), can be seen in the near the wall region

of the plate, as the flow travels over the porous region (BL_3 and BL_4). The peak of the rms velocities, however, diminishes slowly and the peaks becomes flattens downstream of the porous surface (BL_6 and BL_7), peaking at around $y/\delta_{BL_1} \approx 0.5$. It can also be seen that the near-the-wall turbulent energy content increases in the normal direction from the wall and subsequently reduces to the standard boundary layer form (solid surface) at $y/\delta_{BL_1} > 1$. The increase in the energy content of the velocity fluctuations in the vicinity of the porous surface had the effect of increasing the flow shear stress, which can be attributed to the frictional forces due to the rough surface of the material. This is consistent with the surface roughness results obtained in Fig. 4.20.

5.2.1 Velocity power spectra in the boundary layer

Figure 5.6 shows the velocity power spectral density (PSD) as a function of frequency within the boundary layer at different axial locations over the porous surface at BL_3 (x/δ_{BL_1}=2.4) and BL_4 (x/δ_{BL_1}=4.4) and after the porous surface at BL_5 (x/δ_{BL_1}=5.2) and BL_7 (x/δ_{BL_1}=10.6). The velocity fluctuation energy power spectrum is taken at (a) a point near the surface (y/δ_{BL_1}=0.02) (b) at the locations further away from the plate surface (y/δ_{BL_1}=0.5) and (c) at y/δ_{BL_1}=0.75. Results have clearly shown that the porous wall causes an increase in the flow energy content near the surface (y/δ_{BL_1}=0.02) over the whole frequency range, especially for the case of the 25 PPI surface treatment. This is believed to be due to the frictional forces acting on the flow due to the porous surface, which is in agreement with the rms velocity results shown in Fig. 5.5. It is also seen that the frictional forces reduce slowly at the downstream locations and after the porous surface region. The results also show that the overall energy content of the larger turbulence structures associated with the porous surface at about 50% and 75% of the boundary layer thickness are reduced significantly and matches the results of the solid surface. These reductions in the energy content, can be interpreted as a cascade process that takes place at different layers of the boundary layer, where the energy due to the frictional forces or any related sources (*i.e.* internal hydrodynamic field inside the porous medium) increases at the near-the-wall locations but then reduces shortly at locations above the surface (y/δ_{BL_1}=0.5 and 0.75), over and after the porous section.

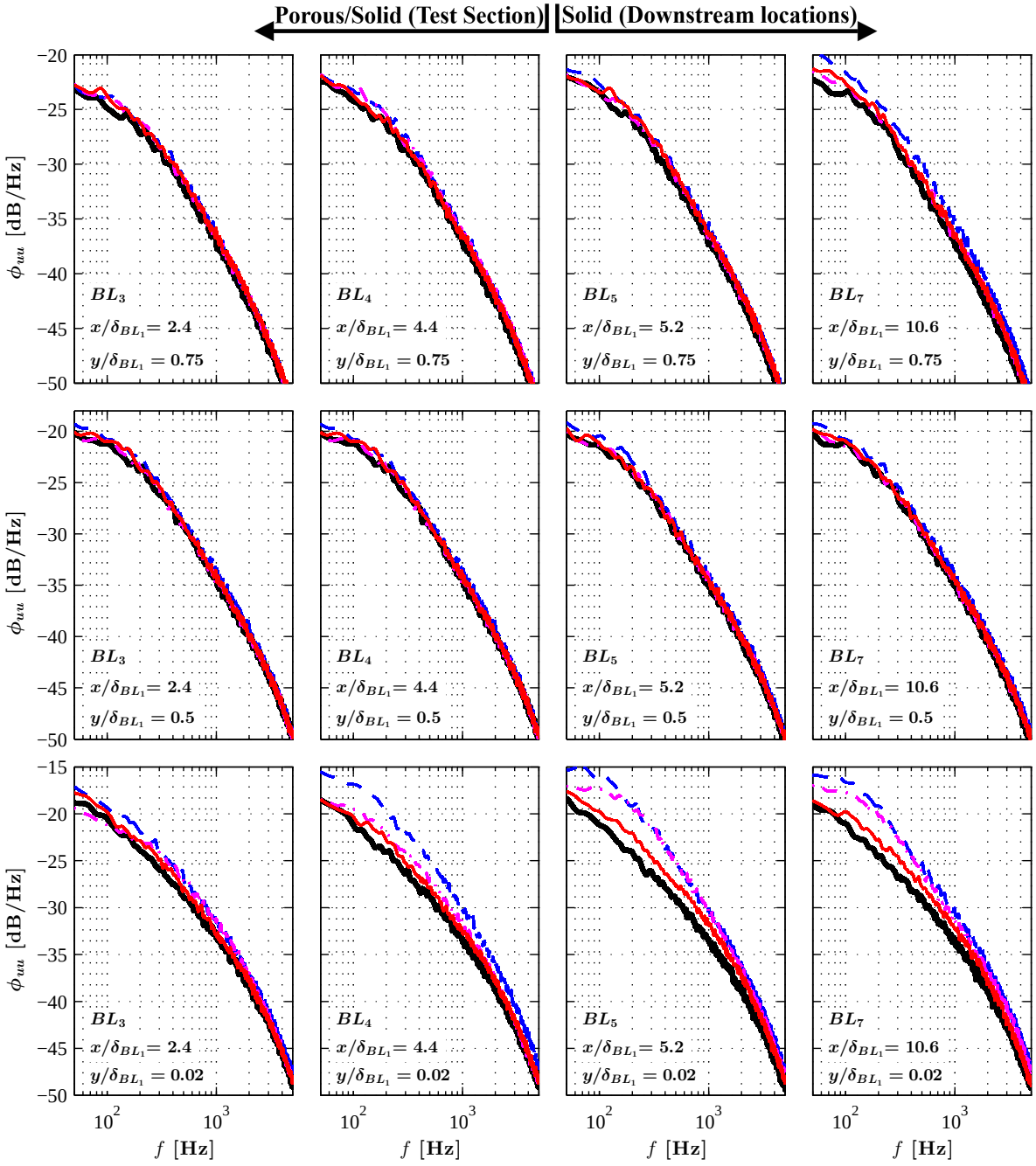

Figure 5.6: Power spectra of the velocity within the boundary layer (ϕ_{uu} [dB/Hz]).

In order to better visualize the results presented in Fig. 5.6, the changes in the energy content of the velocity with respect to the baseline case within the boundary layer over and after the porous surface ($\Delta\phi_{uu}$=$\phi_{uu_{porous}}$-$\phi_{uu_{solid}}$) are presented in Fig. 5.7. Similar to the findings

in Fig. 5.6, the energy content of the boundary layer velocity increases at the near-the-wall locations for all the porous surfaces, especially in the case of 25 PPI material, and their intensity is observed to increase even further as the flow travels downstream beyond the porous section (x/δ_{BL_1}=5.2).

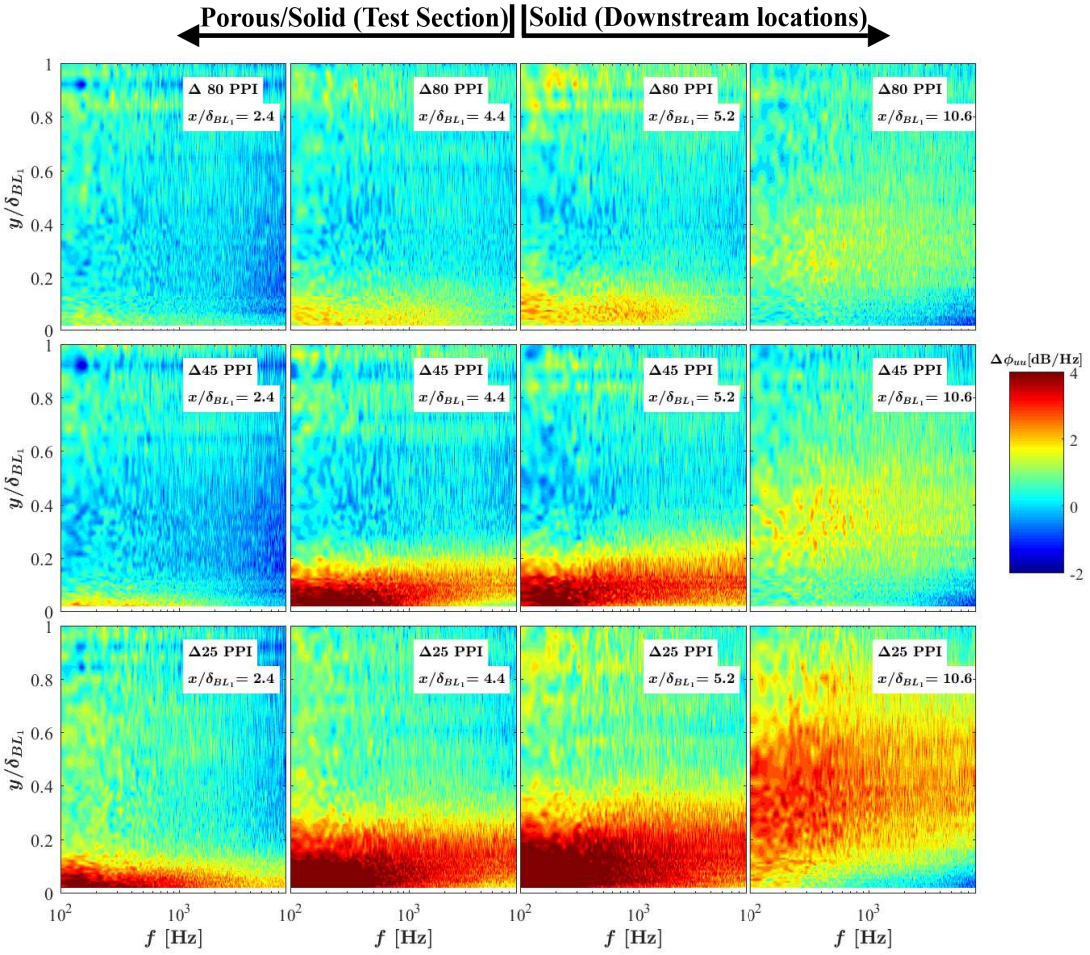

Figure 5.7: Changes in the velocity PSD within the boundary layer ($\Delta\phi_{uu}$ [dB/Hz]).

Interestingly, the energy content of the porous surface treatments reduces and collapses to that of the solid case (≈ 0 dB) further away from the wall (*i.e.* larger boundary layer structures) due to the energy cascade process between different layer of the boundary layer ($0.3 \lesssim y/\delta_{BL_1} \lesssim 1$) for all the measurement locations. Beyond the porous section at x/δ_{BL_1}=10.6, the near-the-wall high intensity region previously observed over the porous section is found to move upwards to $0.05 \lesssim y/\delta_{BL_1} \lesssim 1$, with a much weaker energy content across the whole boundary layer region.

It can also be seen that the energy content in the near-the-wall region has been significantly reduced, specifically at high frequencies ($f \geq 800$ Hz), due to the absence of the frictional forces associated with the rough surface of the porous substrate. From the results presented in Figs. 5.6 and 5.7, one can conclude that the use of porous materials can lead to an increase of the wall shear stress and thus intensify the turbulent pressure fluctuations in the boundary layer but can also lead to much more rapid energy cascade within the boundary layers from the wall to the boundary layer edge ($0.99\delta_{BL_1}$). The results obtained are particularly important as the energy content of the boundary layer structures is indicative of their strength, pressure exerted on the surface and therefore has implications in the context of development of the aerodynamic noise control methods. The effect of porous surfaces on the boundary layer surface pressure exerted on the surface will be studied in § 5.3 and § 5.5.

5.2.2 Skin friction coefficient and log-law representation

Figure 5.8 shows the measured zero-pressure gradient mean velocity profiles at various streamwise locations, over the porous section (BL_3 (x/δ_{BL_1}=2.4) and BL_4 (x/δ_{BL_1}=4.4)) and downstream of the porous section (BL_5 (x/δ_{BL_1}=5.2) and BL_6 (x/δ_{BL_1}=10.6)). The measurements were conducted at the free-stream velocity of U_∞=20 m/s, corresponding to the Reynolds number of Re_{BL_1}=3.6×10^4. The mean velocities for locations $y < 2mm$ are estimated using the Spalding equation [206] as,

$$y^+ = u^+ + e^{-kB} \quad \left[e^{ku^+} - 1 - ku^+ - \frac{(ku^+)^2}{2} - \frac{(ku^+)^3}{6} \right], \tag{5.5}$$

where u^+=u/u_τ and y^+=yu_τ/ν. The friction velocity u_τ is acquired by fitting the measurement data to the log-law region. The dashed line in Fig. 5.8 corresponds to a linear profile of the form $u^+ = y^+$ in the near-wall region and logarithmic profile of the form $u^+ = (1/k) \ln (y^+) + B$ in the overlap region, with the estimated constants of k=0.39 and B=4.3. Due to the complexity of the near-the-wall flow and difficulties in the measurement of the friction velocity (u_τ) for the solid and porous surface, it is rather difficult to accurately determine the viscous sublayer and buffer layer of the boundary layer regions (i.e. $y^+ < 10$). In the case of the solid surface, the measured mean velocities are higher at the measurement points near to the surface, which is believed to

be due to the bias introduced by the velocity gradients across the hotwire measurement. In the overlap region ($40 \leqslant y^+ \leqslant 400$), the mean velocity profile is nearly consistent with the logarithmic law ($u^+ = (1/k)\ln(y^+) + B$). It is clear that the presence of porous treatment have significantly modifies the mean velocity profile.

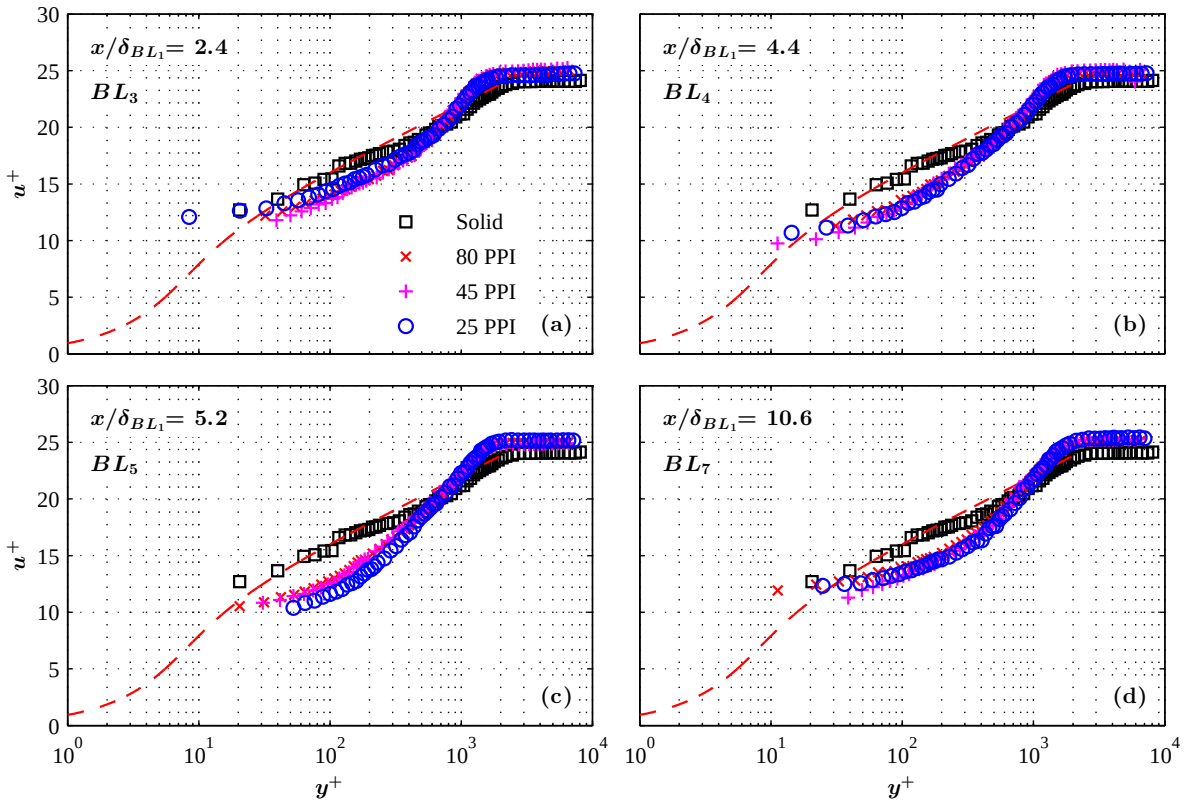

Figure 5.8: Streamwise mean velocity measured at different streamwise locations with and without the porous treatments. The dashed line corresponds to a linear profile of the form $u^+ = y^+$ in the near-wall region and logarithmic profile of the form $u^+ = (1/k)\ln(y^+) + B$ in the overlap region, with k=0.39 and B=4.3.

Results have also shown that there is a velocity deficit in the overlap region, farther from the wall, relative to the solid velocity profile. This velocity deficit increases with distance along the plate (BL_3-BL_5) and appears to reduce at further downstream locations (BL_7), relative to that of the solid case, which is in agreement with the results observed in Fig. 5.5. The mean velocity profiles for the porous cases increase slightly at $y^+ > 2000$, suggesting that the boundary layer exhibits a slight u^+ increase in the outer part of the wake region. Figure 5.8 also shows a clear

evidence of the slip-velocity at the porous interface ($y \approx 0$) at about $u^+ \approx 10\sim 15$. The issue of flow penetration and the boundary layer slip-velocity and their effect on boundary layer y^+ region, however, need further high-quality experimental and numerical investigation.

5.3 Wall pressure power spectra

To gain an insight into the effects of the porous surface on the boundary layer and surface pressure fluctuations exerted on the surface due to the boundary layer, a series of unsteady pressure measurements have been carried out over and after the porous section. The unsteady surface pressure measurement technique is detailed in § 3.2.5. The results of the wall pressure power spectra have also been validated using the Goody's model [203], which was initially developed from the experimental results for zero pressure gradient. The comparison is made between the normalized power spectra of the smooth/ solid case with the Goody curve at the pressure transducer located upstream of the trailing-edge (x/δ_{BL_1}= 2.4), shown in figure 5.9. The spectra show an overall good agreement with the Goody model, particularly for the broadband aspect of the spectra with a slope of $\omega^{-0.7}$ and at higher frequencies region with a slope of $\omega^{-0.5}$. The results, however, show a minor deviations at low frequencies and the middle frequency region.

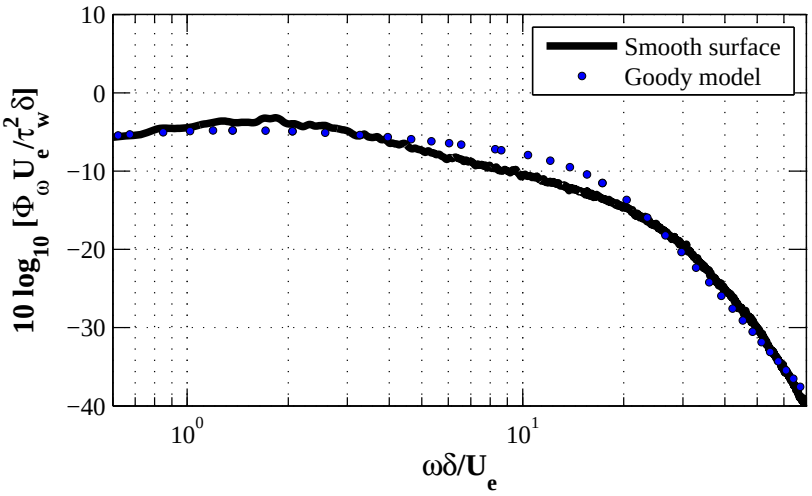

Figure 5.9: Comparison of the nondimensional spectral density with Goody model.

Figure 5.10 presents the point spectra of the surface pressure fluctuations $\phi_{pp}(f)$, obtained from the transducers located over the porous section ($p3$ (x/δ_{BL_1}=2.4) and $p11$ (x/δ_{BL_1}=4.4)) and downstream of the porous section ($p16$ (x/δ_{BL_1}=5.2) and $p41$ (x/δ_{BL_1}=10.6)). The locations of the transducers are shown in Fig. 5.1(a). It has been observed that the use of a porous surface increases the broadband energy content of the pressure fluctuations over the whole frequency range over the porous surface ($p3$ and $p11$). Also, the emergence of a small broadband hump between f= 100 to 400 Hz can be seen at the locations over the porous surface ($p3$ and $p11$) and downstream of the porous surface ($p16$), especially for the porous samples with high permeability (25 and 45 PPI). This broadband hump, however, dissipates very quickly at the further downstream locations, after the test section ($p41$). The increase in the broadband energy content and the development of a broadband hump can be due to either (a) the frictional forces between the rough porous surface and the flow or (b) the existence of a localized strong hydrodynamic field inside the porous medium. This will be further discussed in § 5.4. The results have also shown a reduction of ϕ_{pp} over the high frequency range, f > 7000 Hz, at the locations downstream of the porous section ($p41$) *i.e.* $5.4\delta_{BL_1}$ after the porous section.

Figure 5.11 shows the contour plots of the changes in the surface pressure fluctuations with respect to the baseline (solid surface) ($\Delta\phi_{uu}$=$\phi_{pp_{porous}}$-$\phi_{pp_{solid}}$) as a function of the frequency and streamwise distance (x/δ_{BL_1}). The results are plotted for locations, over and after the porous surface. The dashed line represents the porous-solid interface at x=120 mm. The results show that the porous surface is able to reduce the surface pressure fluctuations at high frequencies, especially for the 25 PPI case (shown by the dashed lines), which is in agreement with the boundary layer velocity power spectra results shown in Fig. 5.7. As expected from the results presented in Fig. 5.10, an area of increased $\Delta\phi_{pp}$ can be seen between f= 100 to 400 Hz for all porous cases, particularly for the 25 PPI case, which corresponds to the emergence of a broadband hump. The results also clearly indicate that the broadband hump disappears quickly downstream of the porous section (solid surface). The emergence of the broadband hump will be further investigated in § 5.4.

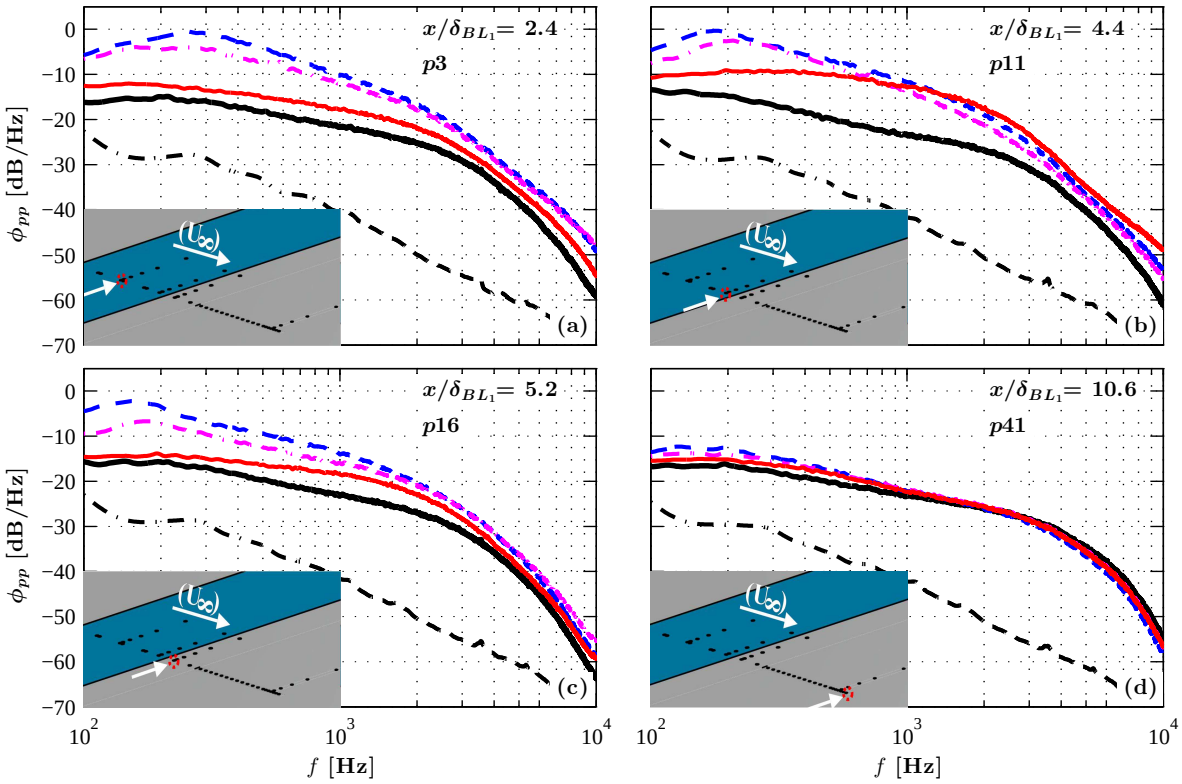

Figure 5.10: Point spectra of pressure fluctuations at different streamwise locations over and after the porous surface. *Solid(——), Porous 80 PPI(——), Porous 45 PPI(- - -), Porous 25 PPI(- - -), Background noise(- - -).*

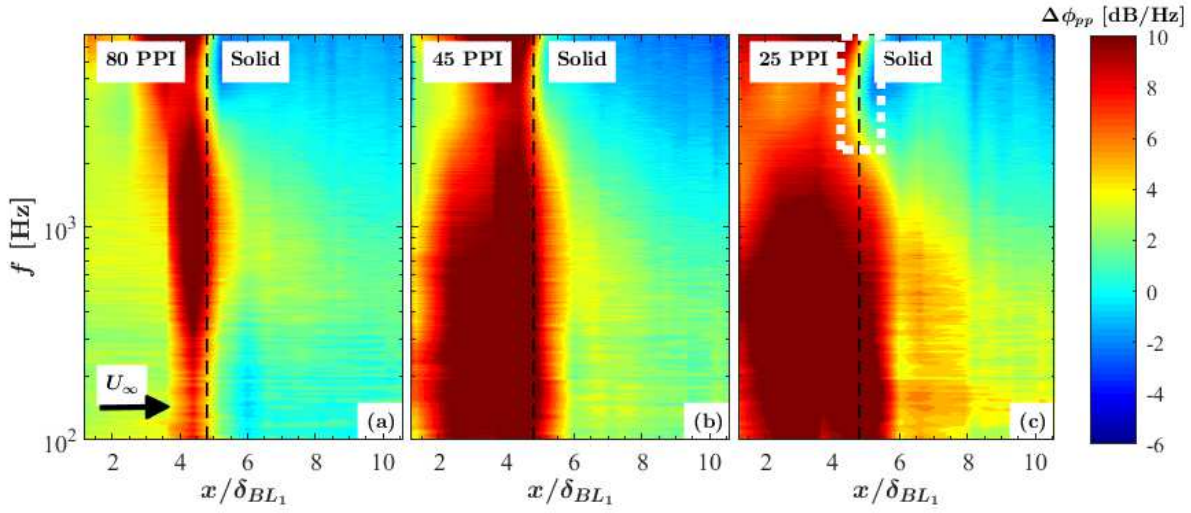

Figure 5.11: Change in the power spectra of the pressure fluctuations within the boundary layer ($\Delta\phi_{pp}$ [dB/Hz] over and after the porous surface).

5.4 On the source of the broadband hump

It is evident from Fig. 4.20 that the porous samples with higher porosity (φ) and permeability (κ) are associated with higher surface roughness (Ra). The results obtained in § 5.3 clearly indicate that the porous material with higher Ra leads to higher ϕ_{pp} in the near-the-wall region, which can be attributed to the frictional forces acting on the porous materials. However, the emergence of a broadband hump, observed in Figs. 5.10 and 5.11 between $f \approx$ 100-400 Hz, can only be seen in the case of highly permeable porous samples (25 PPI and 45 PPI) and dissipates quickly with distance from the plate. In order to examine the effect of the surface frictional forces and the existence of the internal hydrodynamic field, the porous section was filled with a fine grain sand at different heights (h_s), as shown in Fig. 5.12.

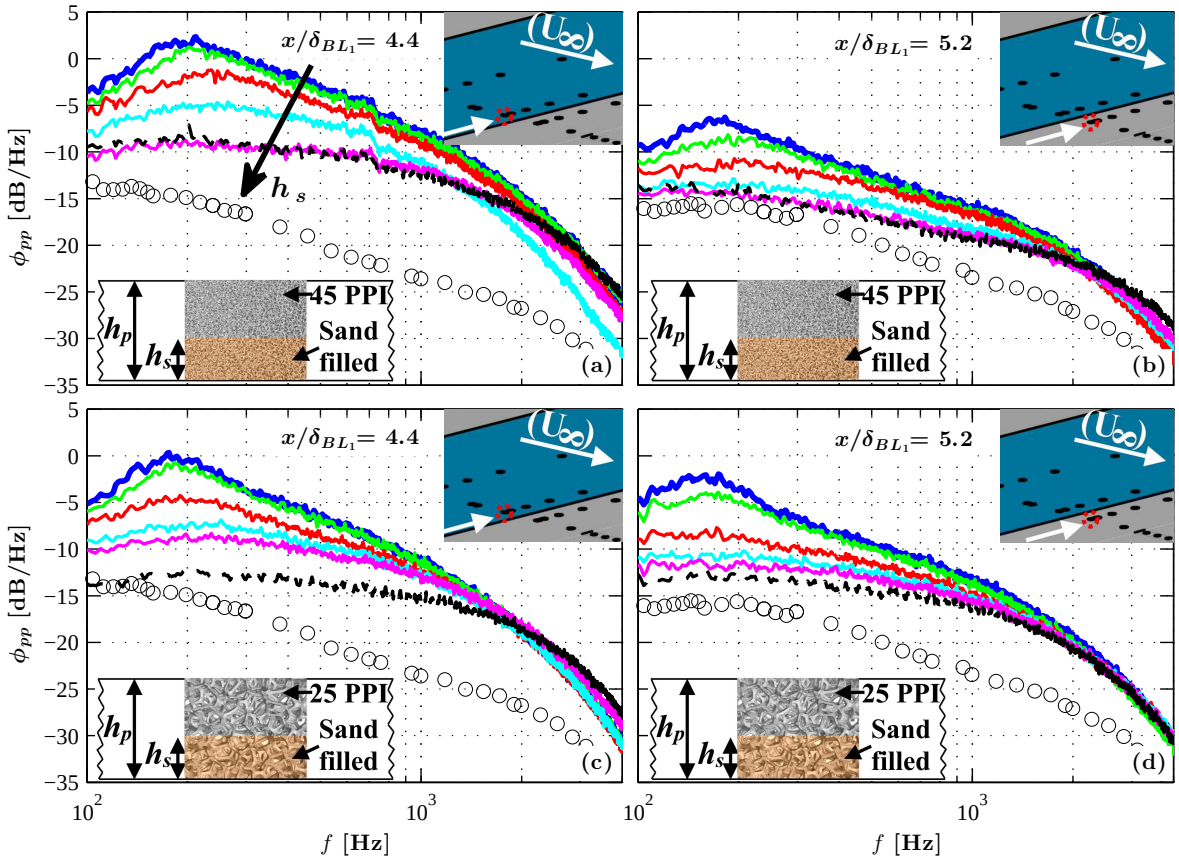

Figure 5.12: Power spectral density of pressure measured by transducers $p11$ and $p16$ with different thickness of porous 45 and 25 PPI filled with sand. *Solid surface (circles);* h_s/h*=1.0(—),* h_s/h*=0.9(—),* h_s/h*=0.75(—),* h_s/h*=0.5(—),* h_s/h*=0.5(—),* h_s/h*=0(—).*

The porous surface roughness effect have been investigated by filling the porous 45 PPI and 25 PPI material with different sand heights (h_s/h), namely h_s/h=0 (fully permeable), h_s/h=0.25, h_s/h=0.5, h_s/h=0.75, h_s/h=0.9 and h_s/h=1.0 (fully blocked but with a rough surface). The surface pressure PSD results are presented for two locations x/δ_{BL_1}= 4.4 ($p11$) and x/δ_{BL_1}= 5.2 ($p16$), *i.e.* over the porous surface and downstream of the porous section, respectively. Figure 5.12 shows that the broadband hump at $f \approx 200$ only appears for the porous medium configurations with fully permeable (h_s/h=0 sand) and slightly filled up (h_s/h=0.25 and 0.5 sand) cases. Results also show that the broadband hump disappears gradually with increasing the sand height (h_s) in the porous medium, in which case there is not enough space available for the development of the internal hydrodynamic field. The results, therefore, confirm that the broadband hump observed at $f \approx 200$ can not be due to the surface roughness effects. Hence, as expected, the emergence of the broadband hump can only be due to the existence of the hydrodynamic field and the flow recirculation inside the high permeability porous inserts.

5.5 Flow velocity and pressure correlation analysis

The results in § 5.2 demonstrated that the utilization of a porous surface can alter the whole energy cascade of the boundary layer and significantly reducing the larger turbulence structures and its energy content within the boundary layer. The results of the surface pressure fluctuations in § 5.3 also showed that a reduction in the surface pressure fluctuations is achieved at the locations downstream of the porous section, over the high frequency range, for all the porous cases. The theoretical relations of the sound source characteristics from the surface pressure fluctuations have been documented by Brooks and Hodgson [207]. They reported that there are two types of coherence that can be related to different aspect of the wall-pressure field, namely the longitudinal (streamwise) and the lateral (spanwise) coherence. The longitudinal coherence is associated with the lifespan or the decay of the flow structures, whereas the lateral coherence is related to the physical size/ scale of the flow structures. The longitudinal and lateral coherence analysis are interrelated since the flow structures with the largest scale will have a longest lifespan. This has been broadly investigated in the present study. In this section, further

investigation on the changes in the boundary layer turbulent flow structures will be conducted by studying the coherence and correlation of the boundary layer velocity and the surface pressure signals over the porous and solid surfaces.

5.5.1 Surface pressure lateral coherence and length-scale

In order to understand and decipher information related to the changes to the flow structures associated with rough-permeable surfaces, it is of significant importance to analyze the stochastic characteristics of the turbulent coherent structures over the porous wall. To understand these effects, the spanwise coherence of the turbulent structures and their corresponding length-scale using the pressure transducers (*p3-p7*, *p11-p15*, *p16-p20* and *p35-p39*), distributed along the span at x/δ_{BL_1}= 2.4 (middle of the porous section), x/δ_{BL_1}= 4.4 (end of the porous section), x/δ_{BL_1}= 5.2 and x/δ_{BL_1}= 10.2, are studied. The coherence ($\gamma^2_{p'_i p'_j}$) and the lateral length-scale (Λ_p) between the spanwise transducers are calculated using Eqs. 5.6 and 5.7, respectively, as,

$$\gamma^2_{p'_i p'_j}(f,\xi_z) = \frac{|\Phi(f,p'_i,p'_j)|^2}{|\Phi(f,p'_i,p'_i)||\Phi(f,p'_j,p'_j)|}, \tag{5.6}$$

and

$$\Lambda_p(f) = \int_0^\infty \gamma_{p'_i p'_j}(f,\xi_z) d\xi_z, \tag{5.7}$$

where $\Phi(f,p'_i,p'_j)$ denotes the cross-power spectral density between two pressure signals, and ξ_z denotes the pressure transducers separation distance in the z-direction. The results are presented only when the pressure signal is at least 10 dB higher than the background noise.

Figure 5.13 shows the lateral coherence ($\gamma^2_{p'_i p'_j}$) as a function of the frequency (f), measured along the span for a wide range of lateral spacings $0 < \xi_z/\delta_{BL_1} < 1.7$ for the solid (baseline) and porous (80, 45 and 25 PPI) cases. In the case of the solid surface, as anticipated, a strong coherence can be seen in the frequency region up to ≈ 400 Hz between the pressure signals at all the span locations. The results for the porous surfaces, on the other hand, clearly show that the porous treatment has a strong impact on the lateral coherence of the flow structures, especially over the test section region. In the case of the porous 80 PPI surface, the lateral turbulent structure decays

quickly with ξ_z over the whole frequency range at x/δ_{BL_1}= 2.4 and x/δ_{BL_1}= 4.4. Immediately downstream of the test section (x/δ_{BL_1}= 5.2 and x/δ_{BL_1}= 10.2), the coherence behaviour for the 80 PPI case changes completely, with the $\gamma^2_{p'_i p'_j}$ of the flow structures increasing significantly, almost twice larger than the results obtained at x/δ_{BL_1} = 2.4.

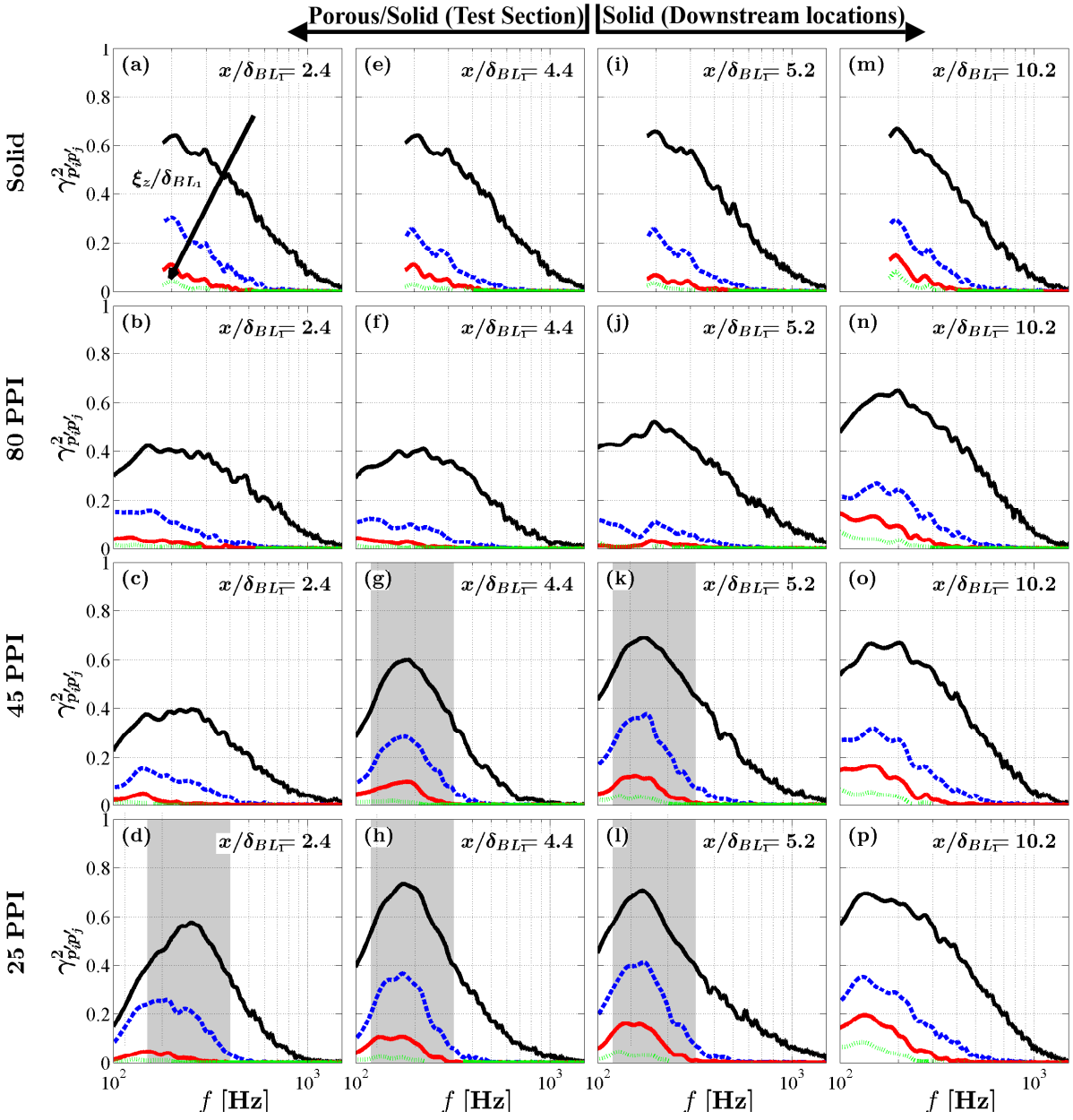

Figure 5.13: Lateral coherence between spanwise transducers at x/δ_{BL_1}= 2.4 (a,b,c,d), x/δ_{BL_1}= 4.4 (e,f,g,h), x/δ_{BL_1}= 5.2 (i,j,k,l) and x/δ_{BL_1}= 10.2 (m,n,o,p). ξ_z/δ_{BL_1}=*0.13(——), ξ_z/δ_{BL_1}=0.45(- - -), ξ_z/δ_{BL_1}=0.96(——), ξ_z/δ_{BL_1}=1.68(·····). The shaded areas signify the broadband hump observed in Fig. 5.10.*

In contrast, the 45 PPI and 25 PPI samples exhibit much lower coherence values compared to that of the solid case over the porous region (x/δ_{BL_1}= 2.4 and x/δ_{BL_1}= 4.4). However, similar to the findings in Fig. 5.10, the emergence of a broadband peak can be seen at the same frequency region between f= 100 to 400 Hz (shaded region) for the smaller transducers spacing distances, ξ_z of 0.13 δ_{BL_1} and 0.45 δ_{BL_1}. As discussed in § 5.4, this phenomenon is believed to be due to the emergence of a strong hydrodynamic field inside the porous medium. This broadband hump is also seen in the immediate locations after the test section (x/δ_{BL_1}= 5.2) for both the 45 PPI and 25 PPI materials, but dissipating rapidly at the further downstream locations. At x/δ_{BL_1}= 10.2, the $\gamma^2_{p'_i p'_j}$ of the boundary layer flow structures begin to behave very similar to the solid surface (Fig. 5.13(m)), indicating the redevelopment of the boundary layer coherent structures.

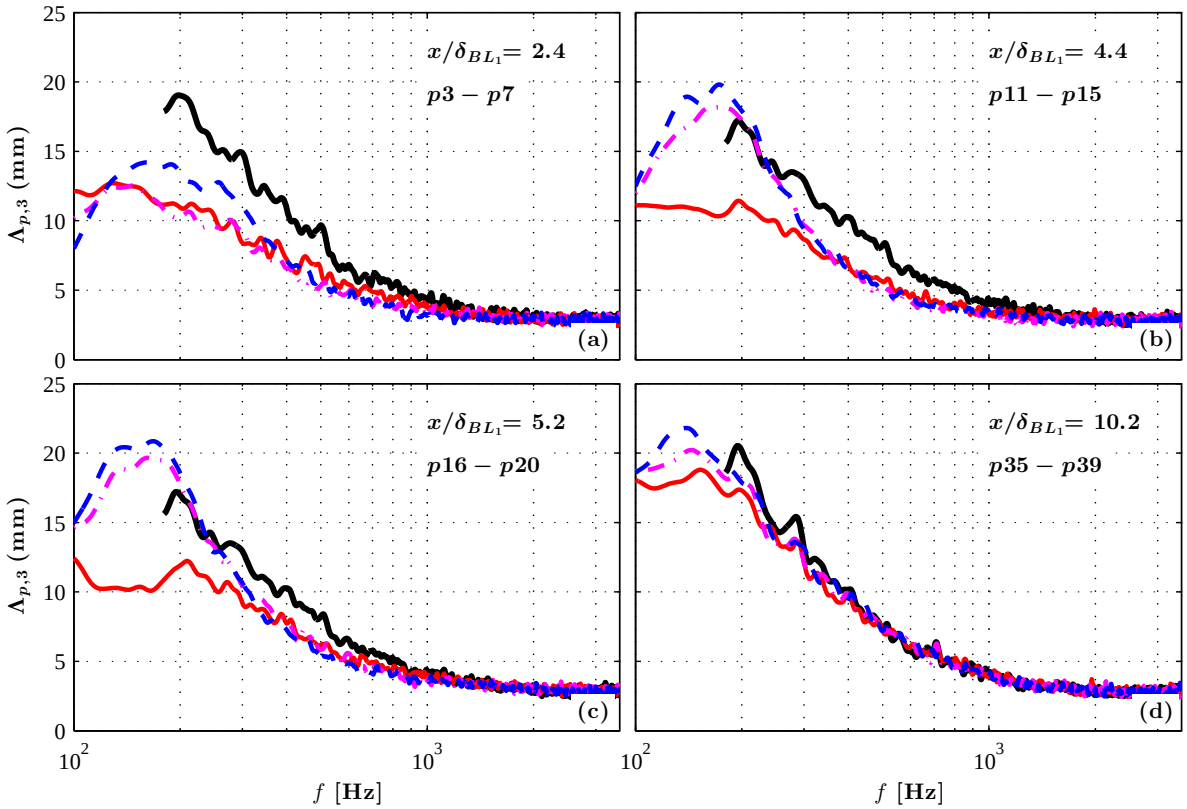

Figure 5.14: Spanwise length-scales at (a) x/δ_{BL_1}= 2.4 , (b) x/δ_{BL_1}= 4.4, (c) x/δ_{BL_1}= 5.2 and (d) x/δ_{BL_1}= 10.2. *Solid(——), Porous 80 PPI(——), Porous 45 PPI(- · -), Porous 25 PPI(- - -).*

Figure 5.14 shows the effect of the porous surface on the spanwise correlation length (Λ_p) calculated using Eq. 5.7, based on the coherence of the pressure fluctuations collected using the

spanwise transducers. The thick black line shows the spanwise correlation length for the baseline (solid) case. As expected, the spanwise correlation length remains very similar for the baseline case over x/δ_{BL_1}= 2.4 to 10.2, which is consistent with the results observed in Figs. 5.6, 5.10 and 5.13. For the porous 80 PPI case, the correlation length is found to be much lower than the baseline case over the whole frequency range (100 Hz $\lesssim f \lesssim$ 700 Hz) for the locations over and immediately after the porous section, consistent with the results in Fig. 5.13.

The length-scale results in the case of the porous 45 PPI and 25 PPI surfaces show a higher broadband hump than that of the solid case in the low frequency range ($\lesssim$ 200 Hz), which is also in agreement with the observations in Figs. 5.11, 5.12 and 5.13. It is observed that the spanwise length scales for both the porous cases increase after the porous section and become very similar to the solid case at x/δ_{BL_1}= 10.2. This is to say that the effects of a porous surface on the large coherent structures seem to have faded away $5\delta_{BL_1}$ after the porous section. It is clear that the porous surface treatment significantly changes the coherence and length-scale of the surface pressure fluctuations at the low frequency range and completely eliminates the pressure fluctuations at high frequency range, especially for the 25 PPI treated surface case.

5.5.2 Surface pressure spatio-temporal correlation analysis

Owing to the intricacy of turbulent flows, the understanding of the flow statistical features are crucial. The spatial and temporal characteristics of the boundary layer structures can be studied from the space-time correlation of the wall pressure fluctuations, defined as,

$$R_{p_i' p_j'}(\xi_x, \tau) = \frac{\overline{p_i'(x_i + \xi_x, t+\tau) p_j'(x_j, t)}}{p_{i_{rms}}'(x_i) p_{j_{rms}}'(x_j)}, \tag{5.8}$$

where p_i' is the wall pressure signal collected from the pressure transducer at the location (x_i, y_i), $p_{i_{rms}}'$ is the root-mean-square of p_i', τ denotes the time-delay between the pressure signals, ξ_x is the distance between the transducers in the x-direction and the overbar represents the time averaging. Equation 5.8 reduces to the temporal autocorrelation, $R_{p_i' p_i'}(\tau)$, when $\xi_x = 0$ as,

$$R_{p_i' p_i'}(\tau) = \frac{\overline{p_i'(x_i, t+\tau) p_i'(x_i, t)}}{p_{i_{rms}}'^2(x_i)}. \tag{5.9}$$

5.5.2.1 Longitudinal autocorrelation

The temporal correlation scale is the time taken for the cross correlation ($R_{p_i'p_i'}(\tau)$) to reach zero, *i.e.* where maximum width of the autocorrelation coefficient is observed along the time-axis. Figure 5.15 shows the temporal autocorrelations of the surface pressure fluctuations, $R_{p_i'p_i'}(\tau)$ for transducers at different axial locations over the porous surface (*p1* (x/δ_{BL_1}=1.2) and *p11* (x/δ_{BL_1}=4.4)) and after the porous surface (*p16* (x/δ_{BL_1}=5.2) and *p41* (x/δ_{BL_1}=10.6)). The data are plotted against the normalized time-delay $\tau^*=\tau U_\infty/\delta_{BL_1}$.

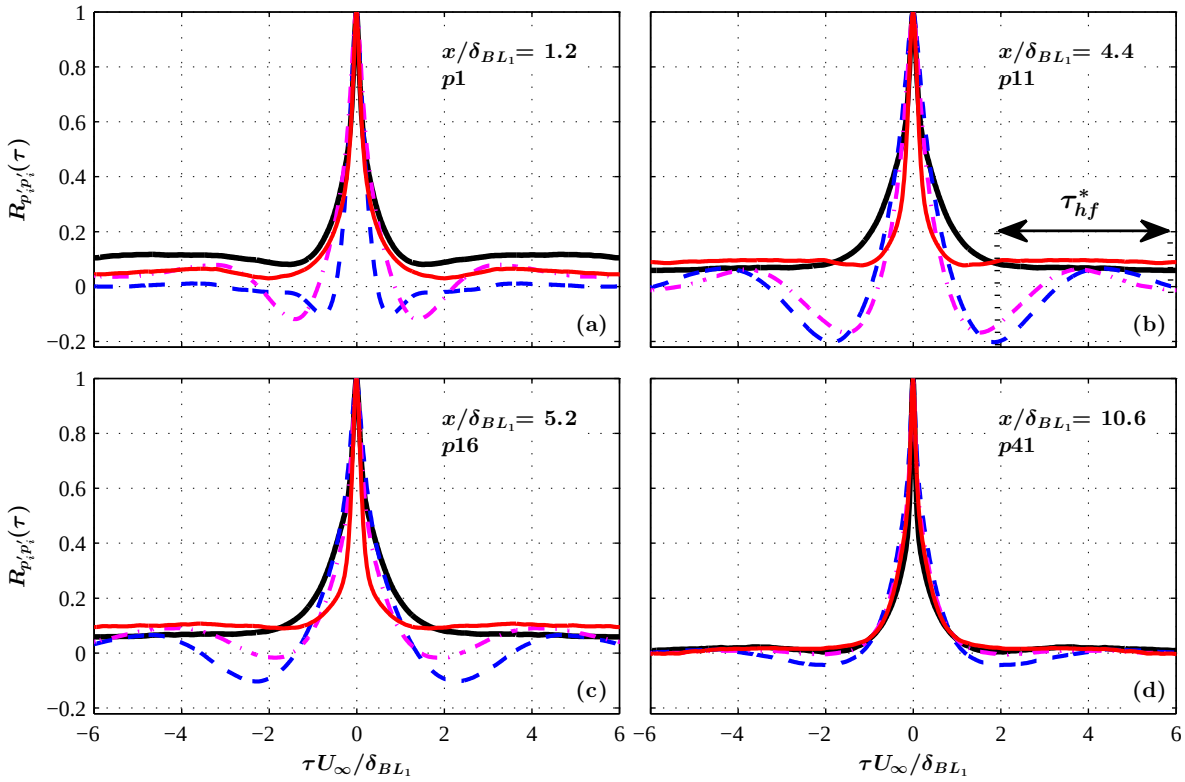

Figure 5.15: Autocorrelation of the wall pressure fluctuations as a function of $\tau^*=\tau\ U_\infty/\delta_{BL_1}$. *Solid(——), Porous 80 PPI(——), Porous 45 PPI(- · -), Porous 25 PPI(- - -).*

The $R_{p_i'p_i'}(\tau)$ results for the solid surface condition show the largest width of the autocorrelation coefficient at τ^* = 0 among all the tested cases and that no regions of negative correlations can be seen, indicating the presence of large-scale turbulence structures in the pressure field. The results also show that the autocorrelation signal width increases by moving in the downstream direction (+x) due to the development of the turbulence boundary layer and the thickening of the

boundary layer. In general, the autocorrelation results for the porous cases change significantly over *p1* and *p11*, and after the porous section (*p16*), and become almost identical to that of the baseline case (solid surface) at further downstream location (*p41*), *i.e.* $5.4\delta_{BL_1}$ away from the porous section. For the porous 80 PPI case, it can be seen that the autocorrelation width at $\tau U_\infty/\delta_{BL_1}$ = 0 is narrower compared to the solid case, indicating a reduction in the temporal scales of the boundary layer structures. The results have also shown that there is a significant change in the nature of the correlation, where a sharp decay in the correlation occurs at $\tau U_\infty/\delta_{BL_1}$=0 for all the measurement locations over the porous surface, which is believed to be due to the pressure exerted by the downstream moving boundary layer turbulence structure at the transducer location. The autocorrelation curves for the 45 PPI and 25 PPI surfaces, on the other hand, show a much faster decay at $\tau U_\infty/\delta_{BL_1}$ = 0, and therefore much narrower band than the other two cases, particularly for the 25 PPI surface at *p1* (x/δ_{BL_1}=1.2), signifying a greater reduction in the temporal scales of the boundary layer structures. In the case of highly permeable porous surfaces (45 PPI and 25 PPI), the sharp decay in the autocorrelation is followed by an area of negative correlation and semi-periodic oscillation. Unlike the solid and porous 80 PPI surfaces, the results indicate that two potential mechanisms can be involved in the abrupt changes in the autocorrelation profiles, namely (a) the existence of quasi-periodic hydrodynamic field with the periodicity of τ^*_{hf} (*i.e.* τ^*=$\tau U_\infty/\delta_{BL_1}$) and (b) a fast-decaying event at $\tau U_\infty/\delta_{BL_1}$ = 0. As observed in Fig. 5.15 (a, b) for the transducers located on the porous surface, the autocorrelation exhibits a fast decay at $\tau U_\infty/\delta_{BL_1}$=0, similar to that of the 80 PPI material, which is due to the pressure signature of the downstream moving boundary layer structures. The autocorrelation result also shows a period behaviour that occurs within $1.5 < \left|\tau U_\infty/\delta_{BL_1}\right| < 5$, which corresponds to the broadband hump frequency observed in Fig. 5.10. This quasi-periodic structure, as discussed in § 5.4, is believed to be due to the internal hydrodynamic field inside the porous medium. The results also show that the spatially and temporally fast-decaying quasi-periodic hydrodynamic field in the case of 45 PPI and 25 PPI materials can only be seen within a certain axial distance from the porous section, of about L_{px}=40 mm. The effect of porous section length on the formation of the internal hydrodynamic field will be further studied in § 5.6.

Generally, the surface pressure fluctuations at short lag distances exhibit the largest correla-

tion, *i.e.* the pressure fluctuations signal with a delayed copy of itself (τ) are correlated if they are located on the same eddy. The information about the time scales (also called as the large eddy turnover) of the flow structures is computed by integrating the temporal autocorrelation $R_{p_i'p_i'}(\tau)$ with respect to the time lag (τ), defined in Eq. 5.10 as,

$$t_{ii} = \int_0^\infty R_{p_i'p_i'}(x,\tau)\mathrm{d}\tau. \tag{5.10}$$

The non-dimensionalized integral time scales t_{ii}^*=$t_{ii}U_\infty/\delta_{BL_1}$ of the flow over the porous and solid surfaces (*p1* (x/δ_{BL_1}=1.2) and *p11* (x/δ_{BL_1}=4.4)) and after the porous surface (*p16* (x/δ_{BL_1}=5.2) and *p41* (x/δ_{BL_1}=10.6)) are shown in Fig. 5.16.

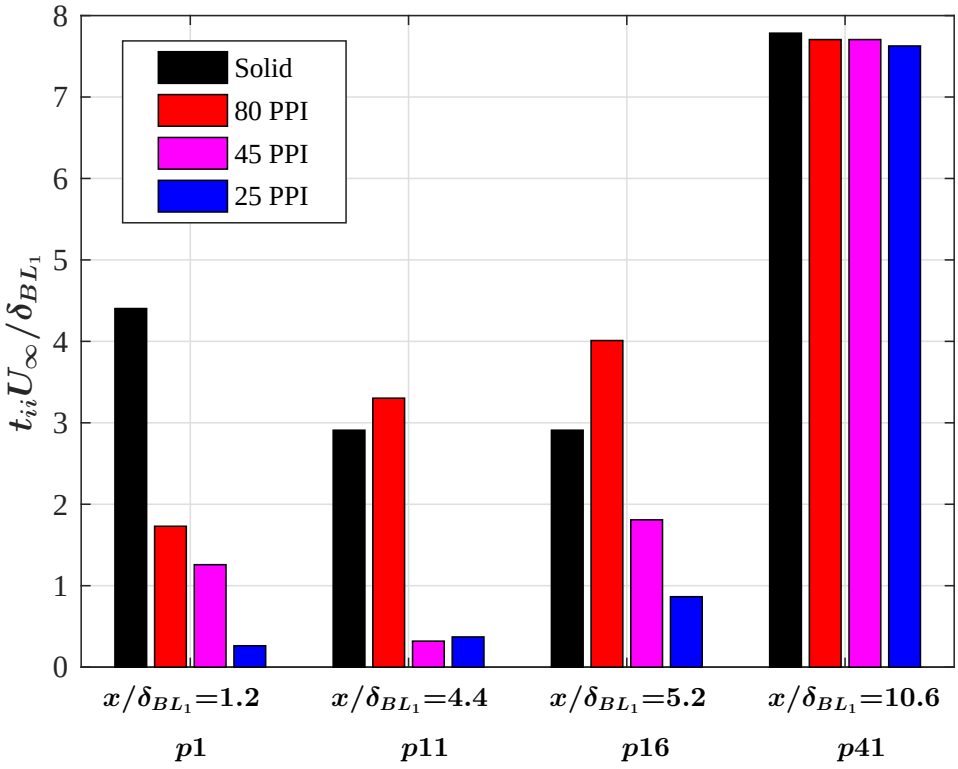

Figure 5.16: Non-dimensional integral time scale t_{ii}^*.

In the case of a solid surface, it can be seen that the time scale is the highest at *p1*, reduces to almost 25% and remain consistent at *p11* and *p16*, and increases abruptly at the downstream location (*p41*). The time scales in the case of porous 80 PPI show an interesting behaviour, where

the time scale observed at *p1* are much smaller than the solid case, however, it rapidly increases at the downstream locations and is found to be higher than the solid case at *p11* and *p16*.

The results for the 45 PPI and 25 PPI surfaces, on the other hand, show a significant reduction of the turbulent structures time scales, especially over the porous surface, at *p1* and *p11*. The time scale of the eddies over the 45 PPI surface was reduced significantly at *p11*, about 10 times than the solid case. In the case of 25 PPI material, the time scale of the eddies is about 16 and 10 times lower than the solid case at *p1* and *p11*, respectively. Note that the integral time scales obtained for the 25 PPI case are the lowest compared to the other cases, and it is consistent at all the measured locations. The eddies size, however, remain fairly constant at further downstream location (*p41*), where the redevelopment of the large coherent structures occurred, as observed in Fig. 5.13. The time scale t_{ii}, along with the convection velocity U_c, obtained from the wall pressure fluctuations, can be used to estimate the longitudinal (streamwise) length scale , $\lambda_x = U_c t_{ii}$, which will be presented and discussed in the next subsection.

5.5.2.2 Longitudinal space-time correlation

Figure 5.17 shows the space-time correlations results obtained from the cross-correlation between the reference transducer downstream of the porous section (*p41*) and the upstream pressure transducers positioned along the mid-chord line. Results are presented for the separation distances ξ_x/δ_{BL_1} of about 0.16 to 9.44. The left column plots (a, c, e and g) show the correlation between all the streamwise transducers, where the black line (ξ_x/δ_{BL_1} = 0) represents the autocorrelation information of the transducer *p41* as the reference probe, while the different shades of gray curves show the cross-correlation between the reference probe and the upstream probes for all the investigated cases. The right column plots (b, d, f and h) show the space-time correlation contour plots, where the results are plotted over the two surface areas, *i.e.* over and after the porous surface. The dashed line represents the interface between the porous and solid surfaces at x=120 mm, see Fig. 5.17. An envelope trend can be clearly seen from the cross-correlations periodicity and the amplitude variations for all the cases considered in this study. The cross-correlation $R_{p'_i p'_j}(\xi_x, \tau)$ results for the solid case show that the surface pressure correlations peak at positive time-delays, *i.e.* $\tau U_\infty/\delta_{BL_1} \geqslant 0$, indicating the presence of a downstream-moving

hydrodynamic field, travelling in the direction of the free-stream flow. The results for the solid surface in Fig. 5.17(a) show that the correlation peaks shift very quickly in the positive time-delay direction, which indicates the existence of a long-lasting energy field ($R_{p'_i p'_j}$ drop to 0.1 within 10 nondimensional time ($\tau U_\infty/\delta_{BL_1}$)) in the pressure field over the flat plate. A similar, but less distinct behaviour can also be observed for the 80 PPI surface case. Finally, in the case of the 45 PPI and 25 PPI surfaces, the $R_{p'_i p'_j}(\xi_x, \tau)$ results show that the surface pressure fluctuations have slightly higher correlation and that the correlation peaks shift slowly (larger time delay) at $\tau U_\infty/\delta_{BL_1} \geq 0$ compared to the solid case, which suggests that the turbulent structures convected in the downstream direction are primarily dominated by a short-lived energy field ($R_{p'_i p'_j}$ drop to 0.1 within $\tau U_\infty/\delta_{BL_1} \approx 5$ (Figure 5.17 (e,g)) in the pressure field over the plate.

The results in Fig. 5.17 show that as the separation distance (ξ_x) between the pressure probes increases, the time-delay of the maximum value in the cross-correlation (cross-correlation peak) increases. Hence, based on the Taylor's frozen flow hypothesis, one can obtain the convection velocity, U_c using the transducers distance and the maximum value of the cross-correlation time-delay ($[\tau\ U_\infty/\delta_{BL_1}]_{max}$) information, *i.e.* U_c=(ξ_x/δ_{BL_1})/$[\tau\ U_\infty/\delta_{BL_1}]_{max}$. The calculated convection velocities are summarised in Table 5.4. The inclined solid line in the contour plots (b, d, f and h), passing through the correlation lobe at $\tau\ U_\infty/\delta_{BL_1} \approx 0$, whose slope indicates the averaged normalized convection velocities U_c/U_∞. Note that, the U_c/U_∞ is only determined from the cross-correlation of the transducers located after the test section region. The non-dimensional convection velocities U_c/U_∞ obtained from the cross-correlation between the reference transducer *p41* and the upstream transducers are found to be about 0.8632, 0.8402, 0.7471 and 0.7135 for the solid, porous 80 PPI, porous 45 PPI and porous 25 PPI cases, respectively. As expected, the flow over the solid surface has the highest convection velocity. In contrast, the convection velocity for the flow over the 25 PPI porous surface is the lowest. It can therefore be concluded that the porous surface can strongly reduce the convection velocity of the boundary layer structures.

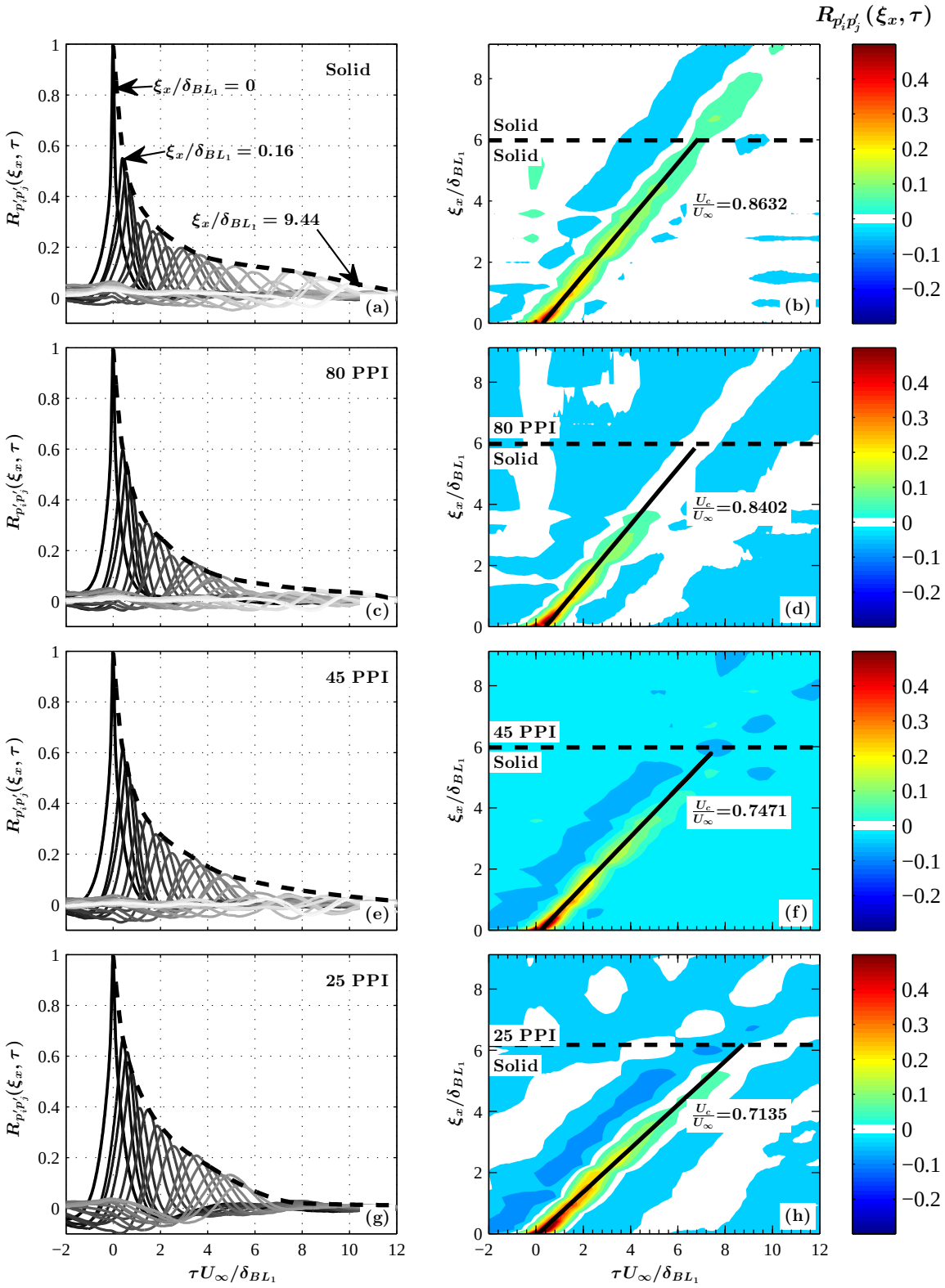

Figure 5.17: Space-time correlations of wall pressure fluctuations between the streamwise transducers as a function of $\tau U_\infty/\delta_{BL_1}$ and the corresponding autocorrelation envelops shown by dashed lines.

Table 5.4: Summary of the convection velocity calculated from the cross-correlation coefficient between the streamwise transducers ($p41$ used as the reference transducer) from the flat plate, for Re_L of 1.99×10^6.

Transducers	ξ_x, (mm)	ξ_x/δ_{BL_1}	U_c/U_∞			
			Solid	**80 PPI**	**45 PPI**	**25 PPI**
R_{p41p40}	3.37	0.13	0.3398	0.3297	0.3201	0.3201
R_{p41p35}	6.75	0.27	0.4757	0.4560	0.4560	0.4468
R_{p41p34}	10.12	0.39	0.5481	0.5222	0.5222	0.5062
R_{p41p33}	16.87	0.66	0.6464	0.6107	0.6040	0.5911
R_{p41p32}	23.62	0.93	0.6818	0.6476	0.6476	0.6216
R_{p41p31}	30.37	1.19	0.7132	0.6655	0.6655	0.6399
R_{p41p30}	37.12	1.46	0.7484	0.7009	0.6969	0.6813
R_{p41p29}	50.62	1.99	0.8706	0.8149	0.8070	0.7804
R_{p41p28}	57.37	2.26	0.7851	0.7330	0.7245	0.7055
R_{p41p27}	64.12	2.52	0.8098	0.7465	0.7360	0.7135
R_{p41p26}	70.87	2.79	0.8280	0.7652	0.7480	0.7224
R_{p41p25}	77.62	3.06	0.8326	0.7791	0.7427	0.7155
R_{p41p24}	84.37	3.22	0.8366	0.7669	0.7503	0.7228
R_{p41p23}	91.12	3.56	0.8568	0.7806	0.7569	0.7238
R_{p41p22}	97.87	3.85	0.8496	0.8341	0.7537	0.7167
R_{p41p21}	112.12	4.41	0.8534	0.8475	0.7197	0.6710
R_{p41p16}	132.12	5.20	0.8862	0.9086	0.7022	0.6834
R_{p41p11}	152.12	5.99	0.8722	0.8909	1.0461	0.6227
R_{p41p10}	168.92	6.65	0.8920	0.8949	1.2858	0.9568
R_{p41p9}	172.12	6.78	0.8874	0.8861	0.8959	0.9503
R_{p41p8}	198.92	7.83	0.8923	0.9188	0.8504	0.8560
R_{p41p3}	202.12	7.96	0.9005	0.9117	0.8410	0.8530
R_{p41p2}	228.92	9.01	0.8902	0.8902	0.8696	1.5876
R_{p41p1}	232.12	9.14	0.8843	0.8625	0.8609	1.4928
R_{p21p16}	20.00	0.79	0.7664	0.6720	0.6456	0.6095
R_{p16p11}	20.00	0.79	0.7664	0.6720	0.4765	0.4473
R_{p11p10}	16.80	0.66	0.7809	0.6839	0.3836	0.3836
R_{p8p3}	3.20	0.13	0.6354	0.5991	0.5376	0.5114
R_{p3p2}	26.80	1.06	0.7805	0.7227	0.3683	0.3946

As mentioned earlier in § 5.5.2.1, the product of time scale t_{ii} and the convection velocity U_c of the wall pressure fluctuations provides an estimation of the longitudinal length scale λ_x, shown in Fig. 5.18. The convection velocity U_c is calculated locally, based on the normalized cross-correlations between the pressure sensors *p3*, *p11*, *p16* and *p40* relative to the downstream reference transducer, *p8*, *p16*, *p21* and *p41*, respectively. The results show a fairly similar value of $\lambda_x \approx 3\delta_{BL_1} - 4\delta_{BL_1}$ for the solid surface over the test section area. The λ_x value estimated for the

porous 80 PPI surface at station *p16* (x/δ_{BL_1}= 5.2) is observed to be slightly higher than the solid. In the case of higher permeability surfaces, on the other hand, the results show that the length scale over the 45 PPI surface is reduced to $\lambda_x \approx 0.4\delta_{BL_1} - 1\delta_{BL_1}$ and more pronounced reduction of λ_x can be seen in the case of 25 PPI surface of about $0.1\delta_{BL_1} - 0.3\delta_{BL_1}$.

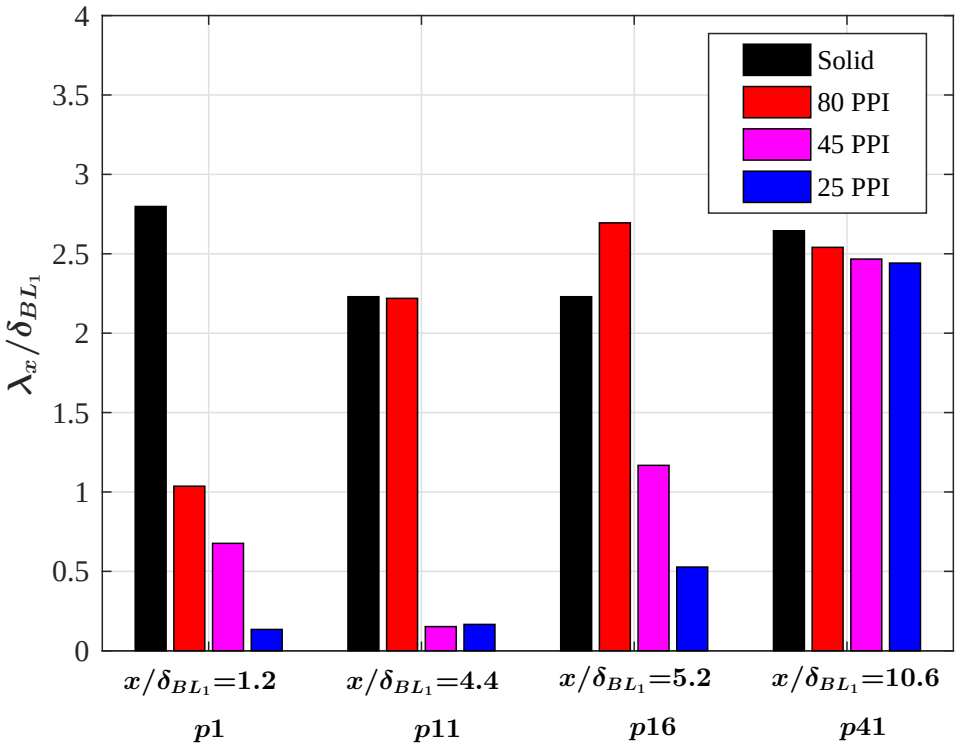

Figure 5.18: Non-dimensional longitudinal length scale λ_x/δ_{BL_1} of the wall pressure fluctuations.

5.5.3 Velocity autocorrelation analysis

The time-scales of the flow structures responsible for the most energetic velocity fluctuations are obtained from the velocity autocorrelation coefficient given as,

$$R_{u_i'u_i'}(\tau) = \frac{\overline{u_i'(y_i, t+\tau)u_i'(y_i, t)}}{u_{i_{rms}}'^2(y_i)}, \tag{5.11}$$

where u_i' is the velocity fluctuations from transducer i at position y_i, τ denotes the time delay between the pressure signals, $u_{i_{rms}}'^2$ is the root-mean-square of u_i' and the overbar denotes the time averaging.

Figure 5.19 shows the temporal autocorrelations of the velocity fluctuations, $R_{u_i'u_i'}(\tau)$, for transducers at different axial locations upstream from the trailing-edge, *i.e.* $x/\delta_{BL_1} = -16$ (*p41*),$x/\delta_{BL_1} = -21$ (*p16*), $x/\delta_{BL_1} = -22$ (*p11*) and $x/\delta_{BL_1} = -25$ (*p1*). The velocity fluctuations autocorrelation is taken at (a) a point near the surface (y/δ_{BL_1}=0.02) (b) at the locations further away from the plate surface (y/δ_{BL_1}=0.5) and (c) at y/δ_{BL_1}=0.75, where maximum difference in the energy cascade between the solid and porous surfaces are observed, as shown in Fig. 5.7. The presented data are plotted against the normalized time-delay $\tau^*=\tau\ U_\infty/\delta_{BL_1}$. As stated previously, the width of the autocorrelation can be related to the Taylor microscale in the area close to zero time delay, whereas the smallest scales of turbulence representing the the Kolmogorov scale is related to the regions very close to zero time delay [208].

In the case of the solid surface, the presence of flow structures with large time-scales (larger autocorrelation width) can be seen almost in the entire boundary layer region at all locations, with a smaller autocorrelation width observed in the mid-region ($y/\delta_{BL_1} = 0.5$) of the boundary layer thickness. In the case of porous surfaces, results have clearly shown that there is a significant changes in the autocorrelation width near-the-porous wall surface, especially for the higher permeability materials. In the case of porous 80 PPI surface, the autocorrelation width reduces compared to the solid case at the near-the-wall locations over the porous region, and becomes similar to the solid case at y/δ_{BL_1}=0.5 and 0.75 of the boundary layer region. In the case of porous 45 PPI and 25 PPI surfaces, a significant reduction of the temporal scales (autocorrelation width) can be seen at the near-the-porous wall surface and at the immediate downstream locations, which can be attributed to the presence of smaller scale structures over the surface. For the 25 PPI case, a slight hump of $R_{u_i'u_i'}(\tau)$ is present in the near surface region, associated with the existence of quasi-periodic hydrodynamic field. This is consistent with the wall pressure autocorrelation ($R_{p_i'p_i'}(\tau)$) results observed in Fig. 5.15, with much smaller periodicity scale. The $R_{u_i'u_i'}(\tau)$ results for the 45 PPI and 25 PPI surfaces are also seen to be reduced in the boundary layer region further away from the wall (y/δ_{BL_1}=0.5 and 0.75), indicating that the flow structures in the streamwise direction exhibits a smaller turbulence scale compared to that of the solid case. The changes in the flow structures and their time scale characteristics are analyzed quantitatively using Eq. 5.10 and the non-dimensionalized integral time scale t_{ii}^* of the velocity fluctuations are

shown in Fig. 5.20. Results show that the porous cases exhibit much shorter time scale compared to the solid case, over and after the test section region, especially in the near surface region.

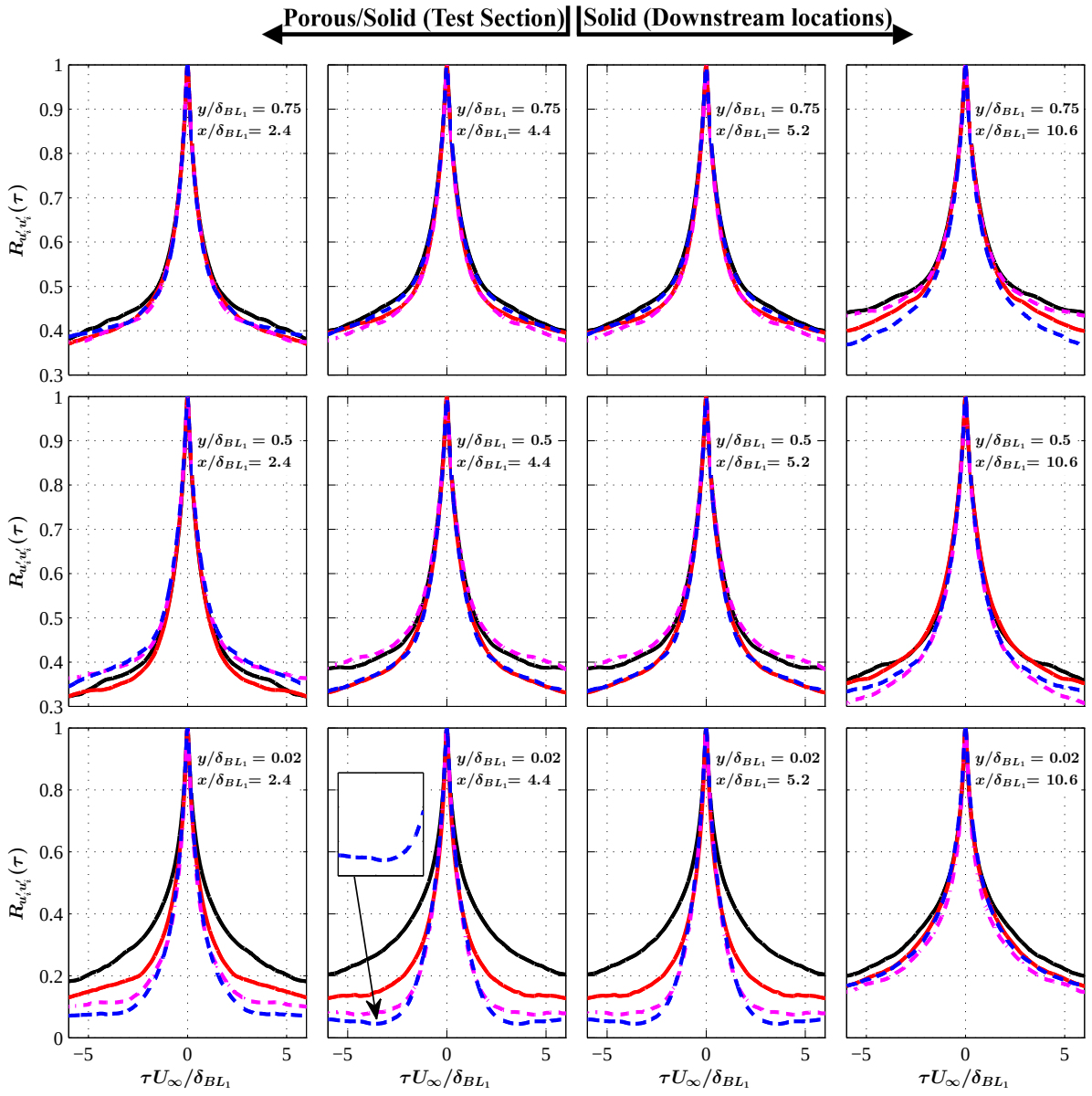

Figure 5.19: Autocorrelation of the velocity fluctuations as a function of $\tau^*=\tau\ U_\infty/\delta_{BL_1}$. *Solid(——), Porous 80 PPI(——), Porous 45 PPI(- · -), Porous 25 PPI(- - -).*

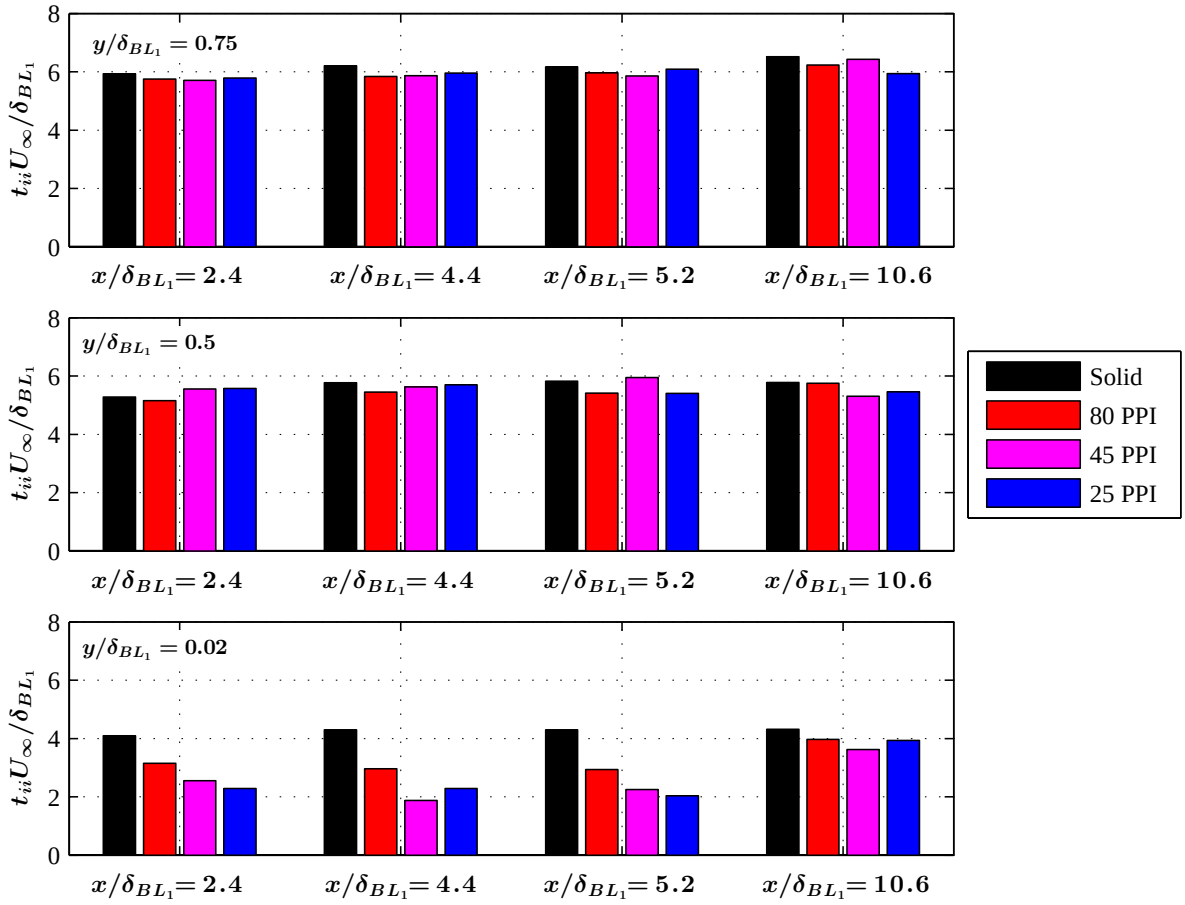

Figure 5.20: Non-dimensional integral time scale t^*_{ii} of the velocity fluctuations within the boundary layer thickness at different vertical locations above the plate. *Solid(—), Porous 80 PPI(—), Porous 45 PPI(- · -), Porous 25 PPI(- - -).*

The time scale t_{ii}, along with the velocity U_x at the point near the surface (y/δ_{BL_1}=0.02) and at the locations further away from the plate surface (y/δ_{BL_1}=0.5 and 0.75) can be used to estimate the velocity-based longitudinal (streamwise) length scale, $\lambda_{x_u} = U_x t_{ii}$, shown in Fig. 5.21. The results show a fairly similar value of $\lambda_x \approx 3\delta_{BL_1}$ for the solid surface over the test section area (x/δ_{BL_1}=2.4 and 4.4) at y/δ_{BL_1}=0.02. As shown in Fig.5.21, the use of porous surfaces can lead to a significant reduction of the longitudinal length-scale (λ_x) to about $2\delta_{BL_1} - 3\delta_{BL_1}$.

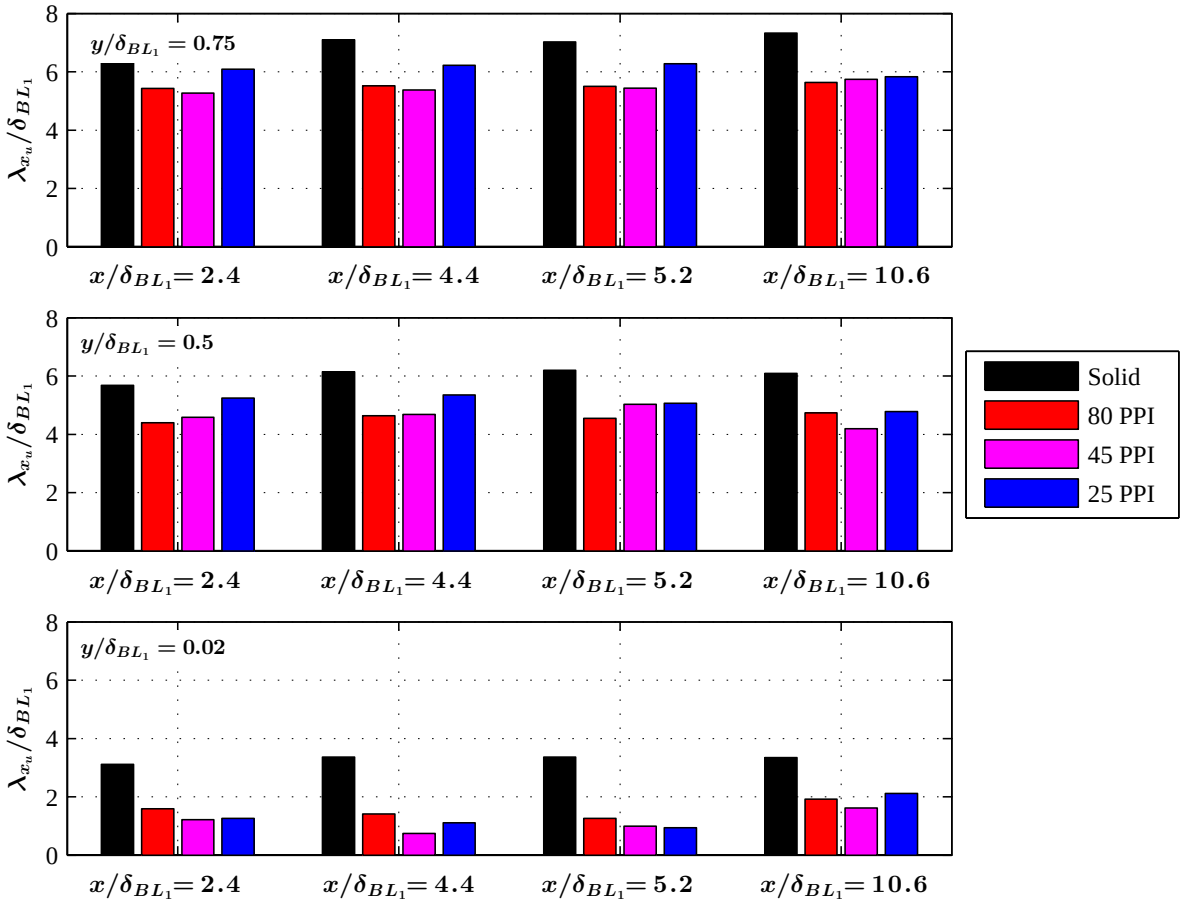

Figure 5.21: Non-dimensional velocity-based longitudinal length scale λ_{x_u}. *Solid(—), Porous 80 PPI(—), Porous 45 PPI(- -), Porous 25 PPI(- - -).*

5.5.4 Boundary layer velocity-pressure coherence analysis

The surface pressure and velocity fluctuations coherence studies at different locations within the boundary layer were conducted in order to characterize the spatial and temporal evolution of the coherent flow structures over the solid and porous surfaces, and their role on the pressure field exerted on the surface. Simultaneous boundary layer flow velocity and surface pressure measurements were performed at four locations, namely *p3*, *p11*, and *p16* for the flow velocity of 20 m/s. A single wire probe was used and the data had been collected between $y \approx 0$ mm and 120 mm normal to the wall at 63 locations above each transducer. The coherence between the velocity and surface pressure signals are analyzed using,

$$\gamma^2_{u'p'}(f,\xi_{y'}) = \frac{|\Phi(f,u',p')|^2}{|\Phi(f,u',u')||\Phi(f,p',p')|}, \tag{5.12}$$

where $\Phi(f,u',p')$ denotes the cross-power spectral density function between the velocity and pressure signals, and $\xi_{y'}$ is the distance of the hotwire probe from the surface.

Figure 5.22 presents the coherence between the flow velocity and the surface pressure fluctuations ($\gamma^2_{u'p'}$) measured at different distances, over the porous section ($p3$ (x/δ_{BL_1}=2.4) and $p11$ (x/δ_{BL_1}=4.4)) and downstream of the porous section ($p16$ (x/δ_{BL_1}=5.2) and $p41$ (x/δ_{BL_1}=10.6)) within the boundary layer region.

The results for the solid surface case show a strong coherence in the low frequency region within about 30 % of the boundary layer thickness ($0.05 \lesssim \xi_{y'}/\delta_{BL_1} \lesssim 0.45$). The velocity-pressure coherence, remains very similar for the solid case over all the locations measured (x/δ_{BL_1}=2.4 to 5.2), which is consistent with results observed in Figs. 5.6, 5.10, 5.13 and 5.14. The pressure-velocity coherence results for the case of porous surfaces are much more complex. The $\gamma^2_{u'p'}$ coherence results for the porous 80 PPI surface show a strong coherence trend at low frequencies, similar to that of the solid case, but with a much lower coherence intensity especially over the porous section (*p11*) and immediately downstream of the porous section (*p16*). The high coherence intensity area for the 80 PPI case is observed to have moved closer to the wall compared to that of the solid case, where the frictional forces are believed to dominate the velocity-pressure coherence, particularly at x/δ_{BL_1} = 2.4. This high coherence peak is, however, strongly suppressed at the downstream locations (x/δ_{BL_1}= 4.4 and 5.2).

The friction-induced high coherence region observed at the near-the-wall locations is found to exists at all porous surface cases, particularly for the cases with high surface roughness (Ra), *i.e.* 45 PPI and 25 PPI surfaces. In the case of the porous 45 PPI surface, a pronounced velocity-pressure coherence reduction can be seen over the porous section (*p11*), which occurs after a certain critical length of the porous surface. The results for the 25 PPI case, on the other hand, show a much weaker $\gamma^2_{u'p'}$ coherence, confined to the near-the-wall area at *p3*, *p11* and *p16*. It can also be seen that a broadband area of high velocity-pressure coherence appears between f = 100 to 400 Hz at *p3* and *p11* (over the porous surface), which overlaps the area of low frequency hump observed in the wall pressure spectra (Fig. 5.10). This broadband region is confined within a

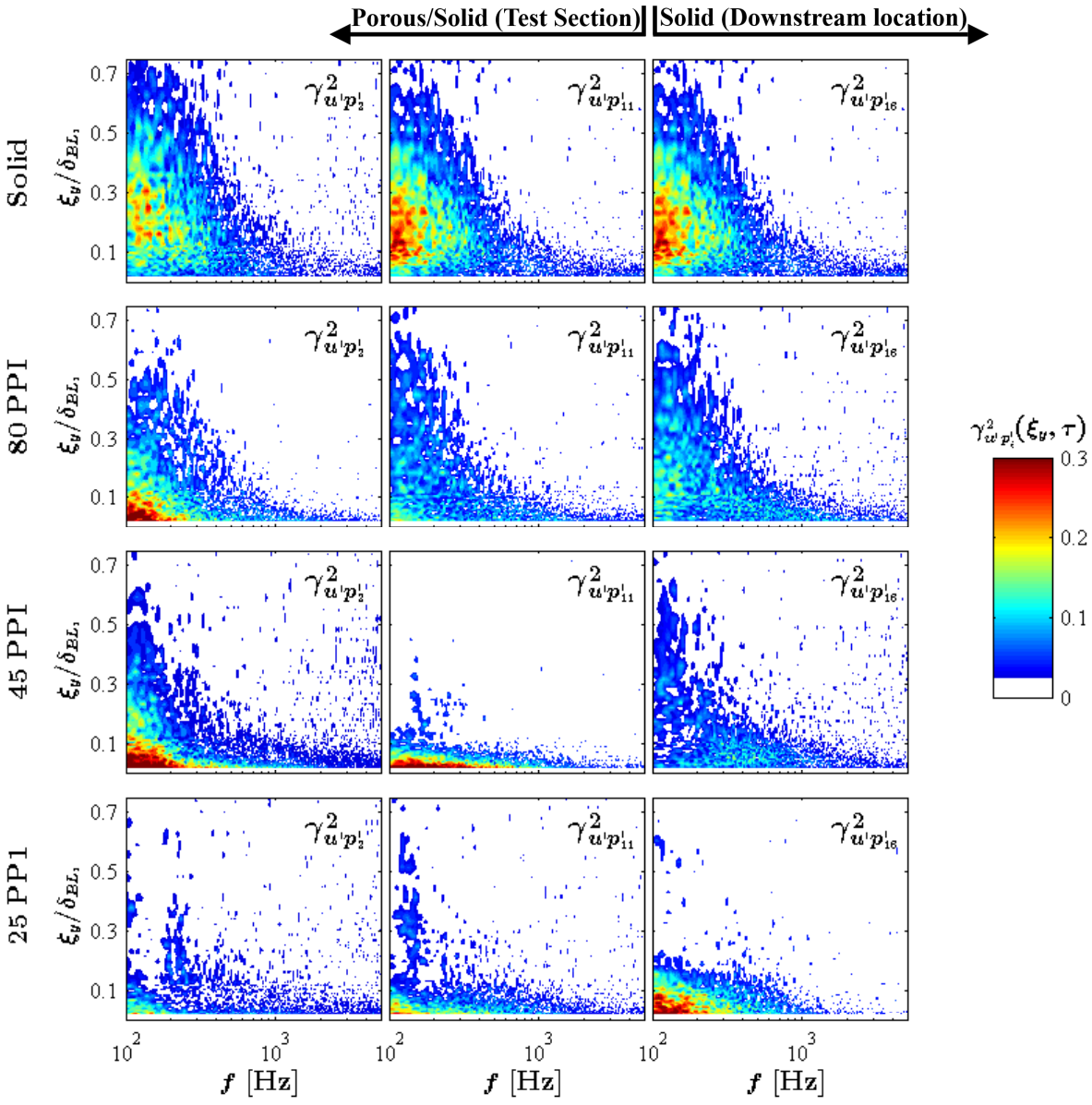

Figure 5.22: Velocity-pressure coherence, $\gamma^2_{u'p'_i}$ at locations *p3*, *p11* and *p16* for solid, porous 80 PPI, porous 45 PPI and porous 25 PPI surfaces.

spatial domain over the porous surface and dissipates quickly at the downstream locations. As mentioned earlier, this is believed to be due to the emergence of a hydrodynamic field inside the porous medium, which takes place only in the case of highly permeable porous materials, *i.e.* 45 PPI and 25 PPI surfaces. As described earlier in § 5.5.2.1, the emergence of this hydrodynamic field requires a long enough porous section to enable the flow penetration into the porous medium.

The effects of the porous section length on the emergence of the internal hydrodynamic field will be shown and discussed in the next section.

5.6 Flow penetration critical length

The results in § 5.2 and § 5.3 have shown that the use of a relatively high permeable substrate can lead to significant changes to the whole energy cascade of the boundary layer, reduction in the surface pressure fluctuations at high frequencies, and the emergence of a strong hydrodynamic field inside the porous medium. The velocity-pressure correlation and coherence analysis in § 5.5 demonstrated that the coherence and the length-scales of the spanwise flow structures can be significantly reduced over the porous surface. The surface pressure spatio-temporal correlation analysis, on the other hand, showed that a quasi-periodic hydrodynamic field may emerge within porous media with high permeability and that the spanwise length-scale of the convected flow structures can reduce significantly.

It is clear from the results that the boundary layer flow penetration into the porous medium has a strong influence on the above-mentioned effects. Hence, in order to allow a proper flow penetration, it is necessary for the flow to remain in contact with the porous medium over a long enough porous section. All the results presented previously were obtained for porous sections with a streamwise length of $L_{px} = 4.8\delta_{BL_1}$ (L_{px}=120 mm). Further experiments have been conducted for the highly permeable porous materials (45 PPI and 25 PPI) with different streamwise lengths L_p with the incremental lengths of 5 mm (0.2 δ_{BL_1}), to investigate the effect of the porous section length on the above-mentioned phenomena. The shorter porous inserts are placed toward the end of the cavity section, while the upstream cavity between $x = 0$ and the porous section is filled with a solid plate of appropriate length and depth of 20 mm. For clarity, the length of the new porous sections is defined as L_{px} in this section. The results are only presented for some selected streamwise lengths, namely L_{px}/δ_{BL_1}=4.8 (120 mm), 3.2 (80 mm), 1.6 (40 mm), 0.8 (20 mm) and 0.6 (15 mm), for the sake of brevity. The effect of the porous section length is analyzed using the power spectral density of the wall surface pressure results (ϕ_{pp}) at x/δ_{BL_1}= 4.4 *(p11)* for the 45 PPI and 25 PPI materials, as presented in Fig. 5.23.

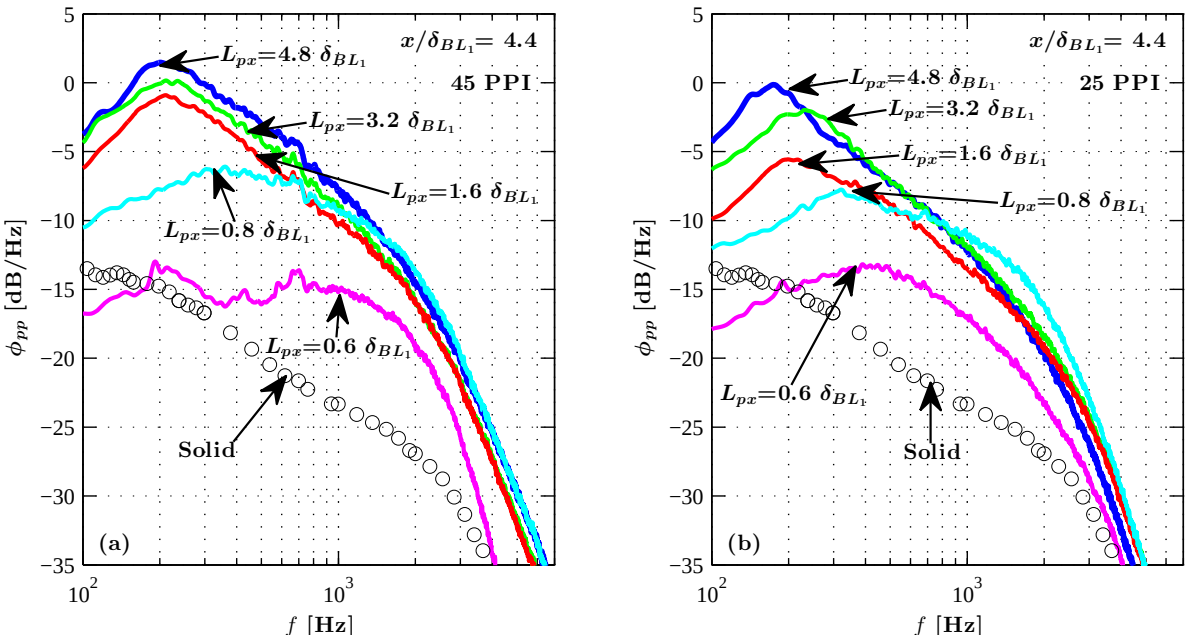

Figure 5.23: Wall pressure fluctuations with different porous 45 PPI and 25 PPI lengths at x/δ_{BL_1}= 4.4 (*p11*).

Results are presented for five porous section lengths and also for the solid surface (circle marker). It is observed that the emergence of the localized broadband hump, previously shown in Figs. 5.10 and 5.15, is very sensitive to the length of the porous section. It can be seen clearly that the broadband hump emerges only for the porous sections with a streamwise length of $L_{px} \geqslant 1.6\delta_{BL_1}$. It is also apparent that the frequency associated with the broadband hump changes with the porous section length, and that the localized broadband hump shifts to higher frequencies with decreasing the porous section length (L_{px}).

Finally, a thorough study on the surface pressure autocorrelation and the velocity-pressure coherence have been carried out to investigate and better understand the emergence of the internal hydrodynamic field and its relationship with the porous treatment length (L_{px}). The autocorrelation and the velocity-pressure coherence ($\gamma^2_{u'p'}$) results for the *p11* transducer (x/δ_{BL_1}= 4.4), where a significant effect on the boundary layer flow-porous interaction is observed, are shown in Figs. 5.24 and 5.25 for the 45 PPI and 25 PPI cases, respectively. Results are presented for different porous treatment lengths. The surface pressure autocorrelation results for the solid surface (circles) are also given for comparison. The autocorrelation results for all the porous

surfaces confirm again that there exists a critical length for the emergence of the quasi-periodic hydrodynamic field within the porous medium. The quasi-periodic internal hydrodynamic field for the long porous treatments for both the 45 PPI and 25 PPI cases, particularly for the cases with $L_{px}/\delta_{BL_1} > 1.6$, reveals itself as (a) a fast decaying oscillation within $1.5 < \left|\tau\ U_\infty/\delta_{BL_1}\right| < 5$ in the pressure autocorrelation results, in agreement with the results observed in Fig. 5.10 and (b) a high coherence broadband region near the surface in the pressure-velocity coherence results. The velocity-pressure coherence results also confirm the suppression of the coherent flow structures and the emergence of a broadband hump for the long porous surfaces.

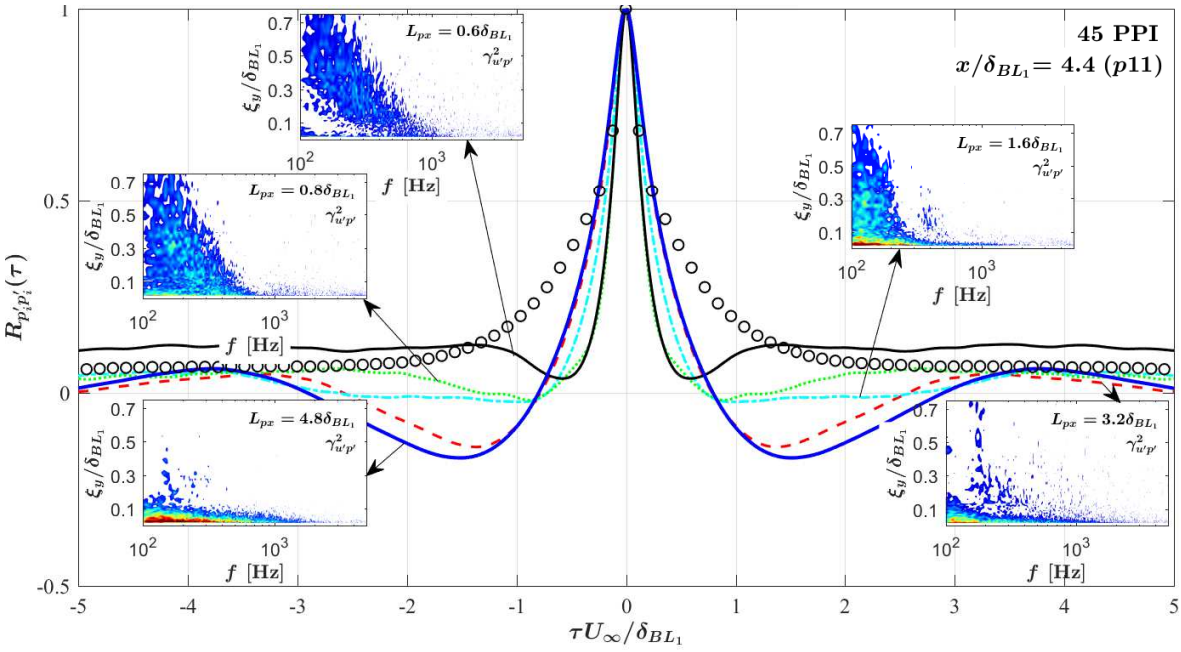

Figure 5.24: Autocorrelation of the wall pressure fluctuations with different porous 45 PPI surface lengths and its velocity-pressure coherence ($\gamma^2_{u'p'}$) results at x/δ_{BL_1}= 4.4 (*p11*).

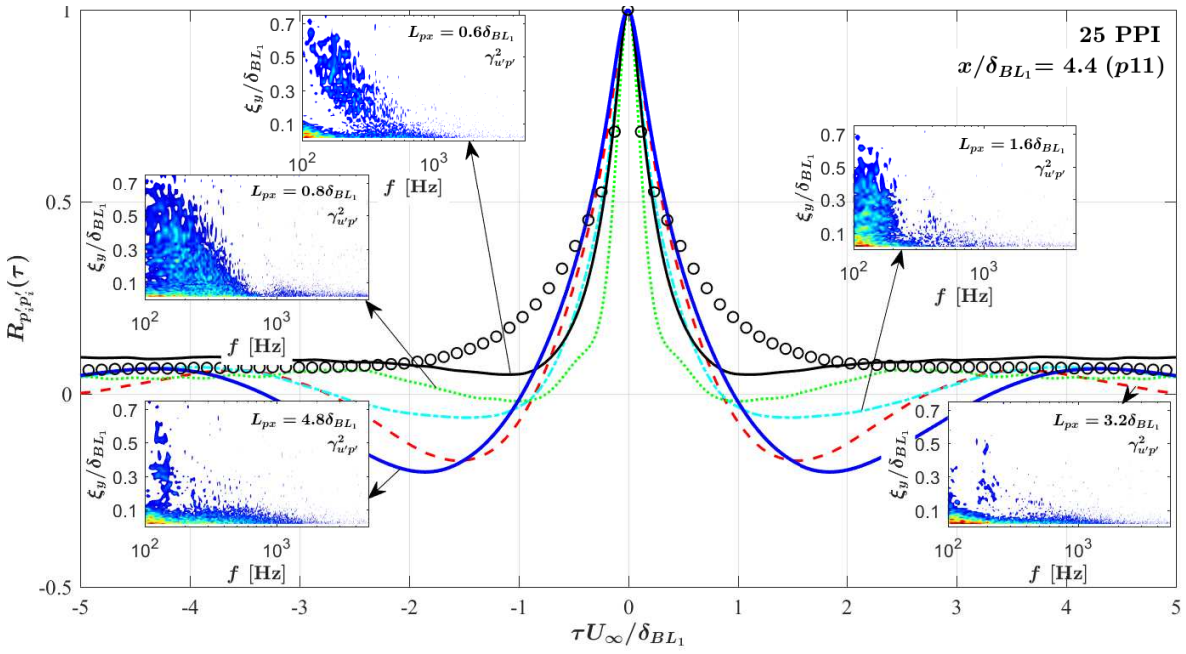

Figure 5.25: Autocorrelation of the wall pressure fluctuations with different porous 25 PPI surface lengths and its velocity-pressure coherence ($\gamma^2_{u'p'}$) results at x/δ_{BL_1}= 4.4 (*p11*).

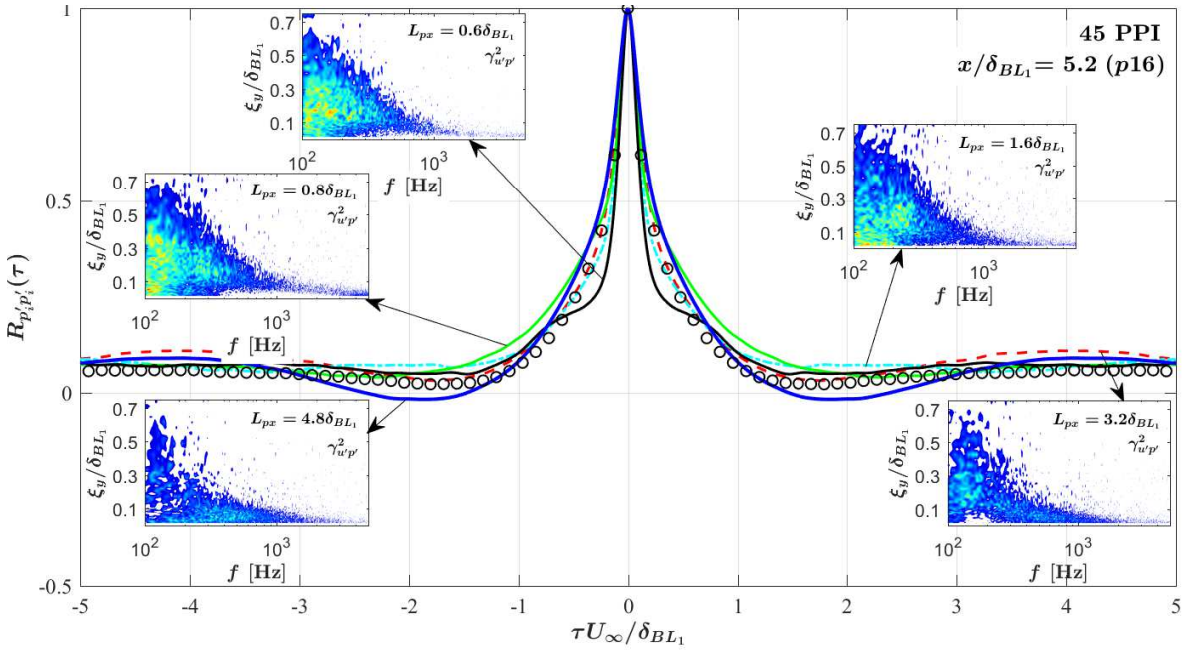

Figure 5.26: Autocorrelation of the wall pressure fluctuations with different porous 45 PPI surface lengths and its velocity-pressure coherence ($\gamma^2_{u'p'}$) results at x/δ_{BL_1}= 5.2 (*p16*).

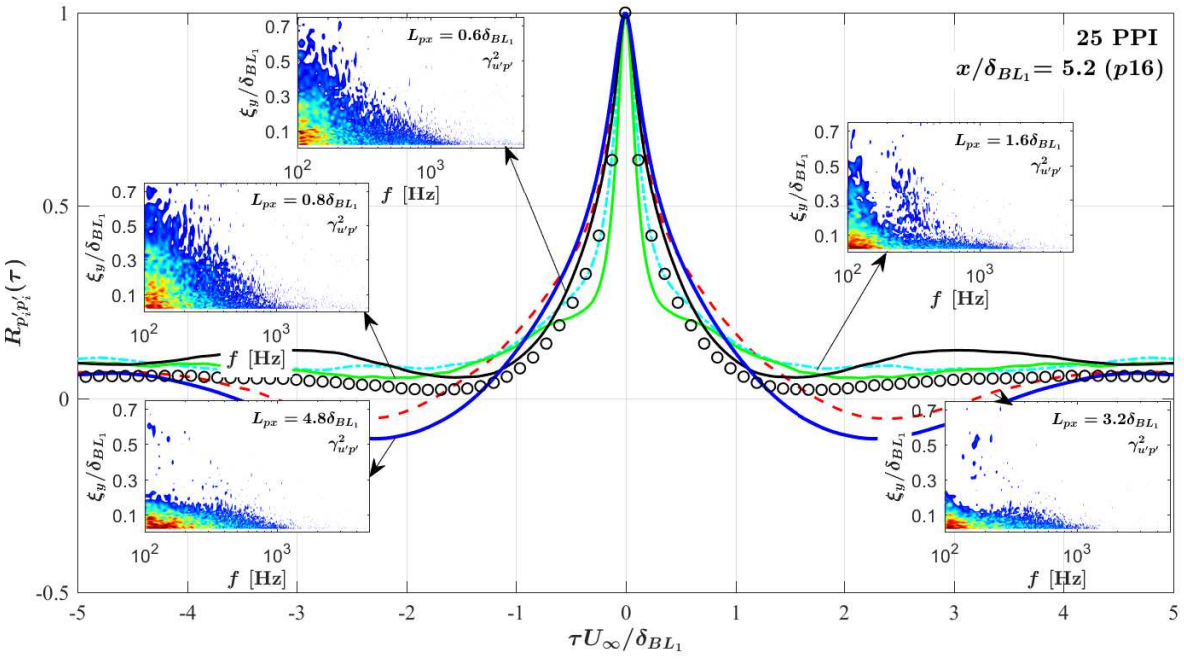

Figure 5.27: Autocorrelation of the wall pressure fluctuations with different porous 25 PPI surface lengths and its velocity-pressure coherence ($\gamma^2_{u'p'}$) results at x/δ_{BL_1}= 5.2 ($p16$).

5.7 Summary

This chapter presented the results of an experimental investigation into the turbulent boundary layer flow interaction with a rough permeable wall on a long flat plate. Despite its simplicity, the experimental test-rig used in this study enabled a large variety of different flow-porous interaction studies, such as the surface roughness, flow penetration, porous-flow viscous interaction and hydrodynamic absorption effects of the porous media. The analysis leads to the following main conclusions.

i. Results have shown that in the case of less permeable surfaces (80 PPI and 45 PPI), the boundary layer thickness, displacement thickness and momentum thickness increase compared to the baseline case (solid surface) at each measurement locations, however the boundary layer thickness for the 25 PPI surface is found to be the lowest compared to the other cases. This is due to the material being very permeable and that the boundary layer

more able to penetrate and sink into the porous media, which causes a reduction in the boundary layer thickness. The use of porous surface treatments also lead to an increase in the energy content of the velocity fluctuations near the surface and a more rapid energy cascade within the boundary layer.

ii. The surface pressure PSD results have also shown that the porous surface treatment causes an increase in the overall pressure exerted on the surface, especially at the locations over the porous surface and right after the porous test section. The results also show a reduction of the surface pressure PSD over the high frequency range at the locations downstream of the porous section, about *i.e.* $5.4\delta_{BL_1}$ after the porous section.

iii. The near-field studies have shown that the penetration of the boundary layer flow into the highly permeable porous media can generate an internal hydrodynamic field, which can, in turn, reduces the frequency-energy content of the large boundary layer coherent structures and their lateral correlation length. Results have also shown that a relatively long porous section is required to enable flow penetration inside the porous substrate. The use of a relatively long porous section can lead to the emergence of a quasi-periodic flow recirculation region inside the high permeable porous section, which then results in a fast-decaying broadband hump.

iv. It has been observed that the existence of the quasi-periodic hydrodynamic field inside the porous medium and the reduction in the velocity-pressure coherence over the porous surface are inter-related and dependent on the effective length of the porous section.

Finally, it is worth noticing that the findings on the use of a rough and permeable surface have direct implications on the complex flow-porous interaction phenomena, potentially leading to the reduction of generated noise, whose understanding will require more in-depth studies.

CHAPTER 6

BLUNTNESS FLOW AND NOISE CONTROL USING POROUS TREATMENTS

The results presented in Chapter 5 focused mainly on the mechanisms involved in the boundary layer flow interaction and the associated noise generation with different porous surfaces. The results showed that the porous surface treatment is capable of altering the boundary layer profile and that it can significantly reduce the surface pressure fluctuations at high-frequency range. It has also been observed that a noticeable reduction in the spanwise coherence and the length-scales of the flow structures can be achieved by using the porous surfaces. In this chapter, we will further investigate the application of porous treatments for blunt trailing edges, based on the findings in Chapter 5. This chapter outlines a comprehensive and systematic experimental investigation and studies various aspects of flow-porous interaction, such as scrubbing effects, break-up of boundary layer coherent structures, flow penetration, internal hydrodynamic field, flow discharge and vortex shedding suppression. To do so, a flat plate with blunt trailing-edge was chosen as it involves some very interesting complex physics and that a trailing-edge porous treatment can alter its aerodynamic and aeroacoustic performance in different ways. The chapter is organized as follows. The experimental setup, including the measurement systems and the model configuration is described in § 6.1. The effect of the porous section on the aerodynamic forces, boundary layer and wake development will be discussed

in § 6.2. A detailed analysis of the turbulent boundary layer correlation and coherence studies is provided in § 6.3. As before, a hypotheses will also be presented with regard to the formation of an internal recirculation zone inside the porous medium. Section 6.4 further discusses the formation of the internal hydrodynamic field and shows its dependency on the porous-flow interaction length. The far-field measurement from the blunt flat plate test-rig and the effect of the porous treatment on the radiated noise is detailed in § 6.5. Finally, § 6.6 concludes the chapter and summarizes the findings concerning the application of porous materials for aerodynamic and aeroacoustic purposes.

6.1 Measurement setup

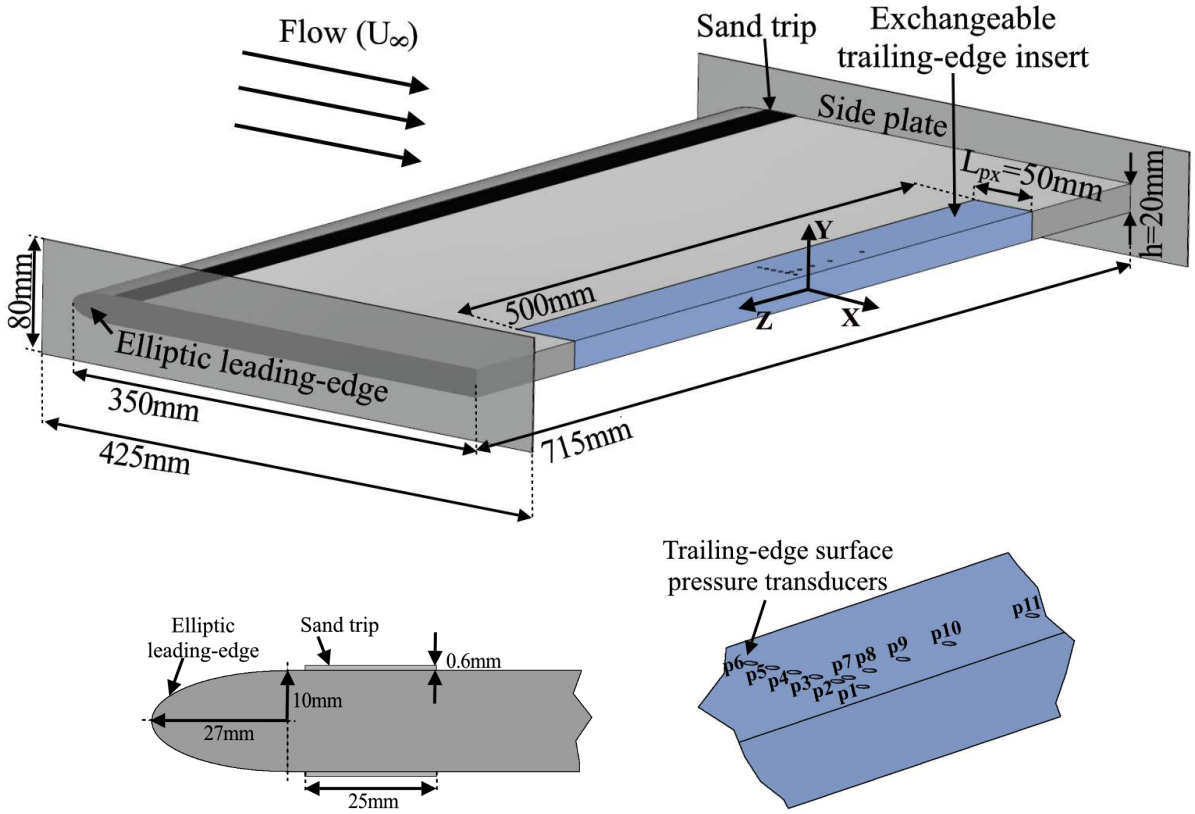

Figure 6.1: (a) The schematic of a flat-plate with an elliptical leading-edge and exchangeable blunt trailing-edge. (b) The geometry of the elliptic leading-edge. (c) The position of the trailing-edge pressure transducer array.

The flow interaction with a blunt trailing-edge poses some very interesting and challenging questions, such as flow acceleration, vortex shedding and flow-induced noise and vibration, etc., and has therefore been chosen for this study. The aerodynamic and flow measurements have been performed for a blunt flat plate with solid and porous trailing-edges in the open-jet and the low turbulence wind tunnel. Results have been obtained for flow velocities of up to 26 m/s, corresponding to the chord-based Reynolds number of 6.0×10^5, with incoming flow turbulence intensity of below 0.5%. To properly understand the effect of the trailing-edge properties (*i.e.* solid and porous), various measurements have been performed, such as the aerodynamic loads, boundary layer growth, wake development and surface pressure fluctuations. The schematic of the flat plate test-rig is shown in Fig. 6.1. The plate has a fore-body length of L_x = 350 mm, spanwise length of L_z = 715 mm and thickness of h =20 mm. The corresponding aspect ratio of the flat plate is $AR_x = L_x/h$ = 17.5. The model in the open-jet wind tunnel gives a blockage ratio of 1.8%, which is expected to have a negligible effect on the results obtained [209]. The flat plate has an elliptical leading-edge with a semi-minor axis of 10 mm and a semi-major axis of 27 mm in order to prevent strong adverse pressure gradient and large leading-edge flow separation. To ensure the presence of vortex shedding, the ratio of the trailing-edge height and the boundary layer displacement thickness should obey the $h/\delta^* > 0.3$ criterion, where δ^* is the boundary layer displacement thickness at the trailing-edge [210]. The bluntness ratio was found to be significantly larger than 0.3, ensuring the existence of vortex shedding. In order to reach a well-developed turbulent flow before the trailing-edge section, a 25 mm wide sand trip was applied just aft of the leading-edge at x=30 mm with a thickness of approximately 0.6 mm and grit roughness of 80, corresponding to the average roughness of Ra=1.8 μm [211].

The bluntness ratio (h/δ^*) was found to be significantly larger than 0.3 in our experiments, ensuring the existence of vortex shedding. In order to reach a well-developed turbulent flow before the trailing-edge section, a 25 mm wide sand trip was applied just aft of the leading-edge at x=30 mm with a thickness of approximately 0.6 mm and grit roughness of 80. The trip was placed on both sides of the plate. The trailing-edge part of the plate is made as an insert, with a width (L_{px}) and span-length of 50 mm and 500 mm, respectively, to enable tests with various trailing-edges, namely solid, porous 80 PPI and porous 25 PPI, see Fig. 6.1. To ensure

two-dimensional flow over the span, rectangular side-plates of dimensions 425 mm by 80 mm, with sharpened leading-edges with an angle of 20° were mounted on the test apparatus. The side-plates extend approximately $1.25h$ upstream of the leading-edge and $2.5h$ downstream of the trailing-edge. The x-, y- and z-coordinates of the blunt trailing-edge is taken as zero at the centre of the trailing-edge. The y' axis is introduced on the top surface of the plate, defined as $y' = y - h/2 = 0$, and is used to define the boundary layer axis in § 6.2. The separation distance used in discussions concerning the pressure and velocity coherence and correlation studies in § 6.3.3 is denoted by ξ_x, ξ_y and ξ_z.

Two metal foams with the pores per inch (PPI) of 25 and 80 have been chosen for this study, with the porosity values of 90.92% and 74.76% and permeability values of $8.2\times\ 10^{-8}\ m^2$ and $7.7\times\ 10^{-9}\ m^2$, respectively. The average roughness (Ra) values for porous 25 PPI and 80 PPI are found to be 1922 μm and 212 μm, respectively. The boundary layer and wake flow measurements were carried out using single-wire Dantec 55P16 and cross hot-wire Dantec 55P51 probes. The hotwire measurements were taken for 15 seconds at each location. The transducers are arranged in the form of an L-shaped array in the streamwise and spanwise directions (see Fig. 6.1). The transducers located in the spanwise direction will be used for the calculation of the spanwise coherence and length-scale of boundary layer structures, while the transducers employed in the streamwise direction provide information on the evolution of the turbulence structures as they move downstream towards the trailing-edge and their convection velocity. The detailed locations of the pressure transducers on the detachable trailing-edge part are provided in Fig. 6.1 and summarized in Table 6.1. The pressure transducers, $p2$ to $p6$, are equally spaced in the streamwise direction, while the transducers, $p7$ to $p11$, are placed 14 mm upstream of the trailing-edge and are spaced unequally in the spanwise direction to maximize the number of correlation distance combinations (ξ_z) between the transducers in order to obtain more accurate results over the whole frequency range.

Table 6.1: Positions of the pinhole transducers upstream of the trailing-edge

Position	**Transducers Number**	**Axial locations,** $x\ (mm)$	**Transverse locations,** $z\ (mm)$
Streamwise	$p1, p2, p3,$ $p4, p5, p6$	-7, -14, -20, -26, -32, -38	0.0
Spanwise	$p7, p8, p9,$ $p10, p11$	-14	4.6, 13.4, 27.4, 46.6, 81.4

6.2 Aerodynamic and flow-field analysis

6.2.1 Steady drag coefficient

A basic but fundamental understanding of the problem can be gained by studying the aerodynamic forces acting on the plate. The steady aerodynamic force measurement of the blunt flat plate with solid and porous trailing-edges are presented and explained in this subsection. The experiments covered a wide range of flow velocities, U_∞=6 m/s to U_∞=26 m/s, corresponding to the Reynolds numbers of $Re_{L_x} = 1.4 \times 10^5$ to 6.0×10^5. The results presented in Fig. 6.2 show the drag coefficient (C_D) of the plate against the Reynolds number for the solid and porous trailing-edges. The drag coefficient (C_D) is calculated using Eq. 3.1. The vertical error bars centered on the C_D mean values denote the estimated C_D uncertainty with 95 % confidence level.

Results have shown that the use of porous treatments can significantly reduce the drag force. The results for the solid case have shown that the drag coefficient experiences a sudden sharp drop at low Re_{L_x} and gradually reaches an area of almost Re_{L_x} independency at higher Reynolds numbers. The sudden decrease in the drag coefficient behaviour at low Reynolds number and the variation in drag, covering an almost one decade of Re_{L_x}, can potentially be due to the laminar to turbulence transition phenomena [212]. This, however, needs further experimental and numerical investigations. It can also be seen that the use of 25 PPI porous material leads to the reduction of C_D by up to 16% compared to the solid case. The trends observed from the solid and 80 PPI porous cases are almost identical at high Reynolds numbers, indicating that the boundary layer and wake flows at high Reynolds numbers behave similarly in the case of 80 PPI and solid trailing-edges. This behaviour can be explained by the fact that for the porous

medium with low permeability, a longer flow and porous-surface interaction is needed to enable flow penetration into the porous medium. Therefore, the porous materials with high PPI and low permeability behave more or less like the solid case. The significant reduction obtained for the case of 25 PPI can be attributed to the flow penetration into the pores, flow discharge into the wake and attenuation of the vortex shedding from the trailing-edge, which will be further discussed in § 6.2.2 and § 6.2.4.

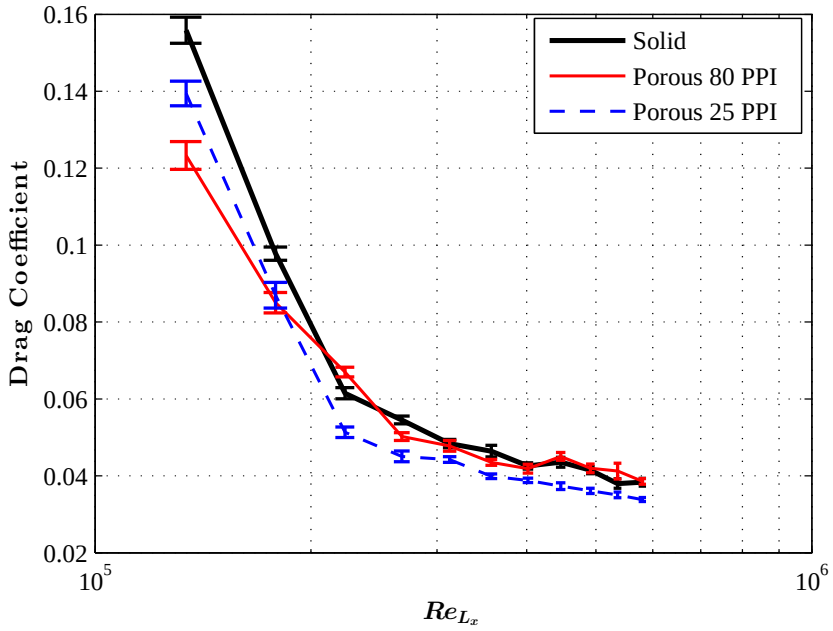

Figure 6.2: The measured drag coefficient for the flat plate with different trailing-edges.

6.2.2 Trailing-edge flow-field

6.2.2.1 Flow pattern using PIV

In order to better understand the effects of the porous trailing-edge on the boundary layer structures, wake development and vortex shedding, measurements have been performed using PIV and hot-wire anemometry at the flow velocity of U_∞=20 m/s, corresponding to the Reynolds number of $Re_{L_x} = 4.6 \cdot 10^5$. Figure 6.4 illustrates the time-averaged normalized streamwise (U) and vertical (V) velocity components for the blunt trailing-edge with and without porous treatment. A dual-cavity laser of 200 mJ Nd:YAG with a wavelength of 532 nm was used to

produce 1 mm laser sheet thickness with the time interval between each snapshot of 25 μs and repetition rate of 15 Hz to obtain a maximum amount of particles in the interrogation window. A total number of 1600 image pairs were captured using a FlowSense 4 MP CCD camera with a resolution of 2072 x 2072 pixels for each case and used to compute the statistical turbulent flow quantities. The measurements were made for a field-view of 158 mm × 158 mm, which corresponds to a domain of $7.9h$ × $7.9h$ in the streamwise and vertical directions, as shown schematically in Fig. 6.3. The measurements iterative process yields a grid correlation window of 16 × 16 pixels with an overlap of 50%, resulting in a facial vector spacing of 0.61 mm, corresponding to the plate thickness of $0.031h$.

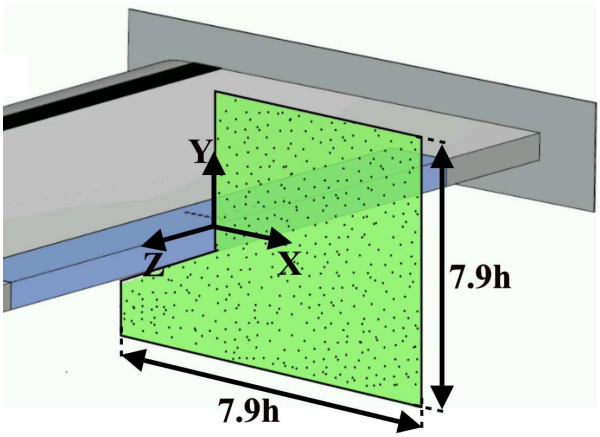

Figure 6.3: PIV measurement plane.

The categorization of vortex shedding regimes in the wake velocity profile, specifically in the near wake flow, can be assessed by looking into the vortex formation length and the vortex cores (mean recirculation) region. The non-dimensionalized vortex formation length (L_f/h) is defined as the distance between the trailing-edge and the end of the vortex region, where the maximum streamwise velocity fluctuations are obtained. The non-dimensionalized vortex cores region (x_{vc}/h), on the other hand, corresponds to the position of the recirculation core [213]. The respective L_f/h and x_{vc}/h locations are illustrated in Fig. 6.4(a). Results in Figs. 6.4(a) and 6.4(b) show that the flow recirculation behind the solid trailing-edge occurs within $0.05 \lesssim x/h \lesssim 1.04$, with a pair of counter-rotating vortices formed in the very near wake with identical symmetric vortex core structure with respect to the centerline of the trailing-edge. The results for the porous

medium with low permeability (80 PPI) show a small shift in the location of the recirculation region, see Figs. 6.4(c) and 6.4(d), with the recirculation occurring within $0.15 \lesssim x/h \lesssim 1.06$. It can also be seen that the counter-rotating vortices formed are nearly symmetric, with a slight shift between the two vortex cores. The use of the porous 25 PPI with higher permeability value, however, leads to significant changes to the vortex core structure and the location of the recirculation zone. It can be seen in Figs. 6.4(e) and 6.4(f) that the recirculation area has moved further downstream to $0.5 \lesssim x/h \lesssim 1.8$. The ($L_f/h$, x_{vc}/h) values for the solid, porous 80 PPI and porous 25 PPI trailing-edges have been found to be (1.04, 1.06) and (1.8, 0.4) and (0.64, 1.2), respectively, indicating a significant delay in the formation of the vortex shedding due to interaction of the flow with the porous treatment. The delay in the formation of the vortex shedding is consistent with the observations in Fig. 6.2, *i.e.* drag reduction using porous treatment. A similar observation was made by Bearman and Tombazis [214], where they had shown that the use of wavy blunt trailing-edge can lead to changes to the length of the recirculation region (L_f), recovery of the base pressure and reduction of drag.

Another interesting feature observed in Fig. 6.4 is the emergence of an area of flow acceleration over the trailing-edge region due to the pressure difference at the trailing-edge. This effect can also be primarily related to the development of the core of a vortex, which in general imposed by a minimum pressure (low-pressure vortex). The low pressure at the vortex core against the high pressure outside the vortex core creates a partial vacuum (suction), forcing the flow to accelerate near the trailing-edge. The flow acceleration region of the U-components can be seen within $-1 \lesssim x/h \lesssim 0.5$ and $-1.3 \lesssim y/h \lesssim -0.5$ for the case of solid trailing-edge (Fig. 6.4(a)), followed by a rapid vertical flow movement, *i.e.* velocity overshoot near the trailing-edge, leading to the flow recirculation in the near wake region. Similar observations can be made in the case of porous 80 PPI (Fig. 6.4(c)) with a broader flow acceleration region and less strong compared to that of the solid case. However, unlike the solid trailing-edge, porous 25 PPI exhibits a much more streamlined behaviour, with a much lower flow acceleration upstream of the trailing-edge and reduced velocity overshoot over the blunt trailing-edge. Results have also shown that the acceleration region of the V-component for the porous 25 PPI in the wake has moved even further downstream compared to the solid and 80 PPI cases. The significant changes observed for the

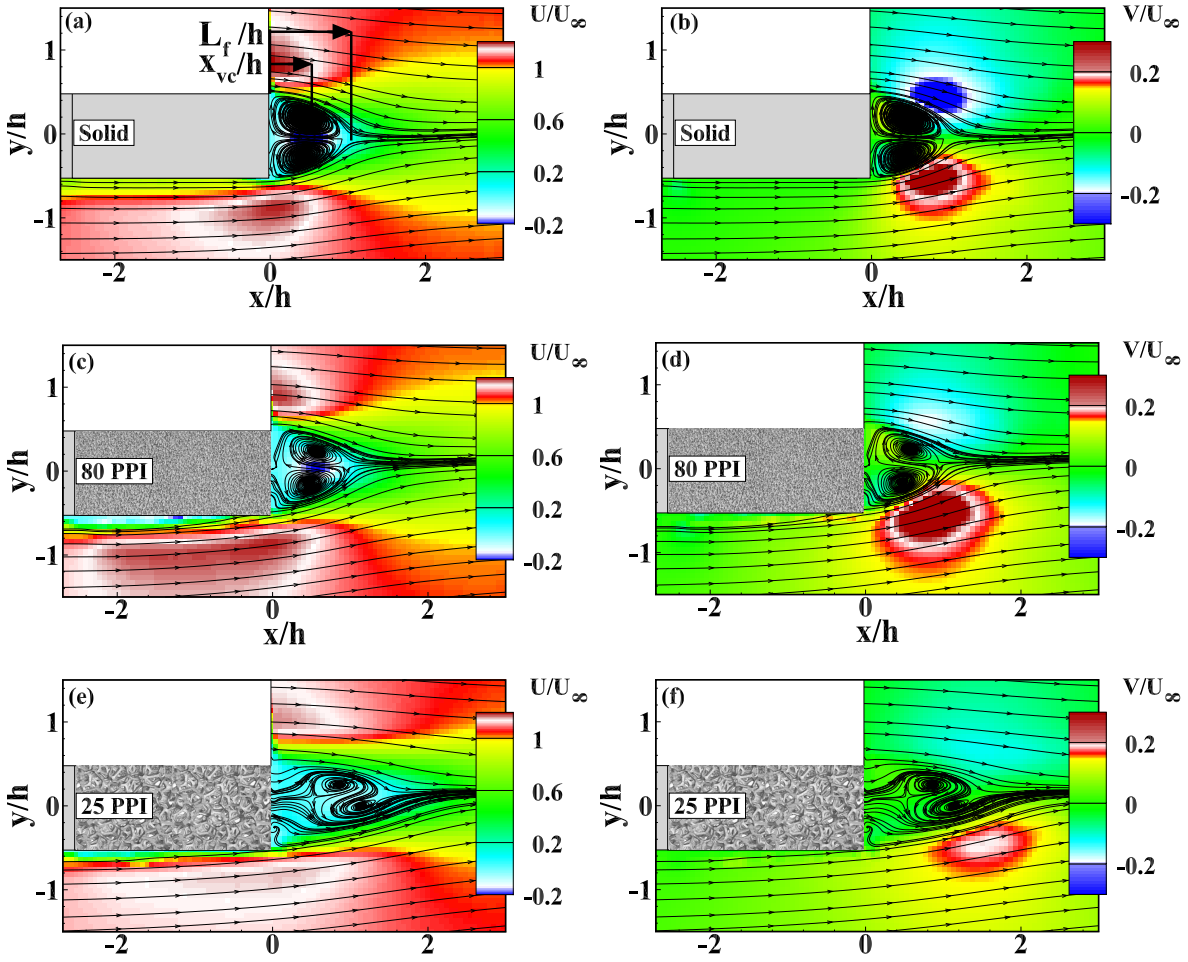

Figure 6.4: Time-averaged flow pattern for normalized streamwise (U) and vertical (V) velocity components for solid (a and b), porous 80 PPI (c and d) and 25 PPI (e and f).

porous 25 PPI trailing-edge is believed to be due to the penetration of the boundary flow into the porous medium, creation of an internal hydrodynamic field and discharge of the flow into the wake region. These phenomena will be further discussed in § 6.2.7 and § 6.2.8.

6.2.2.2 Boundary layer flow structures

Figure 6.6 presents the mean and root-mean-square (rms) boundary layer velocity profiles along the boundary layer (BL) lines shown in Fig. 6.5. The measurements were conducted at the flow velocity of U_∞=20 m/s using a single hot-wire probe and the data have been collected between

$y'/h \approx 0$ and y'/h = 2.5 at 35 stations above the plate for each line, where $y' = 0$ is the plate top surface, as defined in § 6.1. The distance from the surface (y'-axis) has been normalized by the boundary layer thickness at BL_1, x/h=-2.6, upstream of the exchangeable trailing-edge part. Note that at BL_1, the flow velocity approaches to zero at the solid surface, *i.e.* the no-slip condition, which will not be the case over the porous surface due to the flow penetration into the porous medium [205]. The boundary layer velocity results show that there is an increase in the velocity gradient at the wall from BL_1 to BL_4, which implies the presence of a favorable pressure gradient flow upstream of the trailing-edge, which will eventually cause strong flow acceleration over the trailing-edge [215]. The velocity profiles for the solid trailing-edge downstream of BL_1 gradually deviate from that of a standard turbulent boundary layer profile as a result of the bluntness effects, with a clear velocity overshoot, signifying the presence of flow acceleration in the trailing-edge region. The peak of the velocity overshoot occurs at y'/δ_{BL_1} = 1 and does not change greatly with x/h. The rms velocity results clearly show that the solid trailing-edge exhibits a larger level of velocity fluctuations than the porous cases, almost in the whole boundary layer region. In the case of the 80 PPI trailing-edge, the boundary layer profiles observed at all the measurement locations are very similar to that of the solid trailing-edge case, but with slightly milder velocity overshoot in the vicinity of the trailing-edge. It is also noticed that the use of porous 80 PPI treatment reduces the rms velocity value over a large part of the boundary layer compared to the solid trailing-edge. The results obtained for the flat plate with the porous 25 PPI treatment show that the flow is more streamline over the trailing-edge and it experiences much less acceleration and therefore less velocity overshoot in the trailing-edge region. The rms velocity results in the case of the 25 PPI trailing-edge changes rather abruptly over a large part of the boundary layer, particularly in the boundary layer outer regions. This becomes clearly visible at x/h=-0.9 (BL_3) and x/h=-0.05 (BL_4), upstream of the trailing-edge, where the flow acceleration was observed for the solid trailing-edge. However, there is an increase in the rms velocity magnitude near the wall region for the case of porous 25 PPI at both BL_3 and BL_4. Despite the significant reduction of U_{rms} over a large part of the boundary layer, the use of the 25 PPI material is shown to increase the energy content of the velocity fluctuations over a small region in the vicinity of the porous surface, which can be attributed to the frictional

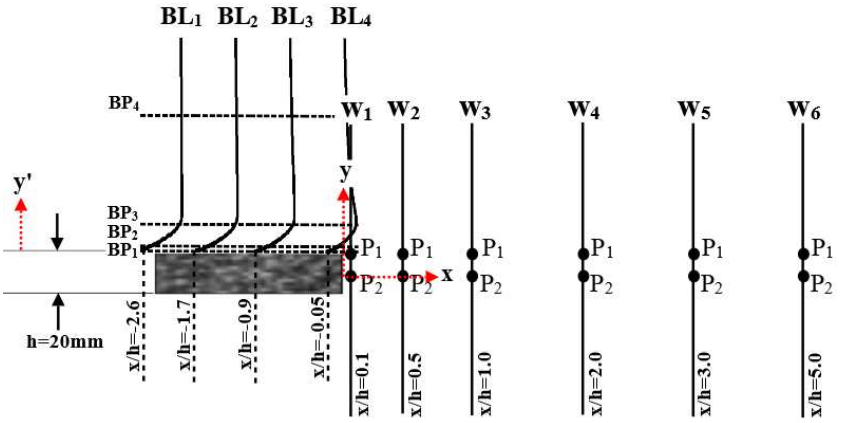

Figure 6.5: The schematic of the blunt trailing-edge rig and the position of the hot-wire boundary layer (BL_i) and wake (W_i) measurements.

forces at the surface of the porous material. This is particularly an interesting result as it shows that the energy content of the large coherent structures in the log-law and outer layer regions, mainly responsible for the low frequency surface pressure fluctuations and the trailing-edge noise generation [168] can be significantly reduced using porous treatments.

6.2.2.3 Wake velocity profile

Figure 6.7 shows the streamwise (U) and vertical (V) velocity profiles at different axial locations, namely x/h= 0.1, 0.5, 1.0, 2.0, 3.0, and 5.0 downstream of the trailing-edge (see Fig. 6.5), covering a wide range of near- to far-wake locations. Note that the measurements have been carried out using hotwire anemometry and therefore, the streamwise velocity component is always positive, *i.e.* showing the absolute value of the velocity. The actual values of the U- and V-components can be found in Fig. 6.4. It is clear from the results that the porous treatments can significantly change the flow structure in the near wake region. Results show that both the porous cases significantly reduce the magnitude of the streamwise velocity in the near-wake. The U-component velocity profiles show that the porous treatments delay the formation of vortex shedding in the wake, *i.e.* near-wake stabilization, which is consistent with the streamline flow pattern observed in Fig. 6.4.

In the case of 25 PPI, the large deficit observed is due to the suppression of the recirculation

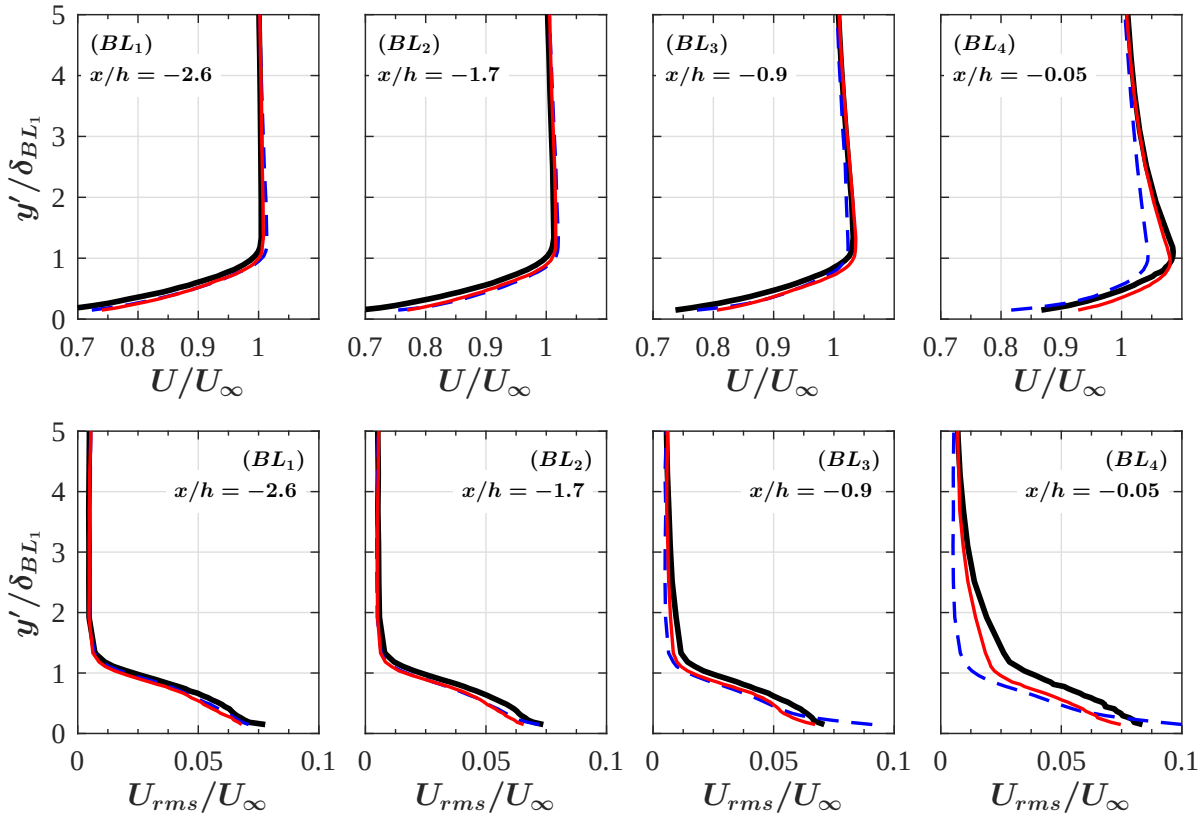

Figure 6.6: Boundary layer mean and RMS velocity profiles at different streamwise locations upstream of the trailing-edge. *Solid trailing-edge (—), Porous 80 PPI trailing-edge (—), Porous 25 PPI trailing-edge (- - -).*

region and reduction of the velocity overshoot over the trailing-edge, resulting in a more streamlined flow over the trailing-edge and larger deficit in the plate near-wake region. The porous material restraints the entrainment of the high momentum fluid from the free-stream into the wake field, which causes lower momentum transfer in the wake and results in larger velocity deficit in the plate near-wake region. The reduced impact of vortex shedding due to the delayed recirculation also enhances the effect of the base pressure recovery in the wake, which in turn, leads to the reduction in C_D. The drag associated with the vortex shedding can be obtained using the wake velocity deficit information. In order to calculate the drag force using the wake velocity results (C_{D_W}), the methodology described by Naghib [216] has been adopted. The wake-based drag coefficient can be found from,

$$C_{D_W} = \frac{2}{A}\int \frac{U}{U_\infty}\left(1-\frac{U}{U_\infty}\right)\mathrm{d}y + \frac{2}{A}\int\left(\frac{U_{rms}}{U_\infty}\right)^2\mathrm{d}y, \tag{6.1}$$

where A is the plate plan view area and the integral must be carried out outside the vortex recirculation region in the near wake area. The two integrals in Eq. 6.1 are estimated based on the streamwise mean and fluctuating velocity components. In the present study, these terms are calculated based on the velocity quantities located at x/h=2, downstream of the trailing-edge. The trend of the total drag estimated from the wake C_{D_W}, at flow velocity of U_∞=20 m/s, corresponding to the Reynolds number of $Re_{L_x} = 4.6\times10^5$, is consistent with the drag coefficient C_D results found using the force balance measurements. The results show that a significant reduction of the total drag C_{D_W} can be achieved in the case of porous 25 PPI trailing-edge, with a reduction of $\approx$ 15 %, relative to that of the solid case, which is in agreement with the drag reduction obtained in Fig. 6.2.

The V-velocity component results in Fig. 6.7 show a different behaviour than the U-velocity component. The vertical velocity component in the near-wake can be linked to the vortex formation and roll-ups mechanism. The V-velocity results for the solid trailing-edge at x/h = 0.1 show the existence of a secondary small recirculation area near the centreline (y = 0) and two larger recirculation area nearer to the trailing-edge. The small recirculation near the centreline disappears quickly further downstream, leading to only one large recirculation area, ending between x/h = 2.0 to 3.0. The V-component velocity profiles observed for the 80 PPI trailing-edge is very similar to that of the solid trailing-edge, but the 25 PPI trailing-edge exhibits a very different behaviour. The main recirculation area of the 25 PPI case is much weaker than the solid case, indicating the stabilization of the shear layer and delay of the vortex shedding formation. The energy content of the boundary layer and wake structures will be further discussed in Figs. 6.8 and 6.14.

6.2.2.4 Reynolds shear stresses velocity profile

Figure 6.8 presents the normalized Reynolds normal stress ($\overline{u'u'}/U_\infty^2$, $\overline{v'v'}/U_\infty^2$) and shear stress ($-\overline{u'v'}/U_\infty^2$) components within the wake at x/h= 0.1, 0.5, 1.0, 2.0, 3.0, and 5.0. It is clear from the results that the Reynolds stresses are symmetrical about the wake centreline for all cases and

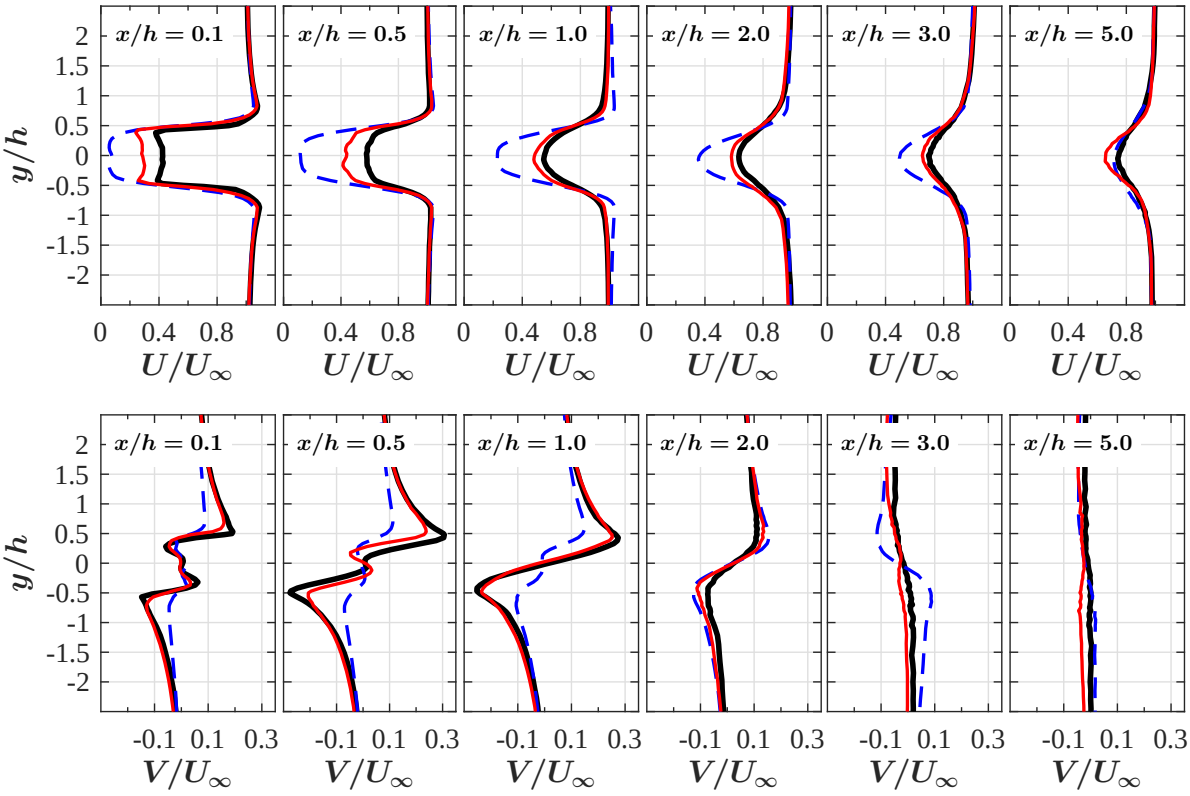

Figure 6.7: Mean streamwise (U) and vertical (V) velocity components in the wake of the blunt trailing-edge. *Solid trailing-edge (—), Porous 80 PPI trailing-edge (—), Porous 25 PPI trailing-edge (- - -).*

peak at about the trailing-edge lip-line at $y/h = \pm 0.5$. The near-wake results show that the use of porous trailing-edge can lead to significant reduction of the normal- and shear-stress terms along the centreline to almost zero and also considerable reduction at the peak location ($y/h = \pm 0.5$). Results have also shown that the use of porous trailing-edge leads to a considerable reduction of the wake width in the y-direction at $x/h = 3.0$ and 5.0. A noticeable difference between the magnitude of the $\overline{u'u'}$ and $\overline{v'v'}$ normal stress components can be observed in the $x/h \gtrsim 0.5$ region, where is dominated by the flow recirculation in the case of the solid or delayed vortex shedding for the porous trailing-edge cases. The results obtained for the solid and porous trailing-edges show that the $\overline{v'v'}$ component can become twice, or more, as large as the $\overline{u'u'}$ at the downstream locations ($x/h \gtrsim 0.5$). The increase in the v-fluctuations indicates the presence of large swirling turbulent structures, *i.e.* the formation of vortex shedding [217]. Also, this suggests the existence of a highly anisotropic flow at these locations due to the vortex formation, which will be further

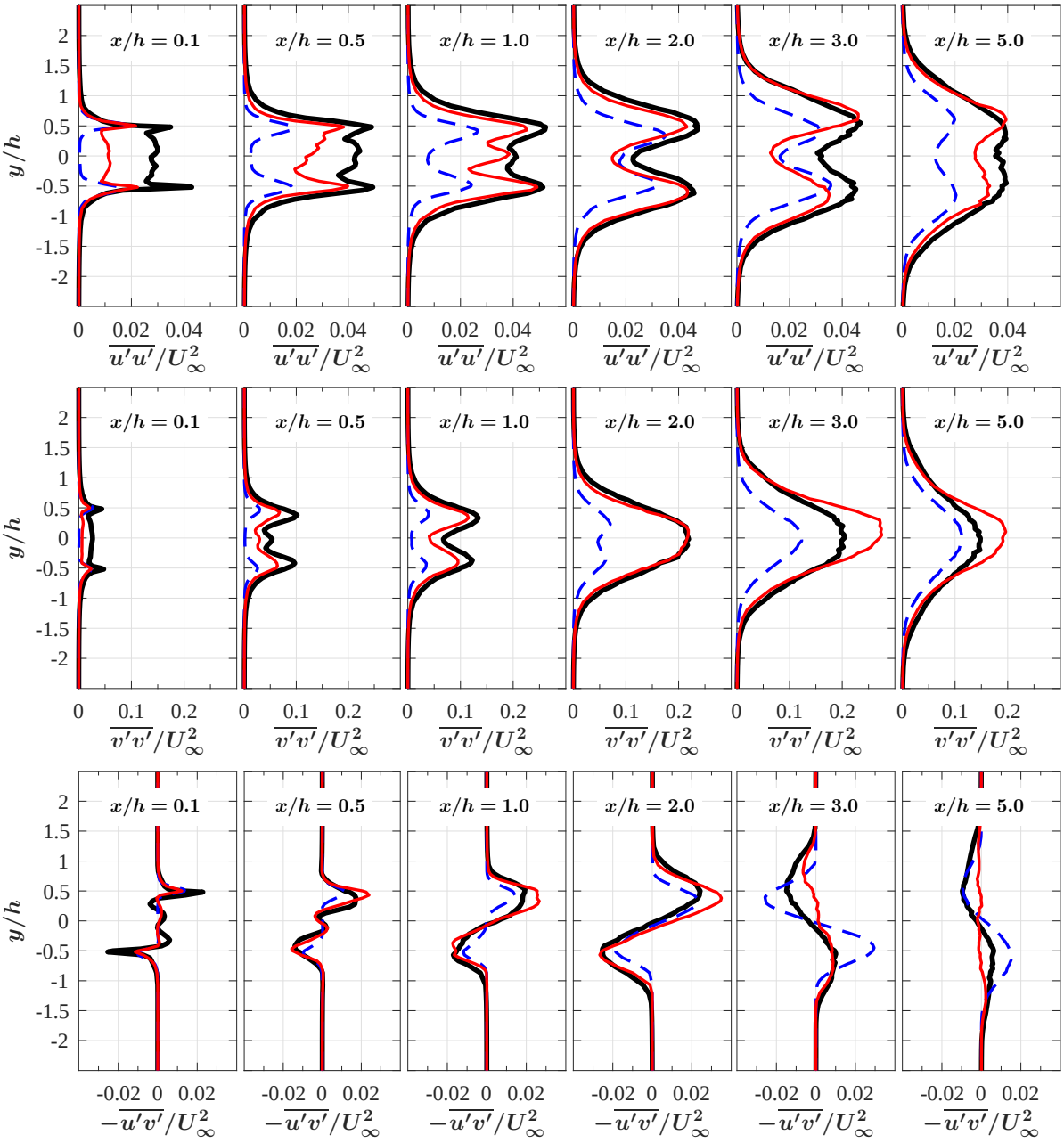

Figure 6.8: Reynolds stress components within the wake. *Solid trailing-edge (——), Porous 80 PPI trailing-edge (——), Porous 25 PPI trailing-edge (- - -).*

discussed in § 6.2.3.

In addition to the normal Reynolds stress terms, studying the shear stress terms helps better understand the energy production within the turbulent media and the mechanisms governing the stabilization of the Tollmien-Schlichting instabilities [218]. It is, therefore, important to

study the Reynolds shear stress component ($-\overline{u'v'}/U_\infty^2$) for both solid and porous trailing-edge cases within the wake region, see Fig. 6.8. The results at each location display a symmetrical distribution of shear stress along the wake centreline. It is clear that the shear stress is reduced significantly within x/h=0.1 to 2.0 due to the larger momentum deficit in the case of 25 PPI. Also, the lower peaks in the case of 25 PPI trailing-edge compared to the solid trailing-edge is due to the elongation of the wake region and the suppression of vortex shedding in the trailing-edge area, as discussed earlier for Fig. 6.7. In contrast, the distribution of $-\overline{u'v'}$ obtained at x/h=3.0 and x/h=5.0 shows a slight increase in the peak magnitude in the porous 25 PPI case, which indicates the presence of a delayed vortical structure in this region, as observed in Fig. 6.4.

6.2.3 Wake anisotropy flow

As shown in § 6.2.2.4, the wake flow is highly anisotropic. The anisotropy level b_{ij} can be estimated and derived from the Reynolds stress anisotropy tensor [219], which represents a symmetric second-order tensor as,

$$\tau_{ij} = \begin{pmatrix} \overline{u'^2} & \overline{u'v'} & \overline{u'w'} \\ \overline{v'u'} & \overline{v'^2} & \overline{v'w'} \\ \overline{w'u'} & \overline{w'v'} & \overline{w'^2} \end{pmatrix}, \tag{6.2}$$

This tensor is then decomposed into the sum of its deviator or known as the "traceless tensor", τ'_{ij} and an isotropic tensor (spherical tensor), τ°_{ij}, as,

$$\tau_{ij} = \tau'_{ij} + \tau^\circ_{ij}, \tag{6.3}$$

where the spherical tensor is defined as,

$$\begin{aligned} \tau^\circ_{ij} &= \frac{1}{3}\tau_{kk}\delta_{ij}, \\ &= \frac{1}{3}q^2\delta_{ij}, \end{aligned} \tag{6.4}$$

where q^2 is the Reynolds stress tensor trace and it is equivalent to the twice of the kinetic energy of turbulence, $q^2 = 2k$. The deviator is then expressed as,

$$\begin{aligned} \tau_{ij}^{'} &= \tau_{ij} - \frac{1}{3}\tau_{kk}\delta_{ij}, \\ &= \overline{u_i u_j} - \frac{1}{3}q^2\delta_{ij}, \end{aligned} \tag{6.5}$$

By normalizing the deviator $\tau_{ij}^{'}$ with the trace of the Reynolds stress tensor, q^2, the anisotropy tensor b_{ij} can be found, given by,

$$\begin{aligned} b_{ij} &= \frac{\tau_{ij}^{'}}{q^2}, \\ &= \frac{\overline{u_i u_j}}{q^2} - \frac{1}{3}\delta_{ij}, \end{aligned} \tag{6.6}$$

Equation 6.6 isolates the Reynolds stress tensor anisotropy from the other flow properties. Equation 6.6 can also be rewritten as,

$$b_{ij} = \frac{\overline{u_i u_j}}{2k} - \frac{\delta_{ij}}{3}, \tag{6.7}$$

where $\overline{u_i u_j}$ is the Reynolds stress term, $k = \overline{u_i u_i}/2$ is the average turbulent kinetic energy and δ_{ij} is the Kronecker delta function.

The overall turbulence anisotropy state can be evaluated by using the second *II* ($-b_{ij}b_{ji}/2$) and third *III* ($b_{ij}b_{jk}b_{ki}/3$) non-linear principal invariants of b_{ij} [220], where *II* indicates the degree of anisotropy and *III* represents the anisotropy nature [221]. The derivation of the second *II* and third *III* non-linear principal invariants of b_{ij} is given below. Considering the fact that the anisotropy tensor is symmetric, where $b_{ij} = b_{ji}$, an orthonomal basis $\underline{n_1}, \underline{n_2}, \underline{n_3}$ (unit vectors that are orthogonal to each other) can be found such that,

$$b_{ij} = \lambda_i \underline{n_i}\,\underline{n_i}, \tag{6.8}$$

or can also be expressed in the matrix form as,

$$b_{ij} = \begin{pmatrix} \lambda_1 & 0 & 0 \\ 0 & \lambda_2 & 0 \\ 0 & 0 & \lambda_3 \end{pmatrix}, \tag{6.9}$$

where vectors λ_i are called the eigenvalues or the principal values of anisotropy tensor b_{ij} and the vectors $\underline{n_i}$ are the eigenvectors or the principal directions that diagonalize anisotropy tensor b_{ij}. All the three and the other associated eigenvalues are real, established by the fact that the anisotropy tensor b_{ij} exhibits a symmetric property. The eigenvalues are resolved using the equation as,

$$|b_{ij} - \lambda\delta_{ij}| = 0, \tag{6.10}$$

Evaluation of Eq. 6.10 leads to a characteristic polynomial of b_{ij} given as,

$$\lambda^3 - I_1\lambda^2 + I_2\lambda - I_3 = 0, \tag{6.11}$$

where the scalar coefficients I_1, I_2 and I_3 are the first, second and third invariant of b_{ij}, given by

$$\begin{aligned} I_1 &= \mathrm{tr}(b_{ij}) = b_{kk}, \\ I_2 &= \frac{1}{2}[(\mathrm{tr}(b_{ij}))^2 - \mathrm{tr}(b_{ij})] = \frac{1}{2}(b_{ii}b_{jj} - b_{ij}b_{ji}), \\ I_3 &= \det(b_{ij}) = \frac{1}{3}(b_{ii}b_{jj}b_{kk} - 3b_{ii}b_{jj}^2 + b_{ii}^3). \end{aligned} \tag{6.12}$$

From Eq. 6.7, it is obvious that the first invariant I_1 is equal to zero. The second and third invariants can be simplified as,

$$\begin{aligned} I_2 &= -\frac{1}{2}\mathrm{tr}(b_{ij})^2 = -\frac{1}{2}b_{ij}b_{ji}, \\ I_3 &= \frac{1}{3}\mathrm{tr}(b_{ij})^3 = \frac{1}{3}b_{ij}b_{jk}b_{ki}. \end{aligned} \tag{6.13}$$

The invariants *II* and third *III* can be found as,

$$\begin{aligned} II &= -2I_2 = b_{ij}b_{ji}, \\ III &= 3I_3 = b_{ij}b_{jk}b_{ki}. \end{aligned} \tag{6.14}$$

The features of the turbulence state can be represented by the anisotropy invariant map (AIM), by plotting the non-linear functions of Reynold stress anisotropy invariant *II* (the degree of anisotropy) versus the invariant *III* (the nature of anisotropy), as shown in Fig 6.9. A short description of the anisotropy invariant map is provided below,

i. The AIM map can be defined using three points (*circled in red*). The point (0,0) corresponds to the isotropic turbulence, the point $\left(-\frac{1}{36},\frac{1}{6}\right)$ corresponds to the isotropic two-component turbulence and the point $\left(-\frac{2}{9},\frac{2}{3}\right)$ corresponds to the one-component turbulence.

ii. The upper AIM boundary line shows the two-component turbulence $\left(\text{II}=\frac{2}{9}+2\ \text{III}\right)$, where the fluctuations of the wall-normal component vanish much faster than the other components [222].

iii. The curve between the point (0,0) and $\left(-\frac{1}{36},\frac{1}{6}\right)$ represents the axisymmetric expansion $\left(\text{II}=\frac{3}{2}\left[\frac{4}{3}III\right]^{2/3}\right)$, where one of the Reynolds stress tensor's diagonal component is larger than the other two equal components.

iv. The curve between the point (0,0) and $\left(-\frac{2}{9},\frac{2}{3}\right)$ corresponds to the axisymmetric contraction $\left(\text{II}=\frac{3}{2}\left[-\frac{4}{3}III\right]^{2/3}\right)$, where one of the Reynolds stress components is smaller than the other two equal components.

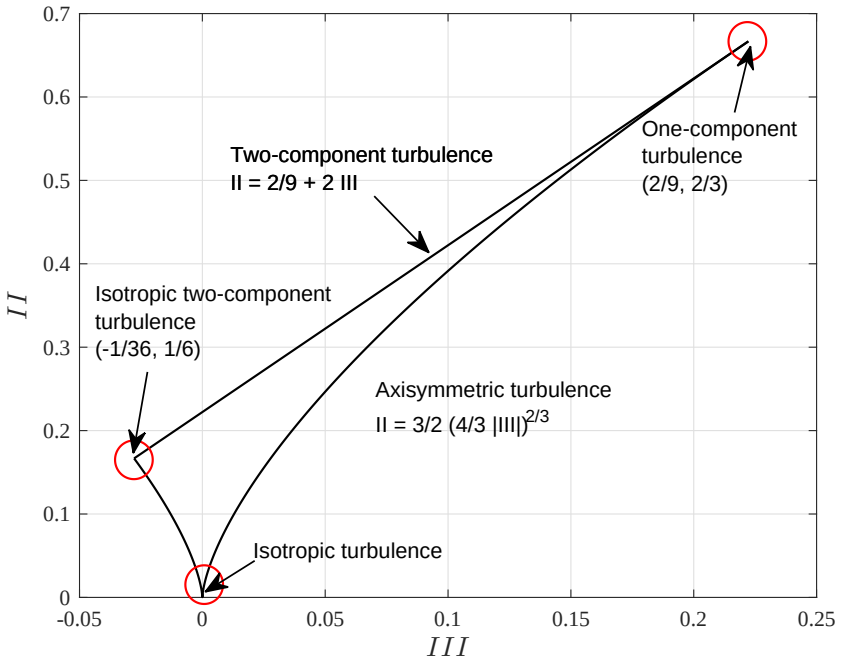

Figure 6.9: Anisotropy invariant map (AIM)

The anisotropy invariant map (AIM) of the Reynolds stress components at all wake locations ($0.1 \leq x/h \leq 5.0$) downstream of the trailing-edge lip-line and along the centreline, with a cross-plot of the invariant II versus invariant III are summarized in Fig. 6.10.

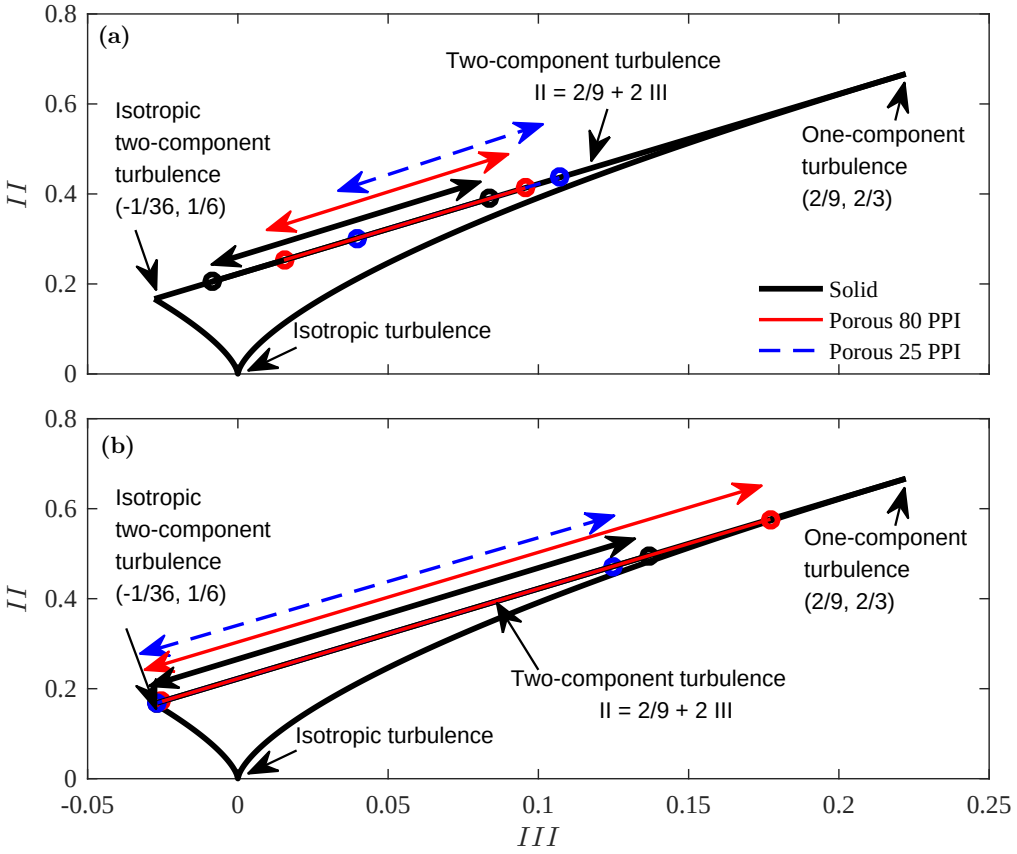

Figure 6.10: Anisotropy invariant map (AIM) of Reynolds stress tensor at several wake locations downstream of the (a) trailing-edge lip-line and (b) trailing-edge centerline. The arrows show the range of anisotropy variation for flow measurements over $0.1 \leq x/h \leq 5.0$.

The turbulence state of the Reynolds stress components is depicted by the boundaries of the AIM. As only the streamwise U and vertical V velocity components are available from the present hot-wire measurements, all the data points gather over the two-component turbulence state at the upper boundary line of the AIM (*i.e.* II=2/9+2III or b_{13}=b_{23} = 0). This is an acceptable assumption as the wake flow is predominantly two dimensional, *i.e.*, $W \approx 0$. Figure 6.10(a) shows that the Reynolds stress components of the wake structures in the case of the porous 25 PPI and 80 PPI at the trailing-edge lip-line gradually separate from the isotropic two-component turbulence

state and move towards a one-component turbulence state. At the trailing-edge centreline, the results in Fig. 6.10(b) show that the Reynolds stress components of all cases are nearly in a $2D$ isotropic turbulence state, which implies that the turbulent kinetic energy tends to be equally distributed among the two velocity-components and distinctly tend towards the $1D$ turbulence state, especially for the case of porous 80 PPI.

The Reynolds stress tensors behaviour presented in Fig. 6.10 can be visualized in the form of an ellipsoidal shape of the tensors in which the principal axes correspond to the stress axes and the radii are the tensor's eigenvalues, see Figs. 6.11 and 6.12. The equation of the shape of the Reynold stress tensor is defined as,

$$\left[\frac{x}{\lambda_1}\right]^2 + \left[\frac{y}{\lambda_2}\right]^2 + \left[\frac{z}{\lambda_3}\right]^2 = 1, \tag{6.15}$$

where λ_1, λ_2 and λ_3 are the eigenvalues of the Reynolds stress tensor.

The limiting state of turbulence based on the tensor's non-zero eigenvalues for one-component state is (λ_1=2/3, λ_2=λ_3=-1/3), for which the shape of the tensor willbe a line. In the case of two-component state (λ_1=λ_2=1/6), λ_3=-1/3), the shape of tensor will be an ellipsoid [223]. As can be seen in Fig. 6.11, a high level of anisotropy has been found in the case of porous trailing-edge within the wake at all measurement locations, x/h= 0.1, 0.5, 1.0, 2.0, 3.0, and 5.0, along the trailing-edge lip-line. A similar trend can be seen at the trailing-edge center-line, except at x/h= 1.0, where the porous cases yield a lower degree of anisotropy compared to the solid one. Additionally, as observed in Figs. 6.11 and 6.12, the degree of anisotropy present in the near wake, x/h= 0.1, 0.5 at the trailing-edge lip-line and center-line for porous 80 PPI is greater than that found for the solid trailing-edge. The porous 25 PPI, on the other hand, shows an even greater degree of anisotropy compared to the other cases in the near wake. It is also worth noting that the porous 25 PPI exhibits a nearly $1D$ turbulence state region downstream of the trailing-edge lip-line due to the suppression of the wall normal stress components, as observed in Fig. 6.11.

The changes in the wake turbulent structure can also be attributed as a direct response to the flow acceleration in the streamwise U and vertical V components of the Reynolds stress anisotropy tensor. For the solid and porous 80 PPI cases in the near wake, a region of higher b_{11}, b_{12} and lower b_{22} is observed, which indicates the establishment of isotropic $2D$ turbulence.

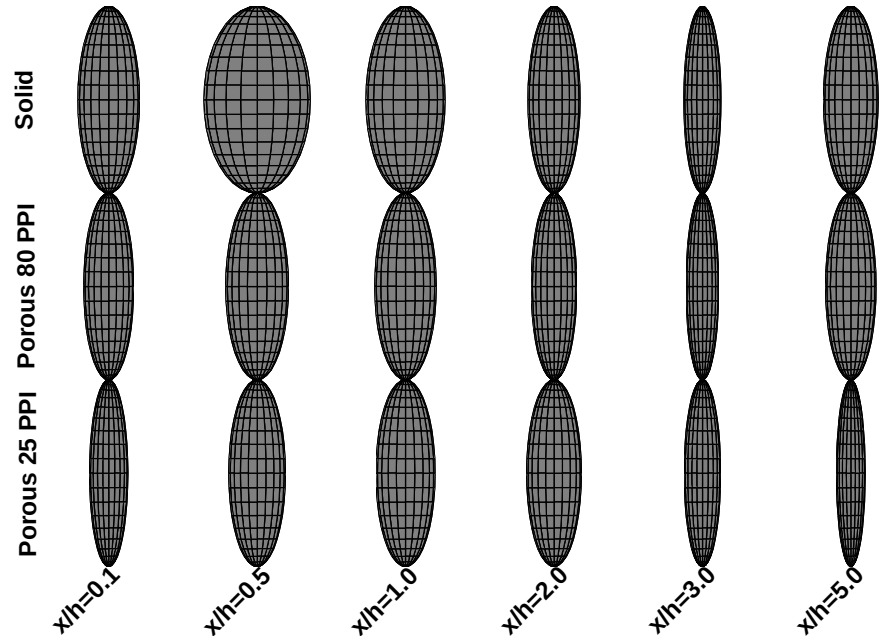

Figure 6.11: Ellipsoid shapes formed by Reynolds stress tensor, as described in Eq. 6.15 at several wake locations downstream of the trailing-edge lip-line.

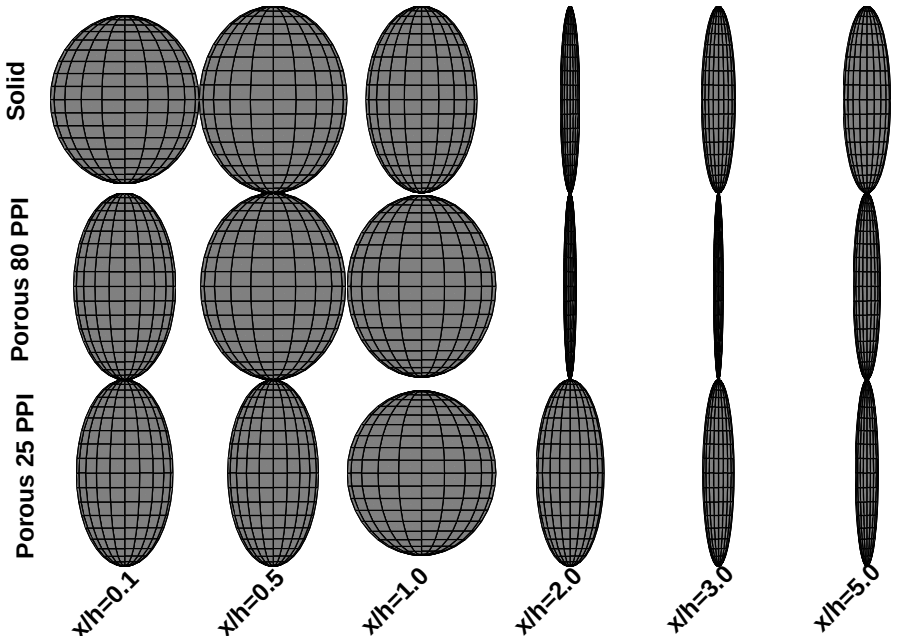

Figure 6.12: Ellipsoid shapes formed by Reynolds stress tensor, as described in Eq. 6.15 at several wake locations downstream of the trailing-edge center-line.

Such flow regions do not exist in the case of porous 25 PPI. This is expected to be due to the reorganization of the near-wall turbulence as a result of the flow acceleration near the trailing-edge. On the contrary, a region of nearly $1D$ turbulence state subjected to a strong acceleration region of the V-components (see Fig. 6.4) can be seen in the further downstream wake location, especially for the porous 25 PPI trailing-edge case. The abrupt changes in the ellipsoid shapes formed by Reynolds stress tensor for the porous cases can also be related to the delayed vortical structures, *i.e.*delay in the formation of vortex shedding, as shown in Fig. 6.4.

6.2.4 Velocity power spectra in the boundary layer

The dominant turbulent structures within the boundary layer and their frequency-energy content can be studied using the velocity power spectrum (ϕ_{uu}). Figure 6.13 presents the velocity power spectral density (PSD) as a function of the Strouhal number ($St{=}fh/\ U_\infty$) at different axial locations upstream of the trailing-edge and provides a comparison between the three investigated trailing-edge cases. In order to estimate the energy content at different frequencies, the Welch's power spectral density of velocity fluctuations (ϕ_{uu}) has been performed based on the time-domain hotwire data using Hamming windowing for segments of equal length with 50 % overlap. The frequency resolution (Δf) was set to 64 Hz and the frequency wavelength was equal to 1/5 of the window length used in the windowing process. The velocity fluctuation energy power spectrum at BP_1 corresponds to the point near the surface (y'/h=0.025), while BP_{2-3}, *i.e.* the top two rows, show the results further away from the wall regions of the boundary layer at y'/h=0.075 and 0.33 (velocity overshoot location). The y' axis is introduced on the top surface of the plate, defined as $y' = y - h/2 = 0$.

Results have shown that in the vicinity of the wall the porous treatment, especially in the case of 25 PPI, causes an increase in the energy content over the whole Strouhal range, which is believed to be, to some extent, due to the increased level of frictional forces acting on the flow near the surface (BP_1), which is also in agreement with the rms velocity results presented in Fig. 6.6. It can also be seen that the level of such frictional forces increases with the flow travelling downstream over the porous section. The investigated spectra at the velocity overshoot location (BP_3,BL_{2-4}) clearly show that the overall energy content of the boundary layer structures

reduces significantly as a result of the boundary layer interaction with the porous surface.

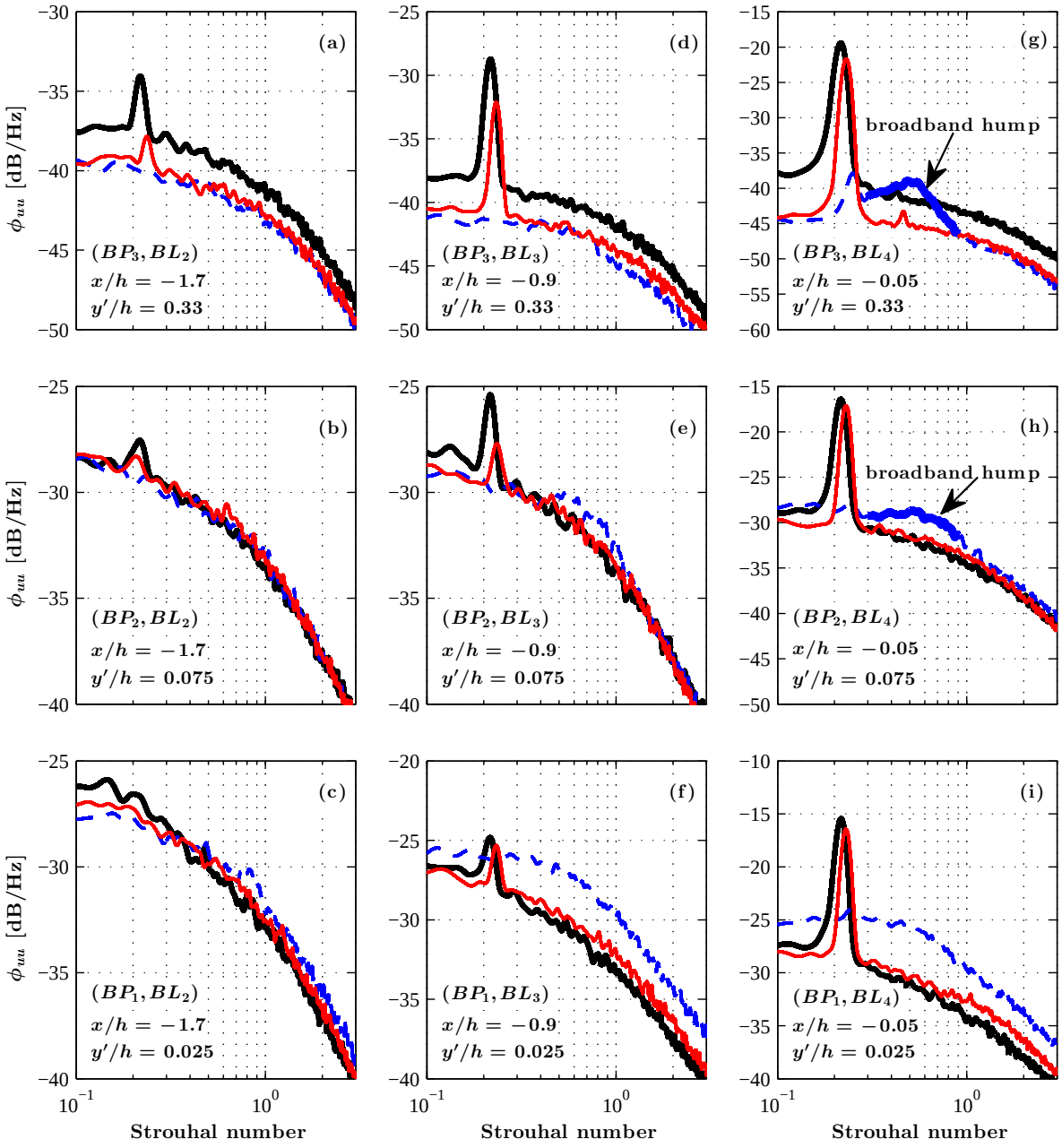

Figure 6.13: The velocity power spectral density at different locations in the boundary layer. *Solid trailing-edge (——), Porous 80 PPI trailing-edge (——), Porous 25 PPI trailing-edge (- - -).*

The results for the solid trailing-edge also show a strong tonal behaviour at $St \approx 0.21$, which can be attributed to the presence of a strong hydrodynamic field travelling upstream from the wake region, where flow recirculation occurs. The issue of the upstream travelling hydrodynamic

field will be further discussed in § 6.2.7. This tonal peak energy has been detected at almost all locations, which is also visible in the case of porous 80 PPI shown in Fig. 6.13, except for regions far upstream of the trailing-edge and very close to the surface. Interestingly, in the vicinity of the trailing-edge at BL_{3-4} results show that the use of 25 PPI porous material results in the complete suppression of the tonal peak and the emergence of a small broadband hump between $St = 0.3$ to 0.9 at BP_3,BL_4. The broadband hump region is shown in plots (g) and (h) with a thick line.

While the near-the-wall frictional forces result in an overall increase in the energy content of the flow over the entire frequency range, the increase over a small frequency band (St=0.3 to 0.9) seems to be due to a different mechanism. This is believed to be due to the presence of a strong hydrodynamic field inside the porous medium, which will be discussed further in § 6.2.7 and proven using various pressure and velocity correlation and coherence studies. This phenomenon can also be seen in the near-wake velocity frequency-energy content and the surface pressure fluctuations (ϕ_{pp}) results in Figs. 6.14 and 6.23. From the velocity PSD results presented in Fig. 6.13, it can, therefore, be concluded that the use of porous treatments can lead to significant reduction of the energy content of the large turbulent structures within the boundary layer and the suppression of the vortex shedding tonal peaks. Understanding of the mechanisms through which the porous treatment causes such changes requires more in-depth analysis of the boundary layer surface pressure fluctuations, which will be dealt with in § 6.2.7 and § 6.4.

6.2.5 Velocity power spectra in the wake

To properly understand the properties of the wake turbulence structures, one needs to study their energy-frequency content, as well as the basic velocity and turbulent kinetic energy profiles. The results of the power spectral density (PSD) analysis of the wake flow velocity (ϕ_{uu}) are presented at several wake locations downstream of the trailing-edge, along the lip-line ($y/h = 0.5$) and along the centreline ($y/h = 0$), see Fig. 6.14. The measurement locations are shown in Fig. 6.5. The fundamental, first and second harmonics of the vortex shedding frequency can be clearly seen from the results of the solid trailing-edge. The slope of the velocity spectra after the second harmonic ($St = 0.6$) for all downstream locations appears close to $f^{-5/3}$. The results show a

significant and consistent reduction of the broadband content of ϕ_{uu} for both porous cases. In the case of the porous 80 PPI, as mentioned before, the treatment is unable to change the tonal characteristics of the flow structures. However, the reduction in the broadband content of the energy spectra in the case of 80 PPI treatment, has made the tones to protrude well above the broadband spectra, even more than that of the solid trailing-edge.

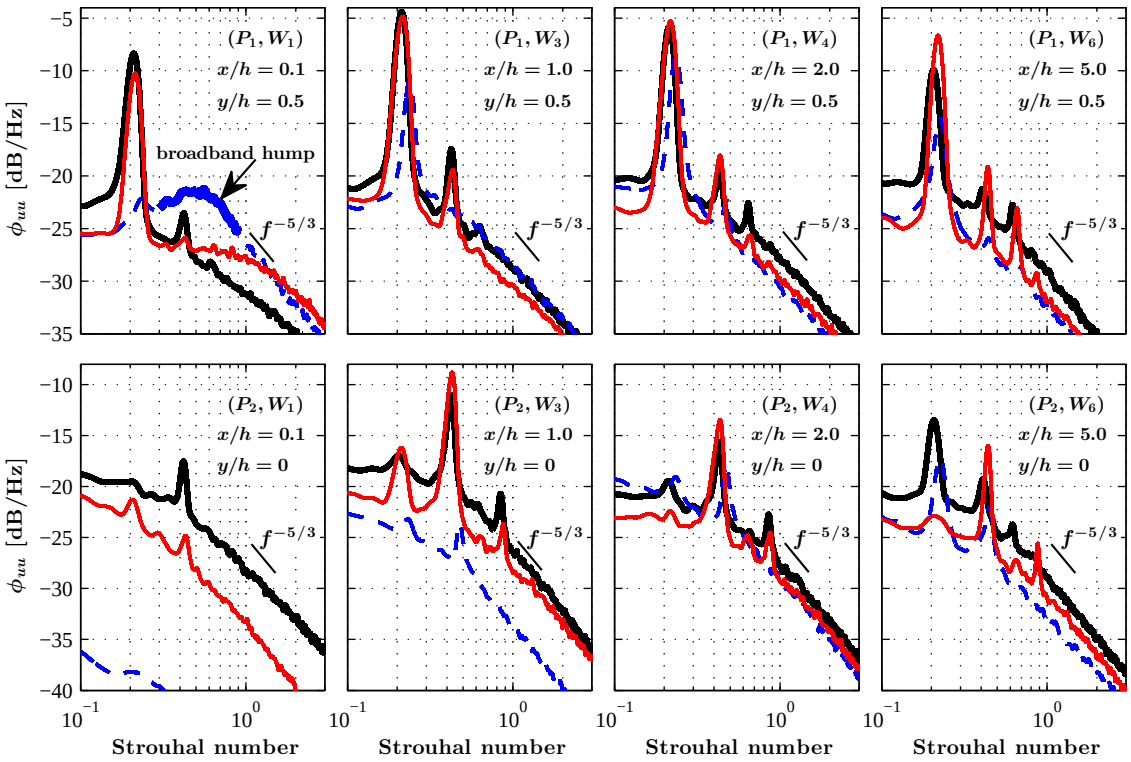

Figure 6.14: The velocity power spectral density at different locations in the wake. *Solid trailing-edge (——), Porous 80 PPI trailing-edge (——), Porous 25 PPI trailing-edge (- - -).*

In the case of the 25 PPI trailing-edge, results have shown that the use of a highly permeable section can lead to the effective suppression of the vortex shedding peaks and also reduction of the broadband content of the fluctuating velocity. Also, a broadband hump region is observed at about $0.3 < St < 1.0$ for the porous 25 PPI case in the near-wake region (P_1, W_1), which was also seen in the boundary layer velocity PSD results (Fig. 6.13(BL_4)). This broadband hump is, however, local to the trailing-edge region, dissipates very quickly further downstream and is

believed to be due to the internal hydrodynamic field of the porous section. This will be further discussed in § 6.2.7 and § 6.4. Furthermore, the results along the centreline have shown that the use of porous 25 PPI can lead to significant reduction of the energy content of the wake flow structures in the near wake region. However, the recirculating vortical structures in the 25 PPI case gain more energy after $x/h = 2.0$, *i.e.* the location of the delayed weak vortex shedding, followed by a significant reduction of the peak magnitude and the broadband energy content in the far-wake region ($x/h = 5.0$).

6.2.5.1 Contour plots of the velocity power spectra in the wake

Figure 6.15 shows the power spectra contour plots of the U velocity components for solid trailing-edge at different x/h locations in the wake. It can be seen that the energy is mainly confined within the wake area, and the same tones can be found in these spectra as seen in Fig. 6.14. This means that high energy content is experienced at St=0.2 and its harmonics. The hydrodynamic energy at St=0.2 can be felt well beyond the wake region, *i.e.* $y/h > 1.0$.

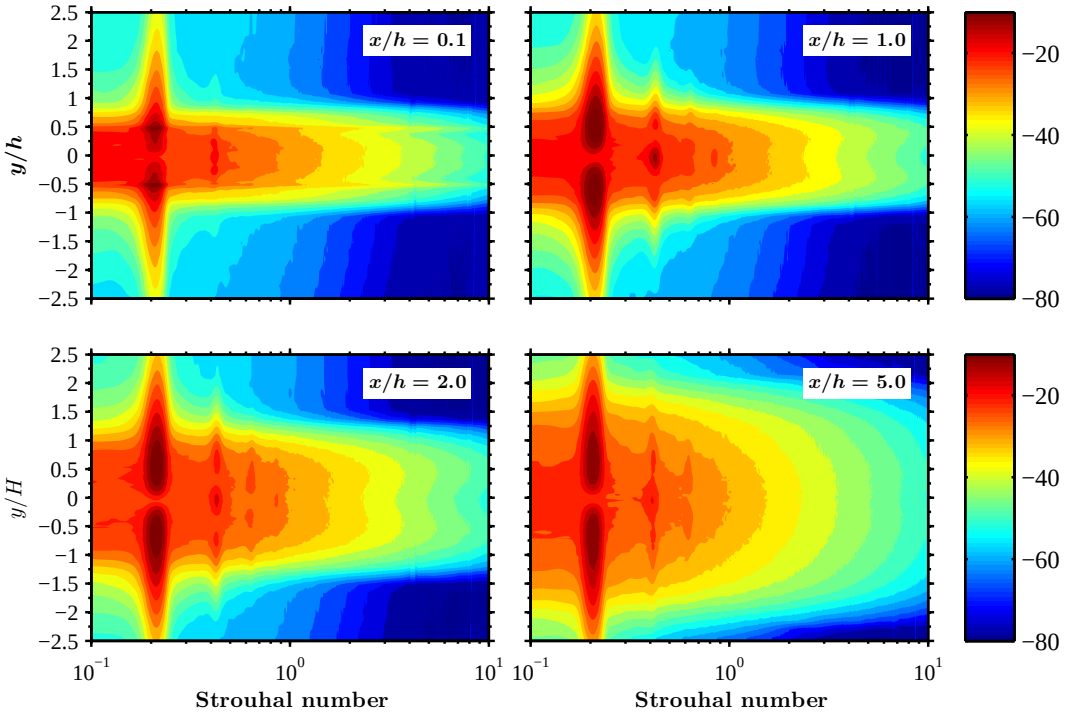

Figure 6.15: Contour plot of the solid blunt trailing-edge power spectra for the U velocity component, (ϕ_{uu}).

Figures 6.16 and 6.17 present the PSD contour plots for porous 80 PPI and porous 25 PPI ϕ_{uu} components, normalized with the results obtained from the solid trailing-edge, *i.e.* $(\phi_{uu})_{porous}$-$(\phi_{uu})_{solid}$. These figures help to identify the locations at which energy reduction or increase occurs in the wake area. It is clearly visible that the energy is reduced mainly at higher frequency region in the near wake by the 80 PPI material, and the energy is almost uniformly reduced at all frequencies in the case of the 25 PPI material. The reduction about the y-axis at about St=0.2 and St=0.4 for both porous cases is due to the slight shift of the tonal peaks, as observed in the power spectral density of the U velocity components in Fig. 6.14.

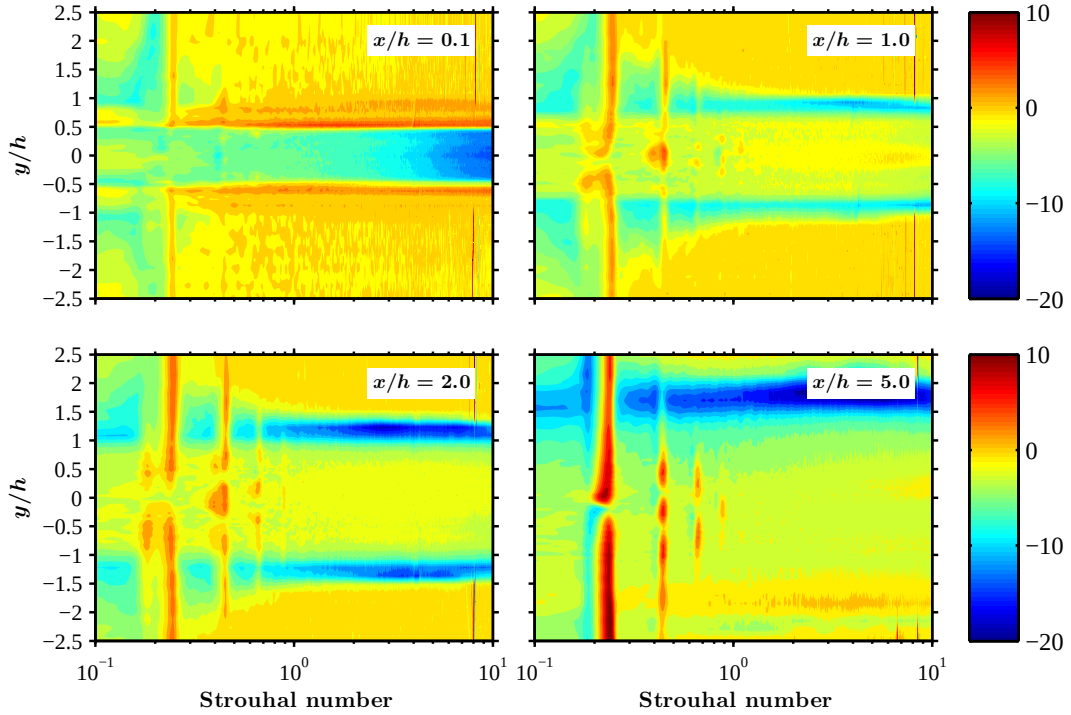

Figure 6.16: Contour plot of the reduction in the power spectra for the U velocity component for the 80 PPI porous material, $(\phi_{uu})_{porous\ 80\ PPI}$-$(\phi_{uu})_{solid}$.

It is also visible that the energy content in Fig. 6.17 for the porous 25 PPI case, at x/h=0.1 increases significantly, which is in agreement with the spectral broadband hump appearing in the case of porous 25 PPI, as observed at (P_1, W_1). However, this broadband hump is observed to consistently reduce and dissipate very quickly in the downstream locations. The emergence of this broadband hump, as stated before, is believed to be due to an internal hydrodynamic field in

the porous medium, which will be further elaborated in § 6.2.7 and § 6.4. It is also apparent that the hydrodynamic energy shows a significant reduction beyond the wake region, *i.e.* $y/h > 1.0$ of the trailing-edge width. It is clear that the energy is reduced significantly in the centerline and the shear layer by the 25 PPI material at all locations. These suggest that the use of porous trailing-edge has led to the suppression or delay of the vortex shedding from the near wake, which is consistent with the findings observed in Fig. 6.4.

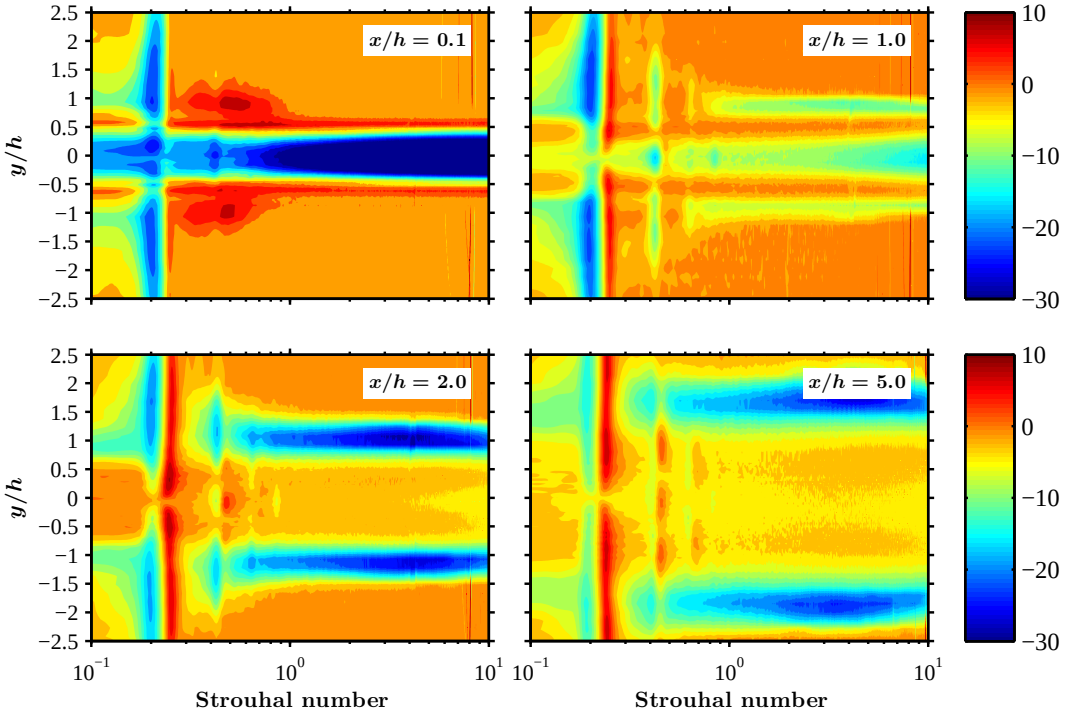

Figure 6.17: Contour plot of the reduction in the power spectra for the U velocity component for the 25 PPI porous material, $(\phi_{uu})_{porous\ 25\ PPI}$-$(\phi_{uu})_{solid}$.

6.2.6 Velocity correlation and length-scale in the wake

The two-point velocity correlation is of importance in the study of turbulence fluid flows. The correlation function is statistically related to the random velocity fluctuations at two points in the flow field, which enables us to obtain information about the turbulent structure and the spectral distribution of the turbulent energy in the flow field. The streamwise, $f(r_1)$, and spanwise (of the streamwise instantaneous velocity), $g(r_1)$ correlations have been measured using two hotwire probes. One of the hotwires has been fixed while the other one was traversed. The spanwise

correlation measurements have been carried out at four different streamwise locations, x/h=0.5, 1.0, 2.0 and 3.0. The streamwise correlation tests, on the other hand, have been performed by locating the fixed probe at $x/h = 0.1$, while the second probe was traversed up to $15h$ downstream of the edge lip-line of the upper trailing-edge. The two-point velocity correlation ($R_{ii}(x,r)$) of the turbulent structures and their corresponding length scale ($L_{11}(x,t)$) along the span of the trailing-edge lip-line in the wake are calculated using Eqs. 6.16 and 6.17, respectively, as,

$$R_{ii}(x,r) = \frac{\overline{u_i'(x_i,t)u_i'(x_i+r,t)}}{\overline{(u_i')^2}}, \tag{6.16}$$

and

$$L_{11}(x,t) \equiv \frac{1}{R_{11}(0,x,t)} \int_0^\infty R_{11}(\mathbf{e}_1 r, x, t)\mathrm{d}r, \tag{6.17}$$

where u_i' is the fluctuating total velocity in the streamwise direction, r is the distance between measurement locations, $\mathbf{e}_1$ is the unit vector in the x_1-coordinate direction and R_{ij} is the two-point autocovariance [224]. The spanwise and streamwise integral length scales have been plotted as a function of the Strouhal number in Figs. 6.20 and 6.21, respectively.

In the near wake region ($x/h = 0.5$), it can be seen that the correlation coefficient ($g(r_1)$) in the case of the solid trailing-edge is the highest at smaller probes spacing ($r_1/h \leq 1$) and a negative $g(r_1)$ region can be seen at higher probes spacing ($r_1/h > 1.5$). In contrast, there appears to be no significant difference in the $g(r_1)$ between the 80 PPI and 25 PPI trailing-edge cases. Note that, the $g(r_1)$ for all the cases (solid and porous trailing-edges) is very small, with almost zero correlation, which suggests that the flow has not been yet fully developed in this region.

At $x/h = 1.0$, a strong correlation coefficient can be clearly seen in the case of the solid trailing-edge at about $g(r_1) \approx 0.8$. Results have shown that the magnitude of $g(r_1)$ for the solid trailing-edge initially decreases with distance along the trailing-edge span and then start to increase thereafter. A negative $g(r_1)$ region is seen at $1.5 \leq r_1/h \leq 4.5$, indicating the existence of low and high shear regions in the flow. It could be also said that the counter rotating spanwise vortex pairs have been identified in the correlation and anti-correlation region. This results are consistent with the results seen in Fig. 6.4(a), where the flow recirculation behind the solid trailing-edge occurs within $0.05 \lesssim x/h \lesssim 1.04$, which is in the region ($x/h = 1.0$) where the two-point correlation was measured. A very similar observation can be made in the case of porous

80 PPI, with a delay in the negative $g(r_1)$ region at about $2.5 \leq r_1/h \leq 5$. The result for the 80 PPI material is consistent with the PIV result in Fig. 6.4(c), where a small shift in the location of the recirculation region is observed within $0.15 \lesssim x/h \lesssim 1.06$. On the contrary, it is evident that the correlation length is reduced by the 25 PPI material at $x/h = 1.0$, and no negative $g(r_1)$ region is seen along the trailing-edge span. This is believed to be due to the delayed vortex formation region behind the trailing-edge, as shown in Fig. 6.4(e). At farther downstream locations (x/h=2.0 and 3.0), the $g(r_1)$ is the strongest for the 80 PPI case where the slight delay in the vortex formation region compared to that of the solid case is more pronounced at this particular locations (x/h=2.0 and 3.0). It is of interest to note that the $g(r_1)$ of the 25 PPI case becomes increasingly more stronger at x/h=2.0 and 3.0, due to the presence of a delayed vortical structure in this region, see Fig. 6.4(e). The spanwise correlation results proposed that in the near wake, the Karman vortex is in two-dimension, resulting in a strong correlation in the far wake.

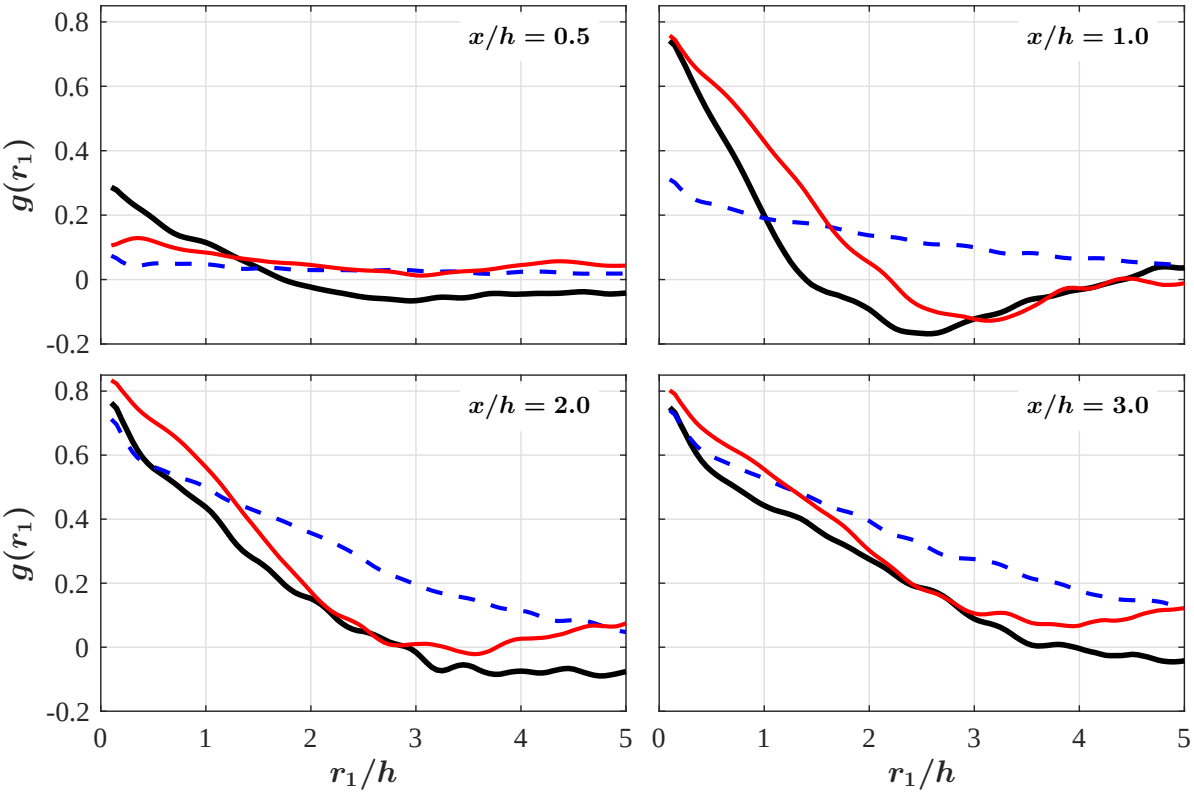

Figure 6.18: Spanwise correlation of the streamwise instantaneous velocity components at different streamwise location. *Solid trailing-edge (——), Porous 80 PPI trailing-edge (——), Porous 25 PPI trailing-edge (- - -).*

The streamwise correlation results are shown in Fig. 6.19. The streamwise results indicate that the shear layer near the wake location is thin and eventually becomes larger in farther downstream locations. Similarly, as observed in the other figures, the use of the 25 PPI material results in a reduction of the streamwise velocity correlation. The streamwise $f(r_1)$ is reduced significantly within x/h=1.0 and 2.0 due to the large momentum deficit in the case of 25 PPI. The lower magnitudes seen in the case of 25 PPI trailing-edge compared to that of the solid trailing-edge is believed to be due to the elongation of the wake region and the attenuation of vortex shedding in the near wake location, as indicated in § 6.2.2.4. It is evident here that the porous trailing-edge can significantly modify the two-point correlation of the velocity fluctuations in both the spanwise ($g(r_1)$) and streamwise ($f(r_1)$) directions.

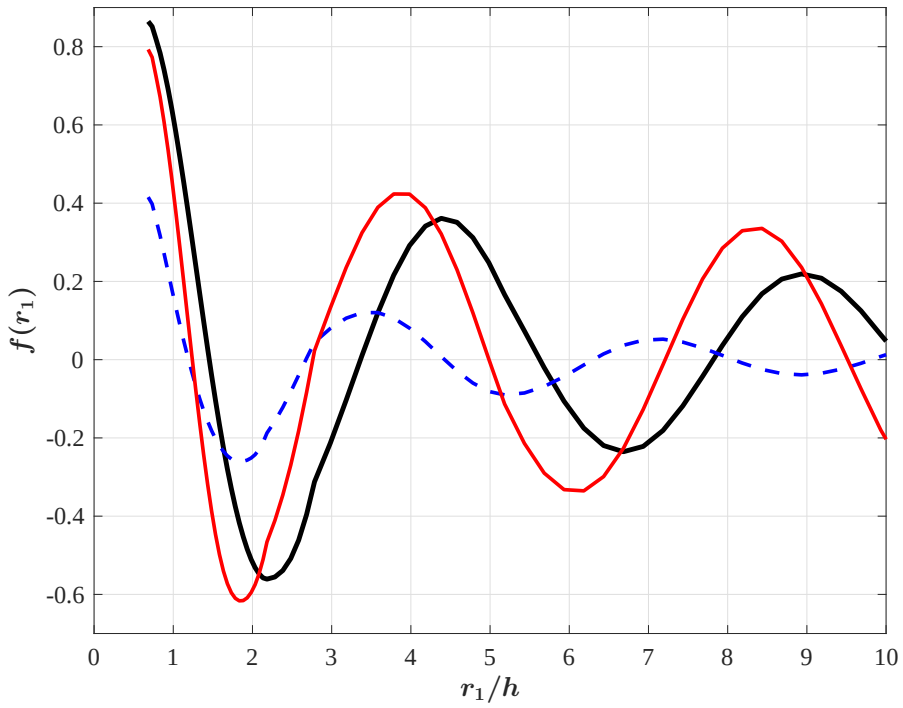

Figure 6.19: Streamwise correlation at $x/h = 0.1$. *Solid trailing-edge (——), Porous 80 PPI trailing-edge (——), Porous 25 PPI trailing-edge (- - -).*

The integral length scales have been calculated using the velocity correlation data using Eq. 6.17. In Fig. 6.20, it is obvious that the solid and porous 80 PPI cases exhibit a double peak at the vortex shedding frequency in the near wake region ($x/h = 0.5$ and $x/h = 1.0$).

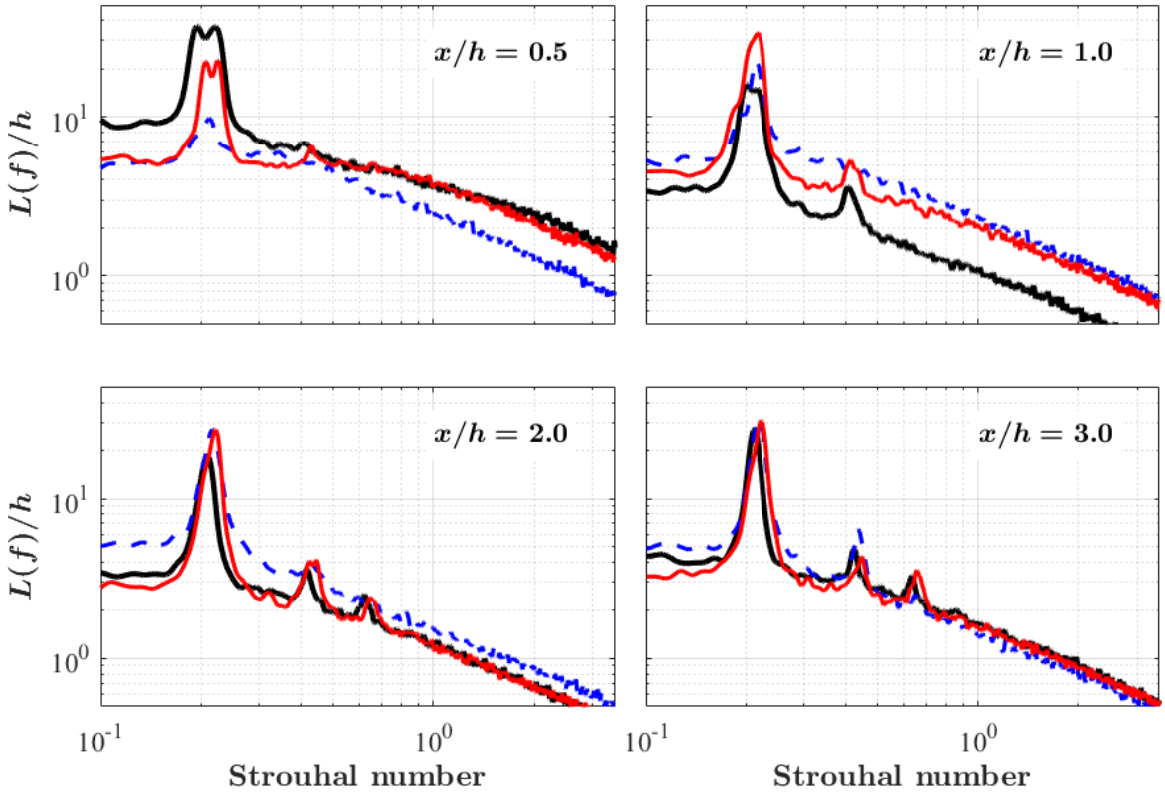

Figure 6.20: Velocity spanwise integral length scales at different x/h locations. *Solid trailing-edge (——), Porous 80 PPI trailing-edge (——), Porous 25 PPI trailing-edge (- - -).*

The double peak for the solid case consists of a dominant peak at St= 0.22 (x/h = 0.5 and 1.0) and a lower amplitude secondary dominant peak at a lower frequency, at St= 0.19 (x/h = 0.5) and St= 0.2 (x/h = 1.0). The double peak for the case of porous 80 PPI consists of a dominant peak at St= 0.22 (x/h = 0.5 and 1.0) and a lower amplitude secondary dominant peak at a lower frequency, at St= 0.21 (x/h = 0.5 and 1.0). It can be seen that both the double peaks decrease in amplitude and becomes a single peak in the further downstream locations. Moreau and Doolan [225] revealed that the multiple dominant peaks in the spectra are because of the cellular variation in spanwise vortex shedding frequency. The existence of the dominant tonal peak is due to the regular Karman vortex shedding from the trailing-edge. The secondary dominant peak, on the other hand, appeared due to a lower frequency shedding near the blunt trailing-edge-wall junction. It is anticipated that the reduction in the shedding frequency is due to the

interaction between the Karman vortices and the changes in the downwash flow originating from the acceleration over the trailing-edge. On the contrary, the results for the porous 25 PPI case does not exhibits any dominant double peak. Results have shown that the use of high permeability porous case can lead to effective attenuation of the vortex shedding peaks and the broadband content of the fluctuating velocity, especially in the near wake region ($x/h = 0.5$). The recirculating vortical structures in the 25 PPI case gain more correlation after $x/h = 1.0$, *i.e.* the location of the delayed weak vortex shedding. It also can be seen that the harmonics develop for all cases at the further downstream.

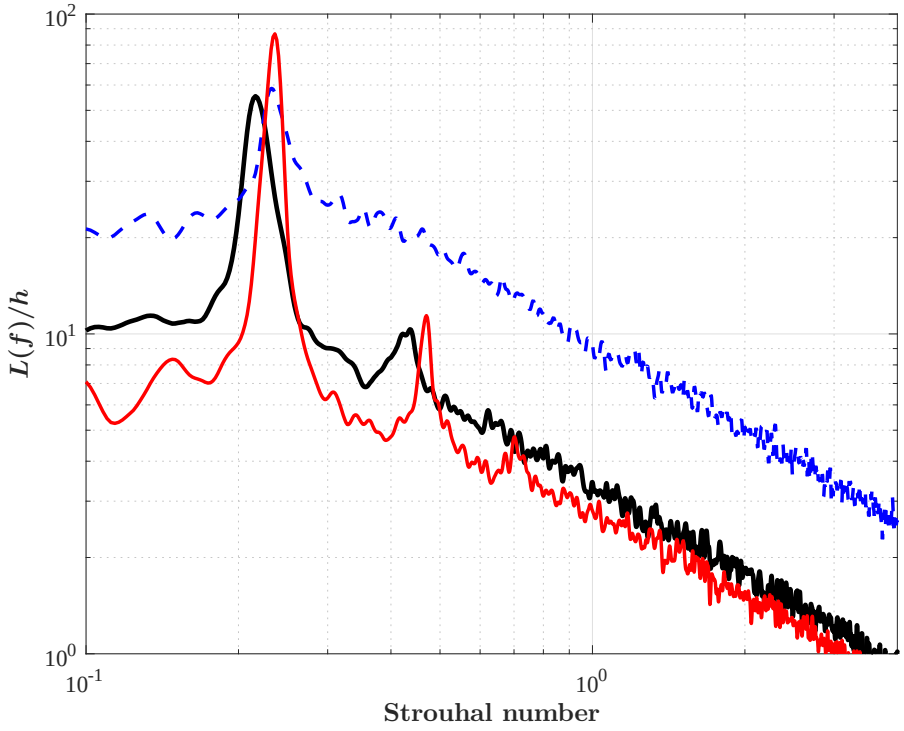

Figure 6.21: Streamwise integral length scales from x/h=0.1. *Solid trailing-edge (——), Porous 80 PPI trailing-edge (——), Porous 25 PPI trailing-edge (- - -).*

The streamwise integral length scale results are presented in Fig. 6.21. It can be observed that the 80 PPI material increases the size of the flow structures compared to that of the solid case at $St = 0.22$. Note that, the vortex shedding frequency of the porous cases is slightly shifted to higher Strouhal number compared to the solid case. The 25 PPI material introduces a broadband increase of $L(f)$ while it decreases the main peak at $St = 0.22$, and eliminates all the harmonics.

Comparing the amplitude of the dominant structures in the streamwise and spanwise directions for the porous materials considered here, it can be deduced that for the solid case, the spanwise length of the flow structures at the first peak ($x/h = 1.0$) is 3 times larger than in the streamwise length. For the 80 PPI case, this number is slightly larger and finally for the 25 PPI material, the ratio is roughly the half of the baseline case. One can, therefore, infer that the use of porous materials has led to the elongation of the turbulent structures in the spanwise direction in the near wake region, which also leads to the significant reduction in the energy content of the velocity fluctuations in the near wake.

6.2.7 Boundary layer surface pressure fluctuations

In the previous section, we focussed our attention on the flow properties of the boundary layer and the wake in the case of a solid blunt trailing-edge and the aerodynamic effects of using porous trailing-edges. To gain a better our understanding of the effects of porous treatments on the boundary layer structures through flow penetration in the porous medium and surface scrubbing effects, the surface pressure fluctuations exerted on the on trailing-edge surface due to the boundary layer structures convected downstream, or the hydrodynamic energy travelling upstream from the vortex shedding region have been studied. The typical surface pressure time-history measured at the trailing-edge, $p1$ ($x/h = -0.35$), where the flow acceleration was observed for the solid trailing-edge is shown in Fig. 6.22. It can be seen that the solid trailing-edge exhibits a square like waveform in the time domain, where the amplitudes are larger than that of the porous cases. The peak-to-peak distance observed in the pressure time-history results for the solid trailing-edge corresponds to the vortex shedding frequency (f_{vs}), as seen in figures 6.13 and 6.14. In the case of porous 80 PPI, the peaks in the time domain have reduced from that of the solid case, while for the porous 25 PPI case, substantial changes in the magnitude and the periodicity of the pressure fluctuations have been observed.

The power spectral density of the surface-pressure fluctuations (ϕ_{pp}) obtained from the pressure transducers *p1*, *p2*, *p4* and *p6* are presented in Fig. 6.23. To demonstrate the validity of the data, the single-point wall-pressure spectrum for the solid trailing-edge case at x/h=-1.9, where the effects of the pressure gradient are minimum, is compared against the Goody

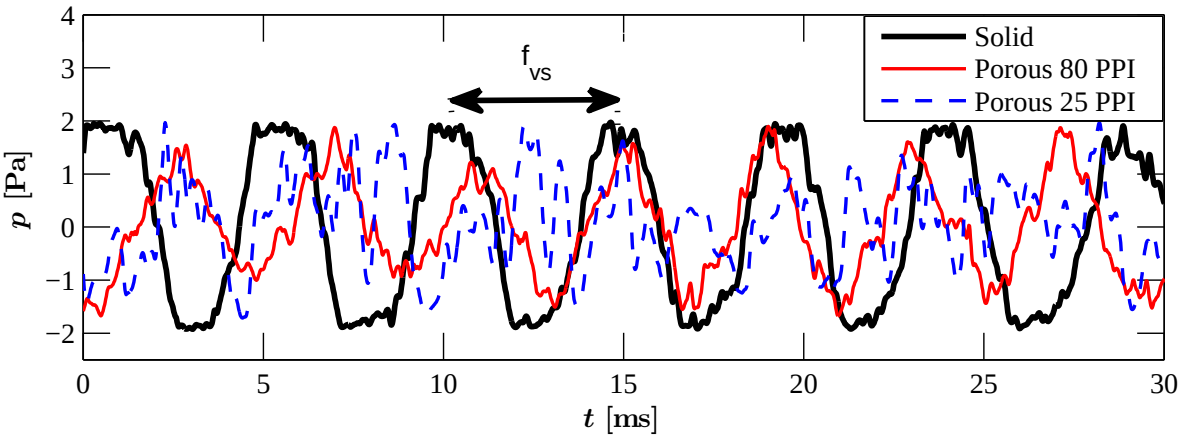

Figure 6.22: Time-history of the surface pressure collected by transducers $p1$ at $x/h = -0.35$ for solid, 80 PPI and 25 PPI porous treatments.

model [203]. The results from Goody's model have been corrected for presentation in figure 6.23 by taking into account the inner layer information of the boundary layer. The comparison shows an overall good agreement, particularly for the broadband aspect of the spectra with a slope of $\omega^{-0.7}$ at low frequencies and $\omega^{-0.5}$ at higher frequencies, as shown by Goody [203]. The results, however, show minor deviations at low frequencies, where the vortex shedding tonal peak is observed and about ± 1.7 dB at the middle and high frequency regions The vortex shedding peak can be seen at $St \approx 0.21$ at all transducer locations for the solid case with the peak for the porous 80 PPI slightly shifted to higher St numbers. Similar to the results obtained in Fig. 6.13, no tonal peak is seen for the case of porous 25 PPI, which again confirms that the vortex shedding has been effectively eliminated using the porous treatment in the near wake region. The tonal peak for the case of solid trailing-edge protrudes by about 10 dB above the broadband energy content while that for porous 80 PPI is in the order of 8 dB, and almost negligible for porous 25 PPI for the transducer located at the trailing-edge (x/h=-0.35). Results have also shown that the porous treatment can increase the broadband energy content in the whole frequency range due to (a) the frictional forces between the flow and the rough porous surface and (b) the hypothesised hydrodynamic field inside the porous medium. The comparison of the surface pressure fluctuations results for the 25 PPI surface and the velocity PSD results near the wall (Fig. 6.13 (BP_{1-3},BL_4)) and near-wake (Fig. 6.14) shows that development of a similar broadband hump at about $St \approx 0.5$.

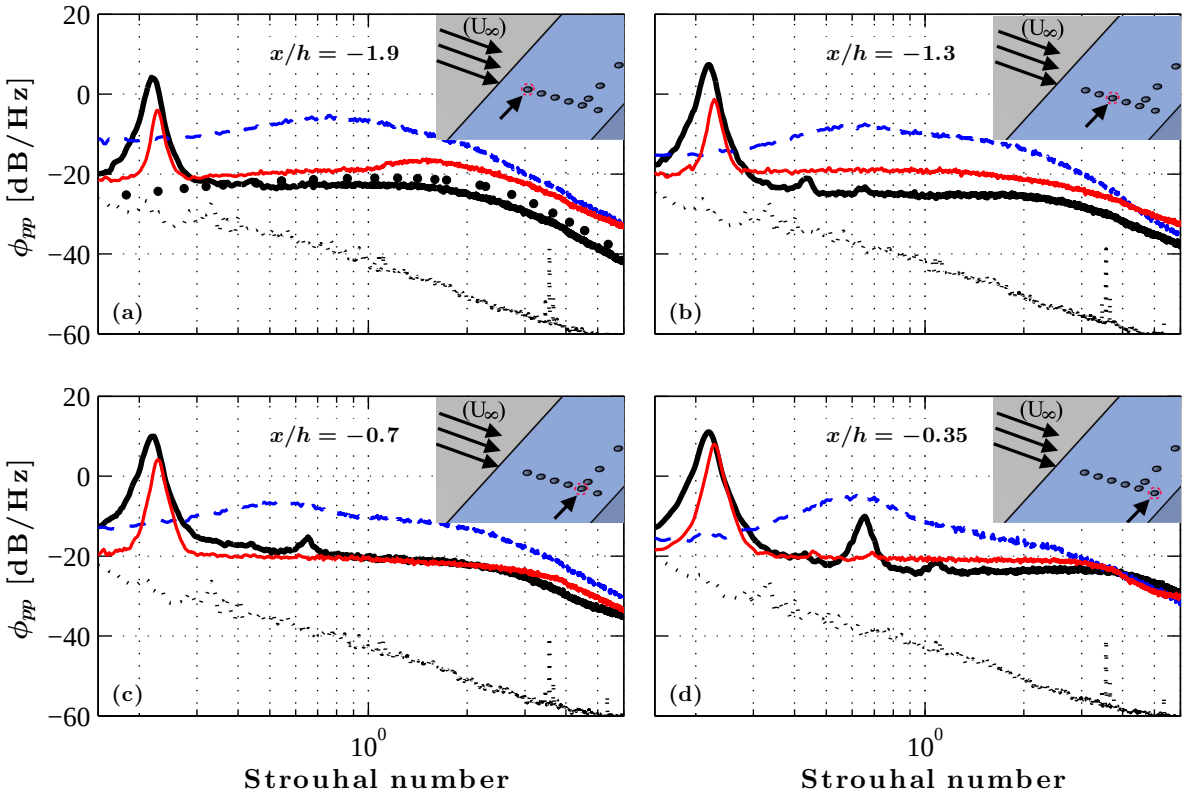

Figure 6.23: Power spectral density of pressure measured by transducers *p6* at *x/h*=-1.9 (a), *p4* at *x/h*=-1.3 (b), *p2* at *x/h*=-0.7 (c), *p1* at *x/h*=-0.35 (d). *Solid trailing-edge (—), Porous 80 PPI trailing-edge (—), Porous 25 PPI trailing-edge (- - -), Background noise (·····), Goody model (•).*

6.2.8 On the source of the broadband hump

As discussed above, the rise in the surface pressure fluctuations and the velocity energy level near the surface in the case of porous trailing-edges is believed to be partly due to the frictional forces acting on the rough surface of the porous materials (Fig. 6.6). However, the roughness alone does not seem to be the sole reason for the existence of a distinct broadband hump at around $St \approx 0.5$, which also only appears for the 25 PPI material and dissipates rapidly with distance. As hypothesised earlier, the broadband hump can also be due to a hydrodynamic field inside the porous medium. In order to only focus on the frictional forces and eliminate the possibility of the emergence of any hydrodynamic field inside the porous medium, the porous medium was filled with very fine grain sand. By filling the porous section with sand, at different heights (h_s), as shown in Fig. 6.24, the effect of surface roughness and the internal hydrodynamic field can be examined independently.

The effects of porous surface roughness has been examined by filling the porous 25 PPI trailing-edge with different sand heights (h_s), namely 0%, 50% (10 mm), 75% (15 mm), 90% (18 mm), and 100% (20 mm) filled, relative to the porous section thickness (h=20 mm), as shown in Fig. 6.24. Therefore, the h_s/h = 0 and h_s/h = 1.0 cases correspond to, respectively, a fully permeable and fully blocked (*i.e.* no internal hydrodynamic field but with rough surface) porous sections. In order to ensure there is no leakage of flow through the sand-porous medium and also to avoid sand leaving the porous section during the wind tests, the sand was slightly dampened. The surface pressure PSD results are presented for two locations $x/h = -1.3$ ($p4$) and -0.7 ($p2$) upstream of the trailing-edge. The comparison of the fully-filled porous section h_s/h = 1.0 with the solid trailing-edge case shows that the surface roughness can generally increase the broadband content of the surface pressure fluctuations over the entire frequency range. This confirms that two different mechanisms are responsible for the increase in the surface pressure PSD and that the broadband hump at around $St \approx 0.5$ is not due to the surface scrubbing effects. The emergence of the broadband hump at $St \approx 0.5$ can only be seen for the configurations with fully permeable (0% sand) or slightly filled (50 % sand) cases. It can also be observed that the broadband hump gradually disappears as the sand level in the porous section increases, *i.e.* no space left for the emergence of a strong hydrodynamic field. Also, results in Fig. 6.24 clearly show that the fundamental vortex shedding tone at $St = 0.21$ disappears only for the partially filled porous cases with $h_s/h < 0.5$. Hence, it is anticipated that the emergence of the broadband hump in the case of highly permeable porous media (25 PPI) is related to the emergence of a flow recirculation zone inside the porous section. To further deepen our understanding of the nature of this flow recirculation zone and its importance for flow control purposes, further pressure-velocity correlation and coherence analysis have been carried out, which will be presented in § 6.3.

6.3 Flow velocity and pressure correlation analysis

The results in § 6.2 showed that the implementation of a porous trailing-edge can lead to effective manipulation of the boundary layer, the wake flow-field and the possibility of elimination of flow recirculation and vortex shedding. The results of the surface pressure and velocity

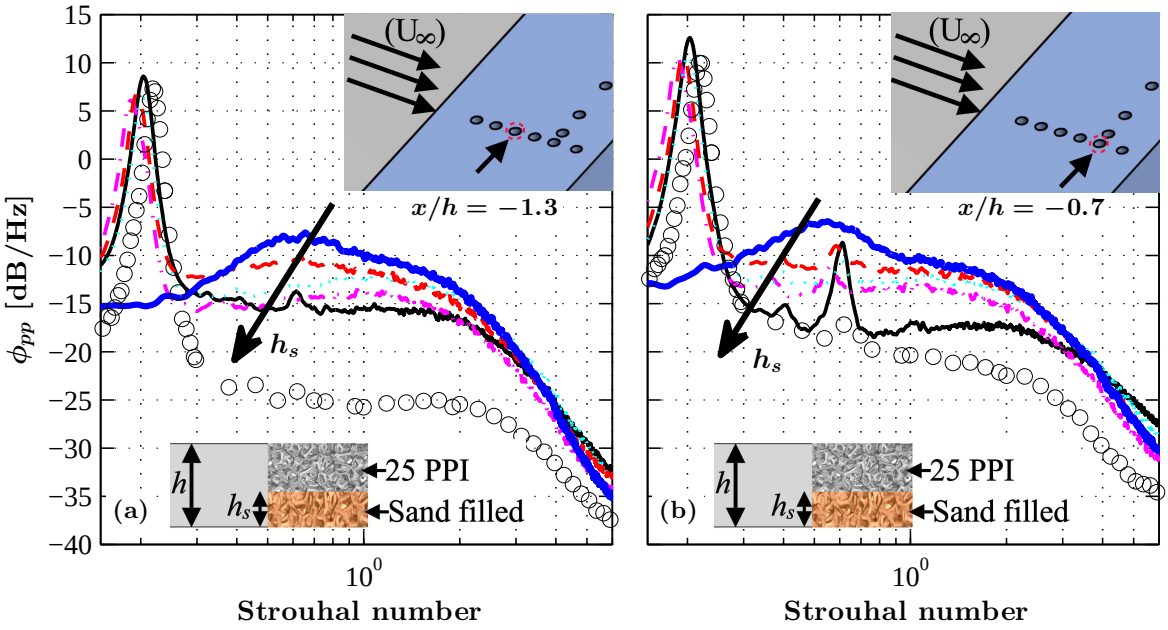

Figure 6.24: Power spectral density of pressure measured by transducers *p4* at x/h=-1.3 (a) and *p2* at x/h=-0.7 (b), with different thickness of porous 25 PPI trailing-edge filled with sand. *Solid trailing-edge (circle line); 100% Sand (——); 90% Sand (- - -); 75% Sand (·····); 50% Sand (- - -); 0% Sand (——).*

fluctuations also demonstrated that the energy content of the boundary layer and wake turbulence structures can be effectively reduced. In this section, further investigation will be conducted on the changes to the boundary layer flow structures by studying the correlation and coherence of the surface pressure and velocity signals over the solid and porous surfaces and the spatio-temporal characteristics of the boundary layer structures in streamwise and lateral directions. These results will enable us to better understand the underlying physics of the flow-porous surface interaction and the mechanisms leading to the stabilization of the flow over the blunt trailing-edge and elimination of vortex shedding.

6.3.1 Surface pressure lateral coherence and length-scale

The interaction of the flow with porous medium will not only change the boundary layer and wake flow velocity profiles, but also the coherence of the turbulent structures in the flow. To understand these effects, the spanwise coherence of the turbulent structures and their corresponding length-

scale using the pressure transducers (*p2*, *p7-p11*), distributed along the span at x/h=-0.7 was studied. The coherence between the spanwise transducers and the lateral length-scale can be found from Eqs. 5.6 and 5.7.

Figure 6.25 presents the lateral coherence measured between the spanwise transducers at x/h=-0.7 for a wide range of lateral spacings $0 < \xi_z/h < 4$. The left column plots (a, c and e) show the coherence for five spanwise distances between the selected transducers while the right column plots (b, d and f) show the coherence contour plots for all 15 combinations of the spanwise distances between the six transducers. The coherence ($\gamma^2_{p'_i p'_j}$) results are plotted as a function of the Strouhal number (fh/U_∞). In the case of the solid trailing-edge, as expected, a strong coherence can be observed at the vortex shedding frequency, $St \approx 0.21$ between the pressure signals. The results clearly show that different porous treatments have a significant and distinct effect on the lateral coherence of the flow structures, depending on the mechanical properties of the porous material. In the case of the porous 80 PPI trailing-edge, while a strong coherence can be observed at the fundamental vortex shedding frequency $St \approx 0.21$, the lateral coherence of the turbulent structure decays quickly with ξ_z at other frequencies. On the contrary, the 25 PPI material exhibits much lower coherence values and eliminates the vortex shedding peak entirely. However, similar to the results in Figs. 6.13 (BP_{1-3},BL_4), 6.14 and 6.23, an area of broadband hump emerges at around $St \approx 0.5$. As discussed in § 6.2.7 and § 6.2.8, this area is believed to be due to the emergence of a strong hydrodynamic field inside the porous medium.

Figure 6.26 shows the effect of porous trailing-edge on the spanwise correlation length ($\Lambda_{p,3}$) calculated using Eq. 5.7, based on the coherence of the pressure fluctuations between the spanwise transducer. In the case of the solid trailing-edge, the spanwise correlation length peaks at the fundamental vortex shedding frequency ($St \approx 0.2$), reaching $\Lambda_{p,3} \approx 3.3h$. The results show another peak at $St \approx 0.4$ ($\Lambda_{p,3} \approx 2.5h$), followed by a gradual decay at higher frequencies. For the porous 80 PPI case, while the results peak at $St \approx 0.2$ and 0.4, reaching similar values of the solid trailing-edge, the correlation length at other frequencies are much lower, consistent with the results in Fig. 6.25. Finally, the results for the trailing-edge fitted with porous 25 PPI show a very different behaviour. The spanwise length-scale over the entire frequency range of interest is significantly smaller ($\Lambda_{p,3} < h$) than the two other cases, with no evidence of strong vortex

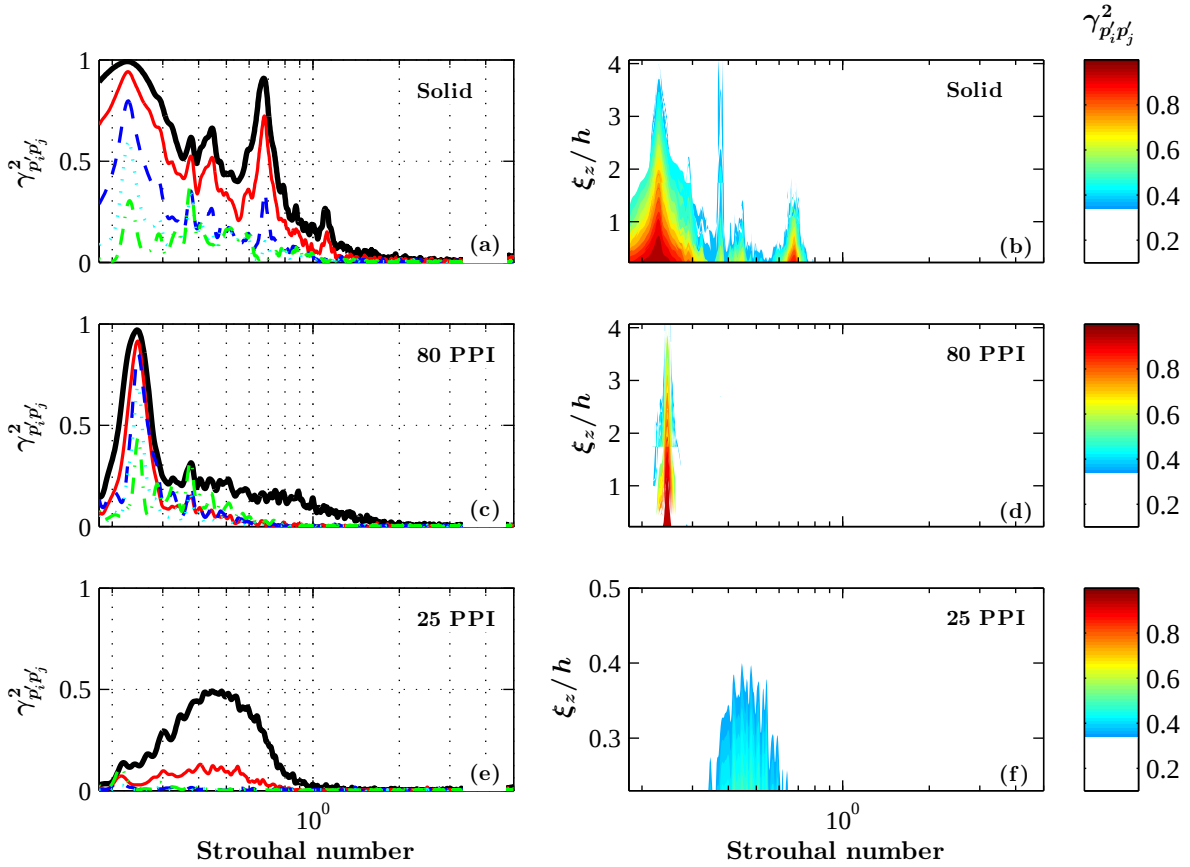

Figure 6.25: Lateral Coherence between spanwise transducers at $x/h = -0.7$, ξ_z/h=0.23 (——), ξ_z/h=0.67 (——), ξ_z/h=1.37 (- - -), ξ_z/h=2.33 (·····), ξ_z/h=4.07 (-·-·-).

shedding. The length-scale curve in the case of the porous 25 PPI trailing-edge shows a mild peak at about $St \approx 0.5$, which is again consistent with the observations in Figs. 6.13(BP_{1-3},BL_4), 6.14 and 6.23.

6.3.2 Surface pressure spatio-temporal correlation analysis

The spatial and temporal characteristics of the boundary layer structures can be acquired from the space-time correlation of the wall pressure fluctuations from Eq. 5.8. Equation 5.8 reduces to the temporal autocorrelation ($R_{p_i'p_i'}(\tau)$) when $\xi_x = 0$.

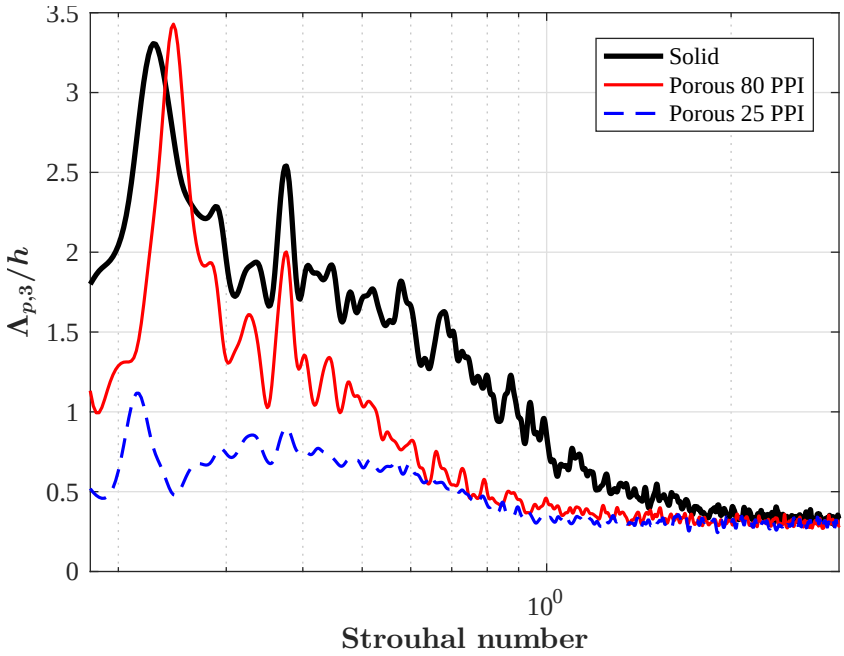

Figure 6.26: Spanwise length-scales based on the wall surface pressure measurement along the span at x/h= -0.7.

6.3.2.1 Longitudinal autocorrelation

Figure 6.27 shows the autocorrelations of the surface pressure fluctuations, $R_{p_i'p_i'}(\tau)$, for transducers at different locations from the trailing-edge, *i.e.* x/h= -0.35 (*p1*), x/h= -0.7 (*p2*), x/h= -1.3 (*p4*) and x/h= -1.9 (*p6*). The results are presented in terms of the normalized time-delay $\tau^*=\tau\ U_\infty/h$. The autocorrelation result of a standard zero-pressure-gradient boundary layer at $Re_\theta = 4.0\times10^3$ is also presented for comparison. For the solid trailing-edge, the autocorrelation results show a slowly-decaying periodic behaviour, indicating the existence of a strong upstream-moving hydrodynamic field, that covers the entire trailing-edge area. This will be discussed in Fig. 6.28. The peak-to-peak distance observed in the $R_{p_i'p_i'}(\tau)$ results for the solid trailing edge (τ^*_{vs}) corresponds to the vortex shedding, occurring in the near-wake region.

The autocorrelation curves for the porous 80 PPI trailing-edge are suggestive of two simultaneous phenomena, namely an envelope of a strong periodic hydrodynamic field and a sharp decay in the correlation that occurs at about τ^*=0. The periodic behaviour observed in the 80 PPI case indicates that a strong upstream-travelling hydrodynamic field due to the vortex shedding

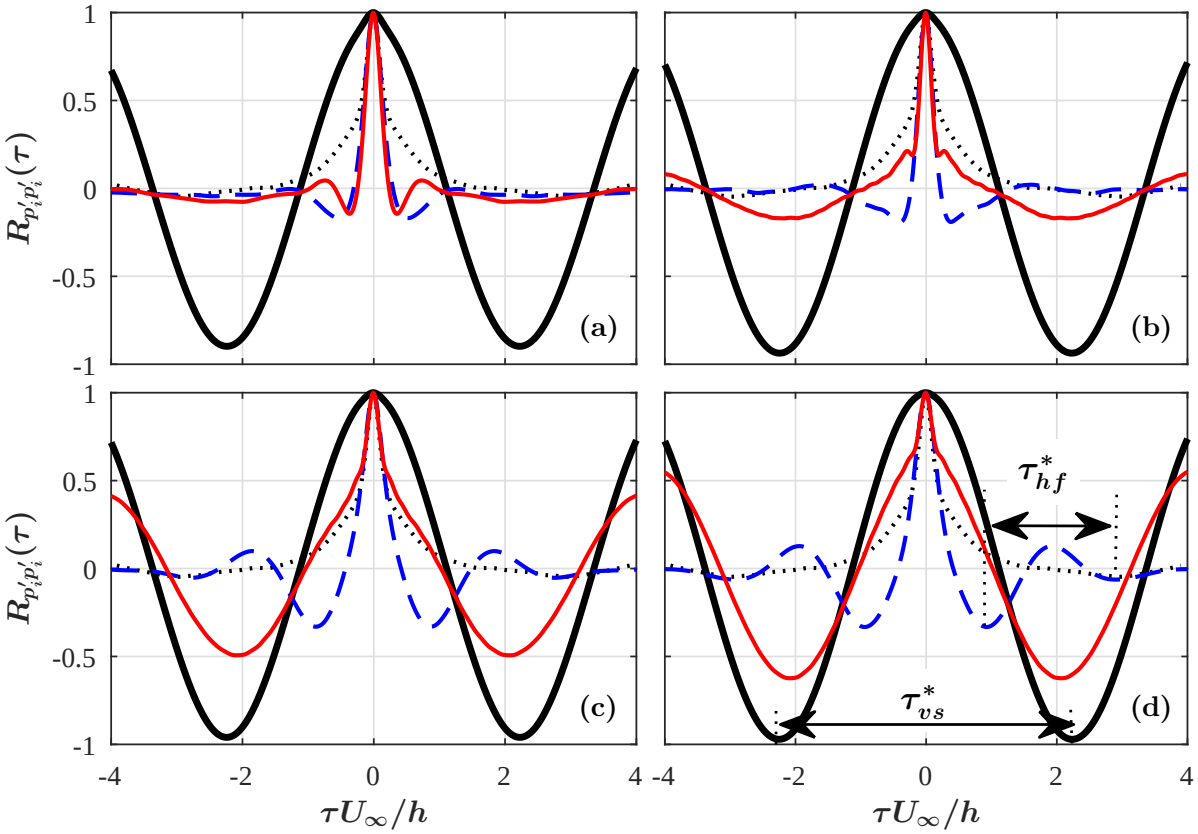

Figure 6.27: Autocorrelation of wall pressure fluctuations as a function of $\tau^* = \tau\ U_\infty/h$ for transducers *(p6)* at x/h=-1.9 (a), *(p4)* at x/h=-1.3 (b), *(p2)* at x/h=-0.7 (c), *(p1)* at x/h=-0.35 (d). *Solid trailing-edge (——), Porous 80 PPI trailing-edge (——), Porous 25 PPI trailing-edge (- - -), Standard boundary layer (·····).*

can still be observed, although its amplitude is lower than the solid trailing-edge and decays faster in the upstream direction. The sharp decay observed at about τ^*=0, on the other hand, is associated with the pressure exerted by the boundary layer turbulent structure at the transducer location. It can be seen that for the porous 80 PPI trailing-edge case, at the furthest upstream transducer location (Fig. 6.27 (a)), the strong upstream-travelling periodic hydrodynamic field has, to a large extent, been eliminated and the autocorrelation is reduced to that of a short-lived downstream-travelling boundary layer related fluctuations.

Finally, the autocorrelation results for the porous 25 PPI trailing-edge seem to indicate the existence of two concurring mechanisms, a quasi-periodic hydrodynamic field with the periodicity of τ^*_{hf} and a fast-decaying event at around τ^*=0. As observed in Fig. 6.27(d) for the transducer

near the trailing-edge (*p1*), the autocorrelation experiences a fast decay at τ^*=0, which is due to pressure signature of the downstream moving boundary layer structures, similar to a standard boundary layer. The autocorrelation results within $|\tau^*| < 3$ also shows a periodic behaviour, whose periodicity corresponds to the hump frequency previously observed in Fig. 6.23 for the surface pressure fluctuations. This quasi-periodic structure, as discussed in Fig. 6.24, is believed to be due to the internal hydrodynamic field within the porous medium. Moving further upstream to x/h= -1.3 (*p4*) and x/h= -1.9 (*p6*), one can observe that the autocorrelation results and the hydrodynamic field decays much faster over a smaller region of τ^*, similar to that of a standard boundary layer, which again corresponds to the pressure exerted by the boundary layer structures travelling over the transducers. The results also show that the fast decaying (spatially and temporally) quasi-periodic hydrodynamic field in the case of highly permeable porous media can only be observed within a certain distance from the trailing-edge (about L_{px}=h). The critical porous section length required to enable flow penetration and generation of the internal hydrodynamic field will be discussed in § 6.4.

6.3.2.2 Longitudinal space-time correlation

Figure 6.28 shows the space-time correlations results obtained from the cross-correlation between the reference transducer near the trailing-edge (*p1*) and the upstream pressure transducers, (*p2* to *p6*). Results are presented for the separation distances ξ_x/h of 0.35, 0.65, 0.95, 1.25 and 1.55. In the figure, the dashed line represents the autocorrelation information of the transducer *p1* as the reference probe, whereas the coloured curves show the cross-correlation between the reference probe and the upstream probes for all the investigated cases. An envelope trend can be clearly seen from the cross-correlations periodicity and the amplitude variations for the three trailing-edge cases considered in this study. The cross-correlation $R_{p_i' p_j'}(\xi_x, \tau)$ results for both the solid and 80 PPI cases show that the surface pressure correlations peak at negative time-delays, *i.e.* $\tau^* \leq 0$ (τ^*= τ U_∞/h), indicating the presence of an upstream-moving hydrodynamic field, travelling in the opposite direction of the free-stream flow. The results for the solid trailing-edge show that the correlation peaks shift very slowly in the negative time-delay direction, which indicates the existence of a long-lasting energy field over the trailing-edge domain, as discussed in Fig. 6.27.

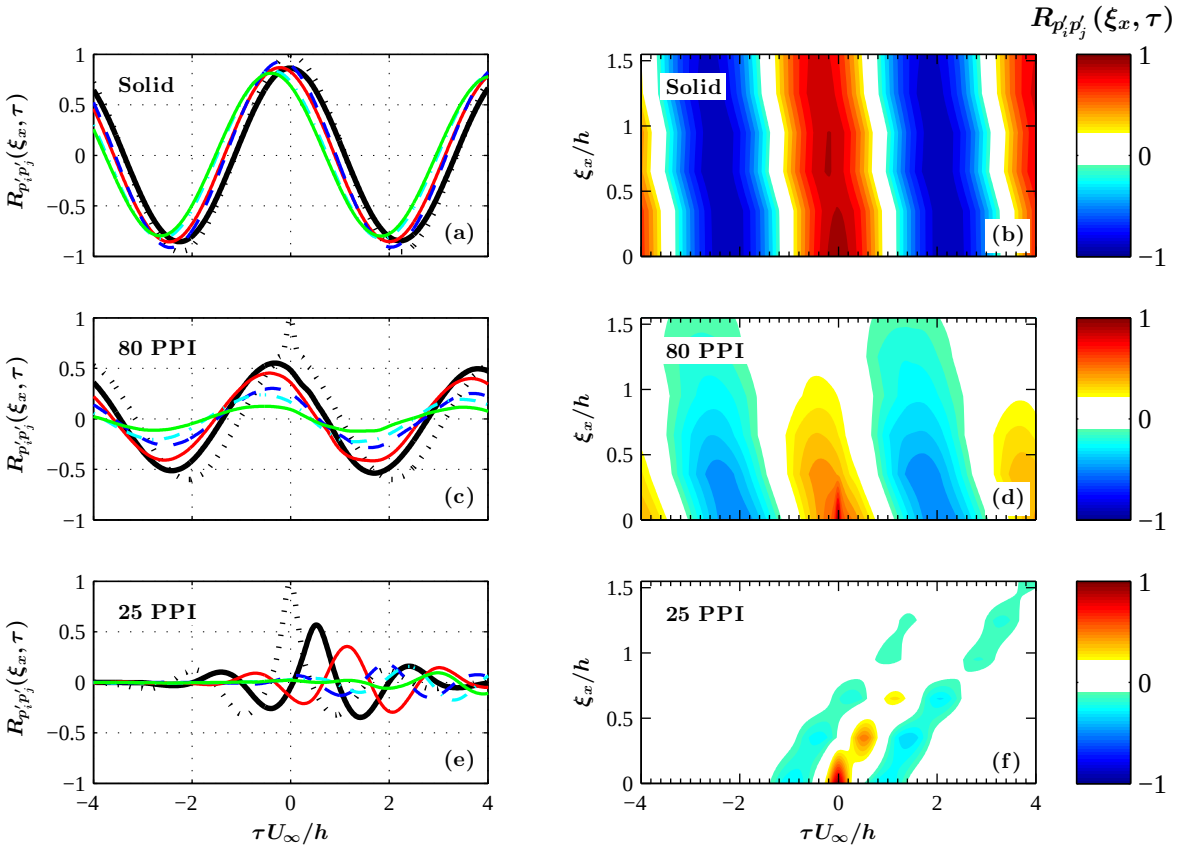

Figure 6.28: Space-time correlation of wall pressure fluctuations for solid, porous 80 PPI and porous 25 PPI trailing-edges. ξ_x/h=0 (·····), ξ_x/h=0.35 (——), ξ_x/h=0.65 (——), ξ_x/h=0.95 (- - -), ξ_x/h=1.25 (- · -), ξ_x/h=1.55 (——).

A similar, but less pronounced behaviour can also be observed for the 80 PPI trailing-edge case. Finally, in the case of the 25 PPI trailing-edge, the $R_{p_i'p_j'}(\xi_x,\tau)$ results show that the surface pressure fluctuations have the highest correlation at $\tau^* \geq 0$, which suggests that the generation of the wall pressure fluctuations are primarily dominated by the downstream convected turbulence structures in the boundary layer.

6.3.3 Boundary layer velocity-pressure correlation analysis

In characterizing the noise generated from the trailing-edge, it is essential to examine both the flow-field and the pressure exerted on the surface. The correlation studies between the surface pressure fluctuations and the velocity field within the boundary layer were conducted in order to

identify the characteristics of the coherent turbulent structure and their role on the pressure field exerted on the surface. Simultaneous boundary layer flow and surface pressure measurements were performed at four locations, namely *p1*, *p2*, *p4* and *p6* for the flow velocity of 20 m/s. A cross-wire probe was used and the data had been collected between $y' \approx 0$ mm and 50 mm at 49 locations above each transducer. Figure 6.29 presents the velocity-pressure correlation ($R_{u'p'}$ and $R_{v'p'}$) results within the boundary layer at different distances from the trailing-edge. To identify the pattern of the turbulent structures in space, the space-time correlation of the velocity and the surface pressure fluctuations are analysed using Eq. 6.18 as,

$$R_{u_i'p'}(\xi_{y'},\tau) = \frac{\overline{u_i'(x,\xi_{y'},t+\tau)p'(x,0,t)}}{u'_{i_{rms}}p'_{rms}}, \tag{6.18}$$

where p' is the wall pressure fluctuations, u_i' corresponds to the u' and v' fluctuating velocities in the streamwise and vertical directions, τ denotes the time-delay between the pressure signals and $\xi_{y'}$ is the distance between the measurement locations normal to the plate (y) direction as defined in § 6.1. The y-axis of the velocity-pressure correlation plots have been normalized by the boundary layer thickness at BL_1 (Fig. 6.5). Equation 6.18 reduces to the two-point correlation function ($R_{u_i'p'}(\xi_{y'})$) when $\xi_{y'} = 0$.

Figure 6.29 presents the correlation between the streamwise (u') and wall-normal (v') velocities and the surface pressure fluctuations at different axial locations for the solid and porous trailing-edges. In the case of the solid trailing-edge, at upstream locations (p_6, x/h= -1.9), where the flow acceleration is absent, an overall negative streamwise-pressure correlation ($R_{u'p'}$) can be observed, which peaks at about the location of the flow velocity overshoot (y'/δ_{BL_1} = 1). Moving closer to the trailing-edge (p_1, x/h= -0.35), where the flow experiences strong acceleration, a much stronger positive $R_{u'p'}$ correlation can be observed. In the case of the pressure and vertical velocity correlation ($R_{v'p'}$), a small negative correlation can be seen for the locations upstream of the trailing-edge locations (x/h= -1.9, -1.3). In the vicinity of the trailing-edge (x/h= -0.35), the $R_{v'p'}$ correlation increases, with its peak at the boundary layer velocity overshoot point (y'/δ_{BL_1} = 1), and negative correlation in the near wall region ($y'/\delta_{BL_1} \lesssim 1$) and positive correlation above the overshoot region. The increase in the correlation value in the trailing-edge area can be attributed to the flow acceleration and strong contribution of the vertical flow velocity component to the

exerted surface pressure, which is also in agreement with the observations made earlier in Fig. 6.6 at x/h=-0.05. In the case of a flat plate fitted with a porous 80 PPI trailing-edge, for locations immediately after the solid part (x/h= -1.9), the $u' - p'$ and $v' - p'$ correlations reduce to nearly zero. However, at the further downstream locations, the porous 80 PPI trailing-edge behaves very similarly to that of the solid case for both of the $R_{u'p'}$ and $R_{v'p'}$ components.

The correlation results obtained for the porous 25 PPI trailing-edge has shown some very interesting features. Results have shown that, in general, the use of a highly permeable surface significantly reduce both the $R_{u'p'}$ and $R_{v'p'}$ correlations compared to the solid and porous 80 PPI trailing-edge cases. More importantly, the contribution from the velocity overshoot region has completely vanished, which is consistent with the results presented in Fig. 6.6. For both the $R_{u'p'}$ and $R_{v'p'}$ components, the correlation over the entire boundary layer region for the porous 25 PPI treatment always remains negative, but it increases in amplitude for locations near the trailing-edge. Another interesting observation is that the $R_{u'p'}$ correlation in the near the wall region ($y'/h \lesssim 0$), dominated by surface frictional forces, is nearly zero (see Fig. 6.13(i)). However, the correlation peak value increases to almost $R_{u'p'} \approx$ -0.2 at about $\xi_{y'}/\delta_{BL_1} \lesssim 1$, which is believed to be associated with the large turbulent structures within the boundary layer. The $R_{v'p'}$ correlation results for the porous 25 PPI trailing-edge remains almost zero within the boundary layer, particularly in the near the trailing-edge locations, which indicates the suppression of the flow acceleration and flow vertical movement. This also shows that the surface pressure at the trailing-edge location is mainly dominated by the flow boundary layer (*i.e.* $R_{u'p'}$ results) and perhaps the hydrodynamic field developed inside the porous medium, which will be further discussed in § 6.4. It is worth mentioning here that in all three cases considered here, particularly for the rough porous surfaces, the correlation at the surface is zero. This shows that despite the increase in the energy content of the velocity fluctuations in the near the wall region, as observed in Fig. 6.13, these structures do not have a strong correlation with the surface pressure exerted on the surface. Therefore, the overall broadband increase in the surface pressure fluctuations is mainly due to (a) the changes to the boundary layer structures away from the surface and (b) the emergence of the internal hydrodynamic field in the case of highly permeable porous media.

To better understand the velocity-pressure correlation results presented in Fig. 6.29, the

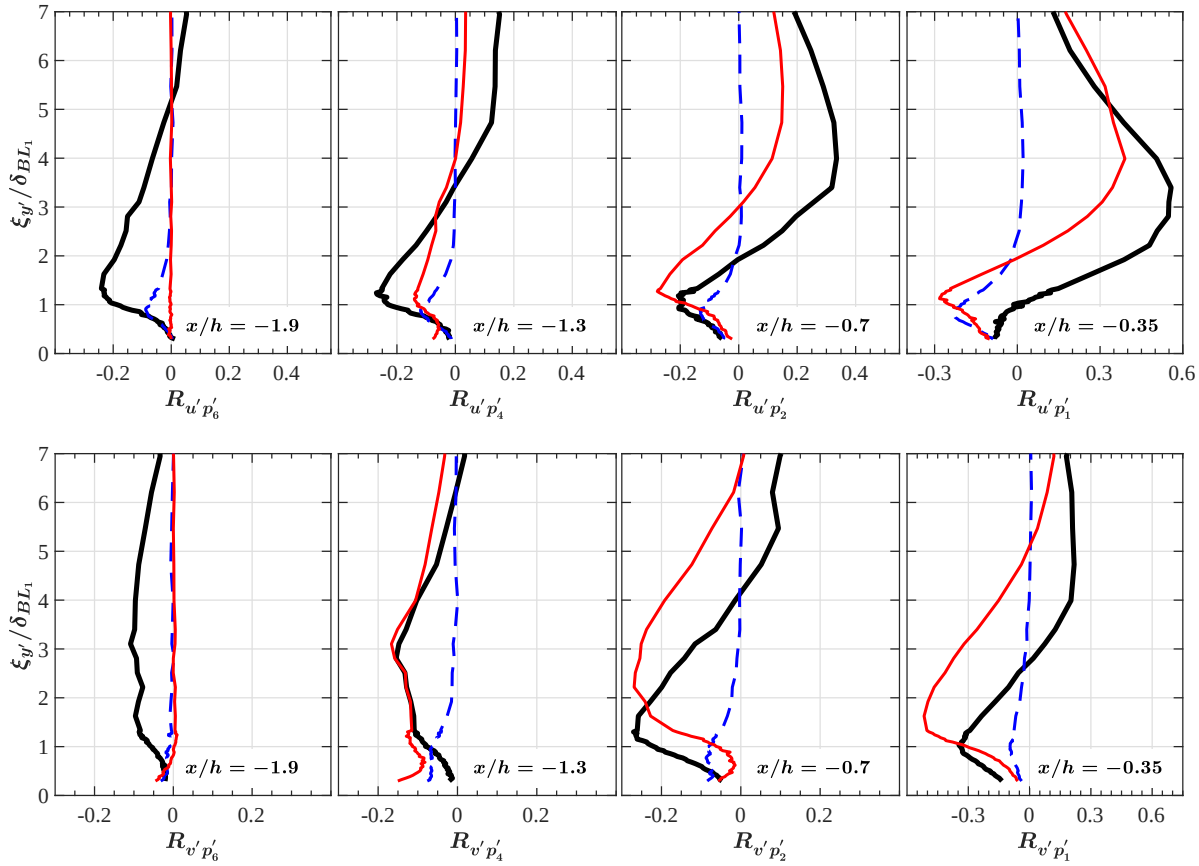

Figure 6.29: Velocity-pressure correlation components, $R_{u'p'}$ and $R_{v'p'}$ at different streamwise locations over the blunt trailing-edge. *Solid trailing-edge (——), Porous 80 PPI trailing-edge (——), Porous 25 PPI trailing-edge (- - -).*

space-time correlations between the velocity and the surface pressure fluctuations have been investigated and the results are presented in Fig. 6.30. The Figs. illustrate the results acquired for the transducers *p1* (x/h=-0.35) near the trailing-edge where strong acceleration is expected and *p6* (x/h=-1.9) where the flow acceleration is absent. At the transducer *p1*, shown in Fig. 6.30, the $R_{u'p'_1}$ cross-correlation for the solid trailing-edge shows the presence of a strong velocity-pressure correlation, with the correlation profiles skewed to the negative correlation time-delay. This signifies that the pressure fluctuations have the highest correlation with the upstream-moving hydrodynamic field (see Fig. 6.28), which is in agreement with the longitudinal space-time correlations of the transducers results presented in Fig. 6.28. The results also show that the largest correlation occurs at $\xi_{y'}/\delta_{BL_1}$ = 1, where the flow experiences strong acceleration over the

trailing-edge, as observed in Fig. 6.6. The correlation profiles in $R_{u'p'_1}$ for the solid trailing-edge case have a periodicity time of $\tau^* \approx 4.5$, which correspond to $St \approx 0.2$, indicating the presence of long-lasting energy field travelling upstream due to vortex shedding. These results are similar to the observations in Figs. 6.13 and 6.23. At a further upstream location, *i.e.* microphone *p6* at x/h=-1.9, the correlation results still show strong tonal behaviour but the profiles are more symmetric and less skewed. In the case of the porous 80 PPI trailing-edge, the $R_{u'p'}$ cross-correlation results observed for the transducer *p1* are very similar to that of the solid trailing-edge case. However, interestingly, further upstream of the trailing-edge at x/h=-1.9, it is noticed that the u' and p'_6 signals only have a weak correlation in the near the wall region and almost zero correlation away from the wall.

As discussed before, the pressure collected in the case of the porous 25 PPI trailing-edge is purely due to the boundary layer structures travelling downstream. The $R_{u'p'}$ cross-correlation results for the porous 25 PPI trailing-edge at upstream locations (x/h=-1.9) also show that the pressure-velocity correlation is very weak and is confined within $\xi_{y'}/\delta_{BL_1} \lesssim 1$. Moving downstream, in the vicinity of the trailing-edge (x/h=-0.35), the level of pressure-velocity correlation increases, but still remain very small compared to the solid or 80 PPI trailing-edges. The highest correlation region seen for $R_{u'p'_1}$ is concentrated at about $\tau^* \approx 2$ near the wall, with a periodicity corresponding to $St \approx 0.5$, which is similar to the development of the broadband hump observed in the boundary layer velocity spectra in Fig. 6.13 at BL_{3-4} and wall pressure power spectra in Figs. 6.23 and 6.24.

Figure 6.31 presents the coherence between the streamwise and vertical flow velocities and the surface pressure fluctuations measured at *p1*, (x/h=-0.35), corresponding to the main region where strong flow acceleration occurs (see Figs. 6.4 and 6.6). The coherence between the velocity and surface pressure signals is analysed using Eq. 5.12. The left and right columns in Fig. 6.31 show the coherence of the u- and v-components of the flow velocity with the pressure signal ($\gamma^2_{u'p'}$, $\gamma^2_{v'p'}$), respectively. The results in Fig. 6.31 show a strong coherence at the vortex shedding frequency, $St \approx 0.2$ for the case of solid trailing-edge. The velocity-pressure coherence becomes broader and covers a wider range of frequencies ($0.15 \lesssim St \lesssim 0.3$) at about the flow velocity overshoot region (y'/δ_{BL_1} = 1), particularly for the coherence between the vertical flow velocity

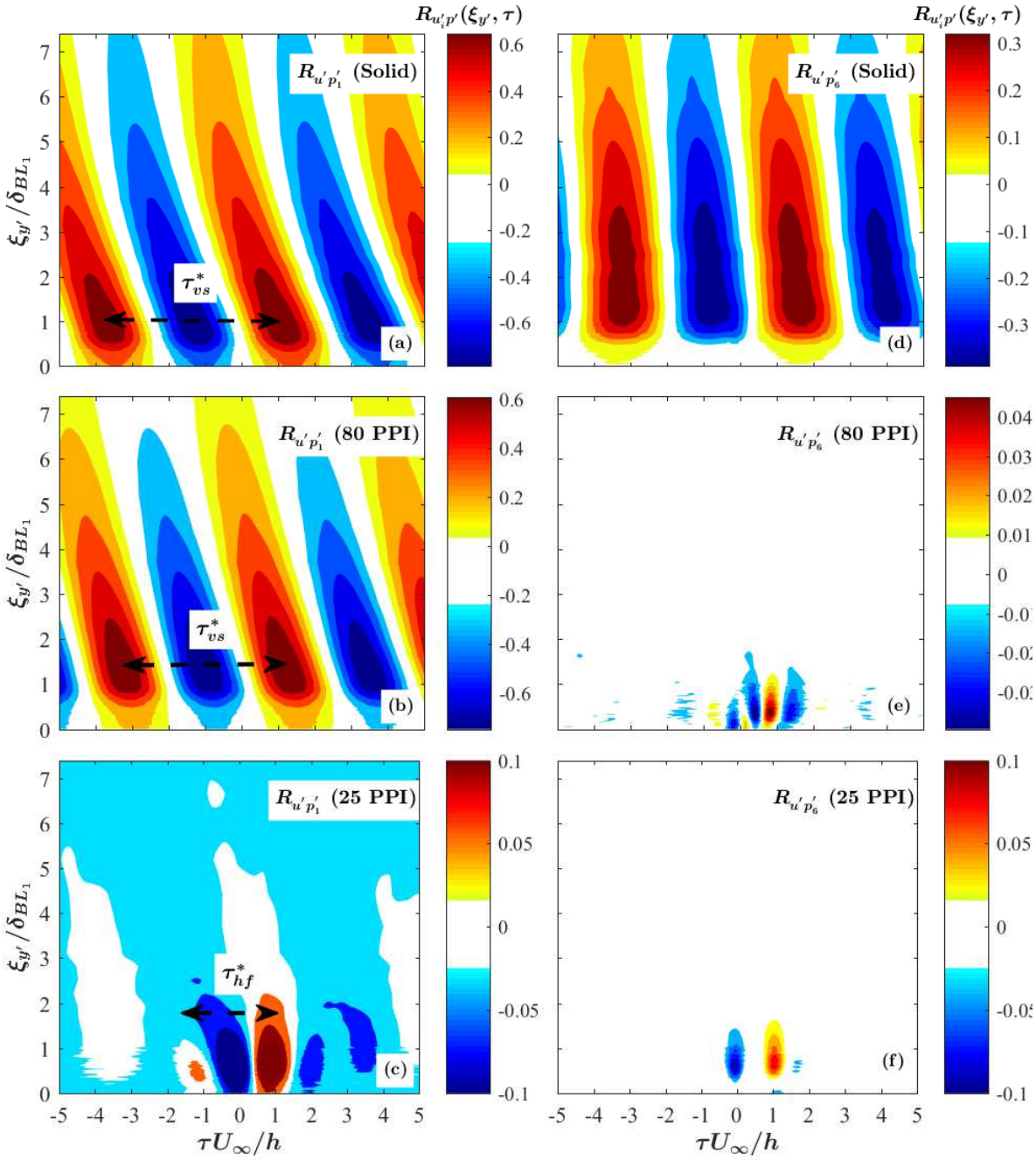

Figure 6.30: Longitudinal space-time correlations between the velocity and the surface pressure fluctuations as a function of $\tau^* = \tau\ U_\infty/h$, at two streamwise locations ($p1$ and $p6$) for solid, porous 80 PPI and porous 25 PPI trailing-edges.

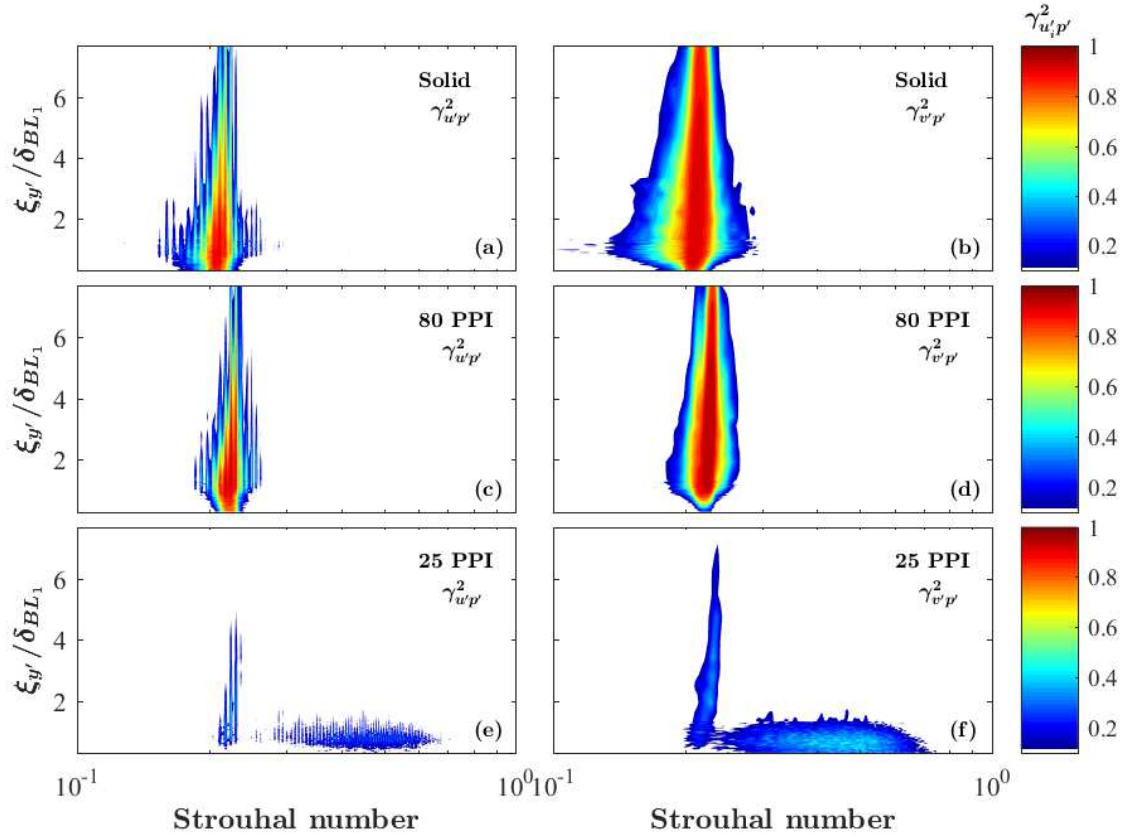

Figure 6.31: Velocity-pressure coherence, $\gamma^2_{u'p'}$ (left column) and $\gamma^2_{v'p'}$ (right column) at location *p1*, (x/h=-0.35) for solid, porous 80 PPI and porous 25 PPI trailing-edges.

component $\gamma^2_{v'p'}$. The $\gamma^2_{v'p'}$ coherence results for the porous 80 PPI trailing-edge show a similar strong coherence at the vortex shedding frequency, $St \approx 0.2$, but with a narrower coherence width ($0.2 \lesssim St \lesssim 0.25$) at $\xi_{y'}/\delta_{BL_1} = 1$, which indicates the reduction of the flow acceleration over the trailing-edge, dominated mainly by the flow vertical movement, as observed in Fig. 6.29. In contrast, a much weaker coherence can be seen at the vortex shedding frequency for the case of the porous 25 PPI trailing-edge, which is consistent with the small peaks observed in Fig. 6.23(x/h=-0.35). Note that, this spectral peak for the case of the 25 PPI material is not visible in the near the wall velocity spectra results (Fig. 6.13(i)). However, at the locations farther from the surface (Fig. 6.13(g)) and in the near wake (Fig. 6.14(x/h=0.1)), the peaks become slightly more visible but strongly attenuated. These findings prove that the energy field due to vortex shedding for the porous 25 PPI trailing-edge is weak, which also corresponds to the delayed

vortical structures from the trailing-edge, as seen in Fig. 6.4. It can be seen that a relatively large area of high velocity-pressure coherence broadband region emerges between St=0.3 to St=0.9 and $0 \lesssim \xi_{y'}/\delta_{BL_1} \lesssim 2$, similar to the results obtained in the boundary layer velocity spectra profiles presented in Fig. 6.13(a, d and g) and 6.23. Unlike the behaviour observed for the energy field from vortex shedding, this broadband region is confined within a spatial domain and dissipates quickly with x and y. This again confirms that this is due to a localized flow circulation hydrodynamic field inside the porous medium, which only occurs in the case of porous materials with high permeability. As shown earlier in Fig. 6.27, the emergence of this hydrodynamic field requires a long enough porous section for enabling flow-porous interaction and flow penetration into the porous medium. In the next section, the effects of the porous section length on the emergence of the internal hydrodynamic field and control of the flow will be examined.

6.4 Flow penetration critical length

The results in § 6.2 have demonstrated that the use of a highly permeable trailing-edge section for a blunt flat plate can lead to the reduction of flow acceleration at the trailing-edge, delay of flow recirculation, suppression of vortex shedding, and reduction of the energy-frequency content of the turbulence structures within the boundary layer and wake. The velocity-pressure coherence analysis in § 6.3, on the other hand, showed that a quasi-period hydrodynamic field may emerge within the porous medium. It has also become clear from the results in the previous sections that the boundary layer flow penetration into the porous medium and then discharges into the near-wake region plays an important role in the above-mentioned effects. To enable a proper flow penetration, the flow requires to remain in contact with the porous section over a long enough surface. The results presented in the previous sections had been obtained for porous sections with a streamwise length of $L_{px} = 2.5h$. In order to find out the critical length required to achieve effective flow control, further experiments have been carried out for porous trailing-edges (25 PPI) with different lengths, *i.e.* $L_{px}/h = 0.5, 1.0, 1.5, 2.0$ and 2.5.

Figure 6.32 compares the time-averaged normalized streamwise velocity (U) around the trailing-edge of the flat plate fitted with different lengths of porous material. The solid trailing-

edge result is also provided for comparison. The hypothesised internal recirculation field is also drawn in the Figs. for illustration purposes only. The results in Fig. 6.32 show that the flow recirculation after the porous trailing-edge shrinks with L_{px} and detaches from the trailing edge surface for $L_{px} > 1$. The results also reveal that the amount of flow discharge from the whole length of the blunt trailing-edge over $-0.5 < y < 0.5$ increases with L_{px}. One can, therefore, link the axial shift in the flow recirculation to the amount of flow discharge from the porous medium, which itself depends on the porous surface length and boundary layer flow penetration into the porous medium. Another interesting observation is the effect of the porous section length on the flow acceleration zone above the trailing-edge. It can be observed that in the case of long enough porous sections, the uniform flow discharge from the blunt trailing-edge reduces the velocity gradient in the vertical direction and weakens the flow acceleration.

The effect of the porous section length can be further analysed using the wall pressure power spectral density results (ϕ_{pp}) at a point near the trailing-edge, x/h=-0.35 *(p1)*, as presented in Fig. 6.33(a). Results are presented for five porous section lengths ($L_{px}/h = 2.5, 2, 1.5, 1$ and 0.5) and also the solid trailing-edge. The localized broadband hump observed previously in the surface pressure results (Fig. 6.23) is shown to be highly sensitive to the porous section length. It can be seen apparently that the broadband hump appears only for the long porous treatments. Results also show that the fundamental vortex shedding frequency at $St = 0.21$ become stronger and approaches that of a solid trailing-edge for the shorter porous treatments. This shows that the shorter porous treatments do not have a particularly strong internal hydrodynamic field and are also unable to eliminate the vortex shedding. The influence of the porous trailing-edge treatment length on the flow recirculation in the near-wake region was also investigated in this study. Figure 6.33(b) shows the wake flow velocity PSD (ϕ_{uu}) at $x/h = 0.5$ and $y/h = 0.5$ obtained using a single hotwire probe. The results evidently show that the use of shorter porous sections ($L_{px} = 1.5h, 1h$ and $0.5h$) can barely change the tonal behaviour of the flow at the fundamental ($St = 0.21$) and the first harmonic ($St = 0.45$) frequencies. The results show that the suppression of the tonal peaks and the emergence of the broadband hump occurs only for the porous section lengths of $L_{px} = 2.5h$ and $2h$. This confirms that the suppression of the near-wake vortex shedding can be attributed to the emergence of a quasi-periodic flow-recirculation field inside the porous

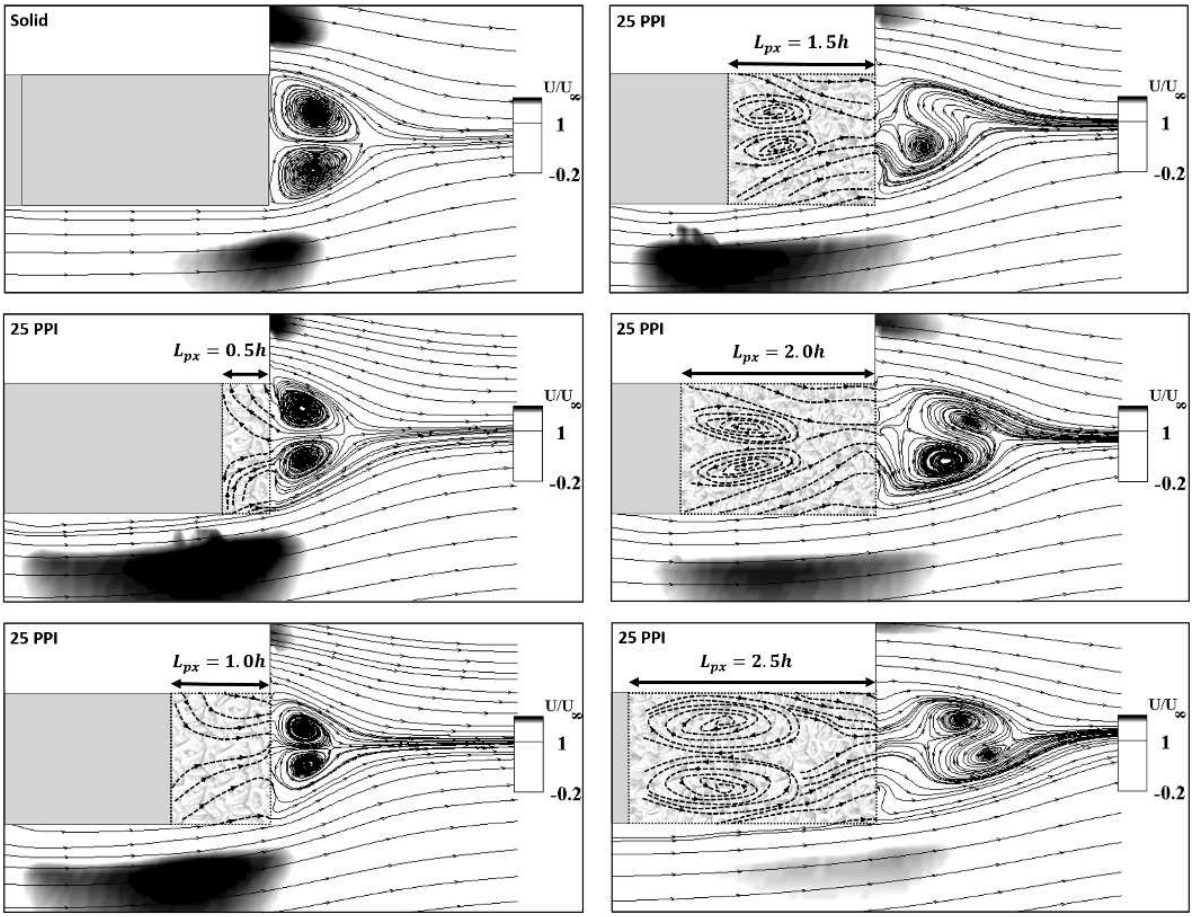

Figure 6.32: Time-averaged streamline flow pattern and illustration of hypothesised flow recirculation zone inside the porous medium with different porous section length (L_{px}). *Illustration of the hypothesised internal recirculation field (- - -).*

medium.

Finally, to better understand the emergence of the internal hydrodynamic field and its relationship with the porous treatment length (L_{px}), detailed pressure autocorrelation and velocity-pressure coherence studies have been carried out. Figure 6.34 summarizes the autocorrelation and the velocity-pressure coherence ($\gamma^2_{u'p'}$) results for the *p1* transducer (x/h= -0.35), where flow acceleration is expected. Results are presented for different porous treatment lengths. The surface pressure autocorrelation result for a standard zero-pressure-gradient boundary layer at $Re_\theta = 4.0 \times 10^3$ (dotted-line) and the solid trailing-edge (circles) are also provided for the sake of comparison. As expected, the autocorrelation for a standard boundary layer decays quickly to nearly zero within $|\tau^*| < 3$, while in the case of the solid trailing-edge $R_{p'_i p'_i}$ has a

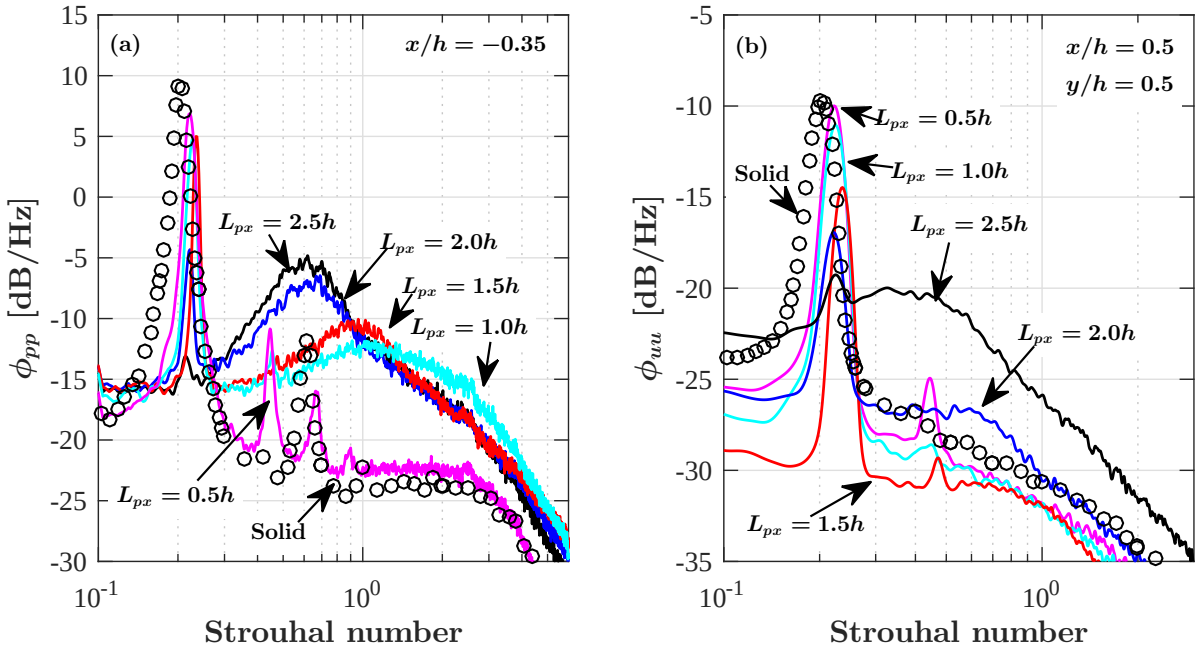

Figure 6.33: (a) Wall pressure fluctuations with different porous 25 PPI trailing-edge lengths at x/h=-0.35 *(p1)*, (b) The power spectral density of the streamwise velocity in the wake at x/h=0.5 and y/h=0.5.

strong periodic behaviour, due to the vortex shedding, and maintains its amplitude for a long period of time (τ^*). The autocorrelation results for the porous trailing-edges confirm again that there exists a critical length for the elimination of the vortex shedding and the emergence of the quasi-periodic hydrodynamic field within the porous medium. The quasi-periodic internal hydrodynamic field for the long porous treatments, particularly for the cases with $L_{px} > 1.5h$, manifests itself as a fast decaying oscillation within $|\tau^*| < 3$ in the pressure autocorrelation results and as a broadband high coherence region near the wall in the pressure-velocity coherence figures. The velocity-pressure coherence results also confirm the suppression of vortex shedding and emergence of a broadband hump for the long porous treatments. Finally, one can conclude based on the pressure and velocity PSD and coherence results that (a) the suppression of flow acceleration and the delay of flow recirculation depends on the level of flow discharged from the porous medium into the wake, (b) to ensure enough flow discharge into the near-wake region, a relatively long porous section of about $L_{px} = 2h$ is required, (c) the use of a relatively long porous section can lead to the emergence of a quasi-periodic flow recirculation region in the porous

section, which then results in a localized fast-decaying broadband hump.

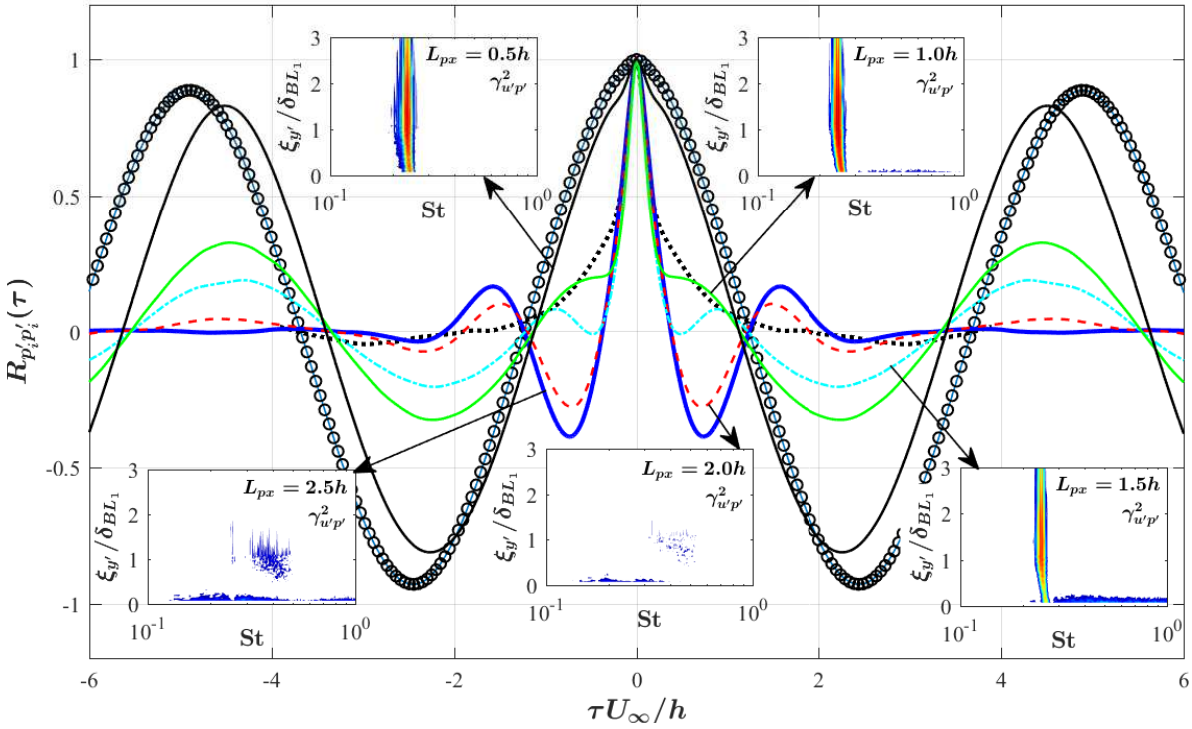

Figure 6.34: Autocorrelation of the wall pressure fluctuations with different porous 25 PPI trailing-edge lengths at x/h=-0.35 *(p1). Solid trailing-edge (circle line);* L_{px}*=2.5h(——);* L_{px}*=2.0h (- - -);* L_{px}*=1.5h (- - -);* L_{px}*=1.0h (——);* L_{px}*=0.5h (——), Standard boundary layer (·····).*

6.5 Aeroacoustic results

This section is concerned with the far-field noise measurement from the blunt flat plate test rig and the effect of the porous treatment on the radiated noise. The far-field noise measurements are carried out in aeroacoustics facility of the University of Bristol. An array of 23 GRAS 40PL free-field microphones, with a dynamic range of 142 dB, placed 1.75 m from the plate trailing edge has been used, as shown in Fig. 6.35. The microphone array covers the polar angle range of 25° to 135°, with a regular interval of 5°. To enable near-field to far-field analysis a single FG-23329-P07 transducer was placed at x/h=-0.35 from the plate trailing-edge. The surface pressure transducer along with the far-field microphone was used simultaneously for the measurement of the coherence between the near-field boundary layer pressure exerted on the plate trailing

edge and the far-field noise. The noise data have been collected for the flow velocities of up to U_∞=60 m/s, corresponding to the plate thickness-based Reynolds number of 1.5×10^6.

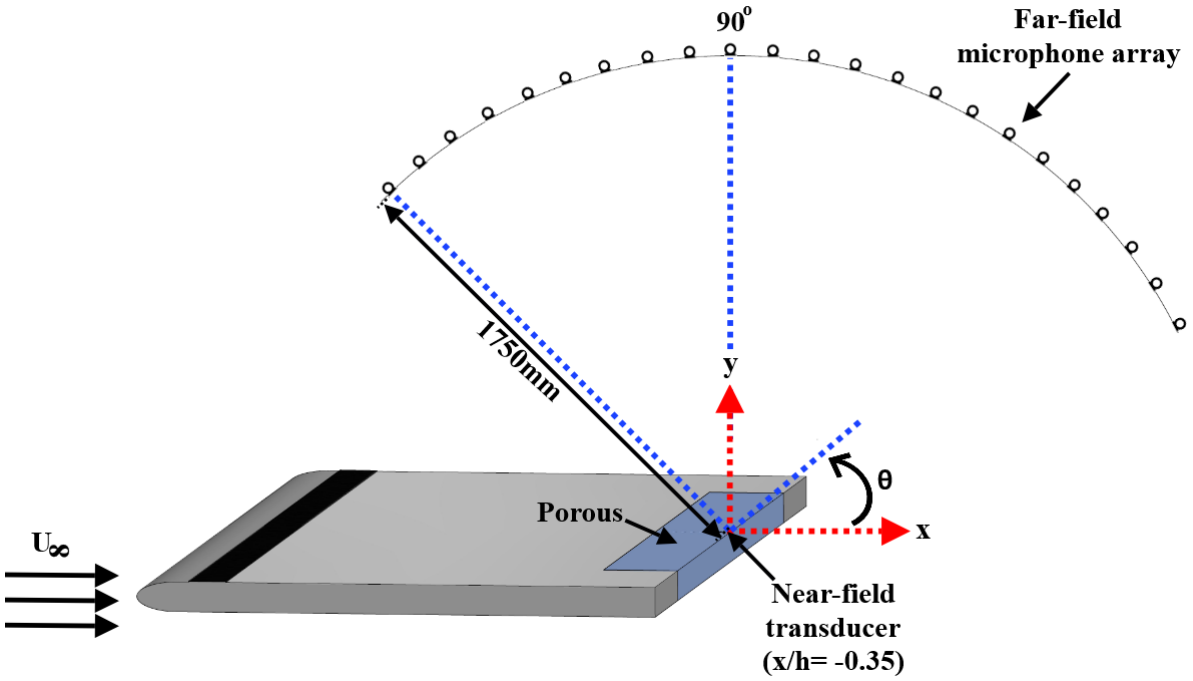

Figure 6.35: Schematic of the setup used for the acoustic measurements (not to scale).

6.5.1 Near-field surface pressure noise results

Figure 6.36 shows the surface pressure level (SPL) obtained from the near-field surface pressure transducer *p1* ($x/h = -0.35$). The trend of the results presented in Fig. 6.36 is very similar to the power spectral density of the surface pressure fluctuations results obtained from the measurements conducted in the open jet wind tunnel (see Fig. 6.23). The vortex shedding peak can be seen at $St \approx 0.18$ for the solid case with the peak for the 80 PPI slightly shifted to higher Strouhal number. Similar to the results obtained in Fig. 6.23, the tonal peak is almost completely suppressed by the 25 PPI case, which confirms that the vortex shedding has been effectively eliminated using the porous treatment in the near-field locations. Results have also shown that the porous treatment leads to an increase in the broadband energy content in the whole frequency range, especially for the 25 PPI case, which is believed to be due to (a) the frictional forces

between the flow and the rough porous surface and (b) the hypothesised hydrodynamic field inside the porous medium. The comparison of the sound pressure level results for the 25 PPI surface, surface pressure fluctuations results (Fig. 6.23) and the velocity PSD results near the wall (Fig. 6.13 (BP_{1-3},BL_4)) and near-wake (Fig. 6.14) shows that development of a similar broadband hump at about $St \approx 0.5$.

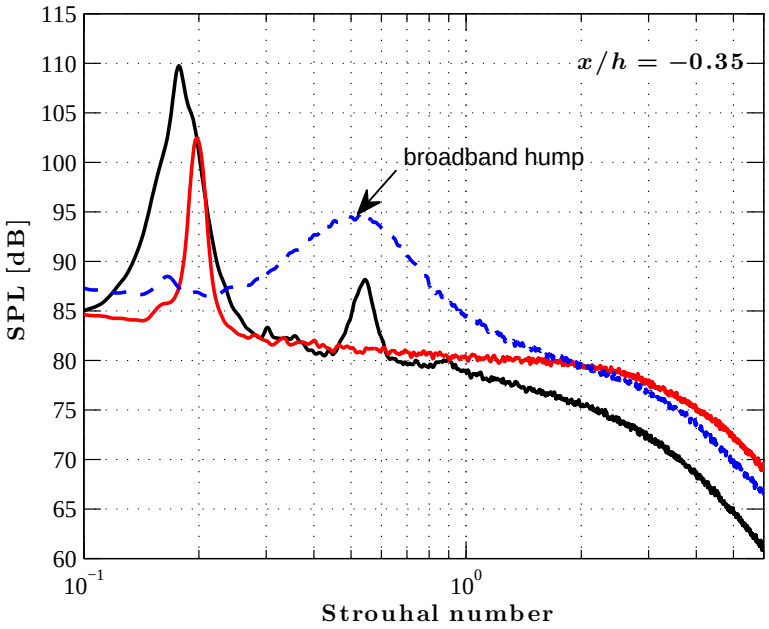

Figure 6.36: Sound pressure level spectra of the surface pressure fluctuations (reference to 20μPa) measured at $x/h = -0.35$ and U_∞=30 m/s. *Solid trailing-edge (——), Porous 80 PPI trailing-edge (——), Porous 25 PPI trailing-edge (- - -).*

6.5.2 Far-field noise results

Figure 6.37 presents the contour plot of the far-field sound pressure level at polar angles of 45°, 60°, 90° and 120° as a function of velocity and frequency with and without the porous treatment. The sound pressure level (SPL) spectrum can be calculated using,

$$\mathrm{SPL} = 20 \cdot \log 10\left(\frac{P_{rms}}{P_{ref}}\right), \tag{6.19}$$

where P_{rms} is the root-mean-square of the acoustic pressure and P_{ref} is the reference pressure at 20 μPa. The power spectrum of the acoustic pressure signal is corrected to a reference distance

of 1 m, as

$$\mathrm{SPL} = \mathrm{SPL}_{87.5h} + 20 \cdot \log 10\left(\frac{R_i}{R_N}\right), \tag{6.20}$$

where $\mathrm{SPL}_{87.5h}$ is the measured sound pressure level, in decibels at the original far-field transducers location, R_i are the original distances from the plate position to the far-field microphones and R_N is the reference distance of 1 m from the plate position to the far-field microphones.

The results for the solid case (Fig. 6.37 (a,d,g,j)) show a clear slope that passes through the Strouhal peaks. These Strouhal peaks correspond to the vortex shedding peak which can be seen at all the microphones measured, at different polar angles. It can be seen that the sound pressure level at the vortex shedding frequencies is relatively stronger at higher polar angles, especially at the polar angle of 90°, above the plate trailing-edge. The vortex shedding peak, however, is not seen at the low velocities ($U_\infty \leq 30$ m/s). Results also shown that the first harmonics of the vortex shedding frequency at different velocities can be clearly seen at the polar angles of 45°, 60°, 90° and 120°, with weaker sound pressure level at the vortex shedding peak. In the case of the porous 80 PPI trailing-edge, while a weak peak can be observed at the fundamental vortex shedding frequency, the first harmonic ($St = 0.4$ line) of the vortex shedding frequency is suppressed compared to that of the solid case. On the contrary, the 25 PPI material eliminates the vortex shedding peak entirely and an area of high broadband sound pressure level emerges at higher frequencies ($f > 1000$ Hz), which is believed to be due to the frictional forces between the flow and the rough porous surface.

In order to visualize the results presented in Fig. 6.37 more clearly, the changes in the sound pressure level of the far-field noise measured between the solid trailing-edge and the 80 PPI and 25 PPI porous trailing-edges ($\Delta\mathrm{SPL} = \mathrm{SPL}_{\mathrm{porous}}\text{-}\mathrm{SPL}_{\mathrm{solid}}$) are presented in Fig. 6.38. The results in Figs. 6.38(a) to 6.38(h) show the contour plots of ΔSPL as a function of the frequency and the mean velocity at the polar angles of 45°, 60°, 90° and 120°, respectively. As observed in Fig. 6.37, a clear slope that passes through the Strouhal peaks at the vortex shedding frequency can be seen at different flow velocities. In the case of $\Delta\mathrm{SPL}_{80\ \mathrm{PPI-Solid}}$, it can be seen that there is a reduction in the sound pressure level of about 15-20 dB along the Strouhal line at all microphones locations, where vortex shedding is at its most prominent.

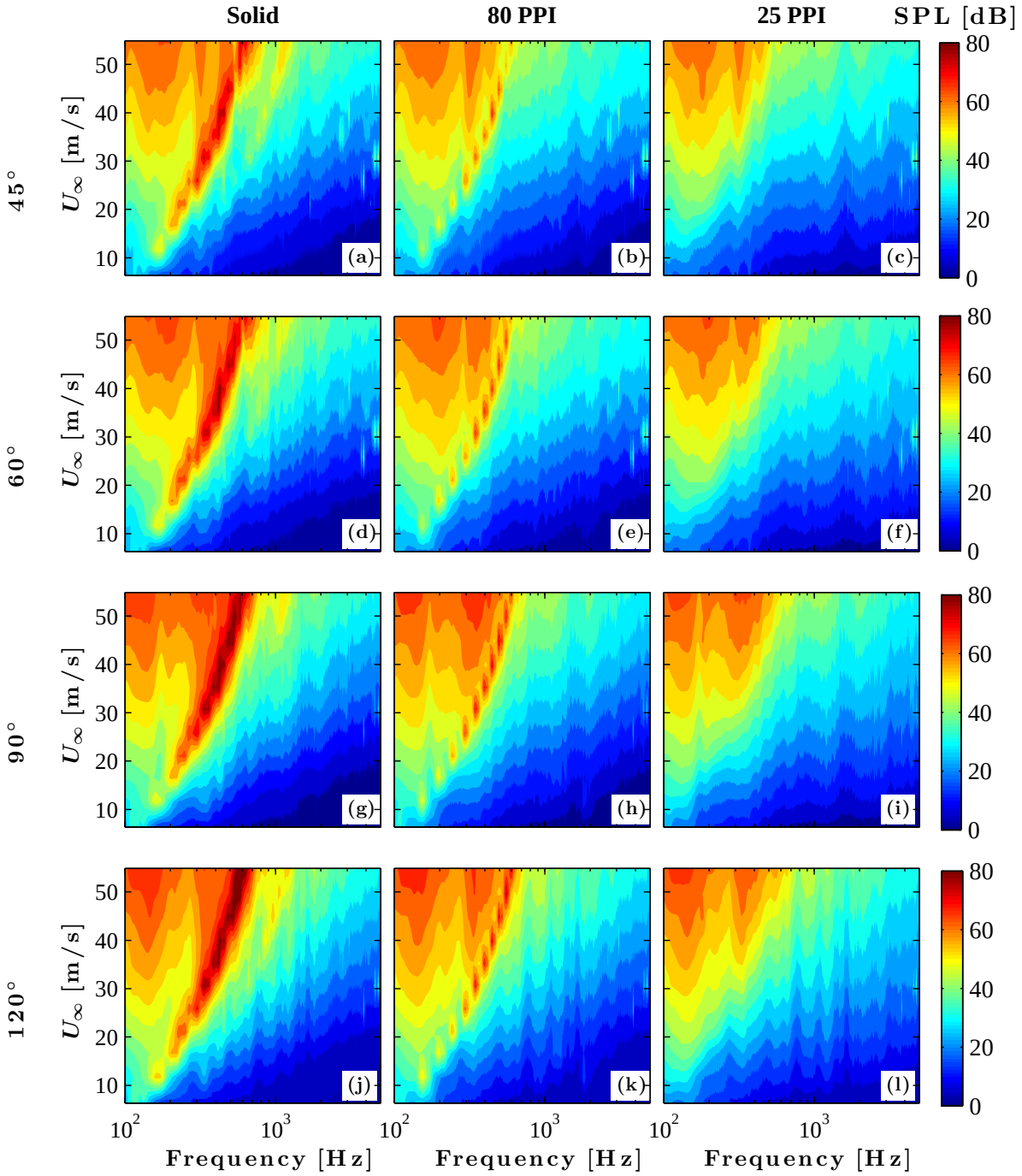

Figure 6.37: Sound pressure level (SPL [dB]) contour plots of the far-field noise with reference to 20μPa at polar angles of 45°, 60°, 90° and 120° as a function of velocity and frequency.

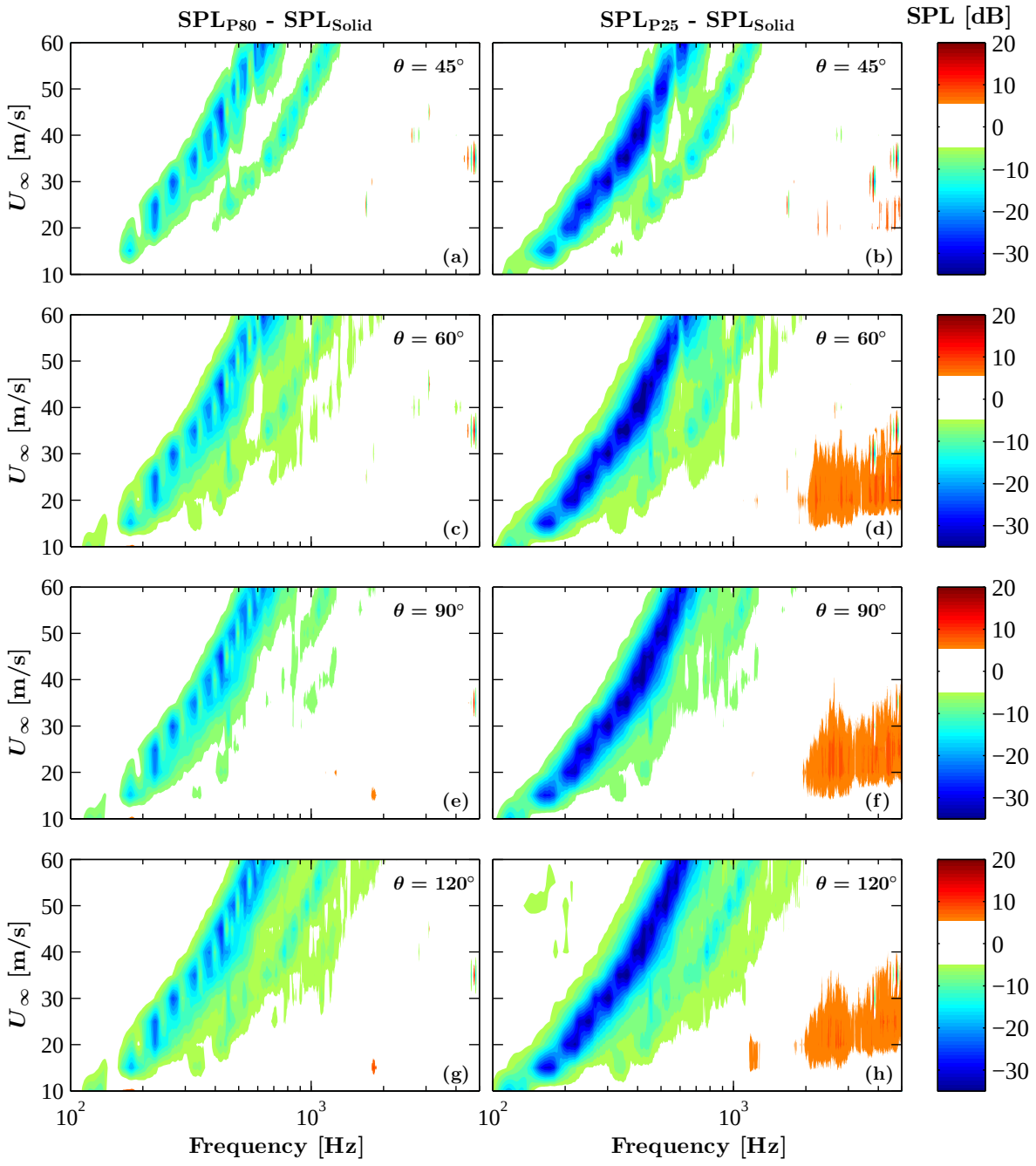

Figure 6.38: Change in the sound pressure level (Δ SPL [dB]) of the far-field noise with reference to 20μPa at polar angles of 45°, 60°, 90° and 120°.

In the case of $\Delta SPL_{25\ PPI-Solid}$, a significant vortex shedding tonal noise reduction in excess of about 35 dB is observed at all microphones locations. However, the results have also shown that the porous 25 PPI treatment can increase the broadband energy content of the radiated

noise in the higher frequency range at all the microphones locations. The fundamental and the first harmonics of the vortex shedding frequency can be clearly seen from the results obtained at all the polar angles measured. The noise increase associated with the frictional forces at the surface of plate seem to have a strong dependency on the radiation angle (θ), particularly at low flow speeds.

In order to interpret the results presented in Fig. 6.38 clearly, the surface pressure level (SPL) as a function of the Strouhal number obtained from the far-field microphones located at the polar angles of 45°, 60°, 90° and 120°, and flow velocity of U_∞=30 m/s are shown in Fig. 6.39.

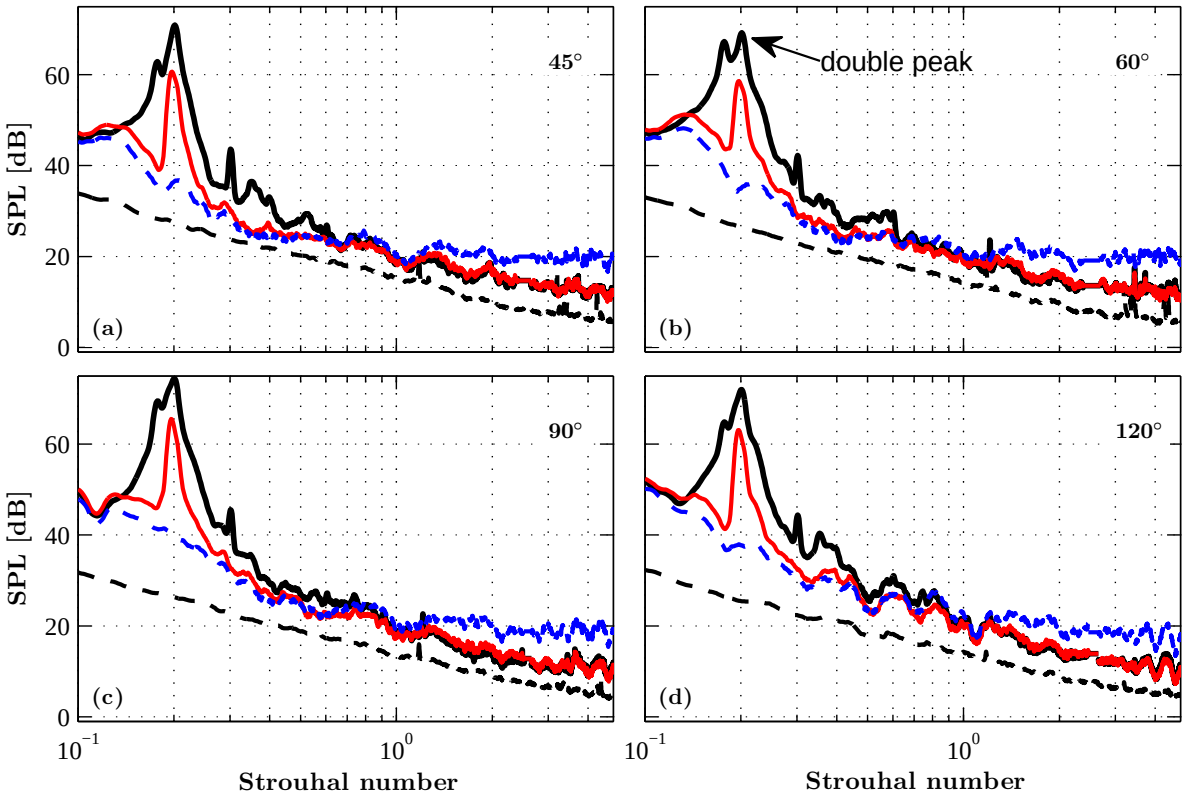

Figure 6.39: Sound pressure level spectra of the far-field pressure fluctuations with reference to 20μPa at polar angles of 45°, 60°, 90° and 120°, measured at U_∞=30 m/s. *Solid trailing-edge (——), Porous 80 PPI trailing-edge (——), Porous 25 PPI trailing-edge (- - -), Background noise (·····).*

The vortex shedding peak can be seen at $St \approx 0.2$ at all microphone locations for the solid case, similar to the surface pressure results observed in Fig. 6.36. The results also have shown the emergence of a double vortex shedding peak at around the fundamental shedding frequency

($St \approx 0.2$) in the case of the solid trailing-edge, indicating the existence of two types of vortical structures in the far-field measurement. This phenomena, however, is not seen in the near-field surface presseure measurement (Fig. 6.36). This double peak consists of a dominant peak at $St \approx 0.2$ and a lower amplitude secondary dominant peak at a lower frequency at $St \approx 0.18$ (at the angle of 90°). Note that the amplitude of the secondary dominant peak for the solid case is much lower at other angles (45°, 60° and 120°). Moreau and Doolan [225] argued that the existence of multiple dominant peaks in the noise spectra is due to the cellular variation in spanwise vortex shedding frequency, *i.e.* the dominant peak is attributed to the strong regular vortex shedding behind the plate trailing-edge, while the secondary dominant peak can be possibly associated to the lower frequency shedding near the plate trailing-edge. This, however, needs further experimental and numerical investigations. In the case of porous 80 PPI, the double peak observed in the solid case becomes a single peak with a decreased amplitude at the shedding frequency. It is also observed that there is a consistent reduction of the tonal peaks in the noise spectra at all angles. Similar to the results obtained from Fig. 6.36, no tonal peak is seen for the 25 PPI case, which again confirms that the vortex shedding has been effectively eliminated using the porous treatment, not only in the near-field locations but also in the far-field locations.

The tonal peak for the case of solid trailing-edge protrudes by about 25 dB above the broadband energy content while that for porous 80 PPI is in the order of about 18 dB, and almost negligible for porous 25 PPI case at all the microphones located at different polar angles. Unlike the results observed in Figs. 6.36 and 6.23, the far-field noise spectra results have shown that the 25 PPI treatment can increase the broadband energy content only in the high frequency range, which is believed to be due to the frictional forces between the flow and the rough porous surface. Also, the comparison of the sound pressure level results for the 25 PPI case and the surface pressure fluctuations results (Fig. 6.36) show that the development of the broadband hump is only local to the plate surface and not observed in the far-field noise spectra. Hence, the broadband hump is seen to be local to the trailing-edge region and dissipates very quickly further downstream (streamwise direction) and above (vertical direction) the plate trailing-edge.

6.5.3 Far-field noise directivity

The measurements of the overall sound pressure level (OASPL) are obtained by integrating the energy spectrum with respect to frequency using,

$$\text{OASPL} = 10 \cdot \log 10 \left[\frac{\int \text{PSD}(f)\, \mathrm{d}f}{P_{ref}^2} \right], \tag{6.21}$$

where PSD is the power spectral density based on the unsteady pressure $p^{'}$ (where $p^{'} = p - p_{mean}$), calculated using the Welch power spectral density method [175]. In the present work, the resolved frequency f ranges from 100 Hz to 32 kHz.

Figure 6.40 shows the directivity of the overall acoustic waves for the solid and porous treated cases at U_∞=20 m/s, 30 m/s, 40 m/s and 50 m/s. The polar angle θ is defined with respect to the flow direction, see Fig. 6.35.

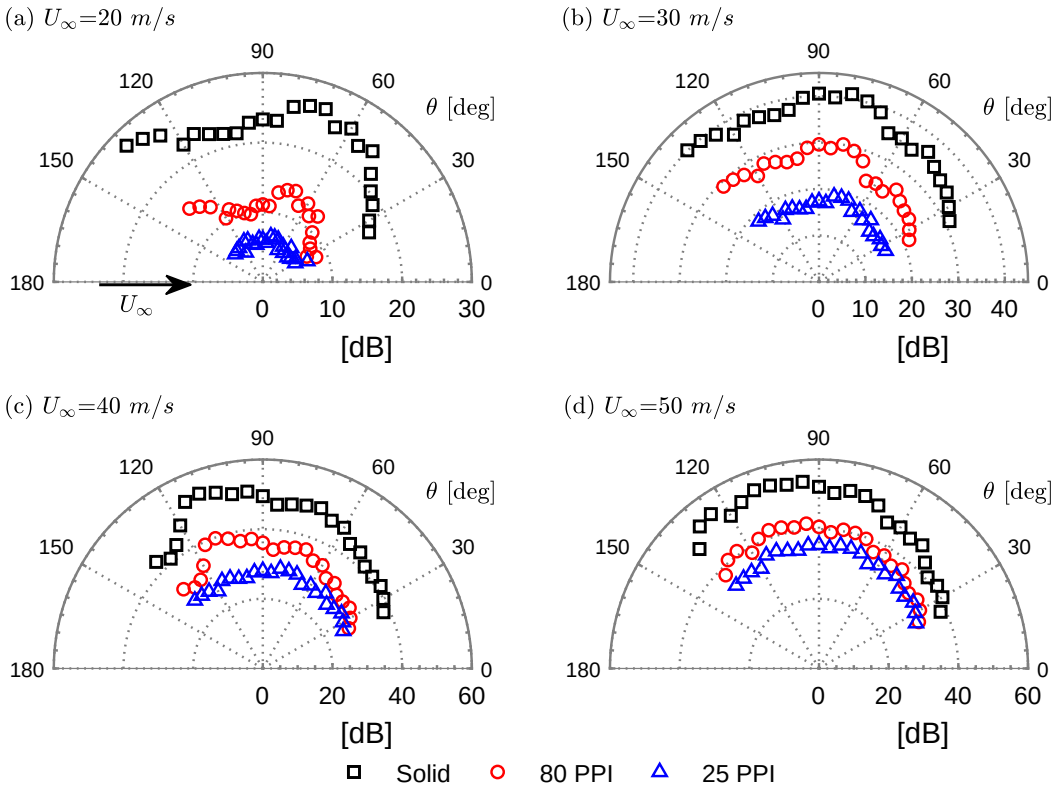

Figure 6.40: Overall sound pressure level (OASPL) of the acoustic waves generated by the trailing-edge configurations with and without the porous treatments at U_∞=20 m/s, 30 m/s, 40 m/s and 50 m/s.

The results clearly show that the porous trailing-edges reduce the overall sound pressure level (OASPL) over the polar angles for all the velocities measured, especially for the 25 PPI material. The results have also shown that the directivity peaks at $\theta = 90^\circ$ for all the cases at high velocities (≥ 30 m/s), and a maximum reduction of about 25 dB can be seen for the 25 PPI case relative to the solid case. In the downstream direction $\theta \leq 45^\circ$, the noise reduction by the porous trailing-edges are much smaller at all the velocities.

The directivity plots at different frequencies with and without the porous treatments at a flow speed of U_∞=30 m/s are shown in Fig. 6.41. The results are presented with different scales for the purpose of better visualization and clarity. The directivity results demonstrate a dipole-like pattern, which is oriented perpendicular to the mean flow velocity. At $St = 0.1$, the amplitude of the acoustic waves seems to remain almost similar for all the cases. At $St = 0.2$, the directivity patterns for all the cases exhibit primary lobes which are more akin to a dipole at $\theta = 90^\circ$ and inclined in the downstream direction ($\theta = 50^\circ$). It can be seen that the amplitude of the vortex shedding tone decreases for the porous treated cases, especially for the 25 PPI case, with up to 35 dB reduction at $\theta = 90^\circ$. The radiated sound directivity is more pronounced at St=0.3 and 0.4, where multiple lobes can be seen in the directivity pattern for all the cases measured. It can also be seen that the reduction in noise for all the treated cases at all the polar angles becomes smaller as the frequencies increases, *i.e.* at higher Strouhal number (St=0.3, 0.4 and 0.5). Note that, at $St = 0.5$, the directivity of the acoustic waves for the 25 PPI porous treatment remains lower than that of the solid case, which is inconsistent with the appearance of a broadband hump at the same St number observed in the near-field surface pressure results (Fig.6.36). The results obtained in Fig.6.41, however, show a good agreement with the far-field results observed in Figs. 6.37, 6.38 and 6.39, where no broadband hump is seen at the far-field locations. This broadband hump is observed to be local to the trailing-edge region, and dissipates very quickly above the plate trailing-edge locations. A noise increase can be seen in the case of the 25 PPI treatment at St=1.0, 1.5 and 2.0 is, due to the roughness of the porous surface. In contrast, the directivity of the acoustic waves generated by the lower permeability material (80 PPI) is almost similar to that of the solid case at high frequencies, which is consistent with the results obtained in Figs. 6.38 and 6.39.

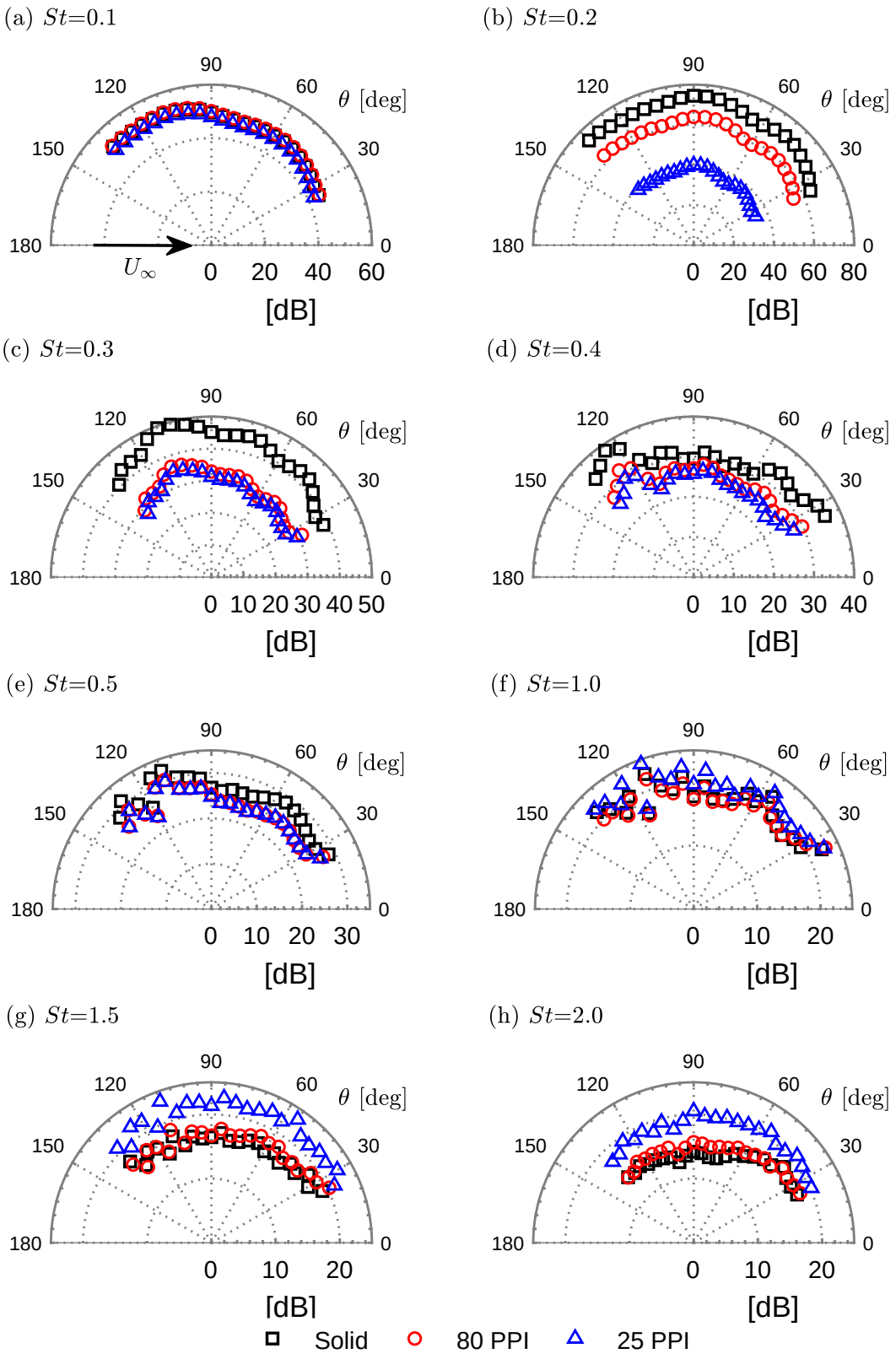

Figure 6.41: Directivity of the acoustic waves generated by the trailing-edge configurations with and without the porous treatments at U_∞=30 m/s for Strouhal number (a) $St = 0.1$, (b) $St = 0.2$, (c) $St = 0.3$, (d) $St = 0.4$, (e) $St = 0.5$, (f) $St = 1.0$, (g) $St = 1.5$ and (h) $St = 2.0$.

6.5.4 Near-field to far-field analysis

Figure 6.42 presents the coherence $\gamma^2_{p'_1 p'_\theta}$ between the surface pressure signals at *p1*, (x/h=-0.35) and the far-field signals at $\theta = 45°$, 60°, 90° and 120° at 30 *m/s*. The *p1* surface pressure transducer location corresponds to the main region where strong flow acceleration occurs (see Figs. 6.4 and 6.6). The coherence between the surface pressure and the far-field pressure signals can be found from,

$$\gamma^2_{p'_1 p'_\theta}(f) = \frac{|\Phi(f, p'_1, p'_\theta)|^2}{|\Phi(f, p'_1, p'_1)||\Phi(f, p'_\theta, p'_\theta)|}, \tag{6.22}$$

where $\Phi(f, p'_1, p'_\theta)$ denotes the cross-power spectral density function between the surface pressure (*p1*) and the far-field pressure signals (p_θ) at different polar angles.

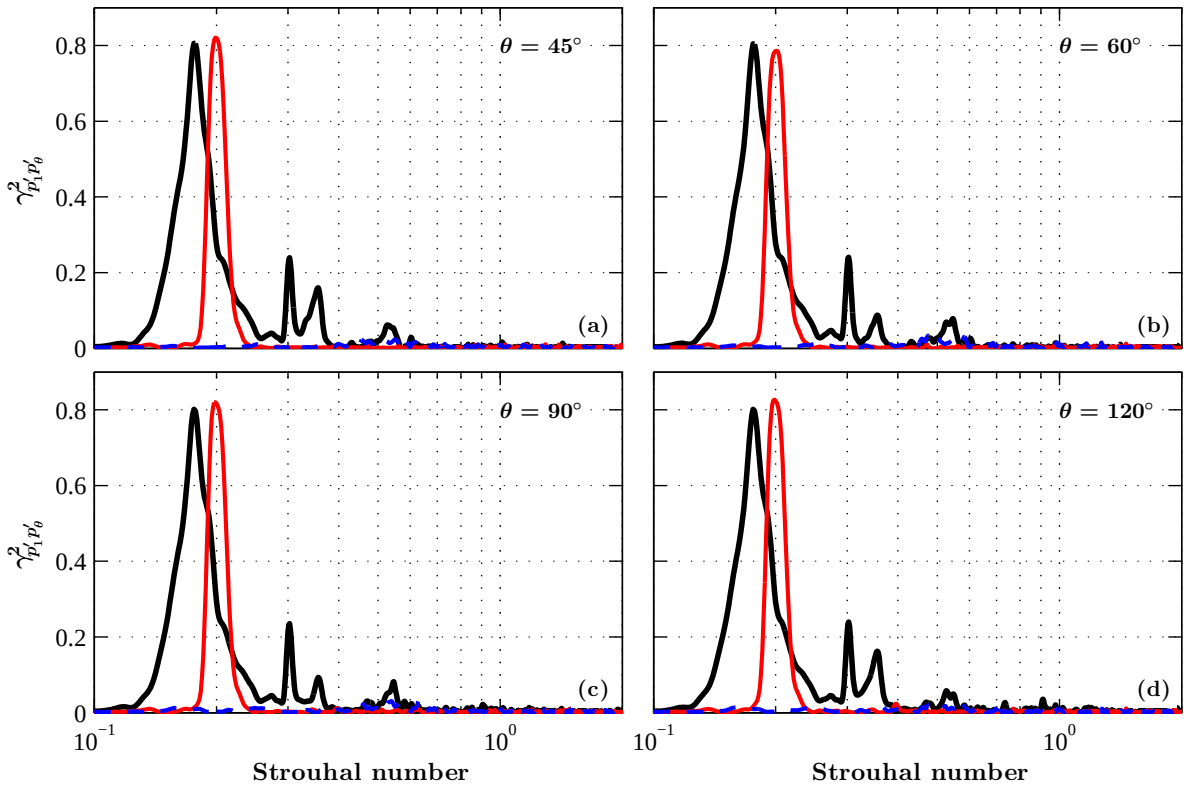

Figure 6.42: Near-field to far-field coherence between a surface pressure transducer at $x/h = -0.35$ (*p1*) and far-field microphones at $\theta = 45°$, $\theta = 60°$, $\theta = 90°$ and $\theta = 120°$. The measurements are taken at U_∞=30 *m/s*.*Solid trailing edge (—), Porous 80 PPI trailing edge (—), Porous 25 PPI trailing edge (- - -).*

The coherence ($\gamma^2_{p'_1 p'_\theta}$) results are plotted as a function of the Strouhal number. In the case of solid trailing-edge, as expected, a strong coherence can be observed at the vortex shedding frequency, about St =0.18 between the pressure signals at all the polar angles measured. The fundamental, first and second harmonics of the coherence ($\gamma^2_{p'_1 p'_\theta}$) at the vortex shedding frequency can be clearly seen from the results of the solid trailing-edge. Interestingly, the $\gamma^2_{p'_1 p'_\theta}$ results for the solid trailing-edge seem to indicate the existence of two different phenomena at the near- and far-field regions, (a) the $\gamma^2_{p'_1 p'_\theta}$ results which peaks at St =0.18 is consistent with the near-field surface pressure results (Fig. 6.36) and (b) the $\gamma^2_{p'_1 p'_\theta}$ results only occur at the lower amplitude secondary dominant peak at St =0.18 observed in the sound pressure level spectra in the far-field region (Fig. 6.39). In the case of porous 80 PPI trailing-edge, the treatment is unable to change the tonal characteristics of the flow structures. However, as observed before in Figs. 6.25, 6.31, the reduction of the broadband energy content has made the tones to protrude well above the broadband spectra, more than that of the solid trailing-edge and eliminates the peak harmonics seen in the case of the solid trailing-edge. On the contrary, the 25 PPI material eliminates the vortex shedding peak entirely and exhibits almost zero-coherence level, indicating that the two pressure signals are completely uncorrelated. Moreover, the area of broadband hump emerges at around $St \approx 0.5$ in Figs. 6.13 (BP_{1-3},BL_4), 6.14, 6.23 and 6.36 is not seen in the results presented in Fig. 6.42, which also indicates that the existence of the broadband hump is local to the plate surface region.

Figure 6.43 presents the coherence $\gamma^2_{p'_1 p'_{90^\circ}}$ between the surface pressure signals at *p1*, (x/h=-0.35) and the far-field signals at $\theta = 90^\circ$ for a wide range of velocities between 10 m/s to 60 m/s. The left column plots (a, c and e) show the coherence between the pressure signals for all the velocities while the right column plots (b, d and f) show the coherence contour plots presented as a function of frequency and velocity. In the case of the solid trailing-edge, as expected, a strong coherence can be observed at the vortex shedding frequencies between the pressure signals. The pressure coherence becomes slightly broader and covers the low frequency region (150 Hz to 350 Hz) at the flow velocity of $U_\infty = 10$ m/s to 30 m/s. A weak coherence level can also be seen at the fundamental, first and second harmonics of the vortex shedding frequency, especially for higher flow speed (Fig. 6.43(b)). In the case of the porous 80 PPI trailing-edge, while

a strong coherence can be observed at the fundamental vortex shedding frequency, the coherence of the turbulent structure is much narrower in width and decays quickly with U_∞ at other frequencies. In contrast, a much weaker $\gamma^2_{p'_1 p'_{90°}}$ can be seen at the lower flow speed (U_∞=10 m/s) and completely eliminates the vortex shedding peak at higher flow speed ($U_\infty > 10 m/s$), which is similar to the results observed in Figs. 6.36 and 6.39. Similar to the results observed in Fig. 6.42, the area of broadband hump is not seen in Fig. 6.43, indicating that the existence of the broadband hump is local to the plate surface region.

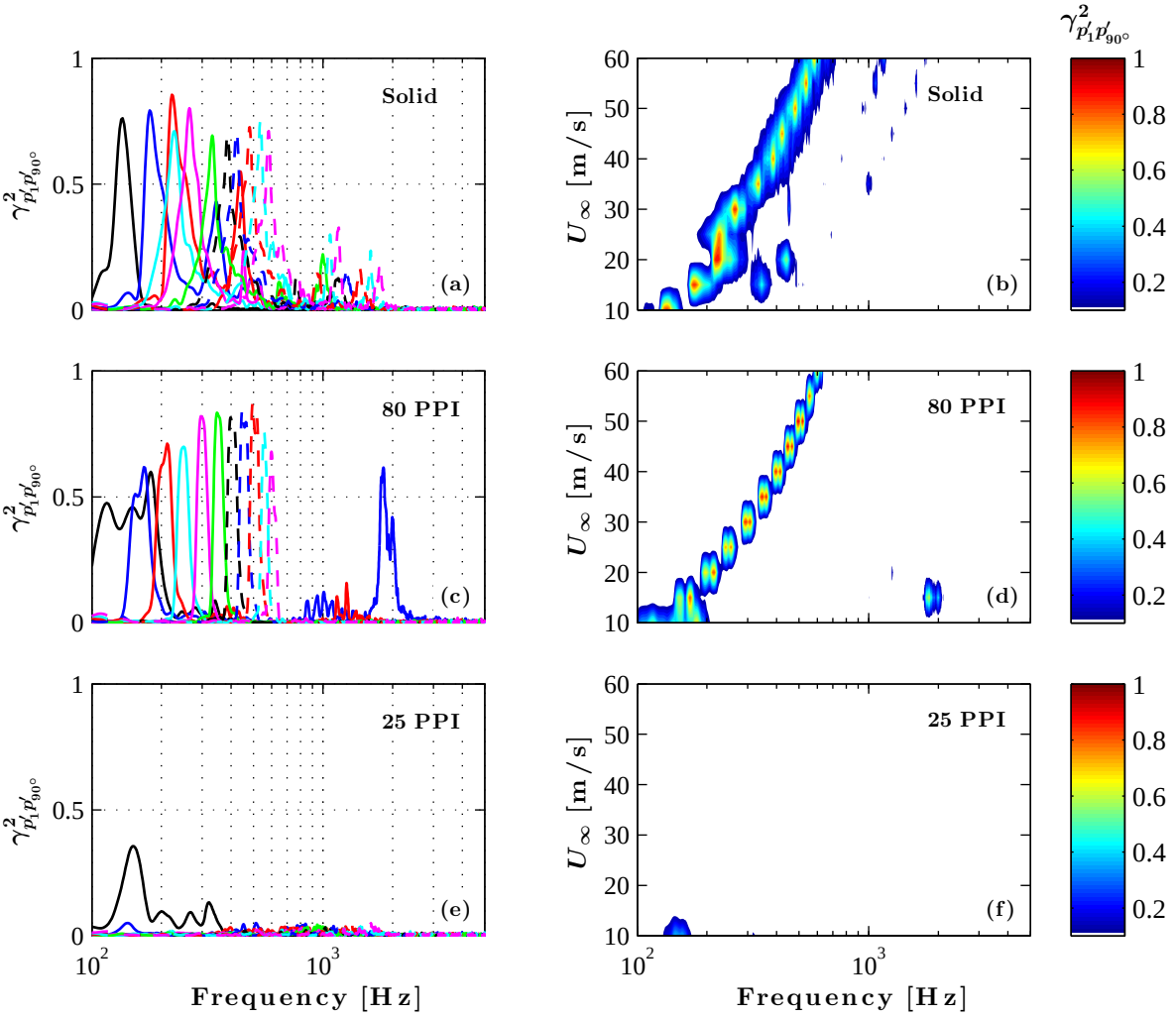

Figure 6.43: Near-field to far-field coherence between a surface pressure transducer at $x/h = -0.35$ ($p1$) and far-field microphones at $\theta = 90°$. The measurements are taken at different velocities. *10 m/s (——), 15 m/s (——), 20 m/s (——), 25 m/s (——), 30 m/s (——), 35 m/s (——), 40 m/s (- - -), 45 m/s (- - -), 50 m/s (- - -), 55 m/s (- - -), 60 m/s (- - -).*

6.5.5 Flow penetration critical length

It has been shown from the previous sections that the boundary layer flow penetration into the porous medium and then discharges into the near-wake region can lead to the reduction of flow acceleration and delay of vortex shedding (Figs. 6.4 and 6.6), reduction of the energy-frequency content of the turbulent structures within the boundary layer and wake (Figs. 6.13 and 6.14), emergence of a quasi-period hydrodynamic field within the porous medium (Figs. 6.24), etc. To allow a proper flow penetration in the porous medium, the flow requires to remain in contact with the porous section over a long enough surface. The results in Fig. 6.33 have shown that the the use of shorter porous sections (L_{px}/h=1.5, 1 and 0.5) can barely change the tonal behaviour of the flow at the fundamental (St=0.21) and harmonic frequencies (St=0.45). However, the use of a longer porous section lengths (L_{px}/h=2.5 and 2) can lead to the suppression of the tonal peaks and the emergence of the broadband hump. The far-field results (Figs. 6.39) obtained for the porous sections with $L_{px}/h = 2.5$ show that the 25 PPI material is able to suppress the vortex shedding tonal peak significantly, with up to 35 dB reduction at θ= 90°. In order to find out the relationship between the porous section length and the far-field noise, further experiments have been conducted using the 25 PPI material with different lengths, *i.e.* $L_{px}/h = 2.5, 2, 1.5, 1$ and 0.5.

6.5.5.1 Far-field noise results

The effect of the porous section length can be further analyzed using the far-field microphones located at the polar angles of 45°, 60°, 90° and 120° at flow velocity of U_∞=30 m/s, as presented in Fig. 6.44. Results are presented for porous section lengths with streamwise lengths of $L_{px}/h = 2.5, 2, 1.5, 1$ and 0.5. The far-field results trend between all the measured cases are similar at all the polar angles, with a slight difference in the amplitude of the fundamental vortex shedding peaks and its harmonics. The results in Fig. 6.44 show that a high amplitude double vortex shedding peak can be observed in the shorter porous section lengths spectra ($L_{px}/h = 2, 1.5, 1.0$ and 0.5), indicating the presence of two types of vortical structures in the far-field measurements. This double peak consists of a dominant peak at St=0.21 for $L_{px}/h = 0.5$ and at St=0.23 for $L_{px}/h = 2, 1.5$ and 1.0. A lower amplitude of the secondary dominant peak can be seen at lower frequency at St=0.19 for L_{px}/h= 2 and 1.5, while in the case with $L_{px}/h = 1.0$, a higher amplitude

of the secondary dominant peak is observed at St=0.21. The amplitude of the both the dominant and secondary dominant peaks for all the cases is much higher at higher angles. As mentioned in § 6.5.2, the multiple dominant peaks can be attributed to the cellular variation in the spanwise vortex shedding frequency [225]. In the case of the longer porous section (L_{px}/h= 2.5), as expected, the vortex shedding tonal peaks and its harmonics have been effectively eliminated. Moreover, the broadband hump observed previously in the surface pressure results Fig. 6.33 for the longer porous section lengths (L_{px}/h=2.5 and 2) is not seen in the far-field noise spectra, which shows that the emergence of the broadband hump is local to the plate surface.

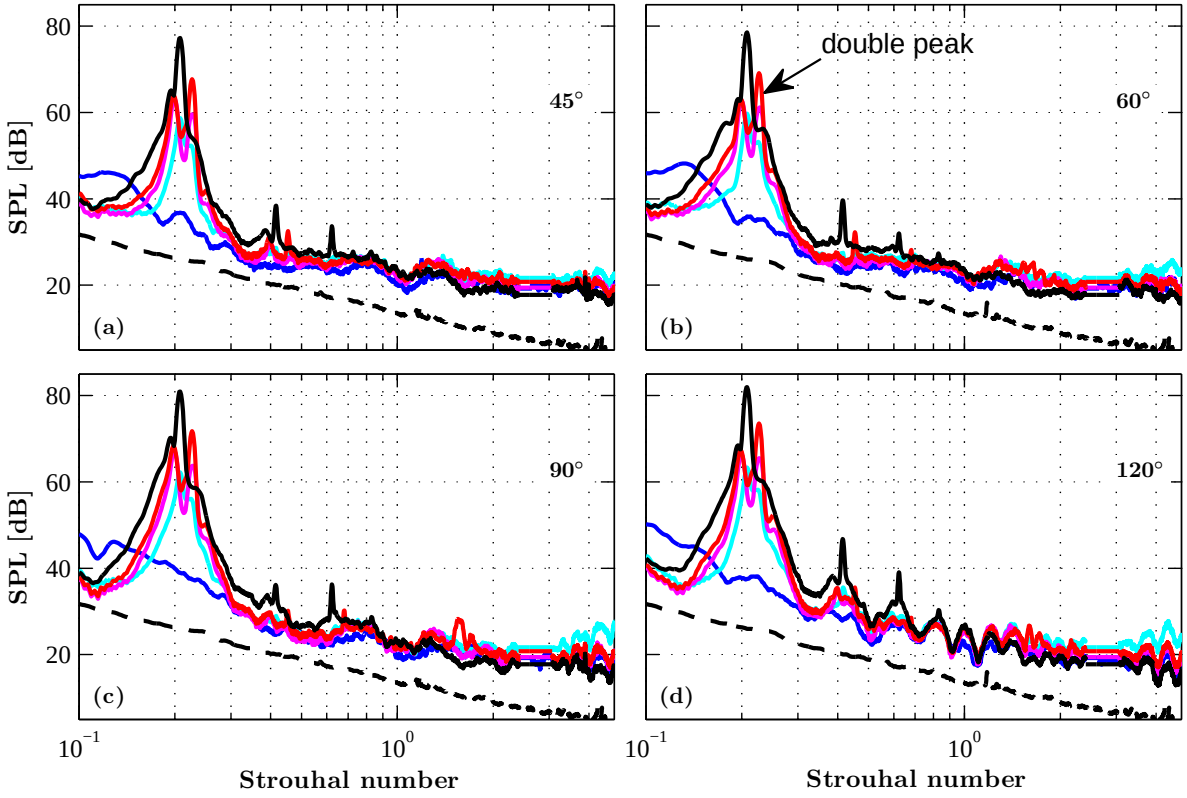

Figure 6.44: Sound pressure level spectra of the far-field pressure fluctuations for different porous 25 PPI section length with reference to 20μPa at polar angles of 45°, 60°, 90° and 120°, measured at U_∞=30 m/s. $L_{px} = 2.5h$ (——), $L_{px} = 2.0h$ (——), $L_{px} = 1.5h$ (——), $L_{px} = 1.0h$(——), $L_{px} = 0.5h$ (——), *Background noise* (·····).

6.5.5.2 Near-field to far-field analysis

Figure 6.45 shows the effects of the porous section length on the coherence, $\gamma^2_{p_1'p_\theta'}$ between the surface pressure at a point near the trailing-edge, x/h=-0.35 *(p1)* and far-field pressure signals at $\theta = 45°$, $60°$, $90°$ and $120°$ at U_∞=30 m/s. Results are presented for five porous 25 PPI section lengths ($L_{px}/h = 2.5, 2, 1.5, 1$ and 0.5).

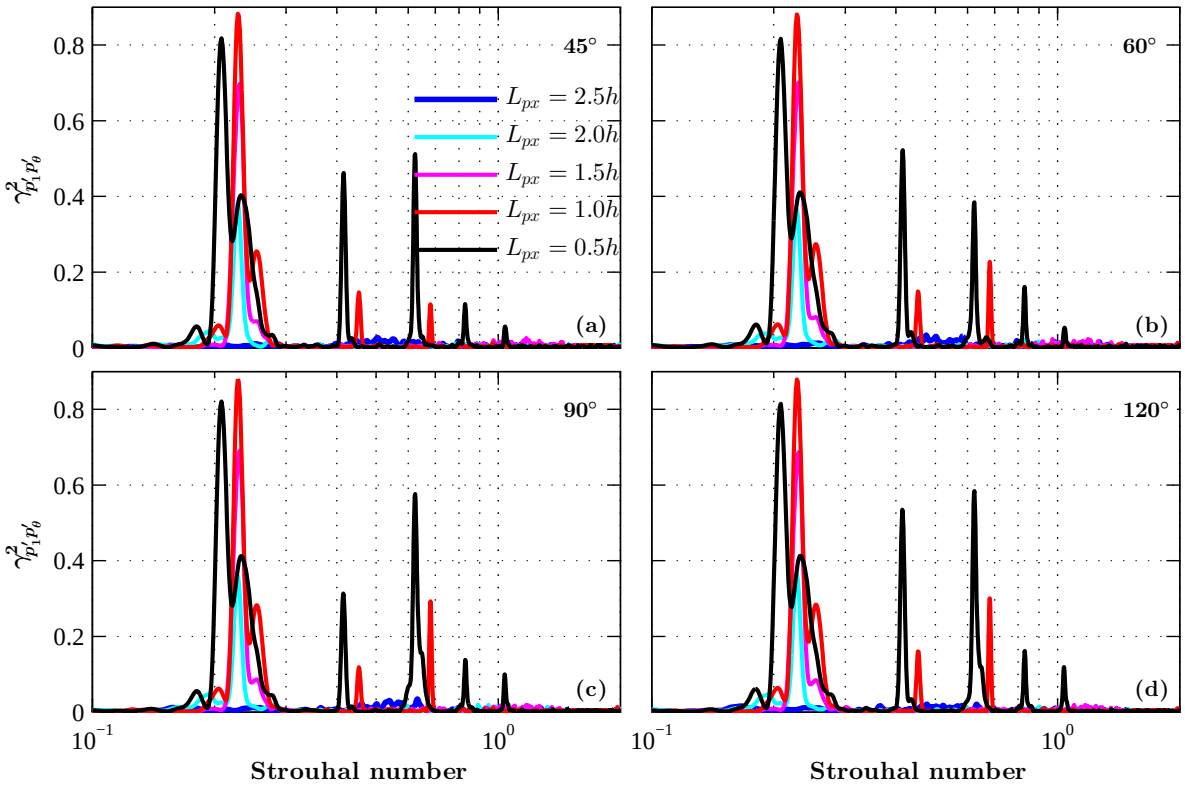

Figure 6.45: Near-field to far-field coherence between a surface pressure transducer at $x/h = -0.35$ *(p1)* and far-field microphones for different porous section lengths at $\theta = 45°$, $\theta = 60°$, $\theta = 90°$ and $\theta = 120°$. The measurements are taken at U_∞=30 m/s.

The localized broadband hump observed previously in the surface pressure results (Fig. 6.23) is shown to be highly sensitive to the porous section length, however, it can be seen that the broadband hump is absent in the coherence $\gamma^2_{p_1'p_\theta'}$ results involving the far-field pressure signals for all the porous 25 PPI section lengths (L_{px}/h). In the case of 25 PPI trailing-edge with $L_{px}/h = 2.5$, the vortex shedding peak has been eliminated entirely. The tonal behaviour of the flow

is seen to be more pronounced for the shorter porous trailing-edge sections ($L_{px} = 2.0h, 1.5h, 1h$ and $0.5h$). Interestingly, a double peak tonal behaviour can be seen at the fundamental vortex shedding peak for the 25 PPI trailing-edge sections with L_{px}= $1h$ and $0.5h$. The double peak consists of a dominant peak at St=0.2 and St=0.22 and a lower amplitude secondary peak at a higher frequency (St=0.25 and St=0.27), for the L_{px}= $1h$ and $0.5h$ configurations, respectively. In addition, the fundamental, first, second, third and fourth harmonics frequencies can be observed for the shortest porous treatment with a streamwise length of L_{px}= $0.5h$. The results trend between all the measured cases are quite similar at all the angles ($\theta = 45°$, $60°$, $90°$ and $120°$), with a slight difference in the amplitude of the $\gamma^2_{p'_1 p'_\theta}$ peaks.

Figure 6.46 shows the effects of the porous section length on the coherence, $\gamma^2_{p'_1 p'_{90°}}$ between the surface pressure at a point near the trailing-edge, x/h=-0.35 *(p1)* and a far-field point at $\theta = 90°$. Results are present at different flow speeds of U_∞=10 m/s to 60 m/s. Figure 6.46 clearly shows that the fundamental vortex shedding frequency at different flow speeds becomes stronger and approaches that of a solid trailing-edge (Fig. 6.43(b)) for the shorter porous treatments (Fig. 6.46(d-j)). It can also be observed that a high amplitude double vortex shedding peak is observed for the shorter porous treatments coherence spectra. The results clearly show that the use of short porous sections ($L_{px} = 2.0h, 1.5h, 1h$ and $0.5h$) can barely change the tonal behaviour of the flow at the vortex shedding fundamental frequency or the first four harmonics. The results also show that the suppression of the tonal peaks occurs only for the porous section lengths of $L_{px} \geq 2.0h$. This confirms that the suppression of the vortex shedding peak can be attributed to the emergence of a quasi-periodic flow-recirculation field inside the porous medium, established from the results obtained in Fig. 6.33. Hence, it can be summarized that the boundary layer flow penetration into the porous medium with enough porous section length can lead to the suppression of the vortex shedding tonal peak. This phenomena is consistent with the findings obtained from the previous sections (§ 6.2, § 6.3, § 6.4 and § 6.5), where the porous 25 PPI treatment can lead to the reduction of flow acceleration, delay of vortex shedding, reduction of the energy-frequency content of the turbulent structures within the boundary layer and wake, the emergence of a quasi-period hydrodynamic field within the porous medium and reduction of far-field noise, etc.

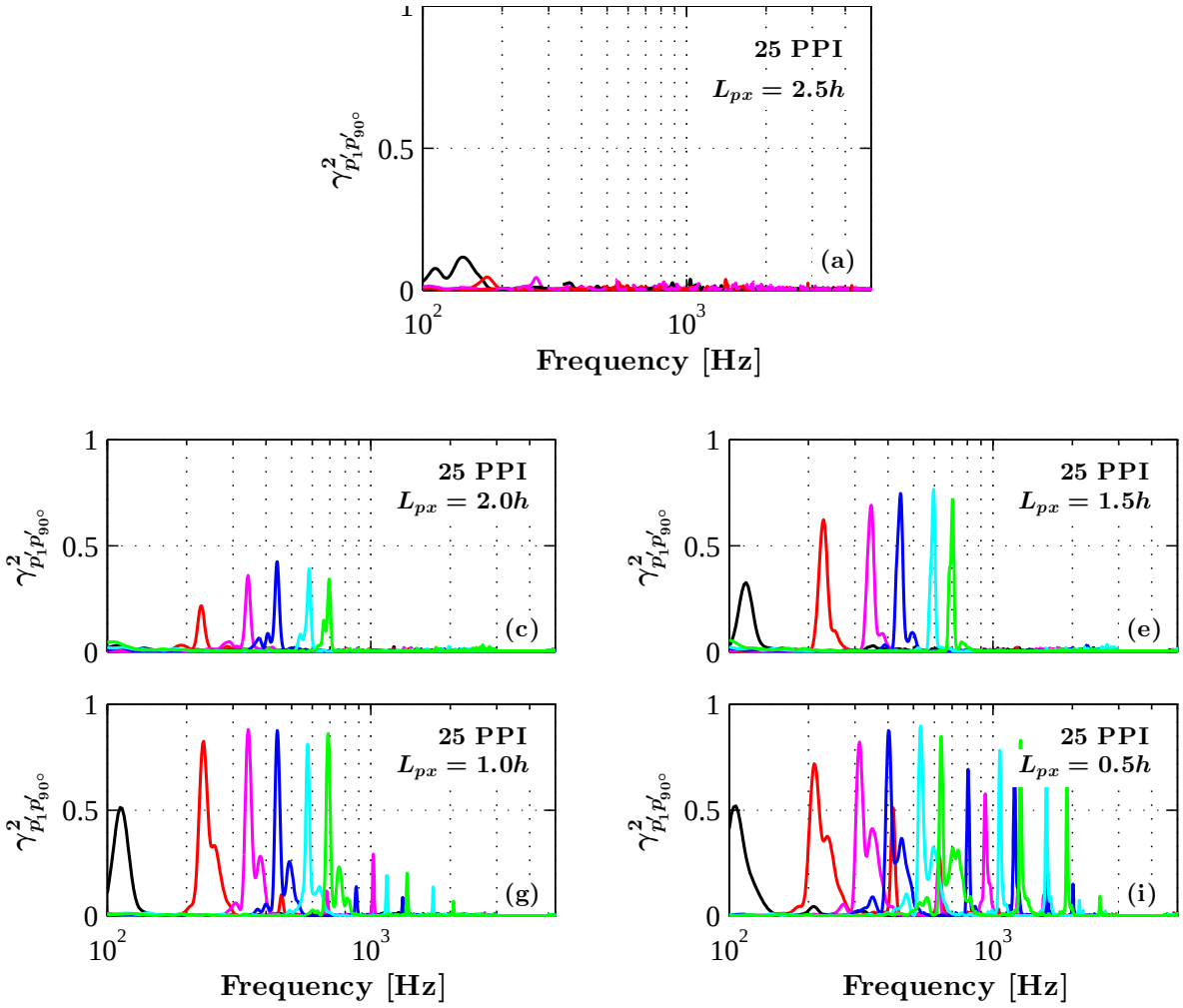

Figure 6.46: Near-field to far-field coherence between a surface pressure transducer at $x/h = -0.35$ ($p1$) and far-field microphones for different porous section lengths at $\theta = 90°$. The measurements are taken at U_∞=30 *m/s*. *10 m/s (—), 20 m/s (—), 30 m/s (—), 40 m/s (—), 50 m/s (—), 60 m/s (—).*

6.6 Summary

A series of experiments were conducted with two different type of porous materials to determine the effect of porous trailing-edge on the aerodynamic and aeroacoustic of a blunt trailing-edge body. The main conclusions of this chapter are given below.

i. Results have shown that the use of the porous materials with high PPI and low permeability behave more or less like the solid case, which can be explained by the fact that for the

porous medium with low permeability, a longer flow and porous-surface interaction is needed to enable flow penetration into the porous medium. In contrast, the use of the highly permeable porous treatments (porous 25 PPI) can significantly reduce the drag force. The significant reduction obtained for the case of 25 PPI can be attributed to the flow penetration into the pores, flow discharge into the wake and attenuation of the vortex shedding from the trailing-edge.

ii. Results have shown that the flow penetration into the porous trailing-edge section and then discharge into the near wake can lead to some complex phenomena, such as the reduction of flow acceleration over the trailing-edge, delay and weakening of the vortex shedding and break-up of large coherent wake structures. A significant delay in the formation of the vortex shedding due to interaction of the flow with the porous treatment, particularly for the 25 PPI treatment case, which also results in the reduction of drag.

iii. The boundary layer results have also revealed that the 25 PPI treatment case exhibits flow which is more streamline over the trailing-edge and experiences much less acceleration in the trailing-edge region. Results also have shown that the energy content of the large low-frequency boundary layer structures can be significantly reduced using a highly permeable surface. The use of the 25 PPI material is shown to increase the energy content of the velocity fluctuations over a small region in the vicinity of the porous surface, which can be attributed to the frictional forces at the surface of the porous material.

iv. The spanwise coherence of the structures has also been shown to reduce considerably, which shows the break-up of these coherent structures. While using permeable surfaces leads to the suppression of the fundamental vortex shedding frequency ($St = 0.2$), the emergence of a broadband hump at higher frequencies ($St = 0.5$) indicated the presence of a weak recirculating flow zone inside the porous medium.

v. Results have shown that the emergence of the internal hydrodynamic field and suppression of the vortex shedding in the near-wake are related and that both depend on the length of the flow porous section interacting with the flow. Based on the experimental observation, a long enough porous section is needed to enable flow penetration into the porous medium and discharge into the wake.

vi. The far-field results have shown that the porous treatments can effectively eliminate the vortex shedding tonal peak, leading to a maximum noise reduction of about 8 dB and 35 dB by the 80 PPI and 25 PPI trailing-edges, respectively compared to that of the solid trailing-edge. The results also have indicated that the development of the broadband hump seen in the near-field noise spectra for the highly permeable surface is only local to the plate surface and not observed in the far-field noise spectra. This shows that the broadband hump dissipates very quickly above (vertical direction) the plate trailing-edge.

The results in this chapter provide the impetus for further experimental and numerical studies on the use of porous treatment and development of tailored porous material for aerodynamic and aeroacoustic applications.

CHAPTER 7

CONCLUSIONS AND FUTURE WORKS

This chapter summarizes the main conclusions from the present work of the applications of porous treatments for aerodynamic and aeroacoustic purposes. The use of porous materials for aerodynamic and aeroacoustic purposes has been the subject of many numerical investigations and a limited number of experimental studies in the past. The present work is an experimental attempt to shed some light on the underlying physics of some of the phenomena observed previously in other studies and provides an evidence-based discussion on other potential candidates responsible for flow and noise control using porous media. To do so, the flow interaction and the aerodynamic noise characteristics have been thoroughly investigated using a long zero-pressure gradient flat-plate and an elongated flat-plate with blunt trailing-edge, with and without the porous treatments. Despite its simplicity, the experimental test-rig used in this study enables a large variety of different flow-porous interaction studies, such as the flow scrubbing, surface roughness, flow penetration, porous-flow viscous interaction, hydrodynamic absorption effects, flow acceleration, vortex shedding and noise generation of the porous media. The use of porous treatments for flow control and suppression of aerodynamic noise at source has been the subject of many studies in the past. With regard to the noise abatement applications, while most recent attention has focused on the reduction of the far-field noise from bluff-bodies and aerofoils using porous treatments, the near-field studies have shown that the changes to the

boundary layer and wake flow structures by the porous media are pivotal to the success of the porous treatment as a passive method. The porosity, permeability and surface roughness of the porous, as well as its geometrical characteristics, has been observed to be the key. also related to the sources of the radiated noise.

The flow and noise generation mechanisms studied have been that relevance to noise from the zero pressure gradient turbulent boundary layer flow with a rough permeable surface and the vortex shedding interaction from a blunt trailing-edge. These complex mechanisms have been comprehensively and systematically investigated experimentally by studying various aspects of flow-porous interaction, such as the scrubbing effects, break-up of boundary layer coherent structures, flow penetration, internal hydrodynamic field, flow discharge and vortex shedding attenuation. The effects of the porous substrate on the flow characteristics have been examined by performing various detailed measurements in the boundary layer and wake using the force balance, hotwire Anemometry, Particle Image Velocimetry (PIV), steady and unsteady surface pressure transducers and far-field microphones. In order to better understand the effects of porous surfaces on the noise generation, simultaneous measurements between the unsteady surface pressure fluctuations and the turbulent boundary layer and wake flow field have been carried out. This provides us with an in-depth understanding of the relationship between the wall pressure fields and the flow field structures responsible for the wall pressure generation, which is also related to the sources of the radiated noise.

The main conclusions for the two experimental campaigns are given below.

i. **Boundary Layer Flow Interaction with a Permeable Wall**

   The interaction of the boundary layer with a porous surface with finite depth can bring about significant changes to the boundary layer structure and the energy cascade within the boundary layer and the frequency-energy content of the large coherent structures within the boundary layer, mainly responsible for the generation of aerodynamic noise. The surface pressure PSD results have shown that the porous surface treatment causes an increase in the overall pressure exerted on the surface. The results also show a reduction of the surface pressure PSD over the high frequency range at the locations downstream of

the porous section. The near-field studies have shown that the penetration of the boundary layer flow into the highly permeable porous media can generate an internal hydrodynamic field, which can, in turn, significantly reduce the frequency-energy content of the large boundary layer coherent structures and their spanwise correlation length. This again can reduce the noise generation efficiency. Results have also shown that a relatively long porous section is required to enable flow penetration inside the porous substrate. Moreover, it has been observed that the existence of a quasi-periodic hydrodynamic field inside the porous medium and the reduction in the velocity-pressure coherence over the porous surface are inter-related and dependent on the effective length of the porous section. In addition to the direct application of the outcomes of this study to the field of aeroacoustics and for development of bespoke aerodynamic-noise control techniques, the data can also be useful in other fields, such as aerodynamics of low drag surfaces, heat transfer of porous media, etc.

ii. **Bluntness Flow and Noise Control Using Porous Treatments**

Employing porous treatments for a plate with blunt edge has shown to delay the flow recirculation in the wake, which can then lead to significant reduction of the unsteady aerodynamic forces acting on the body and consequently reduction of the far-field noise. This is found to be mainly due to the flow penetration into the porous medium and re-ejection of a low momentum fluid into the wake. Results have also shown that the flow penetration into the porous trailing-edge section and then discharge into the near wake can lead to some complex phenomena, such as the reduction of flow acceleration over the trailing-edge, delay and weakening of the vortex shedding and break-up of large coherent wake structures. Moreover, the boundary layer results have revealed that the energy content of the large low-frequency boundary layer structures can be significantly reduced using highly permeable surfaces. The spanwise coherence of the structures has also been shown to reduce considerably, which shows the break-up of these coherent structures. While using permeable surfaces leads to the suppression of the fundamental vortex shedding tonal frequency ($St = 0.2$), the emergence of a broadband hump at higher frequencies ($St = 0.5$) indicated the presence of a weak recirculating flow zone inside the porous medium. The

mechanism of flow penetration and re-injection depends heavily on the hydrodynamic field generated within the porous medium, which itself can depend on the structure and geometrical characteristic of the porous treatment, as defined in Chapter 4. Results have shown that the emergence of the internal hydrodynamic field and attenuation of the vortex shedding in the near-wake are related and that both depend on the length of the flow porous section interacting with the flow. Based on the experimental observations, a long enough porous section is needed to enable flow penetration into the porous medium and discharge into the wake. Finally, the far-field noise results have shown that the porous treatments can effectively eliminate the vortex shedding tonal peak (*i.e.* at St=0.2), leading to a maximum noise reduction of about 8 dB and 35 dB by the 80 PPI and 25 PPI trailing-edges, respectively compared to that of the solid trailing-edge. The results obtained in this work provide the impetus for further experimental and numerical studies on the use of porous treatments and development of tailored porous materials for aerodynamic and aeroacoustic applications.

7.0.1 Future Works

Based on the results in this thesis the porous treatments have been identified as an effective means for the control of flow and aerodynamic noise. The findings in this thesis have answered the majority of the research questions identified in Chapter 2. While the results in this thesis have provided an evidence-based discussion and have shown the great potentials of the technique for flow and noise control purposes, the complexity of the flow-porous interaction problems demands for further high-quality research. The suggestions and recommendations for the future work are listed below.

i. In order to further understand the vortical structures generated in the vicinity of the blunt trailing-edge and in the wake domain, a wavelet analysis could be performed. For instance, the Gaussian and/or the Mexican hat wavelets can be used to analyze the evolution of the vortex shedding frequencies and the quasi-periodic hydrodynamic field generated inside the porous medium. Moreover, the bi-variate continuous wavelet transform technique can be used to characterize the pressure fluctuations from the transducers employed at the vicinity

of the trailing-edge, which is capable in analyzing the pressure fluctuation signals based on the localized wavelet functions. This method enables the decomposition of the original time-history data into various detail components that allow us to observe the different frequencies as a function of time separately, which could provide more high-quality results than the contemporary signal processing method, *i.e.* Fourier method.

ii. The results in Chapter 6 have shown that a high amplitude double vortex shedding peak is observed in the solid trailing-edge velocity correlation and noise spectra, indicating the existence of two types of vortical structures in the near wake and far-field measurement. The existence of multiple dominant peaks in the near wake velocity correlation results and noise spectra are believed to be due to the cellular variation in spanwise vortex shedding frequency. Further high-quality experimental and numerical investigations are needed to reveal the underlying physics of each of the peak separately, and to understand how these vortical structures influence the noise signature in whole.

iii. The boundary layer and hydrodynamic results in most studies in the areas of aerodynamic noise generation and control are presented in terms of the overall boundary layer thickness quantities, such as the boundary layer, displacement or momentum thickness, particularly when the low frequency aspect of the noise generation is of concern. Further processing of the boundary layer flow data could be carried out in wall units format, *i.e.* normalized by quantities such as y^+, u^+, u_τ, etc. This is relevant in studying the context of 'bursting frequency', which will give more insights in understanding the turbulence production near-the-wall, including the violent eruptions near the wall fluid, violent break-up of a low speed streak and shear-layer interface, which is useful for different applications, such as low drag surfaces, flow laminarization, etc.

iv. The present study paves the way for further investigation into the interaction of the porous media with different flow fields and development of tailored porous treatments for improving the aerodynamic and aeroacoustic performance of different aero- and hydro-components. The results from the present work clearly show that the porosity and permeability, as well as its geometrical characteristics, play an important role in the fluid-porous interaction

and its associated noise generation. The porous material used in this study are of a rigid structure with regular pores, and it has been shown that the flow and noise behaviour is dependent on the porous material properties. Further studies will be directed towards investigating the use of isotropic and functionally graded anisotropic porous treatments to control the generation of aerodynamic noise from different configurations.

v. Although various numerical and mathematical models have been developed to better understand the flow and porous medium interaction, in the case of aerodynamic noise generation, the problem with blunt trailing-edge involves several different physical processes and no modelling technique can yet fully capture all aspects of the flow-porous interaction, *i.e.* flow penetration and discharge, roughness effects, hydrodynamic and sound absorption effects, scattering effects, etc. Considering the complexity of the flow-porous interaction problems, as demonstrated in this study, further high-fidelity numerical studies, such as the Lattice Boltzmann Method (LBM) or Large Eddie Simulation (LES), with realistic micro-to-macro-scale modelling can provide more insight into the underlying physics of the phenomena observed in this work.

REFERENCES

[1] World Health Organization et al. “Burden of disease from environmental noise: Quantification of healthy life years lost in Europe”. In: *Burden of disease from environmental noise: Quantification of healthy life years lost in Europe*. 2011, pp. 126–126.

[2] D. Rhodes, E. Weston, and K. Jones. “ERCD Report 1209. Proposed methodology for estimating the cost of sleep disturbance from aircraft noise”. In: *Environmental Research and Consultancy Department. Civil Aviation Authority* (2013).

[3] Airbus. “Getting to Grips with Aircraft Noise”. In: 1 (2003).

[4] Geoscience Australia. “ABARE, Australian Energy Resource Assessment”. In: *Geoscience Australia and ABARE: Canberra, Australia* (2010).

[5] E. Pedersen and Persson W. K. “Perception and annoyance due to wind turbine noise-a dose-response relationship”. In: *The Journal of the Acoustical Society of America* 116.6 (2004), pp. 3460–3470.

[6] S. Oerlemans, P. Sijtsma, and B. M. López. “Location and quantification of noise sources on a wind turbine”. In: *Journal of sound and vibration* 299.4-5 (2007), pp. 869–883.

[7] C. J. Doolan, D. J. Moreau, and L. A. Brooks. “Wind turbine noise mechanism and some concepts for its control”. In: *Acoustics Australia* 40.1 (2012).

[8] D. P. Lockhard and G. M. Lilley. “The airframe noise reduction challenge”. In: (2004).

[9] R. R. Graham. “The silent flight of owls”. In: *The Aeronautical Journal* 38.286 (1934), pp. 837–843.

[10] S. Islam and S. U. Tanzil. “Study the effect of leading-edge serration at owl wing feathers on flow induced noise generation”. In: *International Journal of Biomedical and Biological Engineering* 12.6 (2018).

[11] R. A. Kroeger, H. D. Gruschka, and T. C. Helvey. *Low speed aerodynamics for Ultra-Quiet flight. AFFDL*. Tech. rep. TR 971-75, 1971.

[12] G. W. Anderson. *An experimental investigation of a high lift device on the owl wing*. Tech. rep. Air Force Inst of Tech Wright-Patterson AFB OH School of Engineering, 1973.

[13] G. Lilley. “A study of the silent flight of the owl”. In: *4th AIAA/CEAS Aeroacoustics Conference*. 1998, p. 2340.

[14] J. W. Jaworski and N. Peake. “Aerodynamic noise from a poroelastic edge with implications for the silent flight of owls”. In: *Journal of Fluid Mechanics* 723 (2013), pp. 456–479.

[15] K. Chen et al. “The sound suppression characteristics of wing feather of owl (bubo bubo)”. In: *Journal of Bionic Engineering* 9.2 (2012), pp. 192–199.

[16] Iowa State University. “Engineer looks to owl wings for bio-inspired ideas for quieter aircraft, wind turbines”. In: *Technology.org* (2017).

[17] K. Ishikawa. “Bone substitute fabrication based on dissolution-precipitation reactions”. In: *Materials* 3.2 (2010), pp. 1138–1155.

[18] ZeoFill Inc. *Premium zeolite infill-for cooling synthetic turf playgrounds, sports fields and helps control pet odor*. 2016.

[19] T. F. Brooks, D. S. Pope, and M. A. Marcolini. “Airfoil self-noise and prediction.” In: *NASA Reference Publication 1218* (1989).

[20] S. Probsting. “Airfoil self noise investigation with Particle Image Velocimetry”. PhD thesis. Delft University of Technology, 2015.

[21] R. K. Amiet. “Noise due to turbulent flow past a trailing edge”. In: *Journal of Sound and Vibration* 47.3 (1976), pp. 387–393.

[22] H. Arbey and J. Bataille. “Noise generated by airfoil profiles placed in a uniform laminar flow”. In: *Journal of Fluid Mechanics* 134 (1983), pp. 33–47.

[23] R. D. Blevins. “Flow-induced vibration”. In: (1990).

[24] M. Gad-el Hak. “Flow control: The future”. In: *Journal of Aircraft* 38.3 (2001), pp. 402–418.

[25] A. Seifert and L. G. Pack. “Oscillatory control of separation at high Reynolds numbers”. In: *AIAA Journal* 37.9 (1999), pp. 1062–1071.

[26] B. Smith and A. Glezer. “Vectoring and small-scale motions effected in free shear flows using synthetic jet actuators”. In: *35th Aerospace Sciences Meeting and Exhibit*. 1997, p. 213.

[27] S. J. Lee, S. I. Lee, and C. W. Park. “Reducing the drag on a circular cylinder by upstream installation of a small control rod”. In: *Fluid Dynamics Research* 34.4 (2004), pp. 233–250.

[28] T. Igarashi. “Drag reduction of a square prism by flow control using a small rod”. In: *Journal of Wind Engineering and Industrial Aerodynamics* 69 (1997), pp. 141–153.

[29] H. Akilli, B. Sahin, and N. F. Tumen. “Suppression of vortex shedding of circular cylinder in shallow water by a splitter plate”. In: *Flow Measurement and Instrumentation* 16.4 (2005), pp. 211–219.

[30] S. Ozono. “Flow control of vortex shedding by a short splitter plate asymmetrically arranged downstream of a cylinder”. In: *Physics of Fluids* 11 (1999), pp. 2928–2934.

[31] H. C. Lim and S. J. Lee. “Flow control of a circular cylinder with O-rings”. In: *Fluid Dynamics Research* 35.2 (2004), pp. 107–122.

[32] S. J. Lee and H. B. Kim. “The effect of surface protrusions on the near wake of a circular cylinder”. In: *Journal of Wind Engineering and Industrial Aerodynamics* 69 (1997), pp. 351–361.

[33] P. W. Bearman and J. K. Harvey. “Control of circular cylinder flow by the use of dimples”. In: *AIAA Journal* 31.10 (1993), pp. 1753–1756.

[34] J. Choi. “Mechanism of drag reduction by surface modification on a sphere: Dimples, roughness and trip wire”. PhD thesis. Seoul Natl. Univ., Korea, 2006.

[35] S. Kunze and C. Brücker. “Control of vortex shedding on a circular cylinder using self-adaptive hairy-flaps”. In: *Comptes Rendus Mécanique* 340.1 (2012), pp. 41–56.

[36] H. C. Lim and S. J. Lee. “Flow control of circular cylinders with longitudinal grooved surfaces”. In: *AIAA Journal* 40.10 (2002), pp. 2027–2036.

[37] A. Afshari et al. “Trailing edge noise reduction using novel surface treatments”. In: *22nd AIAA/CEAS Aeroacoustics Conference, AIAA 2016-2384*.

[38] B. Lyu, M. Azarpeyvand, and S. Sinayoko. “Prediction of noise from serrated trailing edges”. In: *Journal of Fluid Mechanics* 793 (Apr. 2016), pp. 556–588. ISSN: 1469-7645.

[39] M. Gruber, M. Azarpeyvand, and P. F. Joseph. “Airfoil trailing edge noise reduction by the introduction of sawtooth and slitted trailing edge geometries”. In: *Proceedings of 20th International Congress on Acoustics, ICA* 10 (2010), p. 6.

[40] M. Azarpeyvand, M. Gruber, and P. F. Joseph. “An analytical investigation of trailing edge noise reduction using novel serrations”. In: *19th AIAA/CEAS Aeroacoustic Conference, AIAA 2013-2009*.

[41] S. Sinayoko, M. Azarpeyvand, and B. Lyu. “Trailing edge noise prediction for rotating serrated blades”. In: *20th AIAA/CEAS Aeroacoustics Conference, AIAA 2014-3296*.

[42] X. Liu, M. Azarpeyvand, and R. Theunissen. “Aerodynamic and Aeroacoustic Performance of Serrated Airfoils”. In: *21st AIAA/CEAS Aeroacoustics Conference, AIAA 2015-2201*.

[43] Q. Ai et al. “Aerodynamic and aeroacoustic performance of airfoils with morphing structures”. In: *Wind Energy* (2015).

[44] S. Bhattacharyya, S. Dhinakaran, and A. Khalili. “Fluid motion around and through a porous cylinder”. In: *Chemical Engineering Science* 61.13 (2006), pp. 4451–4461.

[45] H. Naito and K. Fukagata. “Numerical simulation of flow around a circular cylinder having porous surface”. In: *Physics of Fluids* 24.11 (2012), p. 117102.

[46] H. Liu, J. Wei, and Z. Qu. “Prediction of aerodynamic noise reduction by using open-cell metal foam”. In: *Journal of Sound and Vibration* 331.7 (2012), pp. 1483–1497.

[47] M. A. Hossain et al. “Experimental and numerical investigation of sweeping jet film cooling”. In: *Journal of Turbomachinery* 140.3 (2018), p. 031009.

[48] C. Gmelin et al. “Active flow control concepts on a highly loaded subsonic compressor cascade: résumé of experimental and numerical results”. In: *Journal of Turbomachinery* 134.6 (2012), p. 061021.

[49] S. Oerlemans et al. “Reduction of wind turbine noise using optimized airfoils and trailing-edge serrations”. In: *AIAA Journal* 47.6 (2009), pp. 1470–1481.

[50] J. H. M. Fransson. “Transition to turbulence delay using a passive flow control strategy”. In: *Procedia IUTAM* 14 (2015), pp. 385–393.

[51] A. Sareen et al. “Drag reduction using riblet film applied to airfoils for wind turbines”. In: *Journal of Solar Energy Engineering* 136.2 (2014), p. 021007.

[52] S. A. Showkat Ali, M. Azarpeyvand, and C. R. Ilario da Silva. “Experimental study of porous treatment for aerodynamic and aeroacoustic purposes”. In: *23rd AIAA/CEAS Aeroacoustics Conference, AIAA 2017-3358*.

[53] N. H. Mostafa, U. Vandsburger, and T. A. Economides. “Flow field characteristics of a turbulent round jet subjected to pulsed vortex generating jets”. In: *ASME-Publications-FED* 237 (1996), pp. 535–542.

[54] H. Suzuki, N. Kasagi, and Y. Suzuki. “Active control of an axisymmetric jet with distributed electromagnetic flap actuators”. In: *Experiments in Fluids* 36.3 (2004), pp. 498–509.

[55] D. A. Tamburello and M. Amitay. “Active control of a free jet using a synthetic jet”. In: *International Journal of Heat and Fluid Flow* 29.4 (2008), pp. 967–984.

[56] G. V. Lachmann. *Boundary layer and flow control: Its principles and application*. Elsevier, 2014.

[57] J. L. Gobert et al. *Active flow control activities at ONERA*. Tech. rep. Office National D’etudes Et De Recherches Aerospatiales Toulouse (Fance), 2001.

[58] MCM Wright and PA Nelson. “Wind tunnel experiments on the optimization of distributed suction for laminar flow control”. In: *Proceedings of the Institution of Mechanical Engineers, Part G: Journal of Aerospace Engineering* 215.6 (2001), pp. 343–354.

[59] M. Gad-el Hak, A. Pollard, and J. P. Bonnet. *Flow control: fundamentals and practices*. Vol. 53. Springer Science & Business Media, 2003.

[60] Z. Cai et al. “Active flow separation control by a position-based iterative learning control algorithm with experimental validation”. In: *International Journal of Control* 87.3 (2014), pp. 633–641.

[61] G. Artana et al. “Control of the near-wake flow around a circular cylinder with electrohydrodynamic actuators”. In: *Experiments in Fluids* 35.6 (2003), pp. 580–588.

[62] D. Greenblatt et al. “Active Management of Flap-Edge Trailing Vortices”. In: *4th Flow Control Conference*. 2008, p. 4186.

[63] M. Gupta. “Investigation of active control of aircraft wing tip vortices and wake turbulence”. PhD thesis. Auburn University, 2011.

[64] D. R. Williams and C. W. Amato. “Unsteady pulsing of cylinder wakes”. In: *Frontiers in Experimental Fluid Mechanics*. Springer, 1989, pp. 337–364.

[65] W. Schoppa and F. Hussain. “A large-scale control strategy for drag reduction in turbulent boundary layers”. In: *Physics of Fluids* 10.5 (1998), pp. 1049–1051.

[66] A. Seifert, T. Shtendel, and D. Dolgopyat. “From lab to full scale Active Flow Control drag reduction: How to bridge the gap?” In: *Journal of Wind Engineering and Industrial Aerodynamics* 147 (2015), pp. 262–272.

[67] R. Parker, S. Rajagopalan, and R. A. Antonia. “Control of an axisymmetric jet using a passive ring”. In: *Experimental Thermal and Fluid Science* 27.5 (2003), pp. 545–552.

[68] W. L. Chen et al. “Passive jet control of flow around a circular cylinder”. In: *Experiments in Fluids* 56.11 (2015), p. 201.

[69] J. Ost et al. “Transition delay by oblique roughness elements in a blasius boundary-layer flow”. In: *2018 AIAA Aerospace Sciences Meeting*. 2018, p. 1057.

[70] J. Favier et al. “Passive separation control using a self-adaptive hairy coating”. In: *Journal of Fluid Mechanics* 627 (2009), pp. 451–483.

[71] H. Shan et al. “Numerical study of passive and active flow separation control over a NACA 0012 airfoil”. In: *Computers & fluids* 37.8 (2008), pp. 975–992.

[72] W. L. Chen et al. “Passive jet flow control method for suppressing unsteady vortex shedding from a circular cylinder”. In: *Journal of Aerospace Engineering* 30.1 (2016), p. 04016063.

[73] S. Huang. “VIV suppression of a two-degree-of-freedom circular cylinder and drag reduction of a fixed circular cylinder by the use of helical grooves”. In: *Journal of Fluids and Structures* 27.7 (2011), pp. 1124–1133.

[74] Y. Gao et al. “Experimental study of the effects of surface roughness on the vortex-induced vibration response of a flexible cylinder”. In: *Ocean Engineering* 103 (2015), pp. 40–54.

[75] P. W. Bearman and J. C. Owen. “Reduction of bluff-body drag and suppression of vortex shedding by the introduction of wavy separation lines”. In: *Journal of Fluids and Structures* 12.1 (1998), pp. 123–130.

[76] C. Mimeau, I. Mortazavi, and G. H. Cottet. “Passive flow control around a semi-circular cylinder using porous coatings”. In: *International Journal of Flow Control* 6.1 (2014).

[77] B. Zhou et al. “Force and flow characteristics of a circular cylinder with uniform surface roughness at subcritical Reynolds numbers”. In: *Applied Ocean Research* 49 (2015), pp. 20–26.

[78] S. Bhattacharyya and A. K. Singh. “Reduction in drag and vortex shedding frequency through porous sheath around a circular cylinder”. In: *International Journal for Numerical Methods in Fluids* 65.6 (2011), pp. 683–698.

[79] T. Sueki et al. “Application of porous material to reduce aerodynamic sound from bluff bodies”. In: *Fluid Dynamics Research* 42.1 (2010), p. 015004.

[80] H. Liu, J. Wei, and Z. Qu. “The Interaction of Porous Material Coating With the Near Wake of Bluff Body”. In: *Journal of Fluids Engineering* 136.2 (2014), p. 021302.

[81] H. Liu et al. “Tandem cylinder aerodynamic sound control using porous coating”. In: *Journal of Sound and Vibration* 334 (2015), pp. 190–201.

[82] M. R. Fink and D. A. Bailey. “Airframe noise reduction studies and clean-airframe noise investigation”. In: *NASA Contractor Report, 159311* (1980).

[83] J. D. Revell et al. “Trailing-edge flap noise reduction by porous acoustic treatment”. In: *AIAA Journal* 1646 (1997), pp. 12–14.

[84] M. Choudhari and M. R. Khorrami. “Computational study of porous treatment for altering flap side-edge flow field”. In: *Proceedings of the 9th AIAA/CEAS Aeroacoustic Conference and Exhibit. Hilton Head, South Carolina. AIAA 2003-3113*. 2003.

[85] M. R. Khorrami and M. M. Choudhari. “Application of passive porous treatment to slat trailing edge noise”. In: *NASA Technical Report, 212416* (2003).

[86] D. Angland, X. Zhang, and N. Molin. “Measurements of flow around a flap side edge with porous edge treatment”. In: *AIAA Journal* 47.7 (2009), pp. 1660–1671.

[87] M. Herr. “A noise reduction study on flow-permeable trailing-edges”. In: *Proceedings of the 8th ONERA-DLR Aerospace Symposium (ODAS) Conference. H. P. Kreplin, Gottingen, Germany*. 2007.

[88] E. Sarradj and T. Geyer. “Noise generation by porous airfoils”. In: *Proceedings of the 13th AIAA/CEAS Aeroacoustics Conference. Rome, Italy. AIAA-2007-3719*.

[89] T. Geyer, E. Sarradj, and C. Fritzsche. “Measurement of the noise generation at the trailing edge of porous airfoils”. In: *Experiments in Fluids* 48.2 (2010), pp. 291–308.

[90] T. Geyer, E. Sarradj, and C. Fritzsche. “Porous airfoils: noise reduction and boundary layer effects”. In: *International Journal of Aeroacoustics* 9.6 (2010), pp. 787–820.

[91] D. Venkataraman and A. Bottaro. “Numerical modeling of flow control on a symmetric aerofoil via a porous, compliant coating”. In: *Physics of Fluids* 24.9 (2012), p. 093601.

[92] T. Geyer and E. Sarradj. “Trailing edge noise of partially porous airfoils”. In: *Proceedings of the 20th AIAA/CEAS Aeroacoustic Conference and Exhibit. Atlanta, GA. AIAA 2014-3039*. 2014.

[93] K. J. Standish and C. P. Van Dam. “Aerodynamic analysis of blunt trailing edge airfoils”. In: *Journal of Solar Energy Engineering* 125.4 (2003), pp. 479–487.

[94] T. Winnemoller and C. P. Dam. “Design and numerical optimization of thick airfoils including blunt trailing edges”. In: *Journal of Aircraft* 44.1 (2007), pp. 232–240.

[95] P. B. Jonathon and C. P. Dam. “Drag reduction of blunt trailing-edge airfoils”. In: *International Colloquium on: Bluff Bodies Aerodynamics & Applications. Milano, Italy*. 2008.

[96] C. H. Bruneau, I. Mortazavi, and P. Gilliéron. “Flow regularisation and drag reduction around blunt bodies using porous devices”. In: *IUTAM Symposium on Flow Control and MEMS*. Springer Netherlands. 2008.

[97] Y. Bae, Y. E. Jeong, and Y. J. Moon. “Effect of porous surface on the flat plate self-noise”. In: *Proceedings of the 15th AIAA/CEAS Aeroacoustics Conference. Miami, Florida. AIAA-2009-3311*. 2009.

[98] J. Schulze and J. Sesterhenn. “Optimal distribution of porous media to reduce trailing edge noise”. In: *Journal of Computers & Fluids* 78 (2013), pp. 41–53.

[99] S. R. Koh et al. “Noise sources of trailing-edge turbulence controlled by porous media”. In: *Proceedings of the 20th AIAA/CEAS Aeroacoustics Conference. Atlanta, GA. AIAA-2014-3038*.

[100] B. Y. Zhou et al. “On the Adjoint-based Control of Trailing-Edge Turbulence and Noise Minimization via Porous Material”. In: *Proceedings of the 21st AIAA/CEAS Aeroacoustics Conference. Dallas, TX. AIAA 2015-2530*.

[101] S. R. Koha et al. “Impact of Permeable Surface on Trailing-Edge Noise at Varying Lift”. In: *Proceedings of the 23rd AIAA/CEAS Aeroacoustics Conference. Denver, Colorado. AIAA 2017-3497*.

[102] K. Suga et al. “Effects of wall permeability on turbulence”. In: *International Journal of Heat and Fluid Flow* 31.6 (2010), pp. 974–984.

[103] C. Manes, D. Poggi, and L. Ridolfi. “Turbulent boundary layers over permeable walls: scaling and near-wall structure”. In: *Journal of Fluid Mechanics* 687 (2011), pp. 141–170.

[104] W. P. Breugem, B. J. Boersma, and R. E. Uittenbogaard. “The influence of wall permeability on turbulent channel flow”. In: *Journal of Fluid Mechanics* 562 (2006), pp. 35–72.

[105] F. Kong and J. Schetz. “Turbulent boundary layer over porous surfaces with different surface geometries”. In: *20th Aerospace Sciences Meeting*. 1982, p. 30.

[106] J. Finnigan. “Turbulence in plant canopies”. In: *Annual Review of Fluid Mechanics* 32.1 (2000), pp. 519–571.

[107] D. Poggi et al. “The effect of vegetation density on canopy sub-layer turbulence”. In: *Boundary-Layer Meteorology* 111.3 (2004), pp. 565–587.

[108] J. Jimenez et al. “Turbulent shear flow over active and passive porous surfaces”. In: *Journal of Fluid Mechanics* 442 (2001), pp. 89–117.

[109] M. E. Rosti, L. Cortelezzi, and M. Quadrio. “Direct numerical simulation of turbulent channel flow over porous walls”. In: *Journal of Fluid Mechanics* 784 (2015), pp. 396–442.

[110] Y. Kuwata and K. Suga. “Lattice Boltzmann direct numerical simulation of interface turbulence over porous and rough walls”. In: *International Journal of Heat and Fluid Flow* 61 (2016), pp. 145–157.

[111] W. K. Blake. “Turbulent boundary-layer wall-pressure fluctuations on smooth and rough walls”. In: *Journal of Fluid Mechanics* 44.04 (1970), pp. 637–660.

[112] N. D. Varano. “Fluid dynamics and surface pressure fluctuations of turbulent boundary layers over sparse roughness”. PhD thesis. Virginia Tech, 2010.

[113] T. Meyers, J. B. Forest, and W. J. Devenport. “The wall-pressure spectrum of high-Reynolds-number turbulent boundary-layer flows over rough surfaces”. In: *Journal of Fluid Mechanics* 768 (2015), pp. 261–293.

[114] L. A. Joseph et al. “Pressure fluctuations in a high-Reynolds-number turbulent boundary layer flow over rough surfaces”. In: *22nd AIAA/CEAS Aeroacoustics Conference*. AIAA 2016-2751.

[115] H. Darcy. *Les fontaines publiques de la ville de Dijon: exposition et application*. Victor Dalmont, 1856.

[116] S. Whitaker. “Flow in porous media I: A theoretical derivation of Darcy’s law”. In: *Transport in Porous Media* 1.1 (1986), pp. 3–25.

[117] H. C. Brinkman. “Fluid flow in a porous medium.” In: *Applied Science Research Section* A1(27) (1947), pp. 143–149.

[118] S. Kim and W. B. Russel. “Modelling of porous media by renormalization of the Stokes equations”. In: *Journal of Fluid Mechanics* 154 (1985), pp. 269–286.

[119] P. H. Forchheimer. “Wasserbewegung durch boden”. In: *Zeitz. Ver. Duetch Ing.* 45 (1901), pp. 1782–1788.

[120] K. B. Lee. “Forced convective, conductive, and radiative transfer within a highly porous layer exposed to a laminar external flow field”. In: *Proceedings of the KSME Spring Conference* (1987), pp. 668–674.

[121] V. S. Travkin, I. Catton, and L. Gratton. “Single phase turbulent transport in prescribed non-isotropic and stochastic porous media”. In: *ASME-Publications-HTD* 240 (1993), pp. 43–43.

[122] R. E. Larson and J. J. L. Higdon. “Microscopic flow near the surface of two-dimensional porous media. Part 1. Axial flow”. In: *Journal of Fluid Mechanics* 166 (1986), pp. 449–472.

[123] L. Durlofsky and J. F. Brady. “Analysis of the Brinkman equation as a model for flow in porous media”. In: *The Physics of Fluids* 30.11 (1987), pp. 3329–3341.

[124] K. Vafai and S. J. Kim. “Fluid mechanics of the interface region between a porous medium and a fluid layer-an exact solution”. In: *International Journal of Heat and Fluid Flow* 11.3 (1990), pp. 254–256.

[125] C. T. Hsu and P. Cheng. “Thermal dispersion in a porous medium”. In: *International Journal of Heat and Mass Transfer* 33.8 (1990), pp. 1587–1597.

[126] N. Kladias and V. Prasad. “Experimental verification of Darcy-Brinkman-Forchheimer flow model for natural convection in porous media”. In: *Journal of Thermophysics and Heat Transfer* 5.4 (1991), pp. 560–576.

[127] F. Chen and C. F. Chen. “Convection in superposed fluid and porous layers”. In: *Journal of Fluid Mechanics* 234 (1992), pp. 97–119.

[128] L. J. Snyder and W. E. Stewart. “Velocity and pressure profiles for Newtonian creeping flow in regular packed beds of spheres”. In: *AIChE Journal* 12.1 (1966), pp. 167–173.

[129] N. J. Meegoda, I. P. King, and K. Arulanandan. “An expression for the permeability of anisotropic granular media”. In: *International Journal for Numerical and Analytical Methods in Geomechanics* 13.6 (1989), pp. 575–598.

[130] L. M. Schwartz et al. “Cross-property relations and permeability estimation in model porous media”. In: *Physical Review E* 48.6 (1993), p. 4584.

[131] A. Cancelliere et al. “The permeability of a random medium: comparison of simulation with theory”. In: *Physics of Fluids A: Fluid Dynamics* 2.12 (1990), pp. 2085–2088.

[132] S. Succi, R. Benzi, and F. Higuera. “The lattice Boltzmann equation: a new tool for computational fluid-dynamics”. In: *Physica D: Nonlinear Phenomena* 47.1-2 (1991), pp. 219–230.

[133] D. H. Rothman. “Cellular-automaton fluids: A model for flow in porous media”. In: *Geophysics* 53.4 (1988), pp. 509–518.

[134] G. A. Kohring. “Calculation of the permeability of porous media using hydrodynamic cellular automata”. In: *Journal of Statistical Physics* 63.1-2 (1991), pp. 411–418.

[135] C. K. Lee, C. C. Sun, and C. C. Mei. “Computation of permeability and dispersivities of solute or heat in periodic porous media”. In: *International Journal of Heat and Mass Transfer* 39.4 (1996), pp. 661–676.

[136] J. Koplik, C. Lin, and M. Vermette. “Conductivity and permeability from microgeometry”. In: *Journal of Applied Physics* 56.11 (1984), pp. 3127–3131.

[137] N. S. Martys, S. Torquato, and D. P. Bentz. “Universal scaling of fluid permeability for sphere packings”. In: *Physical Review E* 50.1 (1994), p. 403.

[138] L. M. Schwartz et al. “Transport and diffusion in three-dimensional composite media”. In: *Physica A: Statistical Mechanics and its Applications* 207.1-3 (1994), pp. 28–36.

[139] R. L. Peyton et al. “Fractal dimension to describe soil macropore structure using X-ray computed tomography”. In: *Water Resources Research* 30.3 (1994), pp. 691–700.

[140] T. L. Parrott and W. E. Zorumski. “Nonlinear acoustic theory for rigid porous materials”. In: *NASA Technical Report, D-6196* (1971).

[141] D. K. Wilson, J. D. Mcintosh, and R. F. Lambert. “Forchheimer-type nonlinearities for high-intensity propagation of pure tones in air-saturated porous media”. In: *The Journal of the Acoustical Society of America* 84.1 (1988), pp. 350–359.

[142] F. Peng et al. “Investigation on the sound absorption characteristics of porous metal plates at high sound pressure levels”. In: *Acta Acust* 34 (2009), pp. 266–274.

[143] R. F. Lambert and J. D. McIntosh. “Nonlinear wave propagation through rigid porous materials. II: Approximate analytical solutions”. In: *The Journal of the Acoustical Society of America* 88.4 (1990), pp. 1950–1959.

[144] O. Umnova et al. “Behavior of rigid-porous layers at high levels of continuous acoustic excitation: Theory and experiment”. In: *The Journal of the Acoustical Society of America* 114.3 (2003), pp. 1346–1356.

[145] D. L. Johnson, J. Koplik, and R. Dashen. “Theory of dynamic permeability and tortuosity in fluid-saturated porous media”. In: *Journal of Fluid Mechanics* 176 (1987), pp. 379–402.

[146] Y. Champoux and J. F. Allard. “Dynamic tortuosity and bulk modulus in air-saturated porous media”. In: *Journal of Applied Physics* 70.4 (1991), pp. 1975–1979.

[147] J. F. Allard and N. Atalla. *Propagation of sound in porous media: modelling sound absorbing materials 2e*. John Wiley & Sons, 2009.

[148] J. F. Allard and Y. Champoux. “New empirical equations for sound propagation in rigid frame fibrous materials”. In: *The Journal of the Acoustical Society of America* 91.6 (1992), pp. 3346–3353.

[149] Y. J. Kang and J. S. Bolton. “Finite element modeling of isotropic elastic porous materials coupled with acoustical finite elements”. In: *The Journal of the Acoustical Society of America* 98.1 (1995), pp. 635–643.

[150] R. Panneton. “Modelisation numerique tridimensionnelle par elements finis des milieux poroelastiques: application au probleme couple elasto-poro-acoustique.” PhD thesis. University of Sherbrooke, Canada, 1999.

[151] R. Panneton and N. Atalla. “Numerical prediction of sound transmission through finite multilayer systems with poroelastic materials”. In: *The Journal of the Acoustical Society of America* 100.1 (1996), pp. 346–354.

[152] N. Atalla, R. Panneton, and P. Debergue. “A mixed displacement-pressure formulation for poroelastic materials”. In: *The Journal of the Acoustical Society of America* 104.3 (1998), pp. 1444–1452.

[153] N. A. R. Dauchez. “Etude vibroacoustique des materiaux poreux parelements finis”. PhD thesis. Universite du Maine, France, 1999.

[154] M. A. Hamdi et al. “Novel mixed finite element formulation for the analysis of sound absorption by porous media”. In: *Inter-Noise and Noise-Con Congress and Conference Proceedings*. Vol. 2000. 5. Institute of Noise Control Engineering. 2000, pp. 2914–2919.

[155] F. C. Sgard, N. Atalla, and J. Nicolas. “A numerical model for the low frequency diffuse field sound transmission loss of double-wall sound barriers with elastic porous linings”. In: *The Journal of the Acoustical Society of America* 108.6 (2000), pp. 2865–2872.

[156] J. F. Allard and G. Daigle. “Propagation of sound in porous media: Modeling sound absorbing materials”. In: *Journal of Acoust. Soc. Am.* 95 (1994).

[157] J. F. Allard, A. Aknine, and C. Depollier. “Acoustical properties of partially reticulated foams with high and medium flow resistance”. In: *The Journal of the Acoustical Society of America* 79.6 (1986), pp. 1734–1740.

[158] J. F. Allard, Y. Champoux, and C. Depollier. “Modelization of layered sound absorbing materials with transfer matrices”. In: *The Journal of the Acoustical Society of America* 82.5 (1987), pp. 1792–1796.

[159] J. S. Bolton, N. M. Shiau, and Y. J. Kang. “Sound transmission through multi-panel structures lined with elastic porous materials”. In: *Journal of sound and vibration* 191.3 (1996), pp. 317–347.

[160] W. Lauriks et al. “Modelization at oblique incidence of layered porous materials with impervious screens”. In: *The Journal of the Acoustical Society of America* 87.3 (1990), pp. 1200–1206.

[161] B. H. Song and J. S. Bolton. “A transfer-matrix approach for estimating the characteristic impedance and wave numbers of limp and rigid porous materials”. In: *The Journal of the Acoustical Society of America* 107.3 (2000), pp. 1131–1152.

[162] A. M. Naguib, S. P. Gravante, and C. E. Wark. “Extraction of turbulent wall-pressure time-series using an optimal filtering scheme”. In: *Experiments in Fluids* 22.1 (1996), pp. 14–22.

[163] R. Theunissen et al. “Confidence estimation using dependent circular block bootstrapping: application to the statistical analysis of PIV measurements”. In: *Experiments in Fluids* 44.4 (2008), pp. 591–596.

[164] B. H. Timmins, B. L. Smith, and P. P. Vlachos. “Automatic particle image velocimetry uncertainty quantification”. In: *ASME 2010 3rd Joint US-European Fluids Engineering Summer Meeting collocated with 8th International Conference on Nanochannels, Microchannels, and Minichannels*. American Society of Mechanical Engineers. 2010, pp. 2811–2826.

[165] P. M. Ligrani and P. Bradshaw. “Spatial resolution and measurement of turbulence in the viscous sublayer using subminiature hot-wire probes”. In: *Experiments in Fluids* 5.6 (1987), pp. 407–417.

[166] N. Hutchins et al. “Hot-wire spatial resolution issues in wall-bounded turbulence”. In: *Journal of Fluid Mechanics* 635 (2009), pp. 103–136.

[167] Dantec. *Dantec Dynamics StreamWare Pro Installation and User Guide*. Ed. by Dantec Dyanamic A/S. 5.11.00.14., 9040U4931, 2013.

[168] A. Garcia-Sagrado and T. Hynes. “Wall pressure sources near an airfoil trailing edge under turbulent boundary layers”. In: *Journal of Fluids and Structures* 30 (2012), pp. 3–34.

[169] M. Gruber. “Airfoil noise reduction by edge treatments”. PhD thesis. University of Southampton, 2012.

[170] G. M. Corcos. “Resolution of pressure in turbulence”. In: *The Journal of the Acoustical Society of America* 35.2 (1963), pp. 192–199.

[171] S. P. Gravante et al. “Characterization of the pressure fluctuations under a fully developed turbulent boundary layer”. In: *AIAA journal* 36.10 (1998), pp. 1808–1816.

[172] Frank J Fahy and Paolo Gardonio. *Sound and structural vibration: radiation, transmission and response*. Elsevier, 2007.

[173] P. F. Mish. “Mean loading and turbulence scale effects on the surface pressure fluctuations occurring on a NACA 0015 airfoil immersed in grid generated turbulence”. MA thesis. Virginia Polytechnic Institute and State University, Blacksburg, Virginia, 2001.

[174] G.R.A.S. Sound & Vibration. *Pistonphone Type 42AA*. Denmark, 2011.

[175] P. Welch. “The use of fast Fourier transform for the estimation of power spectra: a method based on time averaging over short, modified periodograms”. In: *IEEE Transactions on audio and electroacoustics* 15.2 (1967), pp. 70–73.

[176] W. Liu and J. A. Zagzebski. “Tradeoffs in Data Acquisition and Processing Parameters for Backscatter and Scatterer Size Estimations”. In: *IEEE transactions on ultrasonics, ferroelectrics, and frequency control* 57.2 (2010), p. 340.

[177] K. A. Wear. “Fundamental precision limitations for measurements of frequency dependence of backscatter: applications in tissue-mimicking phantoms and trabecular bone”. In: *The Journal of the Acoustical Society of America* 110.6 (2001), pp. 3275–3282.

[178] S. J. Kline. “The description of uncertainties in single sample experiments”. In: *Mech. Engg.* 75 (1953), pp. 3–9.

[179] B. Efron and R. J. Tibshirani. “An introduction to the bootstrap: monographs on statistics and applied probability, Vol. 57”. In: *New York and London: Chapman and Hall/CRC* (1993).

[180] A. Doucet, Nando De F., and N. Gordon. “An introduction to sequential Monte Carlo methods”. In: *Sequential Monte Carlo methods in practice*. Springer, 2001, pp. 3–14.

[181] R. Nolen-Hoeksema. “Flow through pores”. In: *Oilfield Review* 26.3 (2014).

[182] J. Haber. “Manual on catalyst characterization (Recommendations 1991)”. In: *Pure and Applied Chemistry* 63.9 (1991), pp. 1227–1246.

[183] T. Geyer. “Trailing edge noise generation of porous airfoils”. PhD thesis. Brandenburgische Technische Universitat (BTU), Cottbus, 2011.

[184] G. M. Ozkan, H. Akilli, and B. Sahin. “Effect of High Porosity Screen on the Near Wake of a Circular Cylinder”. In: *EPJ Web of Conferences*. Vol. 45. EDP Sciences. 2013, p. 01071.

[185] G. M. Ozkan and H. Akilli. “Flow control around bluff bodies by attached permeable plates”. In: *Int. J. Mech. Aerosp. Ind. Mechatron. Eng* 8.5 (2014), pp. 1035–1039.

[186] C. H. Bruneau and I. Mortazavi. “Numerical modelling and passive flow control using porous media”. In: *Journals of Computers & Fluids* 37.5 (2008), pp. 488–498.

[187] J. Bear. *Dynamics of fluids in porous media*. Courier Corporation, 2013.

[188] A. C. Kak and M. Slaney. *Principles of computerized tomographic imaging*. SIAM, 2001.

[189] L. Pal, M. K. Joyce, and P. D. Fleming. “A simple method for calculation of the permeability coefficient of porous media”. In: *Tappi Journal* 5.9 (2006), p. 10.

[190] E. Kruger. “Die Grundwasserbewegung”. In: *Internationale Mitteilungen für Bodenkunde* 8 (1918), p. 105.

[191] G. P. J. Diedericks and J. P. DuPlessis. “Modelling of flow through homogeneous foams”. In: *Mathematical Engineering in Industry* 6.2 (1997), pp. 133–154.

[192] J. E. J. Dupuit. *Etudes theoriques et pratiques sur le mouvement des eaux dans les canaux decouverts et a travers les terrains permeables avec des considerations relatives au regime des grandes eaux, au debouche a leur donner et a la marche des alluvions dans les rivieres a fond mobile*. Second edition, Dunod, 1863.

[193] R. C. Givler and S. A. Altobelli. "A determination of the effective viscosity for the Brinkman-Forchheimer flow model". In: *Journal of Fluid Mechanics* 258 (1994), pp. 355–370.

[194] B. V. Antohe et al. "Experimental determination of permeability and inertia coefficients of mechanically compressed aluminum porous matrices". In: *Journal of Fluids Engineering* 119.2 (1997), pp. 404–412.

[195] K. Boomsma and D. Poulikakos. "The effects of compression and pore size variations on the liquid flow characteristics in metal foams". In: *Journal of fluids engineering* 124.1 (2002), pp. 263–272.

[196] F. P. Mechel. "Formulas of acoustics". In: *Noise Control Engineering Journal* 57.1 (2009), pp. 43–44.

[197] T. R. Thomas. *Rough surfaces*. World Scientific, 1999.

[198] EN ISO. "4287-Geometrical Product Specifications (GPS)–Surface Texture: Profile Method–Terms, Definitions and Surface Texture Parameters". In: *International Organization for Standardization, Genève* (1997).

[199] M. M. Mosallem. "Numerical and experimental investigation of beveled trailing edge flow fields". In: *Journal of Hydrodynamics, Ser. B* 20.3 (2008), pp. 273–279.

[200] A. Silvestri et al. "Attenuation of turbulence by the passive control of sweep events in a turbulent boundary layer using micro-cavities". In: *Physics of Fluids* 29.11 (2017), p. 115102.

[201] F. Ghanadi et al. "Analysis of the turbulent boundary layer in the vicinity of a self-excited cylindrical Helmholtz resonator". In: *Journal of Turbulence* 16.8 (2015), pp. 705–728.

[202] P. Schlatter and R. Orlu. “Assessment of direct numerical simulation data of turbulent boundary layers”. In: *Journal of Fluid Mechanics* 659 (2010), pp. 116–126.

[203] M. Goody. “Empirical spectral model of surface pressure fluctuations”. In: *AIAA Journal* 42.9 (2004), pp. 1788–1794.

[204] H. Schlichting. “Boundary-layer theory”. In: *Pergamon Press. London* (1968).

[205] S. Berg et al. “Flow in Porous Media with Slip Boundary Condition”. In: *Society of Core Analysts. Calgary, Canada. (SCA-2007-13)* (), pp. 10–12.

[206] D. B. Spalding. “A single formula for the law of the wall”. In: *Journal of Applied Mechanics* 28.3 (1961), pp. 455–458.

[207] T. F. Brooks and T. H. Hodgson. “Trailing edge noise prediction from measured surface pressures”. In: *Journal of sound and vibration* 78.1 (1981), pp. 69–117.

[208] J. Mathieu and J. Scott. *An introduction to turbulent flow*. Cambridge University Press, 2000.

[209] W. H. Rae and A. Pope. *Low-speed wind tunnel testing*. John Wiley-Inter Science Publication, United States., 1984.

[210] W. K. Blake. *Mechanics of Flow-Induced Sound and Vibration V2: Complex Flow-Structure Interactions*. Elsevier Science, London., 2012.

[211] Charts. “Design Tools Surface Finish”. In: *LJ Star Incorporated, (2017).* (). URL: `http://www.ljstar.com/product-lines`.

[212] G. Eiffel. “Sur la resistance des spheres dans lair en mouvement”. In: *Comptes Rendus* 155 (1912), pp. 1597–1599.

[213] C. H. K. Williamson. “Vortex dynamics in the cylinder wake”. In: *Annual Review of Fluid Mechanics* 28.1 (1996), pp. 477–539.

[214] P. W. Bearman and N. Tombazis. “The effects of three-dimensional imposed disturbances on bluff body near wake flows”. In: *Journal of Wind Engineering and Industrial Aerodynamics* 49.1-3 (1993), pp. 339–349.

[215] F. H. Abernathy. *Fundamentals of boundary layers*. 1–7. Encyclopaedia Britannica Educational Corporation, National commitee for fluid mechanics films. Harvard University. Film notes-21623 (1970), pp.1-7.

[216] A. Naghib-Lahouti, H. Hangan, and P. Lavoie. "Distributed forcing flow control in the wake of a blunt trailing edge profiled body using plasma actuators". In: *Physics of Fluids* 27.3 (2015), p. 035110.

[217] P. M. Bevilaqua. "Intermittency, the entrainment problem". In: *Aerospace Research Labs Wright-Patterson Air Force Base, Ohio, (ARL Technical Report 1975-0095)* ().

[218] D. M. Bushnell and J. N. Hefner. *Viscous drag reduction in boundary layers*. Progress in Astronautics, Aeronautics, vol. 123, American Institute of Aeronautics, and Astronautics, Washington, D.C, 1990.

[219] J. L. Lumley and G. R. Newman. "The return to isotropy of homogeneous turbulence". In: *Journal of Fluid Mechanics* 82.1 (1977), pp. 161–178.

[220] J. L. Lumley. "Computational modeling of turbulent flows". In: *Advances in Applied Mechanics* 18 (1979), pp. 123–176.

[221] O. Oyewola, L. Djenidi, and R. A. Antonia. "Influence of localised wall suction on the anisotropy of the Reynolds stress tensor in a turbulent boundary layer". In: *Experiments in Fluids* 37.2 (2004), pp. 187–193.

[222] J. Jovanovic. *The statistical dynamics of turbulence*. Springer Science & Business Media, 2013.

[223] A. J. Simonsen and P. Å Krogstad. "Turbulent stress invariant analysis: Clarification of existing terminology". In: *Physics of Fluids* 17.8 (2005), p. 088103.

[224] S. B. Pope. *Turbulent flows*. Cambridge University Press, 2000.

[225] D. J. Moreau and C. J. Doolan. "Flow-induced sound of wall-mounted finite length cylinders". In: *AIAA journal* 51.10 (2013), pp. 2493–2502.